Recognition of Some Metal Ions Using N,N-, N,O- or N,S-Donor Ligands and Cytotoxicity, Cell Imaging Studies

A Dissertation Submitted to the
Indian Institute of Technology Guwahati as
Partial Fulfillment for the Degree of Doctor of Philosophy
in Chemistry

by

SATYAJIT MAHATA
Roll No. 166122020

Department of Chemistry
Indian Institute of Technology Guwahati
Guwahati – 781 039

JANUARY 2022

DEDICATED

TO

MY FAMILY AND FRIENDS.....

Never say 'NO', Never say,

'I cannot', for you are infinite.

All the power is within you.

You can do anything.

.....Swami Vivekananda

DEPARTMENT OF CHEMISTRY
INDIAN INSTITUTE OF TECHNOLOGY GUWAHATI
GUWAHATI–781039

DECLARATION

I do hereby declare that the research work embodied in this thesis entitled "**Recognition of Some Metal Ions Using N,N-, N,O- or N,S-Donor Ligands and Cytotoxicity, Cell Imaging Studies**" is the outcome of research work carried out by me under the supervision of Prof. V. Manivannan, at the Department of Chemistry, Indian Institute of Technology Guwahati, Assam, India.

In keeping with the general practice of reporting scientific observations, due acknowledgments have been made wherever the work described is based on the findings of other investigators.

Satyajit Mahata

IIT Guwahati — Satyajit Mahata

January, 2022 — (Roll.No.-166122020)

Dr. V. Manivannan
Professor
Department of Chemistry
Indian Institute of Technology
Guwahati-781039
Assam, INDIA

Ph: +91 361 258 2306 (O)
E-mail: mani@iitg.ac.in

CERTIFICATE

This is to certify that the research work presented in this thesis entitled "**Recognition of Some Metal Ions Using N,N-, N,O- or N,S-Donor Ligands and Cytotoxicity, Cell Imaging Studies**" is an authentic record of the results obtained from the research work carried out by **Satyajit Mahata** under my supervision in the Department of Chemistry, Indian Institute of Technology Guwahati, India. This work is original and has not been submitted elsewhere for a degree.

V. Manivannan

IIT Guwahati
January, 2022

Prof. V. Manivannan
(Thesis Supervisor)

ACKNOWLEDGEMENTS

Today my thesis might have seen to a successful end unless I had the support and encouragement of numerous people around me. On the verge of completing my PhD journey, I offer my sincere gratitude to every person who helped me in various ways during this tenure.

I am incredibly grateful to my supervisor for his constant guidance and encouragement throughout the last five years. During this time, his valuable suggestions, observations and patience helped me to carry out the research work for successful completion.

I want to acknowledge my sincere gratitude to the doctoral committee members for their valuable suggestions. I am also thankful to the entire faculty and staff in the Department of Chemistry, Indian Institute of Technology Guwahati for providing the working environment throughout this period. I also want to acknowledge Prof. Biman B. Mandal in the Biomaterials and Tissue Engineering Laboratory, Department of Biosciences and Bioengineering, Indian Institute of Technology Guwahati for his cordial help in studying the valuable biological works.

A special thanks to the Central Instruments Facility of the Indian Institute of Technology Guwahati for providing various instrumental facilities.

I am delighted to have friends like Asesh Das, Mihir Manna, Adit Kumar Shah, Gobinda Dolai, Tanumoy Sarkar, Kanu Das, Chiranjib Gogoi and Sandip Mondal.

My heartiest gratefulness goes towards my lab mates Nibedita Behera, Jugal Bori, Araghni Bhattacharya, Sandeep Kumar, Amlan Ranjan Rayasingh, Anisha Mondal for their cooperation during this period. I am thankful to Sourodeep Dey, Jadi Praveen Kumar and G Janani for performing the biological experiments.

The financial support from Indian Institute of Technology Guwahati is duly acknowledged.

Finally, I would like to thank my parents and family members for their blessings, patience, and encouragement during this long period without which it was impossible to complete my PhD degree.

Satyajit Mahata

Preface

This Thesis contains five chapters. Chapter 1 is about Introduction, Materials and Methods. In this chapter introduction about Fluorescence and various sensing mechanisms are explained. Some recent literature reports based on metal ion detection using different fluorescent probes have been discussed. Along with this, materials, methods and instrumentation related to this thesis are described in details. In Chapter 2 the heterocyclic probe 3-(1-isoquinolinyl)imidazo[5, 1-*a*]isoquinoline (**L1**) in CH_3OH/HEPES buffer system (5 mM, pH = 7.4, 6:4, *v/v*), exhibits blue fluorescence (λ_{em} = 454 nm) upon excitation with 359 nm light. Upon adding Pd^{2+} ion solution, **L1** shows "*turn-off*" response. Job's plot and ESI mass spectrometric analysis reveal a 1:1 ratio for binding of **L1** with Pd(II) ion. DFT/TDDFT calculations performed on $[Pd(\mathbf{L1})Cl(CH_3CN)]^+$ ion support the experimental findings. Fluorescence imaging in the absence and presence of Pd^{2+} revealed that **L1** can be successfully applied on living cells with outstanding sensitivity. In Chapter 3 the heterocyclic probe 3-(2-hydroxyphenyl)imidazo[5, 1-*a*]isoquinoline (**L2H**) has exhibited specific recognition of Cu^{2+} ion by forming a complex of formula $[Cu(\mathbf{L2})_2]$, which in turn showed recognition for CN^- ions with in CH_3CN/aqueous HEPES-buffer solution (5 mM, pH = 7.4, 6:4, *v/v*). Based on the cytotoxic analysis, 5 μM of **L2H** was selected for determining its fluorescence attributes in cellular imaging in MDA-MB-231 and HDF cells. In Chapter 4 Schiff base probe (**L3**) containing coumarin and pyrene moieties is synthesized and characterized which can detect trivalent M(III) ions (M = Al, Cr and Fe) through "OFF-ON" fluorescence process. Fluorescence intensity of these M(III) bound **L3** complexes is quenched by fluoride ions. From cytotoxicity analysis, 7.5 μM of probe **L3** was selected to analyze its fluorescence attributes in cellular imaging. In Chapter 5 the probe (**L4**) having hydrazinecarbothioamide and 1,8-naphthalimide moieties has been synthesized and evaluated for its metal ion sensing ability. It exhibits a selective and sensitive colorimetric as well as fluorescent recognition of Hg^{2+} and Ag^+ ions in CH_3OH - HEPES buffer solution (5 mM, 7:3, *v/v*, pH = 7.4). The DFT/TDDFT calculation has revealed a decrease in energy of the HOMO-LUMO gap in mercury and silver complex thereby supporting the experimentally observed red shift in absorption bands. Based on the cytotoxic assay, 5 μM concentration of probe **L4** was considered for intracellular detection of Hg^{2+} and Ag^+ ions in MDA-MB-231 and HDF cells through "*turn-on*" fluorescence response.

Table of Contents

Chapter 1

Introduction, Materials and Methods

Abstract:

In this chapter an attempt has been explored concisely about the fluorescence and sensing mechanisms. Designing of fluorescence signalling unit is described. Various sensing mechanisms such as Dexter energy transfer, photo-induced electron transfer (PET), internal charge transfer (ICT), fluorescence resonance energy transfer (FRET), photo-induced excimer/exciplex formation, excited-state intramolecular proton transfer (ESIPT), C=N isomerisation and aggregation-induced emission (AIE) have been widely discussed for designing of various unique probe molecules. Along with this, based on selected recent literature reports recent developments in metal ion sensing using different fluorogenic probes have been highlighted. At the end of this chapter, materials and their commercial sources, preparation of samples, methods of spectral analysis, specifications of the instruments used for the characterization of the compounds are also briefed.

1. Introduction

1.1. Fluorescence and sensing mechanisms

Coordination chemistry plays an important role in the design and synthesis of fluorescent probes or chemosensors for specific and selective detection of metal ions.[1] It is seen that fluorescent probes have created remarkable attention in both analytical sensing and optical imaging applications due to their simplicity, high sensitivity and quick response.[2-7] Owing to the instrumental flexibility, commercial accessibility, lower detection limit, *in situ* and *in vivo* detection ability, fluorescence techniques have made highly attractive in biological and environmental sciences.[8-12] Fluorescence is an optical phenomenon in which a beam of light that excites the electron in the molecule of certain compounds, and causes them to emit light. There are two essential features to be a fluorescent sensor for metals i.e., chelating unit for metal ion binding and a fluorophore unit for absorbing and emitting light. The main characteristics for a molecule to be a sensor is that photophysical property of the organic receptor or the molecular structure of the sensor will be altered after binding with metal ions and this happens due to electronic perturbation in the sensor that generates fluorescence signal. This change in the electronic structure leads to change in wavelength and/or intensity of absorption and emission light.

Whereas the orientation or distance between a pair of fluorophores that serve as a donor-acceptor pair is altered with changes in the molecular structure.[13] This change generally happens due to metal ion induced electronic communication from metal ion bound receptor unit to the fluorophore unit. Consequent to metal ion binding with the receptor, two types of changes often encountered are either decrease or increase in fluorescence intensity. If upon binding of metal ion by the receptor or the probe lead to an increase of fluorescence intensity, then it will be Chelation-Enhanced Fluorescence (CHEF) or "*turn-on*" fluorescence response, whereas decrease in fluorescence intensity is called Chelation-Enhanced Quenching (CHEQ) or "*turn-off*" fluorescence response.

In nature a large number of transition metal ions are present and they play crucial role in many biological functions.[14] However, if we accumulate excessive amount of these transition metal ions in our body, it may create several diseases[15] and ultimately may lead to fatal consequences. Therefore, it is necessary to know the appropriate distribution of these metal ions inside the cell for better understanding the physiological conditions. Now for detection

and measuring of the analyte concentration with high precision, fluorescence spectroscopy is a very sensitive method. In designing the sensor system, we generally incorporate a signalling (fluorophore) unit and guest-binding (receptor) moieties that are directly joined or they are covalently attached with a spacer unit (Fig. 1). Between these two, the one in which the fluorophore unit is attached with the receptor through a spacer is more favoured because either the fluorophore or the receptor or both fluorophore and receptor units can simultaneously be varied at will.[16]

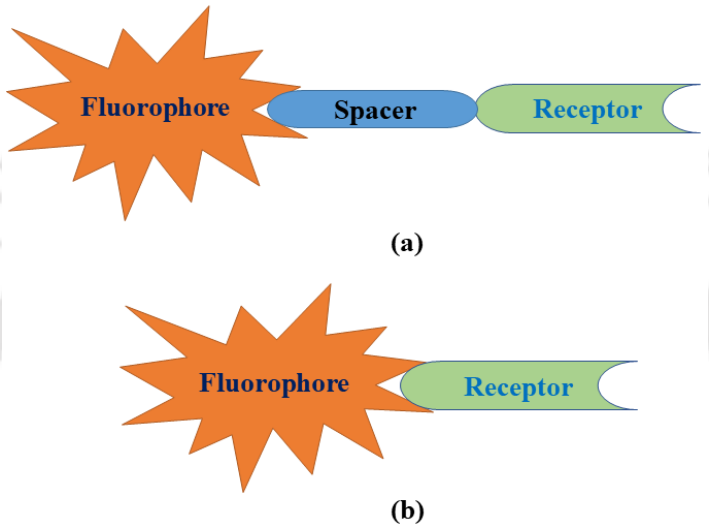

Fig. 1 Design of fluorescence signalling unit (a) Fluorophore and receptor unit linked through spacer signalling unit and (b) Fluorophore and receptor joined signalling unit.

Perfect condition of an ideal chemosensor depends on the fact that the chemosensor will be able to recognise a specific metal ion with high selectivity and sensitivity over different competing metal ions. Therefore, it is necessary to design chemosensors newly, based on recognition and binding principles or to make small changes of the existing mechanisms by making as much effective as possible. To make a preferable coordination of the metal ion, we have to place the suitable donor groups at properly oriented positions so that they can easily bind with metal ions. Upon coordination of metal ion to the receptor there can be changes in fluorescence intensity, lifetime measurement, excitation and emission maxima to indicate the presence of metal ion. Before choosing fluorophores we have to consider some important facts like excitation and emission properties of the fluorophore, solubility, photochemical and thermal stability, magnitude of the Stokes shift *etc*. A large number of literature reports on the chemosensors or probes are dedicated towards changes in their optical properties upon

binding the analyte. This may be due to various characteristics of fluorophores, different material surfaces (like quantum dots, glass or gold surfaces and carbon nanotubes), polymers, solids-gels and mesoporous materials.[17] These probes have been utilized for chemical or environmental detection of various metal ions based on different sensing mechanisms. In some cases, they have been also used for biological detection of transition metals through cell imaging study. Thus, it is essential that in the design of fluorescent probes, there should be intramolecular interaction between the fluorophore and receptor. Conventional mechanisms such as Dexter energy transfer,[18] photo-induced electron transfer (PET),[19,20] internal charge transfer (ICT),[21] fluorescence resonance energy transfer (FRET)[22,23], photo-induced excimer/exciplex formation[24-26], excited-state intramolecular proton transfer (ESIPT),[27-29] C=N isomerisation[30] and aggregation-induced emission (AIE),[31,32] have been widely used for designing of various unique probe molecules.

1.1.1. Dexter energy transfer:

Energy transfer may take place between a photoexcited fluorophore and transition metals that contains partially filled *d*-orbitals of appropriate energy through a double electron exchange process (Fig. 2). This type of energy transfer was first elaborated by Dexter. In Dexter energy transfer process, an excited electron from donor molecule is transferred to the acceptor molecule through a bridge that is linked with bonded and non-bonded interactions.

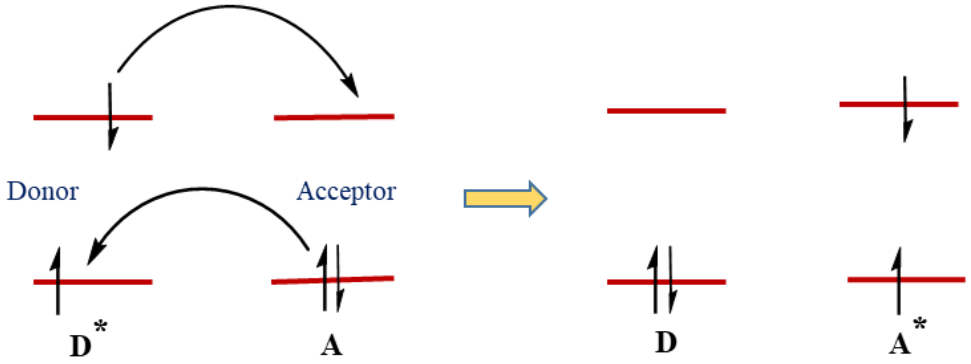

Fig. 2 Schematic representation of Dexter energy transfer process.

As this process requires wave function overlap, it will be allowed in case of very short distances near about less than 10 Å. Various metal ions can quench the fluorescence intensity of organic fluorophores through this electron exchange mechanism.[33,34] So this process will not be appropriate for design of "*turn-on*" sensors in which the fluorescence signal is enhanced in response to metal ions.

1.1.2. Photo Induced Electron Transfer (PET) mechanism:

Upon metal ion binding, fluorescence properties can be attributed to electron transfer between metal and fluorophore unit or within a self-contained fluorophore-chelate unit. For this process, it is required to generate charge separation with excitation of the donor group by light. So this process is typically assigned as photoinduced electron transfer (PET). In this process an excited electron is transferred from donor unit to the acceptor unit. Due to charge separation internal redox reaction takes place between the excited state of the fluorophore unit and the metal ion. Generally, PET process is related to the electron pair located on the hetero atom such as N, O, S and P, for their stronger reducing and oxidizing nature in the excited state.

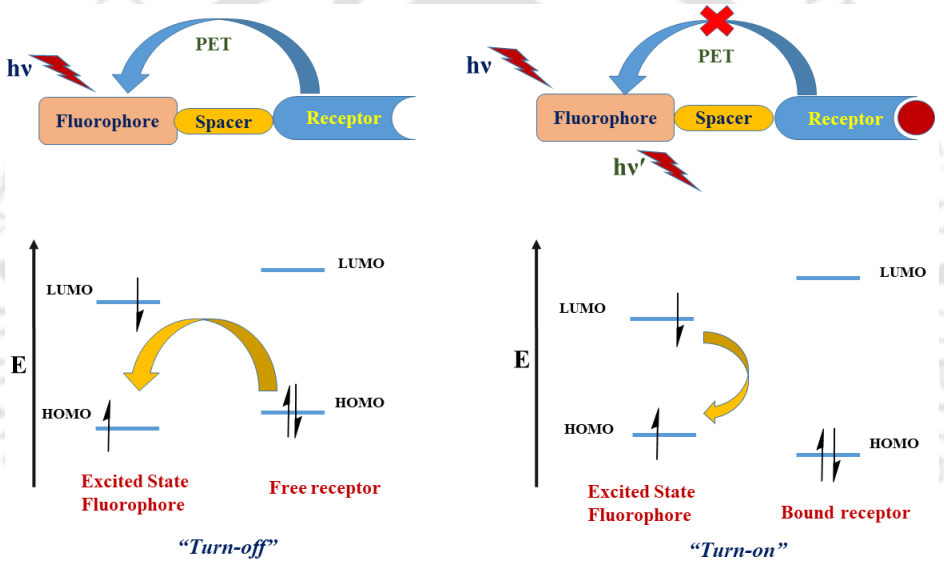

Fig. 3 Schematic representation of "*turn-on*" fluorescence response through inhibition of PET process.

Upon complexation with metal ions the lone pair of these heteroatoms is completely arrested by lowering the energy level. A "*turn-on*" fluorescence signal results through transfer of the electron LUMO to HOMO of the fluorophore unit (Fig. 3). A weak fluorescence molecule shows strong fluorescence in presence of various analytes by inhibition of PET process.

1.1.3. Charge Transfer (CT) mechanism:

Fluorescence enhancement or quenching may be encountered due to charge transfer process. There are two types of charge transfer processes *viz*., intramolecular and intermolecular charge transfer processes. In case of intramolecular charge transfer process, electron is

transferred directly from donor unit to the acceptor unit upon excitation. Whereas in intermolecular process, electron transfer takes place from donor to acceptor unit *via* a spacer. Coordination of metal ion to the acceptor or donor site of the chemosensor results in either red shift or blue shift in the excitation or emission peak. If the metal ion coordination takes place at the donor site of a ICT (Internal charge transfer) based fluorophore then it will increase the energy gap of HOMO and LUMO resulting hypsochromic shift in excitation or emission peak. Bathchromic shift in wavelength will be observed upon coordination of metal ions to the acceptor site of the fluorophore (Fig. 4).

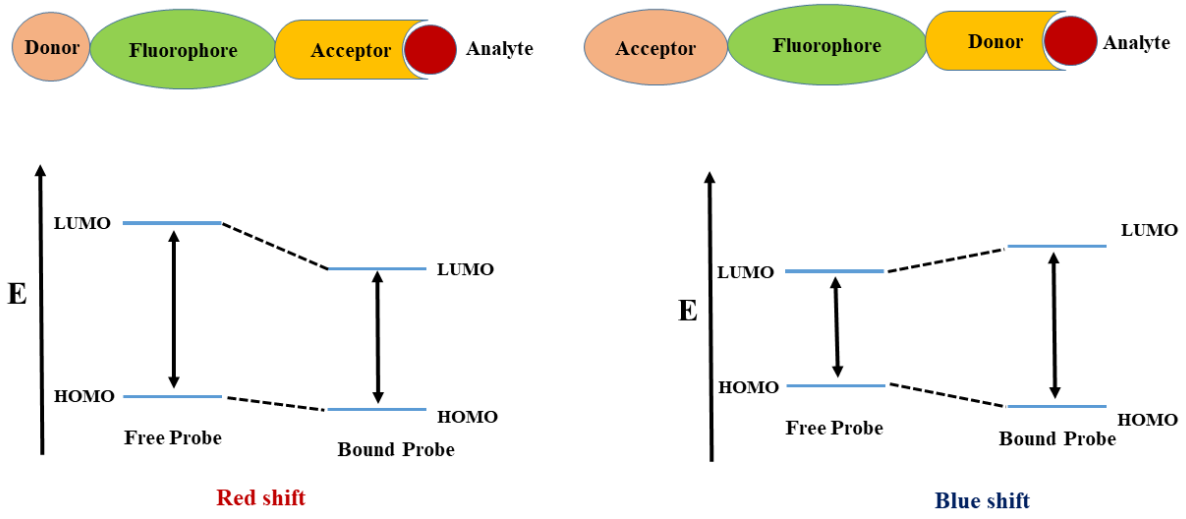

Fig. 4 Schematic presentation of charge transfer mechanism.

1.1.4. Fluorescence Resonance Energy Transfer (FRET):

FRET is a non-radiative energy transfer process that involves the resonance energy transfer between an excited state of a donor fluorophore (D–F) and the ground state of an acceptor fluorophore (A–F) through ‘‘dipole–dipole coupling’’.[35] Effective FRET process takes place when the donor and acceptor units are in close proximity (10-100 Å) to each other so that there will be a considerable overlap between emission spectra of the donor moiety and absorption spectra of the acceptor moiety. Greater overlap will create more effective FRET.

In fluorescence sensing, coordination of metal ion generally decreases the distance between the donor and acceptor unit.

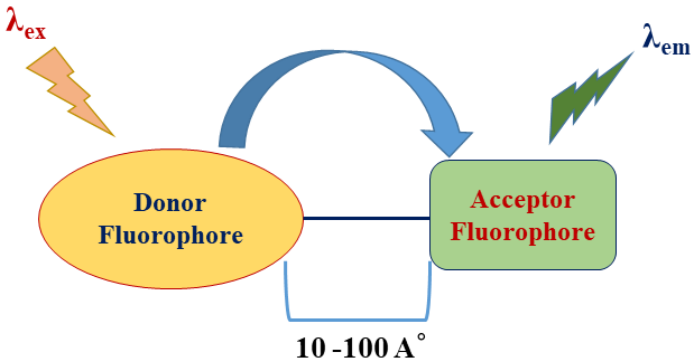

Fig. 5 Scheme of FRET process.

FRET phenomenon is the reason for decrease in donor emission and lifetime, which can be understood by monitoring donor wavelength only. For measuring the donor emission and sensitized emission, two fluorophores are generally employed to all FRET based metal ion sensor to establish ratiometricity. FRET ratio is measured by taking the ratio between sensitized acceptor emission and donor emission. Sensing can be achieved by promoting or disrupting FRET through changes in molecular structure that results in altering either distance, orientation, or both by metal binding.

1.1.5. Monomer excimer formation:

Formation of an excimer (excited dimer) takes place from two species that is a short-lived dimeric or heterodimeric molecule. An excimer is a species that consists of a fluorophore in the excited state with another non-excited fluorophore molecule in the ground state through various weak interactions like π–π* stacking or van der Waals interactions.[36] As shown in Fig. 6 probes of this type consist of two identical fluorophore moieties bridged by a flexible spacer with donor sites, making it capable of being an ionophore. Metal ion facilitates spatial rearrangement of the spacer in such a way that the two fluorephores come in close proximity (within van der Waals contact) and that causes weak interactions between them. This interaction is enhanced upon excitation of one fluorophore, leading to the formation of the excimer formation. A typical observation of red shift and broadening of the peak is consequential of the excimer formation. The emission bands of both monomer and excimer are generally observed simultaneously. Through metal ion coordination, ratio of monomer and excimer emission is altered that helps the design of a ratiometric sensor.

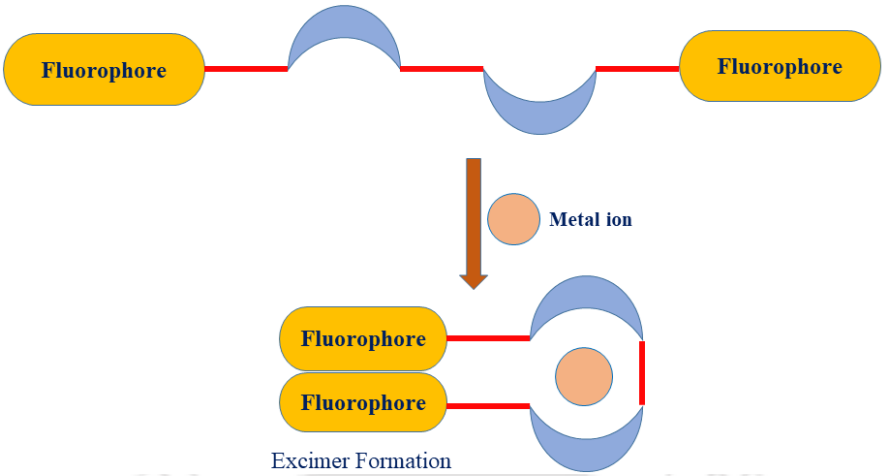

Fig. 6 Monomer excimer based sensing mechanism.

For the synthesis of probes based on monomer excimer formation, molecule containing extended π-delocalized planar ring like pyrene molecule, as the monomer are preferred. Generally, they exhibit poor solubility in aqueous medium. However, this process is very much dependent on the distance that results after metal coordination with excimer unit and hence it is difficult to predict the distance.

1.1.6. Excited State Intramolecular Proton Transfer (ESIPT):

Organic molecules that exhibit ESIPT process (excited state intramolecular proton transfer) has characteristics that depends on the surrounding medium and reveal large Stokes shift of emission.[37,38] In these probes, excited state energy level tends to decrease through shifting of a hydroxyl or amino group proton to a neighbouring hydrogen-bonding atom (e.g., carbonyl oxygen, or imine nitrogen). ESIPT process happens very fast in a time scale of sub picosecond. The energetically favoured enol-form (Form A) is transferred into keto-form (Form B) to the ground state through reversed proton transfer process. Due to formation of more stable excited molecule i.e., tautomer S_1' the ESIPT process yields large Stokes shift emission. In case of sufficiently higher acidic nature of hydroxyl or amino group proton, ESIPT process may be interrupted after coordination with metal ions by removal of the proton (Fig. 7). As a result, there will be a blue shift in the emission.

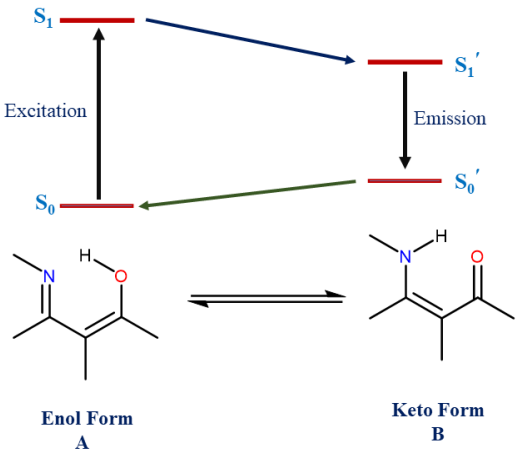

Fig. 7 Mechanism of ESIPT based fluorescence probes towards metal cations.

In ESIPT based fluorophores, emission properties are influenced by many factors like pH of the medium, solvent polarity or hydrogen bonding ability, which may restrict its use in bioimaging studies.

1.1.7. C=N isomerization:

The C=N isomerization as a signaling mechanism originated from the study on photophysical properties of conformationally restricted compounds. It has been found that C=N isomerization is the most important decay process of excited states in compounds containing an unbridged C=N structure and hence those compounds are often non-fluorescent.[39-41] In contrast, fluorescence of their analogs containing a covalently bridged C=N structure increases dramatically due to the suppression of C=N isomerization in the excited states (Fig. 8).

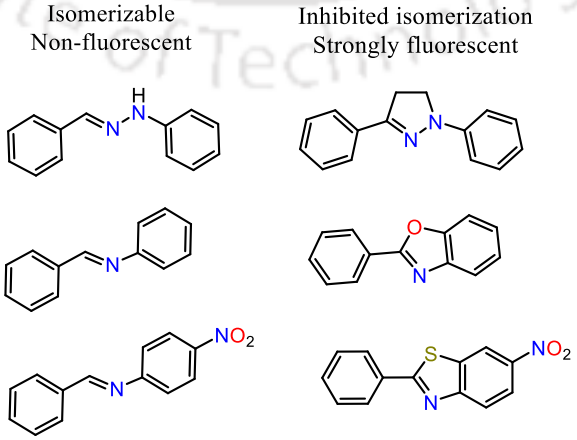

Fig. 8 Molecular structures of unbridged and bridged C=N containing compounds.

Therefore, it can be reasonably expected that C=N isomerization may also be inhibited through complexation of a guest species to a sophisticatedly designed fluorescent-sensing molecule rather than the covalent bridging of the C=N bond.

1.1.8. Aggregation Induced Emission (AIE) and Aggregation Caused Quenching (ACQ):

The photophysical phenomenon associated with chromophore aggregation is called Aggregation Induced Emission (AIE). The luminogens which does not show any emission form an aggregate which induces emission.[42] Currently AIE phenomenon paved the way to an emerging and important field of research for its potential application in organic light emitting diodes (OLEDs), organic field-effect transistors (OFETs), solar cells, laser dyes etc.[43-45] AIE based probes are being employed meticulously for *in vivo* bio imaging and phototheranostatics studies, research on cancer cells.[46,47] As most of the AIE based molecules contain organic luminogens, they are highly soluble in organic solvents. As a result of that they are weakly emissive in organic solvents but in non-organic (water/buffer) solvents the luminogens aggregate and show strong emission band.[48,49] In aggregated or solid-state, restriction in intramolecular rotation (RIR), intramolecular vibration (RIV) and/or intramolecular motion (RIM) within the molecule lead to the appearance of AIE properties.[50] On the other hand some fluorophore show quenching in fluorescence intensity upon aggregation in solvent medium. This phenomenon is referred as Aggregation Caused Quenching (ACQ).

1.2. Recent developments in metal ion sensing using different fluorogenic probes:

In this section, some selected reports on mechanisms described above are discussed. A chemosensor containing pyrene and antipyrine unit was reported for thorium(IV) detection through "*turn-on*" fluorescence resoponse.[51] Chemosensor (**1**) showed weak fluorescence due to operation of photoinduced electron transfer (PET) process occurring from involvement of lone pair of electrons on the imine group nitrogen with pyrene ring. Nitrate salt of thorium was used for the sensing process. Complexation of Th(IV) with **1** resulted enhancement in emission intensity by the inhibition of PET process. A visual colour change from yellow to colourless was observed upon gradual addition of Th(IV) into probe **1** solution and a blue shift (from 446 to 418 nm) was observed in emission spectrum.

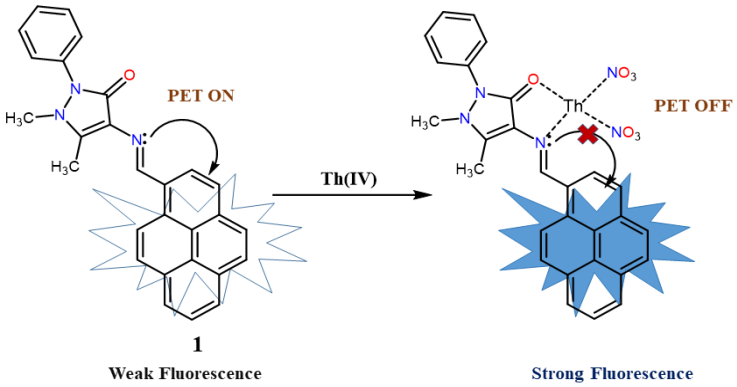

Scheme 1 Proposed Binding mode of Th(IV) with **1**.

Probe **2** was synthesized for detection of divalent Fe^{2+} and Cu^{2+} ions through both colorimetric and fluorescence methods.[52] Probe **2** exhibited fluorescence intensity enhancement upon binding with Fe^{2+} ion by restriction of PET process, on the other hand exhibited quenching of fluorescence intensity after addition of Cu^{2+} ion, through charge-transfer process.

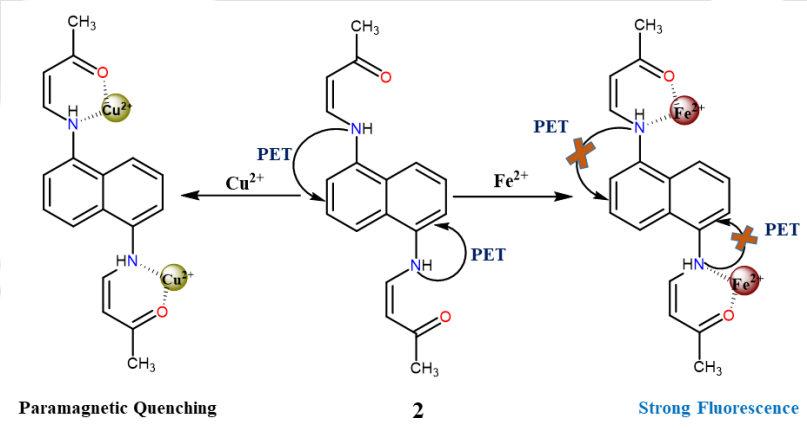

Scheme 2 Binding mode of probe **2** for the detection of Fe^{2+} and Cu^{2+}.

A Schiff base was designed and synthesized by condensation of 2-hydroxynaphthaldehyde and diethylenetriamine for Al^{3+} ion detection.[53] Nitrate salt of aluminium was used in this sensing process. Chelation of Al^{3+} with **3** decreased the ICT process thereby rendering an enhancement in fluorescence intensity (Scheme 3).

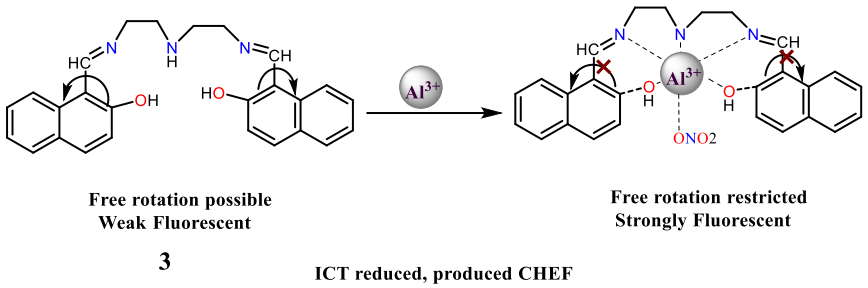

Scheme 3 ICT based probe for Al^{3+} ion detection.

A coumarin and benzothiazole based probe **4** was designed for recognition of Cu^{2+} ions in presence of various interfering metal ions through UV-Visible and fluorescence spectral studies.[54] Copper nitrate was taken in this sensing process. Proposed sensing mechanism of **4** towards Cu^{2+} ion was through chelation enhanced quenching (CHEQ) and intramolecular charge transfer (ICT) processes.

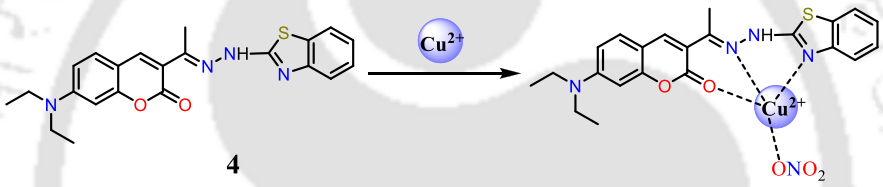

Scheme 4 Binding mode of Cu^{2+} ion with probe **4**.

For generating a FRET pair, probe **5** was designed by covalently linking BODIPY and rhodamine units, as a fluorescent donor-acceptor system for recognition of Hg^{2+} ion.[55] Thiosemicarbazide moiety present in the probe **5** underwent cyclization to form 1,3,4-oxadiazole ring upon interaction with Hg^{2+} thereby allowing FRET process.

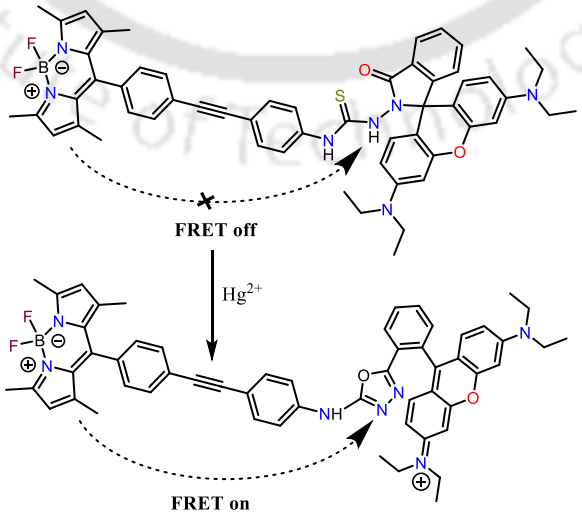

Scheme 5 FRET based probe **5** containing BODIPY and rhodamine unit for Hg^{2+} detection.

A probe **6** bearing quinoline–benzothiazole and rhodamine units was designed for ratiometric Cd^{2+} ion sensing.[56] Chloride salt of cadmium was used. Ring opening of spirolactam of the rhodamine moiety occurred that allowed operation of FRET process from quinoline–benzothiazole to rhodamine moiety.

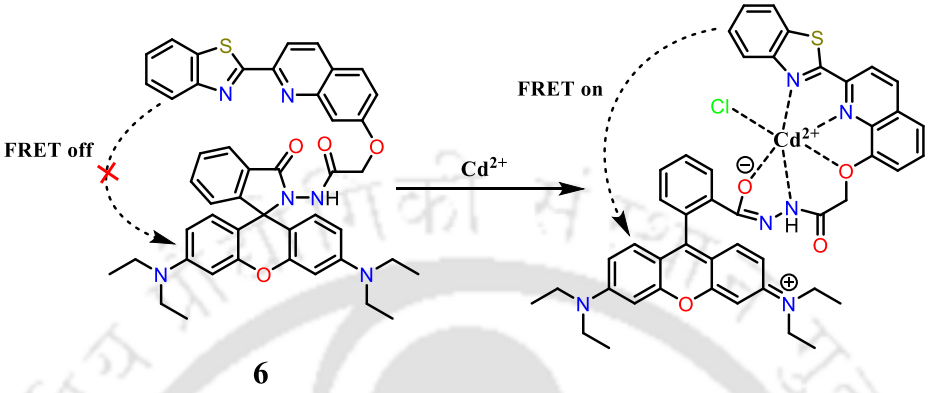

6

Scheme 6 Cd^{2+} ion detection using FRET based probe **6**.

Based on FRET mechanism, a strip of rhodamine tethered with carbon nanodots **7** was designed for the detection of Al^{3+} ion.[57] Probe **7** consisted rhodamine B moieties immobilized on the surface of water-soluble C-dots. Probe **7** showed enhancement in emission intensity upon addition of Al^{3+} ion. Its binding occurred through chelation of the rhodamine moiety with Al^{3+} ion that induced opening of rhodamine ring. As a result a spectral overlap happened between absorptions due by C-dots (that acts as donor unit) and emission of ring-opened rhodamine unit (that acts as acceptor unit)

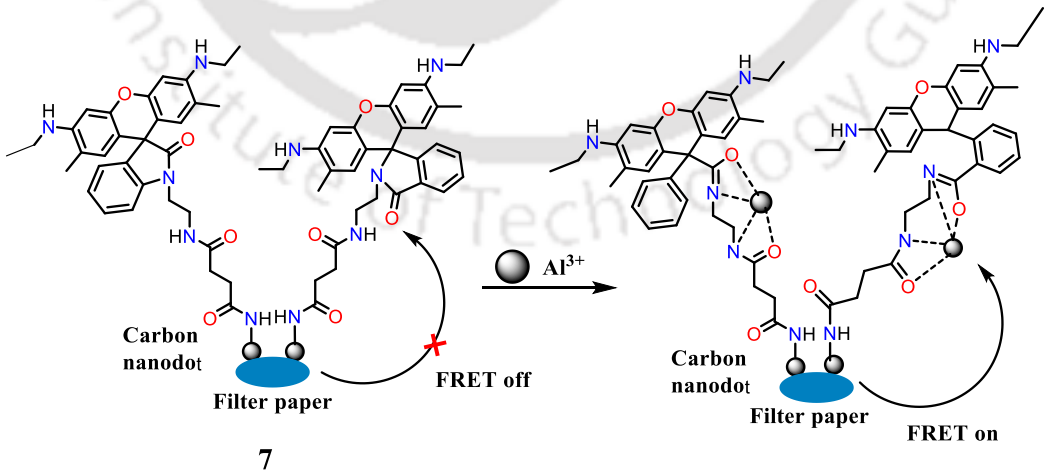

7

Scheme 7 Detection of Al^{3+} using a FRET-Based C-dots-rhodamine probe **7**.

Molecule **8** containing two pyrene rings was synthesized that exhibited formation of intramolecular excimer in solution.[58] In a mixed organic-aqueous solvent, interaction of Cu^{2+} and Hg^{2+} ions with **8** produced an interruption of excimer formation of **8**. Metal ion coordination with **8** lead to the selective detection of these two ions through excimer *switch off* process.

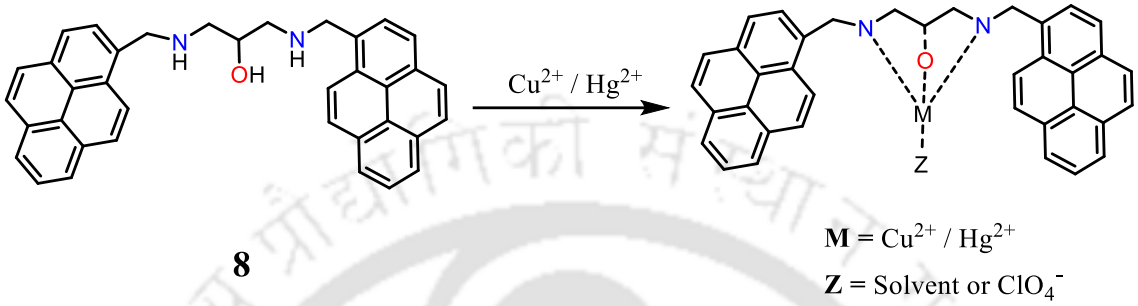

8

Scheme 8 Fluorescence sensing of Cu^{2+} and Hg^{2+} ions with molecule **8** through excimer-*switch off* mechanism.

Based on monomer-excimer mechanism, lower rim calix[4]arenes **9a** and **9b** were synthesized which exhibited selectivity towards detection of Hg^{2+} and Ag^{+}. In these molecules, thiourea unit and pyrene or methylene-pyrene unit were used as spacer and fluorophore respectively.[59]

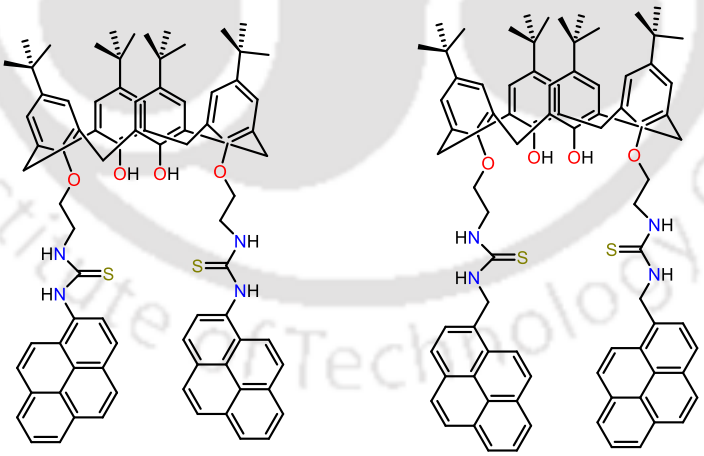

9a **9b**

Scheme 9 Detection of Ag^{+} and Hg^{2+} ions ratiometrically through excimer fluorescence quenching and enhancement.

Probe **10** which functions based on ESIPT process was designed and synthesized for selective detection of Al^{3+} ion.[60] Upon complexation with Al^{3+} ion, ESIPT process in **10** was inhibited and due to CHEF process fluorescence intensity got enhanced.

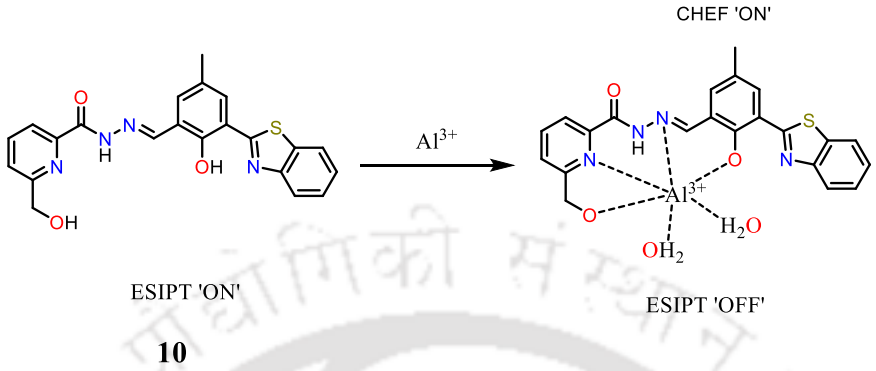

10

Scheme 10 Selective detection of Al^{3+} ion through ESIPT and CHEF mechanisms.

Probe **11** was synthesized for ratiometric detection of Al^{3+} ion through ESIPT process.[61] Molecule **11** showed high selectivity for detection of Al^{3+} ion with a prominent fluorescence color change from pale green to deep blue that was accompanied by a six fold enhancement in emission intensity.

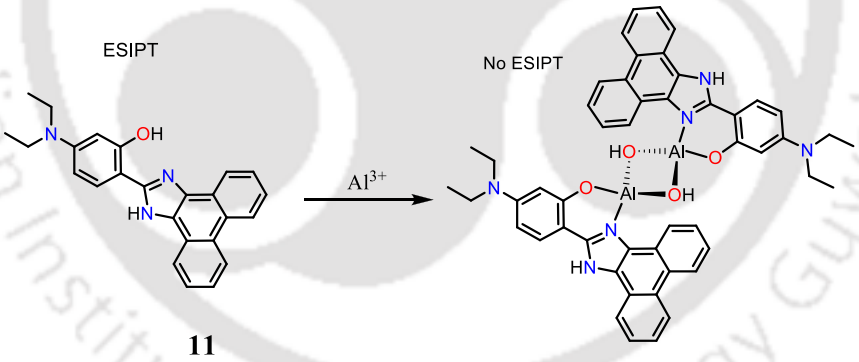

11

Scheme 11 Selective detection of Al^{3+} through ESIPT mechanism.

For ratiometric detection of Zn^{2+} ion, a BINOL-based fluorescent probe **12** was designed and synthesised.[62] Probe **12** detected Zn^{2+} ion through ratiometric fluorescence response based on ESIPT process. After coordination with Zn^{2+} probe **12** displayed a significant variation by shifting emission wavelength more than 100 nm. Emission color change from yellow to blue was seen upon addition of Zn^{2+} into solution of **12**.

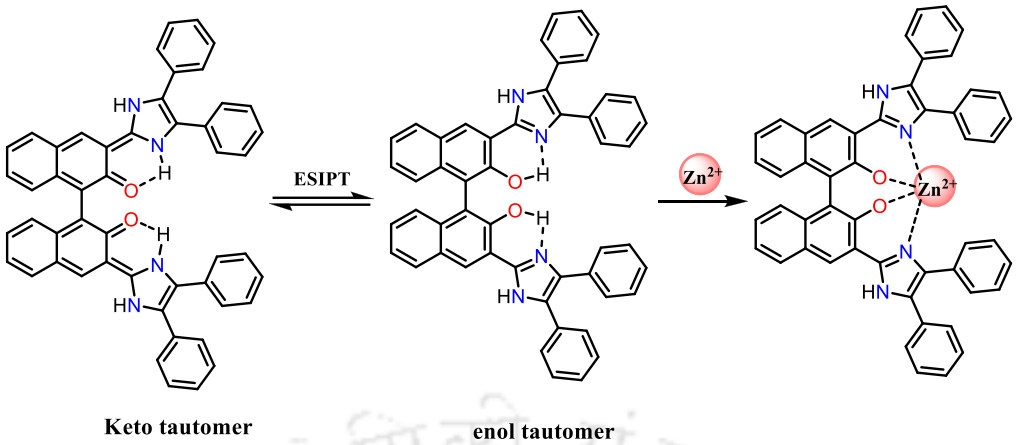

12

Scheme 12 Proposed binding of Zn^{2+} ion to **12**.

Based on C=N isomerization process, a probe **13** containing coumarin unit was synthesized for selective detection of Zn^{2+} ion.[63] Due to rapid isomerization of C=N bond of imine in the excited state, probe **13** was non fluorescent in nature (Scheme 13). But after addition of Zn^{2+} ion, a remarkable enhancement in fluorescence intensity with a red shift in the emission maxima from 500 to 522 nm was observed due to inhibition of C=N isomerization upon coordination of **13** to Zn^{2+} ion.

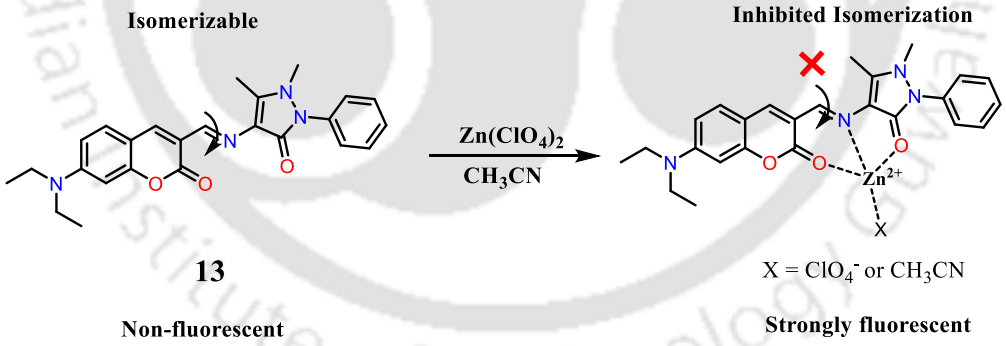

Scheme 13 Schematic presentation of Zn^{2+} binding with **13** that resulted in enhancement of fluorescence intensity by restricting C=N isomerization.

Three phosphorus containing hydrazones were designed for Cu^{2+} ion sensing.[64] In case of **14** and **14a** fluorescence quantum yield values increased 15 and 10 times, respectively upon interaction with Cu^{2+} ions. But in case of hexa-armed probe **14b** similar enhancement in fluorescence quantum yield was not observed. Due to complexation with Cu^{2+} these three molecules exhibited an increase in fluorescence intensity. Large enhancement in fluorescence intensity was observed in case of **14** due to participation of both 'arms' of coumarin and

imine during complexation with Cu^{2+} ion. But due to steric hindrance in **14a** (three armed) and **14b** (hexa armed) C=N isomerization was not completely inhibited and therefore enhancement in fluorescence happened comparatively to lesser extent than **14**.

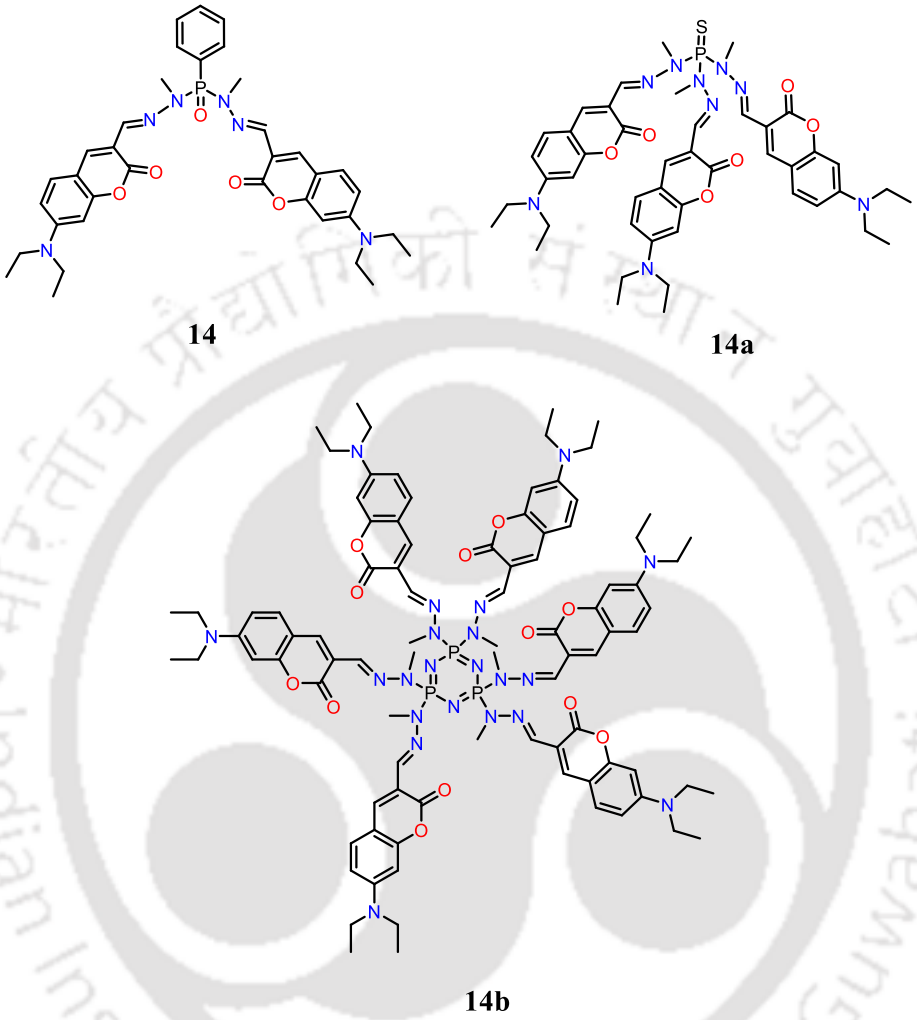

14 **14a** **14b**

Scheme 14 Schematic presentation of three ligands for detection of Cu^{2+} ion based on C=N isomerization.

A Schiff base probe **15** was synthesized for Cu^{2+} ion detection based on aggregation induced emission (AIE) behaviour. Probe **15** showed bright yellow fluorescence through AIE process in DMSO-water medium.[65] Perchlorate salt of copper was used for the sensing process. The aggregated probe selectively detected Cu^{2+} ion over a series of different interfering metal ions through fluorescence "*on-off*" response by CHEQ process.

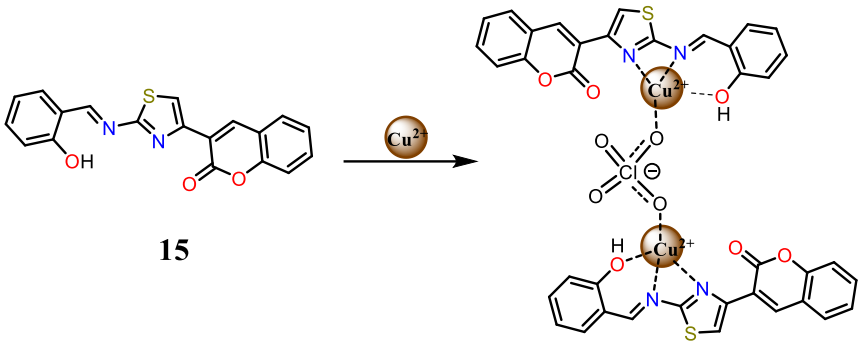

Scheme 15 Proposed sensing mode of **15** with Cu^{2+} ions.

A Schiff base probe **16** containing pyrene unit was synthesized that exhibited high selectivity and sensitivity for fluorescence "*turn-on*" detection of Al^{3+} ion. The probe also displayed AIE enhancement behaviour in its aggregated state upon binding with excess Al^{3+} ion.[66]

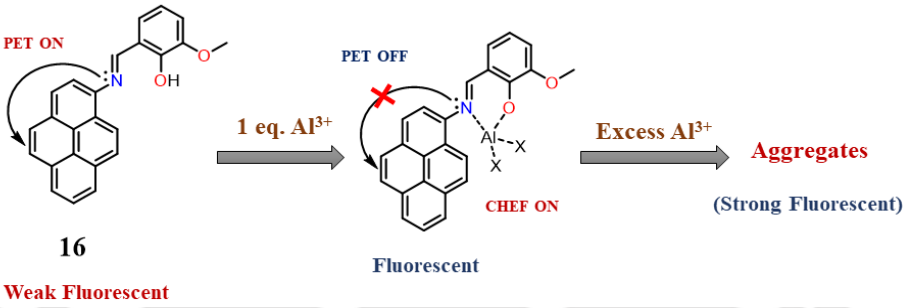

Scheme 16 Proposed sensing mode of **16** with Al^{3+} ion based on complexation and Al^{3+} Induced Aggregation.

Terpyridyl phenyl-substituted triphenylamine based probes **17** and **17a** with AIE properties were synthesized.[67] Terpyridyl units attached with **17** have a prominent effect towards the detection of Zn^{2+}, Cd^{2+} and CN^{-} ions. Probe **17** exhibited significant red-shift and enhanced fluorescent intensity after the addition of Zn^{2+} and Cd^{2+} ions. Probe **17a** was able to detect only CN^{-}.

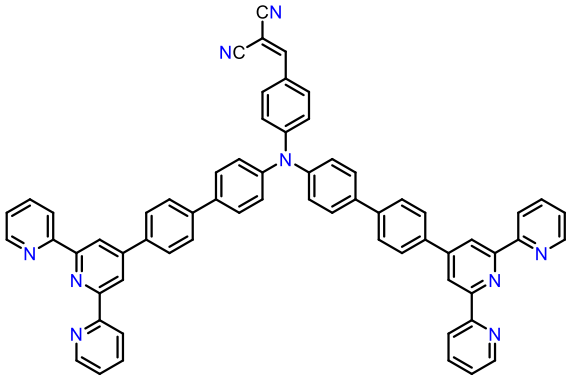

17

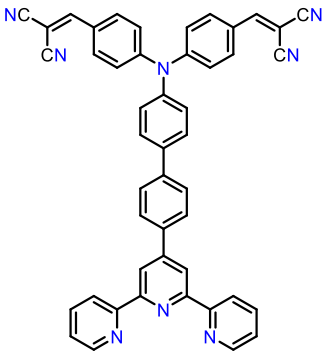

17a

Scheme 17 Fluorescence probes **17** and **17a** with aggregation-induced emission (AIE) characteristics and detection of Cd^{2+}, Zn^{2+} and CN^{-}.

Fluorescent probe **18** was found for ratiometric Pd^{2+} ion recognition based on the FRET and rhodamine ring opening processes.[68] In this probe **18** coumarin unit served as energy donor side and the rhodamine unit as energy acceptor. Probe **18** exhibited two well-separated fluorescence emission peak in presence of Pd^{2+} ion.

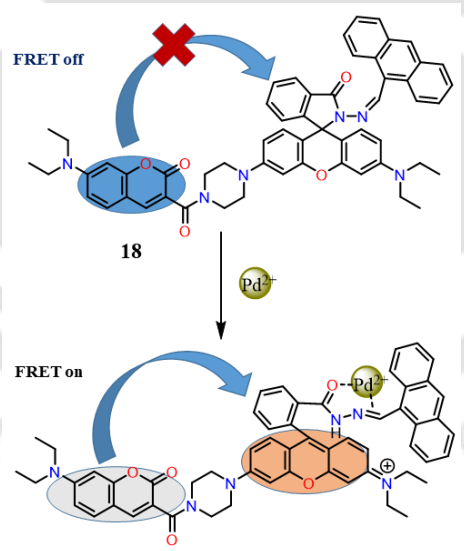

Scheme 18 Binding mode of Pd^{2+} ion with fluorescent probe **18**.

Selective detection of Ba^{2+} was performed using a phenoxazine-based probe **19**.[69] Using DFT studies intramolecular charge transfer (ICT) mechanism was established for the sensing process of Ba^{2+} by **19**. Specific detection of Ba^{2+} in living cells was also studied through live cell imaging in MCF-7 cells.

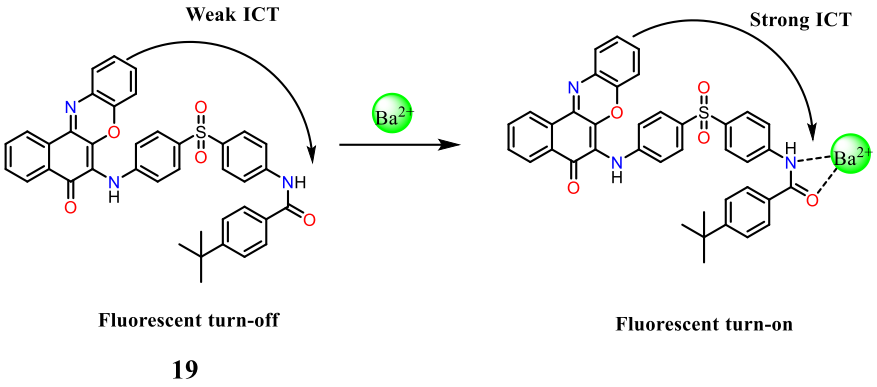

Scheme 19 Sensing of Ba^{2+} ion through ICT Mechanism.

Based on CHEF effect ethylenediamine derivative of a rhodamine 6G silica particle was covalently grafted on the surface of mesoporous silica to generate a fluorescent probe **20** for detection of Fe^{3+}.[70] Rhodamine spirolactam ring opening took place in **20** upon coordination with Fe^{3+} that created enhancement a fluorescence response through CHEF process.

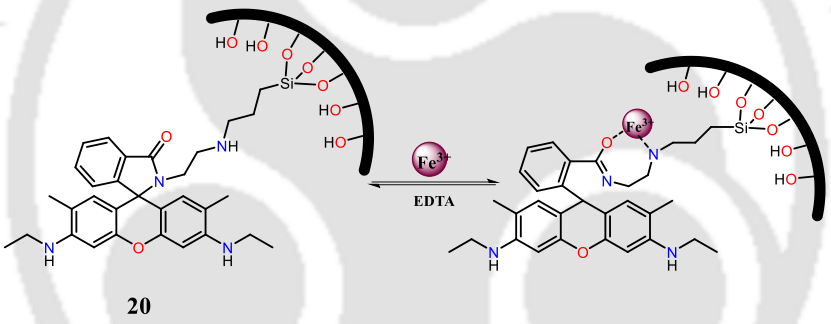

Scheme 20 Chelation of Fe^{3+} with **20**.

Probe **21** exhibited selective colorimetric sensing property for the detection of cobalt(II) ion by changing color from colorless to pale violet color.[71] Probe **21** was also capable for naked eye detection of Co^{2+} with oxidation of Co^{2+} to Co^{3+}. This oxidation of Co^{2+} to Co^{3+} in the complex is taking place by oxygen molecule under aerobic conditions. Proposed sensing mechanism was achieved by the ligand-to-metal charge-transfer process.

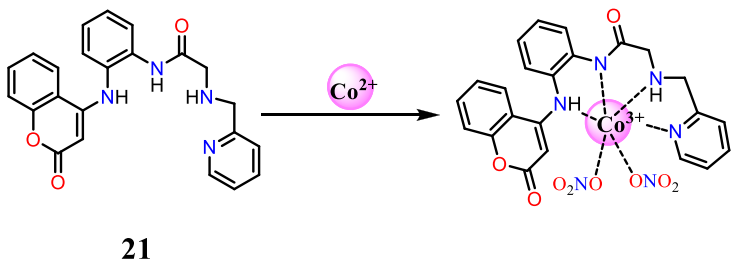

Scheme 21 Possible binding of Co^{3+} with the chemosensor **21**.

Probe **22** containing pyrazoline and benzimidazole groups were designed for selective detection of Ni^{2+} through internal charge transfer (ICT) process. A rapid color change from blue to green was observed upon gradual addition of Ni^{2+} into the solution of **22**.[72]

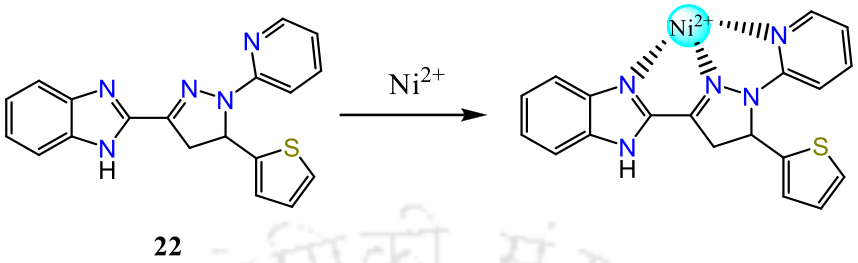

22

Scheme 22 Recognition mechanism of Ni^{2+} ion.

Borondipyrrolemethene-based probe **23** was used for Ag^+ ion detection through "*turn-on*" fluorescence response. A 40-fold fluorescence enhancement was observed upon addition of Ag^+ ion, which operate by inhibiting the PET process.[73]

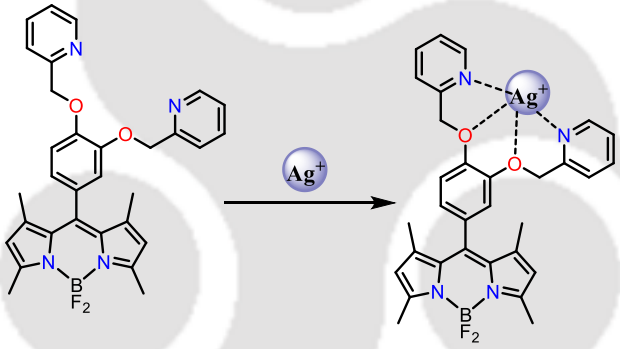

23

Scheme 23 Proposed binding mode of Ag^+ ion with **23**.

A probe **24** was designed by integrating a *Z*-enynol motif into a BODIPY-based fluorophore scaffold.[74] In the presence of gold species, it was observed that substituted *Z*-enynols efficiently cyclized to their corresponding furan derivatives.

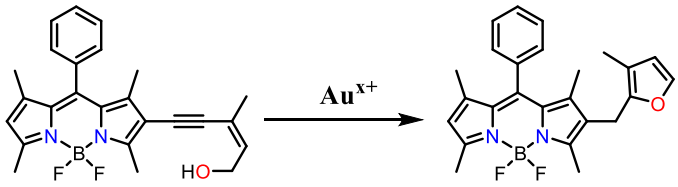

24

Scheme 24 The strategy for ratiometric sensing of gold species with **24**.

For selective detection of trivalent metal ions (Al^{3+}, Fe^{3+} and Cr^{3+}) a colorimetric probe **25** was synthesized. It was observed that probe **25** was able to detect three trivalent metal ions both visually and spectrophotometrically, in presence of other biologically relevant metal ions.[75]

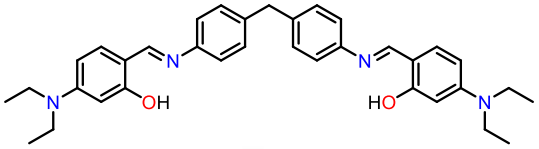

25

Scheme 25 Probe **25** for detection of Al^{3+}, $Fe^{3+}$and Cr^{3+} ions.

Based on monomer-excimer formation principle, probe **26** was synthesized that can selectively detect Pb^{2+} ion ratiometrically. Upon binding through thioether-S with Pb^{2+} ion, probe **26** induced an excimer formation through interaction among pyrene rings, providing ratiometric quantitative determination of lead.[76]

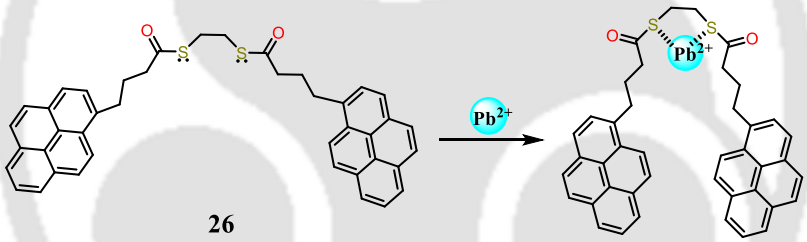

26

Scheme 26 Possible binding mode of Pb^{2+} ion with **26**.

Thiosemicarbazide based probe **27** was developed for the detection of Ce^{4+} ion with *turn-on* fluorescence reponse.[77] Oxidative cyclization took place upon binding with Ce^{4+} ion. The probe **27** showed selectivity towards detection of Ce^{4+} ion in nanomolar level in aqueous ethanolic solvent medium.

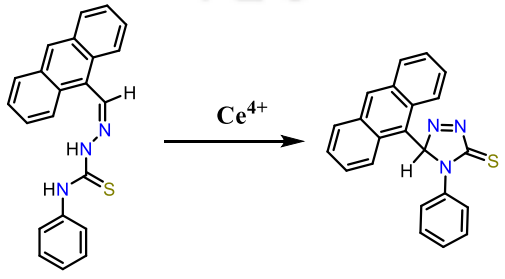

27

Scheme 27 Proposed sensing mode for detection of Ce^{4+} ion with **27**.

1.3. Objective of thesis:

Some fluorophores containing pyrene, BODIPY, benzimidazole, coumarin derivative, benzothiazole, rhodamine, napthalimide and napthyl moieties have been reported in the literature for the selective detection of metal ions. The probe molecules acted as "*turn-on*", "*turn-off*" or "*ratiometric*" sensors for the detection of metal ions. From these background, it was planned to evaluate two 3-substituted imidazo[5,1-*a*]isoquinolines as metal ion sensors along with two other N,O- and N,S- donor ligands.

1.4. Materials and methods:

1.4.1. Materials:

NaCl, KCl, LiCl, $CaCl_2$, $MgCl_2$, $AlCl_3$, $CrCl_3$, $MnCl_2$, $FeCl_3{\cdot}6H_2O$, $FeSO_4{\cdot}7H_2O$, $CoCl_2{\cdot}6H_2O$, $NiCl_2{\cdot}6H_2O$, $CuCl_2{\cdot}2H_2O$, $ZnCl_2$, $CdCl_2$, $HgCl_2$, $Pb(NO_3)_2$, $PdCl_2$, $PtCl_2$, $AuCl_3$, $AgNO_3$, SeO_2, $NH_2NH_2{\cdot}H_2O$, spectroscopic grade DMSO, CH_3CN and MeOH solvents were supplied by Merck India. Ethanolamine and 2-Methoxyethanol were purchased from Alfa Aesar. Isoquinoline, salicylaldehyde, 1-pyrenecarboxaldehyde, naphthylisothiocyanate, HEPES buffer, $CDCl_3$ and DMSO–d_6, were purchased from Sigma Aldrich and 3-aminocoumarin, and 4-bromo-1,8-naphthalic anhydride from TCI Chemicals. All the chemicals and solvents were of reagent grade and were used for synthesis, characterization and experimental work without further purifications.

1.4.2. Instrumentation and methods:

A Perkin Elmer Lambda-35 and an Agilent Cary 100 spectrophotometer were used for recording the absorption spectra with quartz cuvettes of 1 cm path length in the range of 200-800 nm. A Horiba Fluoromax-4 spectrofluorometer was used for recording emission spectra with 1 cm path length quartz cuvettes. Mass spectrum was obtained using a Waters q-ToF Premier mass spectrometer. NMR studies were performed using a Bruker Advance 600 MHz NMR instrument.

1.4.3. UV–Vis and fluorescence spectroscopic studies

Solution studies were carried out using CH_3OH or CH_3CN /aqueous HEPES buffer (5 mM, pH = 7.4, 6:4, *v/v*) and unless otherwise specified, solution refers to this buffered solution. Change in the absolute pH of the resultant solution after adding the trivalent ion is only marginal. Deionised water was used to make stock solutions of all metal chlorides (10×10^{-3}

M), while for $PdCl_2$ small amounts of DMSO was used initially to dissolve and then diluted with deionised water. Stock solution of **L1** (2×10^{-3} M) was prepared in DMSO and diluted to (2×10^{-5} M) with CH_3OH/aqueous HEPES buffer for UV-Visible and fluorescence study. In the UV-Visible and fluorescence experiments, 3.0 mL of **L1** solution (2×10^{-5} M) was placed into a quartz optical cell of 1 cm path length and then adding appropriate amounts of stock solutions of respective metal ions (prepared by dissolving in a minimum amount of DMSO then diluting with buffer). Similar procedures were followed during the preparation of **L2**, **L3** and **L4** solution. The UV-Visible and fluorescence titration experiments were done with the standard 0.1 mM solution metal chloride salts, which were prepared after dilution from the stock solution prepared earlier. For the fluorescence experiment, of **L1** the excitation wavelength used here was 359 nm and the emission spectra were recorded in the range of 379-700 nm. All spectra were taken immediately after 1 minute of mixing of **L1** with the metal chloride solutions.

1.4.4. Fluorescence quantum yield in solution

Two types of procedures were followed for the determination of fluorescence quantum yield in solution. We have followed the Petite integrating Sphere method to determine the quantum yield by Horiba Jobin Yvon Fluoromax-4 Spectrofluorometer for **L1**, **L3** and **L4**. It was measured in CH_3OH/ aqueous HEPES buffer medium with a definite amount of **L1** and its palladium complex by exciting at 359 nm. The equation was employed for the determination of the quantum yield (as per the instruction given in the official website of Horiba).

$$\varphi = [(E_c - E_a)/(L_a - L_c)] \qquad (1)$$

E_c = Emission of the Sample, E_a = Emission of the blank, L_c = Scatter of the Sample & L_a = Scatter of the blank.

Fluorescence quantum yield was calculated for **L2** in CH_3CN / aqueous HEPES solution with respect to quinine sulphate (QS) in 0.1 (M) H_2SO_4, using the following formula.[78]

$$\Phi s = \Phi_R \, (A_R \, F_S / A_S \, F_R)(\eta_S/\eta_R)^2 \qquad (2)$$

Here,

Φ_S = quantum yield of sample; Φ_R = quantum yield of reference; F_S = relative integrated fluorescence intensity of sample; F_R = relative integrated fluorescence intensity of reference; A_R = absorbance of the reference; A_S = absorbance of the sample; η_S = refractive index of sample; η_R = refractive index of reference.

Quantum.Yield of quinine sulphate = 0.54; Refractive Index: water = 1.33

1.4.5. Determination of Stern-Volmer constant

Stern Volmer constant was calculated by the standard procedure of plotting I_0/I *vs* concentration of Pd^{2+} or Cu^{2+} ion.[79]

$$I_0/I = 1 + K_{sv}[Pd^{2+}] \text{ or } [Cu^{2+}] \quad (3)$$

Where, I_0 and I are the fluorescence intensities of the compound **L1** or **L2** in absence and presence Pd^{2+} or Cu^{2+} ions, respectively.

1.4.6. Calculation of Detection Limit

Detection limit of the probe **L1** towards Pd^{2+} ion was determined following the widely used procedure using equation (4). At first, the standard deviation (σ) of fluorescence intensity of emission maximum of the blank (the probe **L1**) was determined 20 times in 2 mins interval each. Then the same was measured after each addition of the $PdCl_2$ solution and plotted against the concentration of Pd^{2+}. Slope of the fitted straight line k was calculated from the plot.[80]

$$\text{Detection limit} = 3\sigma/k \quad (4)$$

To know the binding stoichiometry between **L1** with Pd^{2+} the method of continuous variation of mole-fraction was employed and Job's plot was obtained The binding constant was determined from the Benesi-Hilde-Brand plot after plotting $1/(I-I_0)$ *vs* $1/[Pd^{2+}]$.[81]

$$1 / (I - I_0) = 1 / \{K_b(I_0 - I_{min})[Pd^{2+}]\} + 1/(I_0 - I_{min}) \quad (5)$$

Where, I and I_0 are the emission intensity of **L1** in presence and absence of Pd^{2+} ion and I_{min} is the minimum intensity of **L1** in presence of Pd^{2+} ion. K_b was obtained by the ratio of intercept and slope of plot $1/(I-I_0)$ *vs* $1/[Pd^{2+}]$. Similar methods were applied in case **L2**, **L3** and **L4**.

1.4.7. Time Resolved Fluorescence Spectroscopy

The fluorescence transients were measured by a time correlated single photon counting set up from Horiba.[82] The laser diode 375 was used as a source with the excitation wavelength of 375 nm for **L1**.

1.4.8. Computational methods

Geometry optimization was done using the density functional theory (DFT/TDDFT) method at the B3LYP level for $[Pd(\mathbf{L1})(CH_3CN)Cl]^+$ ion. The 631-G (d, p) was assigned for all elements in **L1**, **L2H**, **L3** and LanL2DZ basis set for their complexes. In Chapter 5 geometry optimization was carried out using the basis set B3LYP/631-G (d, p) for **L4** and its complex with Hg^{2+} and Ag^+ ion using CAM-B3LYP/LanL2DZ basis set. All calculations were performed with Gaussian09 program[83] and molecular orbitals were visualized with the aid of Gauss View program.

1.4.9. Appendices

The chapter appendix has been included at the end of references of each chapters.

References:

1. Z. Liu, W. He and Z. Guo, *Chem. Soc. Rev.*, 2013, **42**, 1568-1600.
2. D. Wu, A. C. Sedgwick, T. Gunnlaugsson, E. U. Akkaya, J. Yoon and T. D. James, *Chem. Soc. Rev.*, 2017, **46**, 7105–7123.
3. J. Chan, S. C. Dodani and C. J. Chang, *Nat. Chem.*, 2012, **4**, 973–984.
4. Z. Guo, S. Park, J. Yoon and I. Shin, *Chem. Soc. Rev.*, 2014, **43**, 16–29.
5. L. You, D. Zha and E. V. Anslyn, *Chem. Rev.*, 2015, **115**, 7840–7892.
6. H. Zhu, J. Fan, B. Wang and X. Peng, *Chem. Soc. Rev.*, 2015, **44**, 4337–4366.
7. Z. Yang, A. Sharma, J. Qi, X. Peng, D. Y. Lee, R. Hu, D. Lin, J. Qu and J. S. Kim, *Chem. Soc. Rev.*, 2016, **45**, 4651–4667.
8. J. R. Lakowicz, *Principles of Fluorescence Spectroscopy*, Kluwer/Plenum, New York, 2nd edn, 1999.
9. *Fluorescent Chemoprobes for Ion and Molecule Recognition, ed.* A. W. Czarnik, American Chemical Society, Washington, D.C., 1993.

10. B. Valeur, *Molecular Fluorescence: Principles and Applications*, Wiley-VCH, Weinheim, 2001.
11. H. Kobayashi, M. Ogawa, R. Alford, P. L. Choyke and Y. Urano, *Chem. Rev.*, 2010, **110**, 2620.
12. R. Y. Tsien, *Annu. Rev. Biochem.*, 1998, **67**, 509.
13. Kyle P. Carter, Alexandra M. Young, and Amy E. Palmer, *Chem. Rev.*, 2014, **114**, 4564−4601.
14. (a) W. Kaim and B. Schwedeski, in *Bioinorganic Chemistry: Inorganic Elements in the Chemistry of Life*, John Wiley and Sons, New York, 1994; (b) *Perspectives on Bioinorganic Chemistry*, ed. R. W. Hay, J. R. Dilworth and K. B. Nolan, JAI Press, London, 1991; (c) *Metal Ions in Biological Systems*, ed. H. Sigel, Marcel Dekker, New York, 1973; (d) R. Wever and K. Kustin, *Adv. Inorg. Chem.*, 1990, **53**, 81.
15. (a) P. S. Dobbin and R. C. Hider, *Chem. Br.*, 1990, **26**, 565; (b) W. Mertz, *Science*, 1981, **213**, 1332; (c) A. Butler and C. J. Carrano, *Coord. Chem. Rev.*, 1991, **109**, 61.
16. S. Pal, N. Chatterjee and P. K. Bharadwaj, *RSC Adv.*, 2014, **4**, 26585–26620.
17. (a) Fluorescent Chemosensors for Ion and Molecule Recognition; American Chemical Society: Washington, DC, 1993. (b) L. Basabe-Desmonts, N. D. Reinhoudt and M. Crego-Calama, *Chem. Soc. Rev.*, 2007, **36**, 993. (c) P. A. de Silva, S. T. Moody and D. G. Wright, *Analyst*, 2009, **134**, 2385. (d) S. S. Tan, J. S. Kim and T. E. Kool, *J. Am. Chem. Soc.*, 2011, **133**, 2664.
18. D. L. Dexter, *J. Chem. Phys.*, 1953, **21**, 836.
19. B. Valeur and I. Leray, *Coord. Chem. Rev.*, 2000, **205**, 3.
20. A. P. de Silva, T. S. Moody and G. D. Wright, *Analyst*, 2009, **134**, 2385.
21. P. J. Jiang and Z. J. Guo, *Coord. Chem. Rev.*, 2004, **248**, 205.
22. T. Forster, *Ann. Phys.*, 1948, **437**, 55.
23. E. Deplazes, D. Jayatilaka and B. Corry, *Phys. Chem. Chem. Phys.*, 2011, **13**, 11045-11054.
24. A. P. de Silva, H. Q. N. Gunaratne, T. Gunnlaugsson, A. J. M. Huxley, C. P. McCoy, J. T. Rademacher and T. E. Rice, *Chem. Rev.*, 1997, **97**, 1515–1566.
25. R. Martinez-Manez and F. Sancenon, *Chem. Rev.*, 2003, **103**, 4419.
26. J. F. Callan, A. P. de Silva and D. C. Magri, *Tetrahedron*, 2005, **61**, 8551.
27. A. C. Sedgwick, L. Wu, H.-H. Han, S. D. Bull, X.-P. He, T. D. James, J. L. Sessler, B. Z. Tang, H. Tian and J. Yoon, *Chem. Soc. Rev.*, 2018, **47**, 8842–8880.

28. S. Sinha, B. Chowdhury and P. Ghosh, *Inorg. Chem.*, 2016, **55**, 9212–9220.
29. M. Y. Berezin and S. Achilefu, *Chem. Rev.*, 2010, **110**, 2641–2684.
30. J. S. Wu, W. M. Liu, X. Q. Zhuang, F. Wang, P. F. Wang, S. L. Tao, X. H. Zhang, S. K. Wu and S. T. Lee, *Org. Lett.*, 2007, **9**, 33–36.
31. Y. N. Hong, J. W. Y. Lam and B. Z. Tang, *Chem. Commun.*, 2009, 4332–4353.
32. M. Shyamal, P. Mazumdar, S. Maity, S. Samanta, G. P. Sahoo and A. Misra, *ACS Sens.*, 2016, **1**, 739–747.
33. A. J. Kemlo and M. T. Shepherd, *Chem. Phys. Lett.*, 1977, **47**, 158.
34. L. Fabbrizzi, M. Licchelli, P. Pallavicini, D. Sacchi, A. Taglietti, *Analyst*, 1996, **121**, 1763.
35. K. E. Sapsford, L. Berti and I. L. Medintz, *Angew. Chem., Int. Ed.*, 2006, **45**, 4562.
36. Z. Liu, W. He and Z. Guo, *Chem. Soc. Rev.*, 2013, **42**, 1568-1600.
37. M. M. Henary, Y. Wu and C. J. Fahrni, *Chem.–Eur. J.*, 2004, **10**, 3015.
38. M. M. Henary and C. J. Fahrni, *J. Phys. Chem. A*, 2002, **106**, 5210.
39. G. Q. Yang, F. Morlet-Savary, Z. K. Peng, S. K. Wu and J. P. Fouassier, *Chem. Phys. Lett.*, 1996, **256**, 536.
40. Z. M. Li and S. K. Wu, *J. Fluoresc.*, 1997, **7**, 237.
41. P. F. Wang and S. K. Wu, *J. Photochem. Photobiol. A: Chem.*, 1995, **86**, 109.
42. J. Mei, N. L. C. Leung, R. T. K. Kwok, J. W. Y. Lam and B. Z. Tang, *Chem. Rev.*, 2015, **115**, 11718–11940.
43. H. Nie, J. Huang, Z. Zhao and B. Z. Tang, *Aggregation-Induced Emission: Materials and Applications*, 2016, ch. 7, **2**, 173–198.
44. J. Deng, Y. Xu, L. Liu, C. Feng, J. Tang, Y. Gao, Y. Wang, B. Yang, P. Lu, W. Yang and Y. Ma, *Chem. Commun.*, 2016, **52**, 2370–2373.
45. G. Feng, R. T. K. Kwok, B. Z. Tang and B. Liu, *Appl. Phys. Rev.*, 2017, **4**, 021307.
46. C. Chen, H. Ou, R. Liu and D. Ding, *Adv. Mater.*, 2019, **31**, 1806331.
47. X. Ni, X. Zhang, X. Duan, H.-L. Zheng, X.-S. Xue and D. Ding, *Nano Lett.*, 2019, **19**, 318–330.
48. Y. Hong, J. W. Y. Lam and B. Z. Tang, *Chem. Soc. Rev.*, 2011, **40**, 5361–5388.
49. J. Mei, Y. N. Hong, J. W. Y. Lam, Y. H. Tang and B. Z. Tang, *Adv. Mater.*, 2014, **26**, 5429–5479.
50. H. Qian, M. E. Cousins, E. H. Horak, A. Wakefield, M. D. Liptak and I. Aprahamian, *Nat. Chem.*, 2017, **9**, 83–87.

51. K. Rani and S. A. John, *New J. Chem.*, 2017, **41**, 12131-12138.
52. G. T. Selvan, C. Varadaraju, R. T. Selvan, I. V. M. V. Enoch, and P. M. Selvakumar, *ACS Omega*, 2018, **3**, 7985−7992.
53. A. Sahana, A. Banerjee, S. Das, S. Lohar, D. Karak, B. Sarkar, S. K. Mukhopadhyay, A. K. Mukherjee and D. Das, *Org. Biomol. Chem.*, 2011, **9**, 5523-5529.
54. K. S. Mani, R. Rajamanikandan, B. Murugesapandian, R. Shankar, G. Sivaraman, M. Ilanchelian and S. P. Rajendran, *Spectrochim. Acta A Mol. Biomol. Spectrosc.*, 2019, **214**, 170–176.
55. X. Zhang, Y. Xiao and X. Qian, *Angew. Chem. Int. Ed.*, 2008, **47**, 8025 –8029.
56. K. Aich, S. Goswami, S. Das, C. D. Mukhopadhyay, C. K. Quah and H.-K. Fun, *Inorg. Chem.*, 2015, **54**, 7309–7315.
57. Y. Kim, G. Jang, and T. S. Lee, *ACS Appl. Mater. Interfaces*, 2015, **7**, 15649−15657.
58. V. Chandrasekhar and M. D. Pandey, *Tetrahedron Lett.*, 2011, **52**, 1938–1941.
59. J. R. Lavado, A. Lorente, E. Flores, A. Ochoa, F. Godoy, P. Jaque and C. Saitz, *RSC Adv.*, 2020, **10**, 21963–21973.
60. S. Das, S. Goswami, K. Aich, K. Ghoshal, C. K. Quah, M. Bhattacharyya and H. K. Fun, *New J. Chem.*, 2015, **39**, 8582-8587.
61. S. Sinha, B. Chowdhury and P. Ghosh, *Inorg. Chem.*, 2016, **55**, 9212–9220.
62. K. Zhang, S. Wu, D. Qu and L. Wang, *Tetrahedron Lett.*, 2016, **57**, 1133–1137.
63. J. S. Wu, W. M. Liu, X. Q. Zhuang, F. Wang, P. F. Wang, S. L. Tao, X. H. Zhang, S. K. Wu and S. T. Lee, *Org. Lett.*, 2007, **9**, 33–37.
64. V. Chandrasekhar, P. Bag and M. D. Pandey, *Tetrahedron*, 2009, **65**, 9876–9883.
65. S. K. Padhan, N. Murmu, S. Mahapatra, M. K. Dalai and S. N. Sahu, *Mater. Chem. Front.*, 2019, **3**, 2437-2447.
66. M. Shyamal, P. Mazumdar, S. Maity, G. P. Sahoo, G. S. Morán and A. Misra, *J. Phys. Chem. A*, 2016, **120**, 210−220.
67. Y. Li, Z. Gu, T. He, X. Yuan, Y. Zhang, Z. Xu, H. Qiu, Q. Zhang and S. Yin, *Dyes Pigments*, 2020, **173**, 107969−107978.
68. L. Wang, M. Ren, Z. Li, L. Dai and W. Lin, *New J. Chem.*, 2019, **43**, 552−555.
69. P. Ravichandiran, S. A. Subramaniyan, A. P. Bella, P. M. Johnson, A. R. Kim, K. S. Shim, and D. J. Yoo, *Anal. Chem.*, 2019, **91**, 10095−10101.
70. H. Kim, B. A. Rao, J. Jeong, S. Angupillai, J. S. Choi, J. O. Nam, C. S. Lee, Y. A. Son, *Sens. Actuators B: Chem.*, 2016, **224**, 404–412.

71. Y. J. Na, Y. W. Choi, G. R. You, C. Kim, *Sens. Actuators B: Chem.*, 2016, **223**, 234–240.
72. Z. Han, J. Yan, H. Q. Tang, Y. He, Y. Zhu and Y. Q. Ge, *Tetrahedron Lett.*, 2017, **58**, 1254–1257.
73. Z. Li, J. O. Yang, Y. J. Fu, C. Y. Li, Y. F. Li and S. J. Li, *Tetrahedron Lett.*, 2017, **58**, 3536–3540.
74. M. Üçüncü, E. Karakuş and M. Emrullahoğlu, *Chem. Commun.*, 2016, **52**, 8247–8250.
75. R. Chandra, A. K. Manna, K. Rout, J. Mondal and G. K. Patra, *RSC Adv.*, 2018, **8**, 35946–35958.
76. C. Hou, Y. Xiong, N. Fu, C. C. Jacquot, T. C. Squier and H. Cao, *Tetrahedron Lett.*, 2011, **52**, 2692-2696.
77. A. Shaikh, P. Mukherjee, S. Ta, A. Bhattacharyya, A. Ghosh and D. Das, *New J. Chem.*, 2020, **44**, 9452-9455.
78. M. Grabolle, M. Spieles, V. Lesnyak, N. Gaponik, A. Eychmu¨ller and U. Resch-Genger, *Anal. Chem.*, 2009, **81**, 6285–6294.
79. R. M. Melavanki, R. A. Kusanur, J. S. Kadadevaramath and M. V. Kulakarni, *J. Lumin.*, 2009, **129**, 1298–1303.
80. A. B. Bon, A. M. Costero, S. Gil, M. Parra, J. Soto, R.M. Manez and F. Sancenon, *Chem. Commun.*, 2012, **48**, 3000–3002.
81. I. D. Kuntz, J. F. P. Gasparro, M. D. Johnston and R. P. Taylor, *J. Am. Chem. Soc.*, 1968, **90**, 4778–4781.
82. H. S. Jung, P. S. Kwon, J. W. Lee, J. I. Kim, C. S. Hong, J. W. Kim, S. Yan, J. Y. Lee, J. H. Lee, T. Joo and J. S. Kim, *J. Am. Chem. Soc.*, 2009, **131**, 2008–2012.
83. M. J. Frisch, G. W. Trucks, H. B. Schlegel, G. E. Scuseria, M. A. Robb, J. R. Cheeseman, G. Scalmani, V. Barone, B. Mennucci, G. A. Petersson, H. Nakatsuji, M. Caricato, X. Li, H. P. Hratchian, A. F. Izmaylov, J. Bloino, G. Zheng, J. L. Sonnenberg, M. Hada, M. Ehara, K. Toyota, R. Fukuda, J. Hasegawa, M. Ishida, T. Nakajima, Y. Honda, O. Kitao, H. Nakai, T. Vreven, J. A. Montgomery, Jr., J. E. Peralta, F. Ogliaro, M. Bearpark, J. J. Heyd, E. Brothers, K. N. Kudin, V. N. Staroverov, R. Kobayashi, J. Normand, K. Raghavachari, A. Rendell, J. C. Burant, S.

S. Iyengar, J. Tomasi, M. Cossi, N. Rega, J. M. Millam, M. Klene, J. E. Knox, J. B. Cross, V. Bakken, C. Adamo, J. Jaramillo, R. Gomperts, R. E. Stratmann, O. Yazyev, A. J. Austin, R. Cammi, C. Pomelli, J. W. Ochterski, R. L. Martin, K. Morokuma, V. G. Zakrzewski, G. A. Voth, P. Salvador, J. J. Dannenberg, S. Dapprich, A. D. Daniels, Ö. Farkas, J.B. Foresman, J.V. O rtiz, J. Cioslowski and D.J. Fox, Gaussian 09, Revision D.01, Gaussian Inc, Wallingford CT, 2009.

Chapter 2

Naked-Eye Detection of Pd^{2+} Ion Using a Highly Selective Fluorescent Heterocyclic Probe by "*Turn-Off*" Response and *in vitro* Live Cell Imaging*

Abstract:

The heterocyclic probe 3-(1-isoquinolinyl)imidazo[5, 1-*a*]isoquinoline (**L1**) in CH_3OH/HEPES buffer system (5 mM, pH = 7.4, 6:4, *v/v*), exhibits blue fluorescence (λ_{em} = 454 nm) upon excitation with 359 nm light. Upon adding Pd^{2+} ion solution, **L1** shows "*turn-off*" response when observed under long UV light. Using **L1** bivalent palladium can be detected with a low limit of detection (0.210 μM) within the pH range of 2-8. In the presence of large varieties of metal ion, colorimetric and fluorescence responses did not exhibit any perceptible change. A small change in fluorescence life-time in TRPL study indicates the static nature of quenching. Binding of probe **L1** with Pd^{2+} ion can be reversed using Na_2EDTA. Job's plot and ESI mass spectrometric analysis reveal a 1:1 ratio for binding of **L1** with Pd(II) ion. DFT/TDDFT calculations performed on $[Pd(\mathbf{L1})Cl(CH_3CN)]^+$ ion support the experimental findings. Cytotoxic studies showed that probe **L1** suppressed the growth of L929 and Hela cells in a dose-dependent manner. Fluorescence imaging in the absence and presence of Pd^{2+} revealed that **L1** can be successfully applied on living cells with outstanding sensitivity.

*This work has been published in:

S. Mahata, A. Bhattacharya, J. P. Kumar, B. B. Mandal and V. Manivannan, *J. Photochem. Photobiol. A: Chem.*, 2020, **394**, 112441.

2.1. Introduction

Palladium, being one of the members of valuable platinum group, due to its unique catalytic reactivity, became an indispensable organometallic catalyst in pharmaceutical industries.[1,2] Complexes of palladium (zero or bivalent) are used in many coupling reactions like Heck, Suzuki, Stille, Negishi, Sonogashira and Kumada.[3–6] Moreover, palladium has also found significant utility in the production of jewels, alloys, fuel cells, dental and medicinal devices.[7–10] In spite of its significance in above mentioned utilities in our daily life, it also has some adverse effects which cause toxicity in the human body and other living organisms. Some of the adverse effects of palladium are like cytotoxicity that ultimately leading to damage or death of living cells,[11,12] damage and degradation of DNA by binding to thymidine base,[13] inhibition of enzymes e.g., creatine-kinase, aldolase, alkaline phosphatase, carbonic anhydrase, trypsin, chymotrypsin, cellulose etc.[14,15] The maximum permissible limit of dietary intake of palladium is 15 μg / day per person.[16] Hence a check on its concentration in the environment is necessary. Some analytical methods for the quantitative and qualitative detection of palladium with high sensitivity involve techniques like atomic absorption spectrometry, plasma emission spectroscopy, solid-phase micro-extraction high performance liquid chromatography and X-ray fluorescence.[17–20] However, these techniques are extremely expensive and need expert individuals.[21] On the other hand, colorimetric detection and fluorescence-based methods are very simple, highly sensitive and can be tuned for biological applications.[22–26]

Palladium(II) ion could be detected using strong fluorescent ligands through the fluorescence quenching mechanism.[27,28] Pd(II) ion is an efficient fluorescence quencher as it has open-shell electronic configuration and itself is a heavy transition metal ion. A coumarin based "*turn-on*" fluorometric chemosensor has been shown to exhibit a yellow fluorescence in presence of Pd(0).[29] Rhodamine based fluorescent chemosensors show a colorimetric response, which is helpful for visual detection Pd^{2+} ion in solution.[30,31] A probe containing both coumarin and rhodamine moieties has been reported to detect Pd^{2+} ion with high precision.[32] A combination of indole and rhodamine groups containing chemosensor has been used to detect Pd(II) ion ratiometrically.[33] Other sensing methods for Pd(II) ion include the use of metal-organic frameworks and carbon nanoparticles. An ultra-sensitive Eu(III) and 2,5-bis(allyloxy)terephthalate framework detects Pd^{2+} ion in water.[34] The highly fluorescent carbon nanoparticles exhibit "*turn-off*" mode of dual sensing towards Pd^{2+} and Hg^{2+} ions.[35] The probe having phthalimide-rhodol combination was reported to detect Pd(II) ion

ratiometrically and rapidly by ESIPT-FRET mechanism.[36] Some of the heterocyclic systems used for the detection of Pd^{2+} ion include a benzo-oxadiazole based chromophore for visual detection.[37] Pyridine-2, 6-dicarboxamide bearing naphthyl groups have Pd(II) sensing ability in aqueous medium.[38] The NIR fluorescent sensor containing acridinone moiety[39] and benzo[d]imidazole attached with thiophene[40] show "*turn-off*" responses in the presence of Pd(II) ion. Metal-binding sensors are advantageous because the response is very fast as it alters the absorption wavelength, emission or excitation maxima, fluorescence intensity and lifetime, in the presence of metal ions. Hence it is necessary to design and synthesize suitable coordination sensors that will exhibit high selectivity and sensitivity towards palladium as well as to be safe for biological applications.

To the best of our knowledge, there are very few reports on the use of heterocyclic compounds as palladium(II) ion sensor (Table A1). The small, relatively new diazaheterocycle bearing isoquinoline ring, 3-(1- isoquinolinyl)imidazo[5, 1-*a*]isoquinoline (**L1**), is fluorescent as well as can act as a bidentate chelating ligand. Encouraged by these two properties of **L1** that are essential for a compound to be a metal ion sensor, a study to examine the potential of **L1** as a sensor was undertaken. Indeed it has been found to be an excellent candidate for selective sensing of palladium(II) ion, these results and evaluation of its biological compatibility are described, in this Chapter.

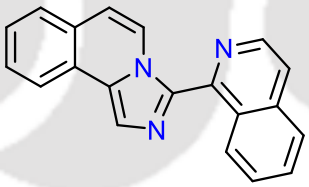

L1

Scheme 1 L1 is used as ligand in this Chapter.

2.2. Experimental section

Probe **L1** was synthesised by following reported procedure[44] and all the spectral characteristic of **L1** matched perfectly with the values reported earlier.

2.2.1. In vitro studies

2.2.1.1. Cell culture

Mouse fibroblast (L929) and human cervical cancer (Hela) cells were procured from National Centre for Cell Science, India. They were cultured and maintained using high glucose

Dulbecco's modified Eagle's medium (Gibco, USA), supplemented with 10% Fetal bovine serum (Gibco, USA) and 1X antibiotic-antimycotic solution (Himedia, India).

2.2.1.2. MTT assay

Cytotoxic effect of **L1** on L929 and Hela cells was assessed using MTT assay.[41,42] Briefly, cells cultured in 96 well plate were treated with 0, 1.25, 2.5, 5.0, 7.5, and 10.0 µM of **L1** for 24 h and incubated with thiazolyl blue tetrazolium bromide (Sigma, USA) for 4 h. Formazan was solubilized with dimethyl sulfoxide (DMSO, Merck, India), and absorbance was recorded at 570 nm using multiplate reader (Multiskan Sky, Thermo scientific, USA).

2.2.1.3. Fluorescence imaging

Fluorescence emitted by **L1** in live cells was studied using the protocol of Chen et al.[43] In brief, L929 and Hela cells (1×10^5) cultured in 6 well plates were treated with 5 µM of **L1** for 30 min. After 30 min, spent media was removed, cells were washed with phosphate buffer saline (PBS, pH 7.4) to remove excess **L1**, and visualized using fluorescence microscopy (EVOS FLC, Life technologies).

2.2.1.4. Detection of Pd^{2+} in cells

Presence of Pd^{2+} in cells was detected using **L1** with the modified protocol of Chen et al.[43] Briefly, L929 and Hela cells cultured in 6 well plates were treated with **L1** for 30 min followed by PBS wash and incubated with 5 µM of $PdCl_2$ for 30 min at 37 °C. Post incubations, cells were washed and covered with PBS and visualized using fluorescence microscopy.

2.2.2. Statistical analysis

Experiments were carried in triplicates, obtained data was analyzed and represented as mean ± standard deviation. One-way ANOVA was carried out by the Holm-Sidak method using Sigma-plot software.

2.3. Results and discussion

The chemosensor **L1** was synthesized by adopting the reported procedure, observed to be a very good fluorescence active molecule.[44] This is relatively a new diazaheterocycle that bears 1-isoquinoline ring substituted at the 3rd position of imidazo[5, 1-*a*]isoquinoline nucleus. This fluorescent molecule **L1**, is a potential bidentate chelating ligand, which can bind metal ions by using two nitrogen atoms, one from isoquinoline ring another from

imidazo-nitrogen at 2nd position of the fused nucleus, thereby forming a favourable 5-membered chelate ring. These two characteristics are essential for a compound to be a metal ion sensor, which encouraged us to examine the potential of **L1** as a metal ion sensor. In this direction, UV-Visible and fluorescence spectra of this probe were examined in MeOH / HEPES buffered aqueous solution (5 mM, pH = 7.4, 6:4, *v/v*). Absorption and emission spectra of **L1** were recorded for the titration with chloride salts of Na^+, K^+, Li^+, Ca^{2+}, Mg^{2+}, Mn^{2+}, Fe^{2+}, Co^{2+}, Ni^{2+}, Cu^{2+}, Zn^{2+}, Cd^{2+}, Hg^{2+}, Pb^{2+}, Fe^{3+}, Cr^{3+}, Al^{3+} and Pd^{2+} ions.

2.3.1. UV-Vis spectroscopic studies of L1 in presence of metal ions

The UV–Vis spectrum of the sensor **L1** recorded in MeOH:HEPES buffer solution showed an absorption band having a maximum at 359 nm. The intensity of this absorption maximum remains unchanged or slightly decreased with the addition of up to two equivalents of metal chlorides mentioned above. However, upon the gradual addition of $PdCl_2$ solution to **L1** solution, 359 nm peak gradually decreased in intensity (Fig. 1). Three new overlapping absorption bands having their maxima at 395, 420 and 440 nm grew in intensity along with an isosbestic point at 388 nm (Fig. 2). The presence of isosbestic point indicates that only two species *viz*., free **L1** and **L1**-bound Pd(II), are involved during the course of the titration. A significant change in colour from light blue to yellow was observed, which is the consequence of red shift of the absorption band. This color change can easily be observed by the naked eye and hence **L1** enables visual detection of Pd^{2+} ion. Since with other metal ions noted above such a red shift was not observed, it is imperative that **L1** is very selective towards Pd(II) salts.

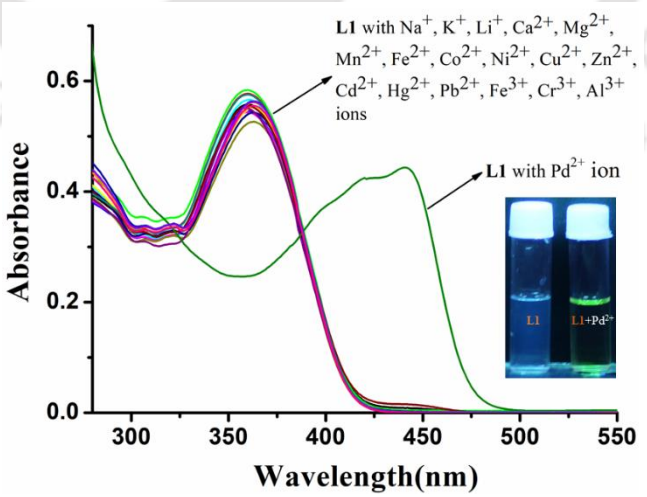

Fig. 1 The emission spectra of **L1** with solutions of various metal ions along with Pd^{2+} ion. Inset compares colors of **L1** and **L1** + Pd^{2+} ion.

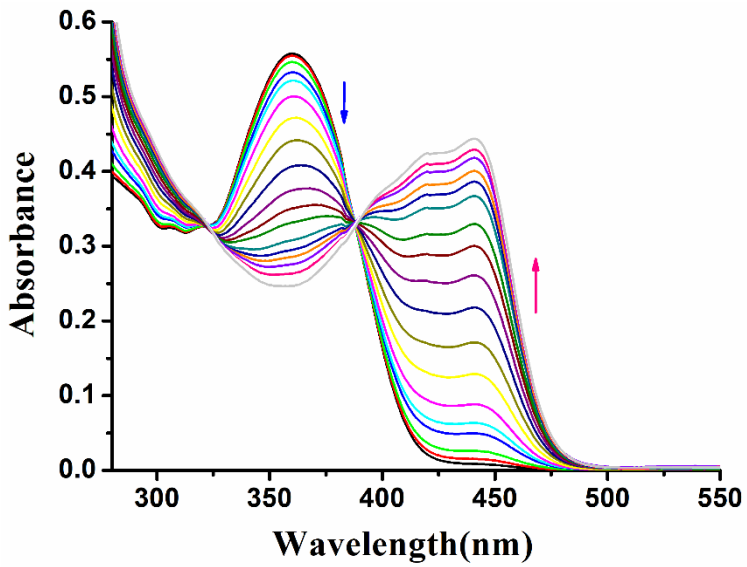

Fig. 2 The change in absorption spectra of solution of **L1** upon gradual addition of $PdCl_2$.

2.3.2. Fluorescence spectroscopic studies of L1 in presence of metal ions

Upon irradiation of solution of **L1** with λ_{ex} = 359 nm using an emission slit of 3 nm, emission at λ_{em} = 454 nm was observed. In order to evaluate the possible selective fluorescence behaviour of **L1** towards palladium(II) in presence of various other metal chloride salts, a study of fluorescence emission behaviour was performed. Upon titrating **L1** with chloride salts of Na^+, K^+, Li^+, Ca^{2+}, Mg^{2+}, Mn^{2+}, Fe^{2+}, Co^{2+}, Ni^{2+}, Cu^{2+}, Zn^{2+}, Cd^{2+}, Hg^{2+}, Pb^{2+}, Fe^{3+}, Cr^{3+}, Al^{3+} and Pd^{2+} ions, the pattern of emission at λ_{em} = 454 nm was largely invariant, but Fe(III) exhibited a small reduction (~10%) in the fluorescence intensity (Fig. 3). The exception is Pd(II) salts, which caused an outstanding decrease in the fluorescence intensity (Fig. 4) of **L1** (~90%) and significant colour change from deep sky blue to yellow. This colour change is readily observable by the naked eye (Fig. 5). It is evident that **L1** has high selectivity towards Pd^{2+} cations with respect to other metal salts. The decrease in fluorescence intensity of **L1** in presence of Pd^{2+} ion is due to chelation enhanced quenching (CHEQ) mechanism. Again, to check the practical utility of **L1**, competition experiments were performed by first treating **L1** (Fig. 6) with equimolar amount of competing metal salts and then adding one equimolar quantity of Pd^{2+} cations. From this experiment, it was seen that the fluorescence of the compound **L1** was greatly quenched by Pd(II) in presence of other metal salts. These results clearly indicate that **L1** is highly selective towards the Pd^{2+} ion, even in presence of other metal ions.

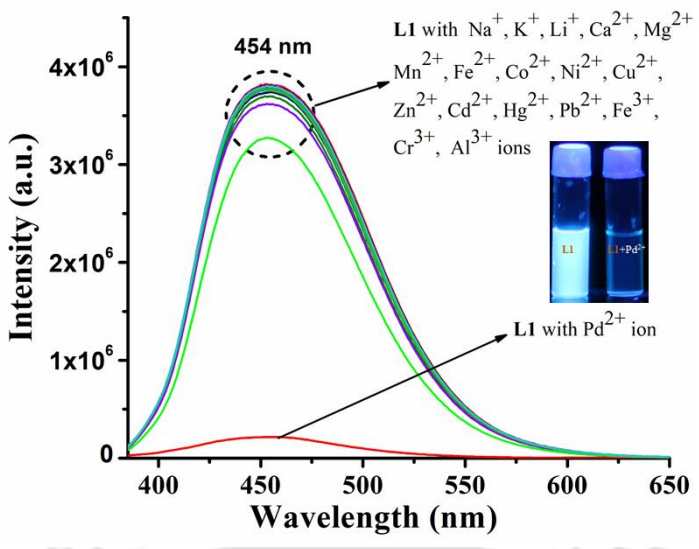

Fig. 3 The emission spectra of **L1** with solutions of various metal ions along with Pd^{2+} ion. Change in fluorescence of the solution in presence of Pd^{2+} ion while illuminated in UV-chamber is shown in the inset.

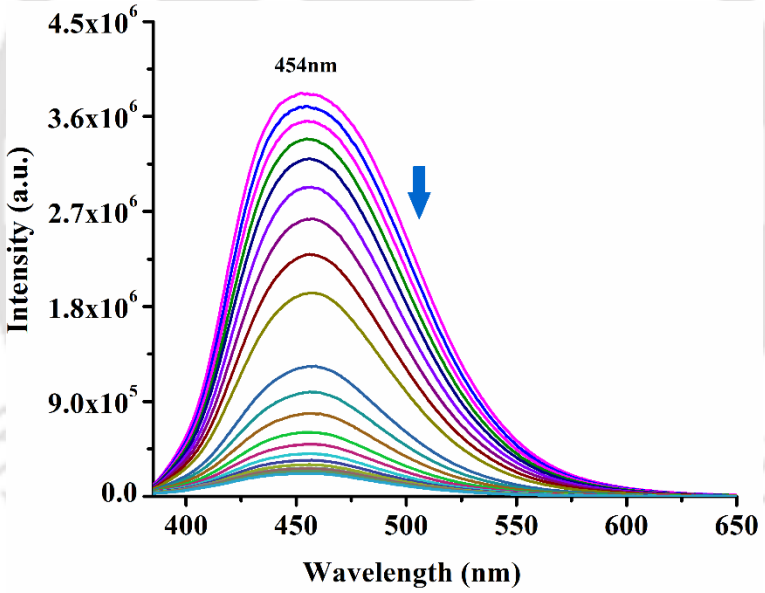

Fig. 4 The change in fluorescence intensity of solution of **L1** upon adding of Pd^{2+} solution.

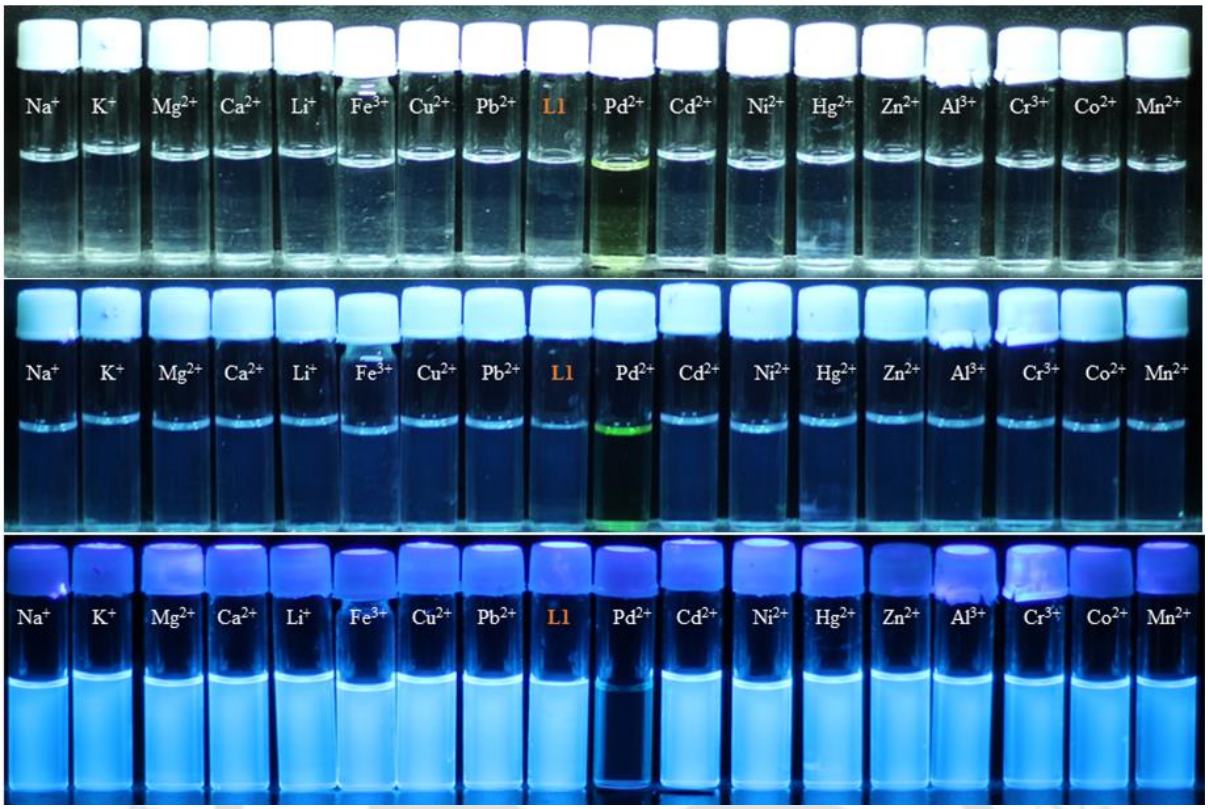

Fig. 5 Photograph of **L1** solutions in presence of various metal ions observed under visible light (top), short UV light (middle) and long UV light (bottom).

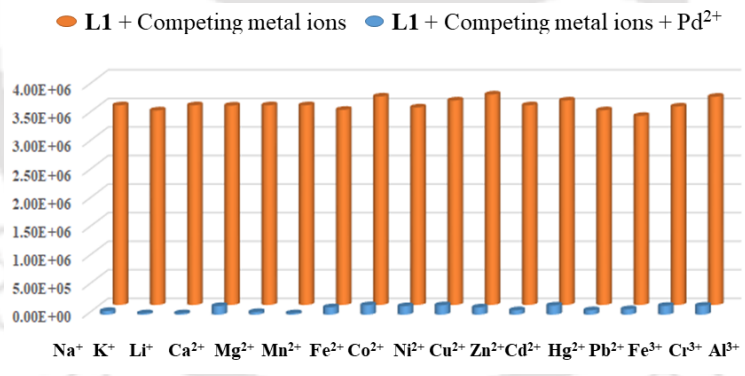

Fig. 6 Bar diagram of fluorescence intensity of solution of **L1** in the presence of other metal chloride and after addition of equimolar solution of $PdCl_2$ into them.

In order to ascertain the pH window for selective detection of Pd^{2+} ion by **L1**, fluorescence of free **L1** and in presence of Pd^{2+} cation was recorded using MeOH-HEPES buffer solution (pH was adjusted using HCl or NaOH solutions). In the case of free **L1**, the fluorescence intensity increased on increasing the pH from 2 to 7 and then did not deviate much in the range 8–14. Upon carrying out the same experiment in presence of one equivalent of $PdCl_2$, initially, the solution was non-fluorescent in the range of pH = 2–8. Then fluorescence intensity gradually enhanced with further increase in pH (Fig. 7). This indicates that in alkaline conditions free

L1 is released into the solution. Hence it could be concluded that the fluorescence intensity of **L1** was effectively quenched by $PdCl_2$ in the pH range of 2–8, which is the favourable range.

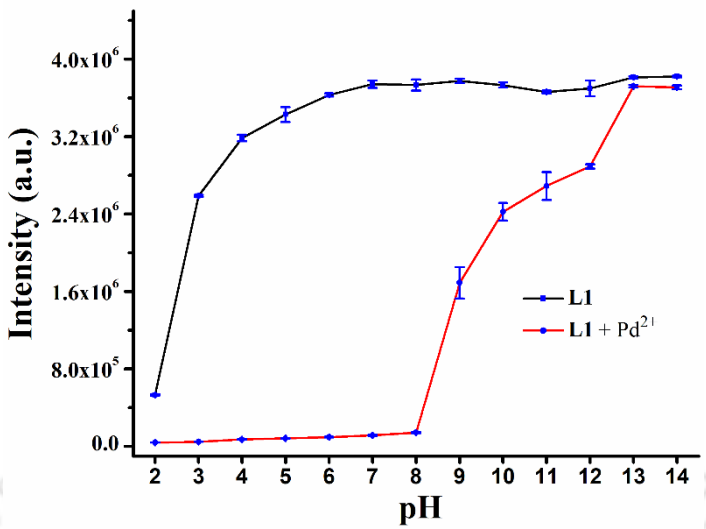

Fig. 7 Plot of fluorescence intensities at λ_{em} = 454 nm *vs* pH.

Further, the reversibility of **L1** binding to Pd^{2+} ion has also been established using Na_2EDTA method. The fluorescence emission at λ_{em} = 454 nm of solution of **L1** bound with Pd^{2+} ion, was restored upon addition of one equivalent Na_2EDTA solution (Fig. 8). This indicates that Na_2EDTA effectively sequester Pd(II) ion thereby releasing free **L1** into the solution thus re-establishing the fluorescence intensity (Scheme 2). After that, the fluorescence intensity at 454 nm was quenched again after the addition of another equivalent of $PdCl_2$. From this experiment, it can be inferred that **L1** binding can be reversed and be utilised multiple times.

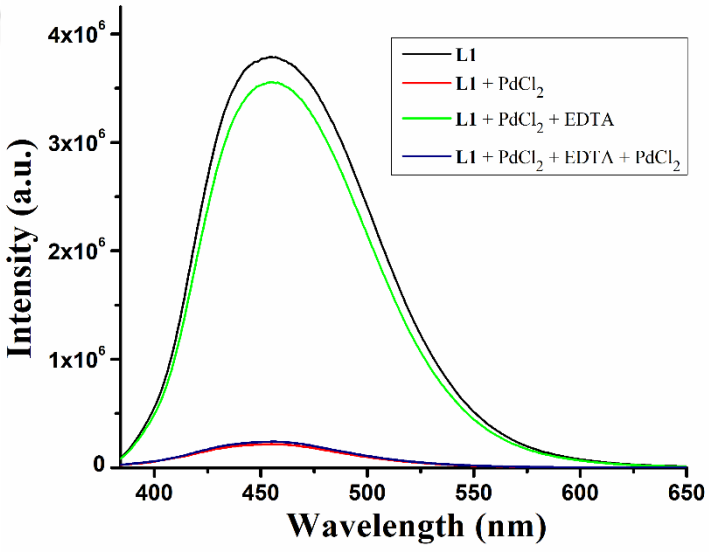

Fig. 8 Fluorescence response for reversibility of **L1** binding to $PdCl_2$.

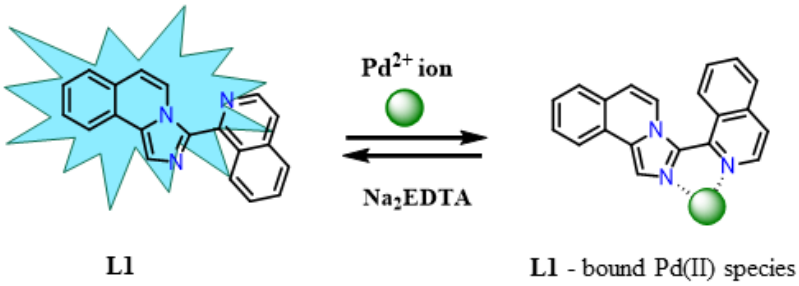

Scheme 2 Possible mode of sensing Pd^{2+} ion.

2.3.3. Fluorescence response of L1 towards some counter ions

The other two major palladium(II) compounds *viz*., $Pd(OAc)_2$ and $Pd(PPh_3)_2Cl_2$ are also commonly used as a catalyst in the industry. The effect of ligands bound to palladium(II) on fluorescence intensity of **L1** was examined using $Pd(OAc)_2$ and $Pd(PPh_3)_2Cl_2$. These two complexes showed similar fluorescence quenching (Fig. 9) as exhibited by $PdCl_2$. This proves that ligands bound to palladium(II) had merely any effect on the sensing behaviour of **L1**. In addition, effect of presence of anions *viz*., F^-, Cl^-, Br^-, I^-, CN^-, SCN^-, PO_4^{3-}, S^{2-}, NO_3^-, ClO_4^-, $H_2PO_4^-$, AcO^-, HSO_4^- and SO_4^{2-} in solution does not show any interfering effect on the sensitivity and selectivity of **L1** towards palladium(II) ion (Fig. 10).

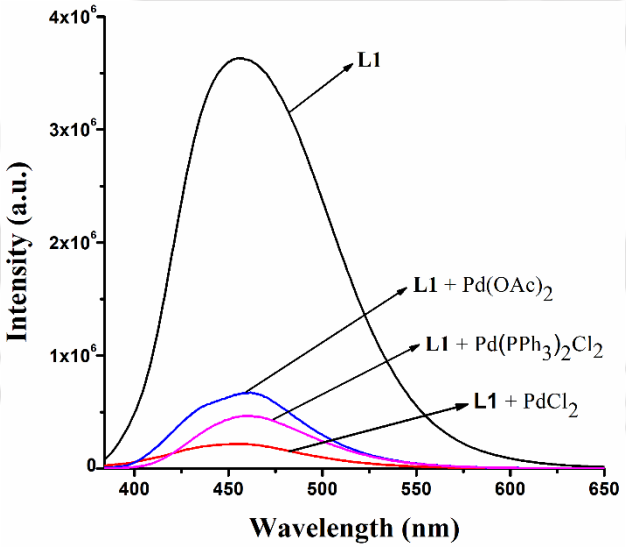

Fig. 9 Fluorescence intensity changes of **L1** in the presence of different palladium complexes.

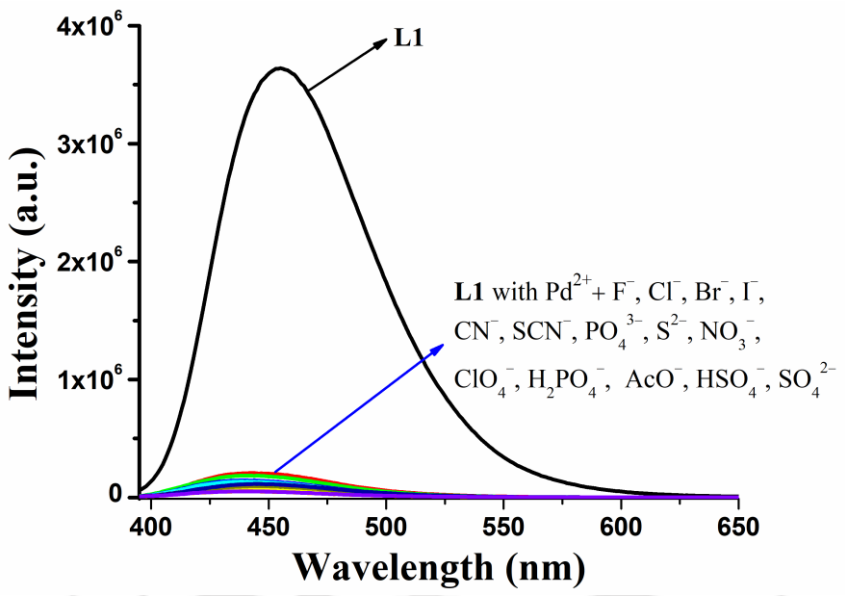

Fig. 10 Effect of presence of anions towards Pd^{2+} ion in **L1** solution.

2.3.4. Detection of Pd^{2+} in real samples

The utility of **L1** for practical application towards detection of Pd^{2+} ion in real water samples through fluorescence experiment was examined. Samples of tap water and drinking water from the institute as well as from river Brahmaputra (near I.I.T Guwahati campus, Assam, India) were collected, filtered through 0.22 μm membrane and then adjusted to pH 7.4. At first, a blank experiment was done to check the presence of Pd^{2+} ion in these samples but found to be negative based on absence of change in fluorescence intensity of the probe. Fluorescence intensity of **L1** was recorded using solutions of $PdCl_2$ prepared from these water samples. A plot of emission intensity at λ_{em} = 454 nm *vs* Pd(II) concentration (shown in Fig. 11) confirms that **L1** is a suitable probe for detection of Pd^{2+} ion in these real water samples.

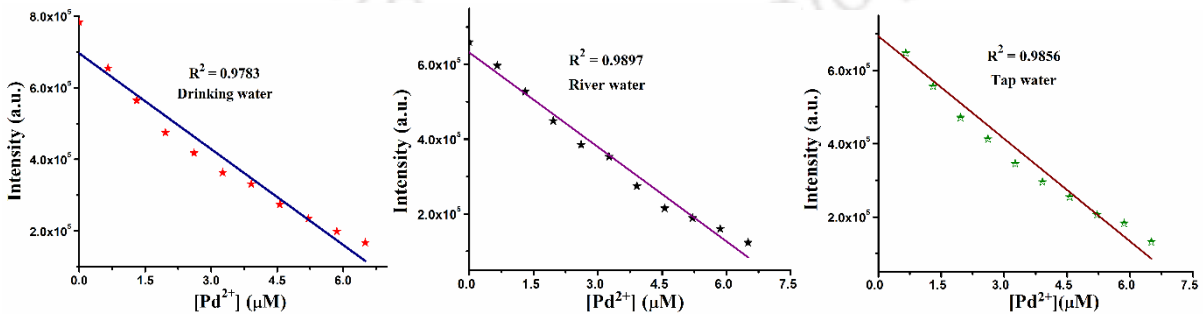

Fig. 11 Fluorescence intensity changes of **L1** in real water samples.

2.4. Binding stoichiometry for Pd^{2+} ion with L1

The Job's plot was used to ascertain the binding ratio between **L1** and Pd(II) ion. It was evident from the Job's method of continuous variation of mole fraction that the binding ratio is 1:1 (at the value of 0.5 mole fraction, the intersection point in (Fig. 12)). This suggests that one equivalent of **L1** is good enough for effective sensing of Pd^{2+} ion. The Benesi–Hildebrand plot yielded a higher value for the binding constant, 3.86×10^3 M^{-1}, which is suggestive of bidentate chelating nature of the probe. This result is also consistent with 1:1 ratio between the probe and the metal ion (Fig 12).

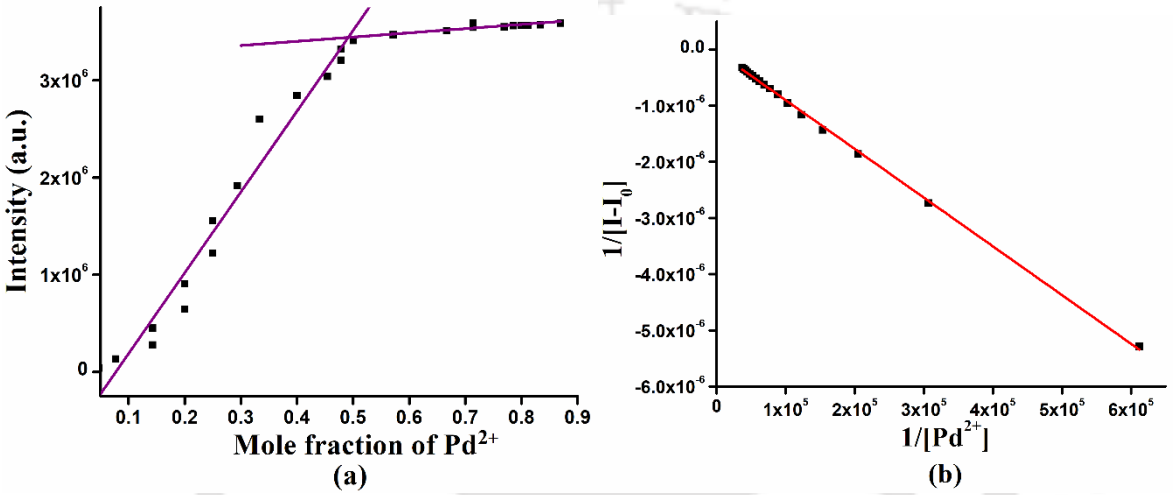

Fig. 12 Job's plot (a) and Benesi–Hildebrand plot (b) of **L1** for Pd^{2+} metal ion.

The formation of a 1:1 complex was further confirmed by mass spectral analysis. In ESI-mass spectrum, the significant peak at *m/z* = 477.012 (calculated for $^{106}PdC_{22}H_{16}{}^{35}ClN_4$ = 477.010) assignable to $[Pd(\mathbf{L1})Cl(CH_3CN)]^+$ ion, established the formation of the 1:1 complex between the probe and Pd^{2+} ion. The experimentally observed mass spectral fragments matched excellently with that calculated using mMass software (Fig. A1 and A2).

The change in fluorescence intensity of **L1** at λ_{em} = 454 nm was investigated by the incremental addition of Pd^{2+} ion till a complete quenching was attained. The calculated fluorescence quantum yield for free **L1** is 0.58 whereas quantum yield of its Pd(II) complex decreases to 0.04. The quenching efficiency can be conveniently understood by calculating the Stern–Volmer constant (K_{SV}) which was found to be 1.91×10^4 M^{-1} (Fig. 13) from Stern–Volmer plot. From the fluorescence titration curve and by using the detection limit formula ($3\sigma/k$) the limit of detection was calculated to be 0.210 μM (Fig. 14). It is remarkable that this detection limit by **L1** is well below the permissible threshold limit for palladium (47 to 94 μM) as prescribed by the World Health Organisation.[45]

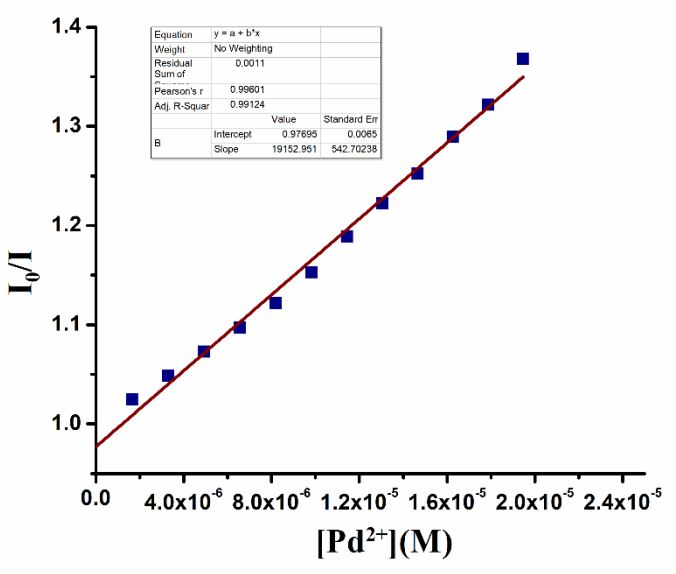

Fig. 13 Stern-Volmer plot of **L1** with Pd^{2+} ion.

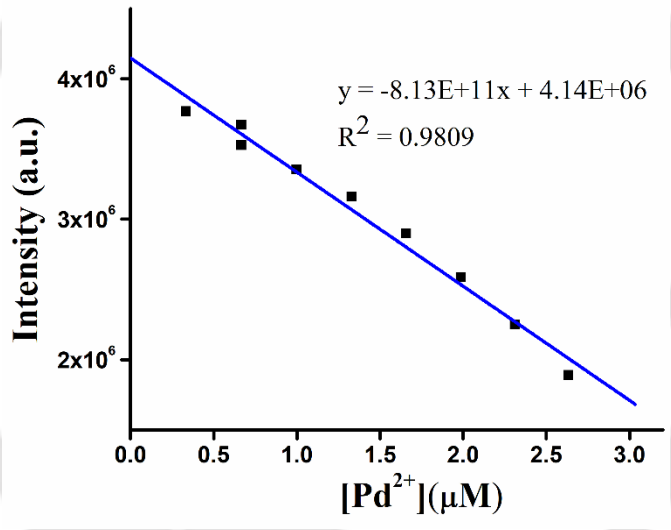

Fig. 14 Fluorescence intensity *vs.* concentration of Pd^{2+} ion plot for determination of detection limit.

2.5. TRPL Measurements

In general, the effect of metal ions on fluorescence intensity of organic fluorophores is due to different types of molecular interactions including energy transfer, molecular rearrangements, excited state reactions, static and dynamic quenching. Quenching of emission intensity of **L1** by Pd^{2+} is probably due to formation of complex between them. The time resolved fluorescence lifetime experiment was performed to confirm static nature of quenching between **L1** and Pd^{2+} in the absence and presence of Pd^{2+}. Fluorescence decay curves for free **L1** and **L1** in presence of $PdCl_2$ are shown in Fig. 15 and Table 1. The calculated average fluorescence life time (τ) value of free **L1** was 2.5 ns while that of with added $PdCl_2$ is 1.7 ns.

This change in τ indicates that quenching of emission intensity of **L1** in presence of $PdCl_2$ is due to formation of a non-fluorescent complex that is *via* static quenching.

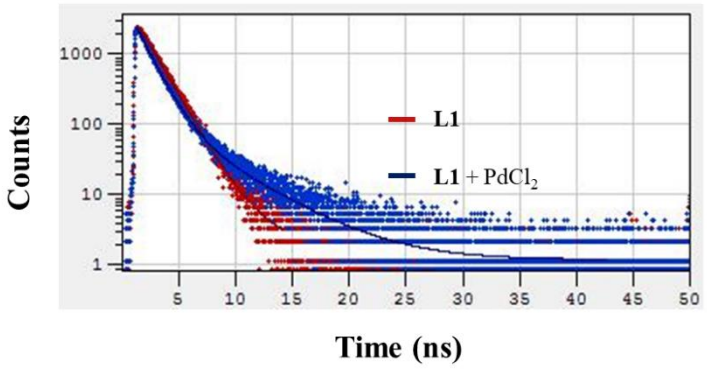

Fig. 15 Time-resolved fluorescence decay profile of **L1** in absence and presence of $PdCl_2$.

Table 1 Fluorescence decay parameters of **L1** with Pd^{2+} ion

Sample	τ (ns)	χ^2
L1	2.5	1.14
L1 + Pd^{2+}	1.7	1.04

2.6. Computational studies

To examine the effect on the energies of frontier molecular orbitals of **L1** upon coordination to Pd^{2+} ion density functional theory (DFT/TDDFT) calculations using Gaussian09 program were performed on $[Pd(\mathbf{L1})Cl(CH_3CN)]^+$ ion. The optimized geometry of $[Pd(\mathbf{L1})Cl(CH_3CN)]^+$ ion is shown in Fig. 16, which illustrates that Pd^{2+} ion is bound by **L1** in a bidentate fashion *via* nitrogen atom of imidazo ring in imidazo[5, 1-*a*]isoquinoline nucleus and another nitrogen from 1-isoquinolinyl ring that is substituted at 3rd carbon atom of the fused central ring. The N atom of acetonitrile molecule and one Cl^- ion coordination make square planer geometry around the central metal ion.

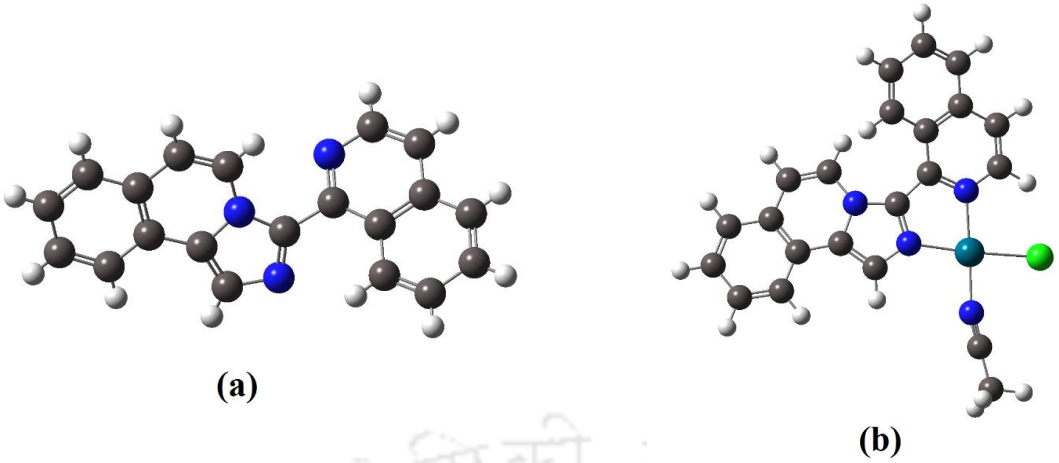

Fig. 16 The energy optimized structures of (a) **L1** and (b) [Pd(**L1**)Cl(CH_3CN)]$^+$ complex ion (atom colors: gray=C, blue=N, white=H, green=Cl, teal green=Pd).

The π electron density on the HOMO of [Pd(**L1**)Cl(CH_3CN)]$^+$ ion is mostly distributed on whole molecule of 3-(1-isoquinolinyl)imidazo[5,1-*a*]isoquinoline. The LUMO is mainly composed of orbitals from imidazo ring in imidazo[5, 1-*a*]isoquinoline and 1-isoquinolinyl ring as well as from a π-type orbital of central Pd^{2+} ion. The spatial distributions of HOMO and LUMO in [Pd(**L1**)Cl(CH_3CN)]$^+$ ion are nearly the same as reported for the free **L1** but their energies were found to be greatly decreased upon coordination to the palladium center. The net effect of complex formation on the frontier orbitals is that the energy of HOMO is stabilized to the extent of 3.416 eV while that of LUMO by 4.030 eV in [Pd(**L1**)Cl(CH_3CN)]$^+$ ion as depicted in Fig. 17.

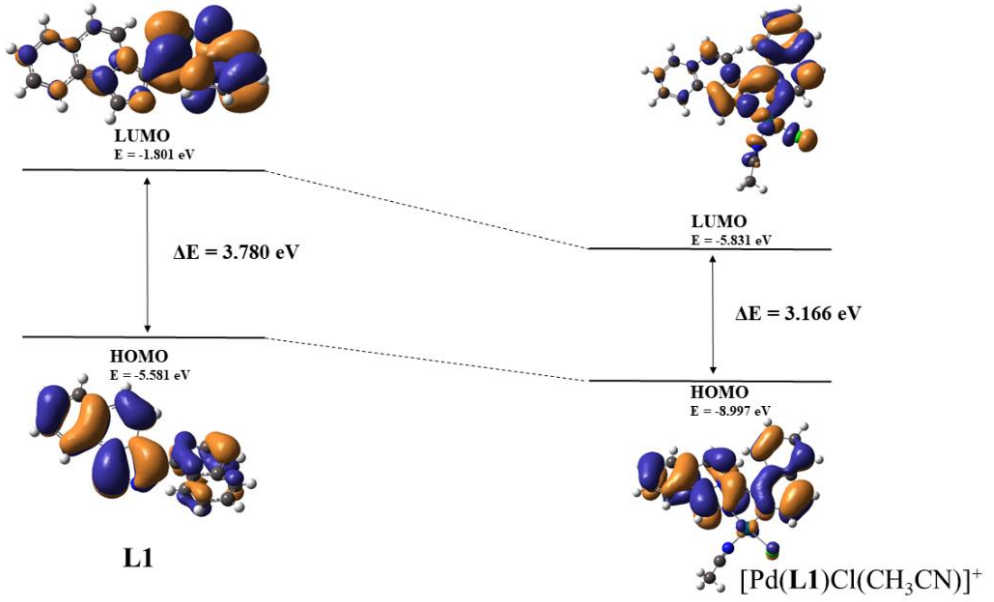

Fig. 17 Energy levels diagram depicting HOMO and LUMO in **L1** and [Pd(**L1**)Cl(CH_3CN)]$^+$ ion.

Hence the HOMO-LUMO energy gap in $[Pd(\mathbf{L1})Cl(CH_3CN)]^+$ ion is lowered to 3.166 eV which was calculated to 3.780 eV in free **L1**. The net effect is that the energy difference between HOMO and LUMO is lowered in the complex ion, is consistent with red shift observed in the absorption maximum of **L1** upon binding to Pd^{2+} ion (Fig. A3).

2.7. Paper Strip and TLC Plate Test

In order to find out the practical utility, few strips of qualitative Whatman filter paper was dipped in the solution of **L1**, after that they were allowed to dry in air dried. One of the **L1** absorbed test strips was then dipped directly into a solution of $PdCl_2$ for few seconds and then dried in air. Both paper strips upon being observed under the longer UV light, paper absorbed with **L1** exhibited fluorescence while the other one absorbed with **L1** and treated with $PdCl_2$ is non-fluorescent as shown in Fig. 18. From this test it is evident that Pd^{2+} ion can be practically detected using a low cost filter paper technique with a high degree of sensitivity and selectivity with **L1**. Alternatively, this test can be performed using TLC plates with the same degree of sensitivity and selectivity. Typically, few drops of **L1** solution were loaded with a syringe on two TLC plates coated with silica gel. After drying in air one of the loaded TLC plates was treated with a solution of Pd^{2+} ion. Both TLC plates upon being observed under the longer UV light, the plate absorbed only with **L1** exhibit fluorescence while the other treated with Pd^{2+} ion is non-fluorescent as shown in Fig. A4.

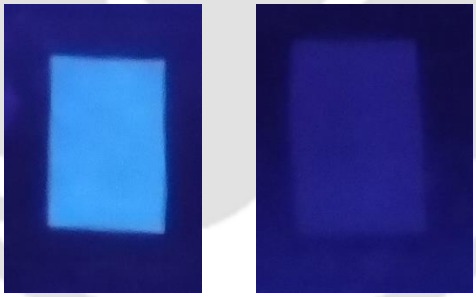

L1 **L1** + $PdCl_2$

Fig. 18 Images of paper strip under longer UV light.

2.8. MTT assay

The cytotoxicity of **L1** was assessed using MTT assay. It showed dose-dependent cytotoxicity on L929 and Hela cells. In comparison with control cells (untreated cells), the viability of L929 and Hela cells significantly reduced with increasing **L1** concentration (Fig. 19). 5 µM concentration of **L1** was selected to investigate fluorescence properties due to its low cytotoxicity towards L929 (75.25 ± 1.62) and Hela cells (100.88 ± 6.96).

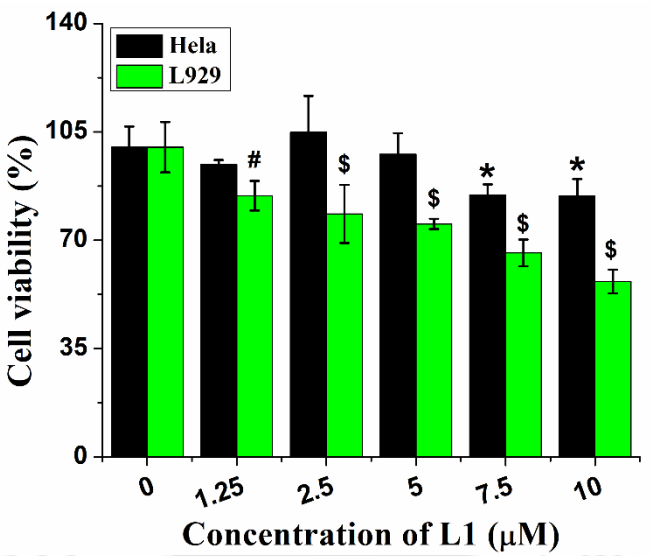

Fig. 19 The cytotoxic effect of **L1** on Hela and L929 cells determined using MTT assay. ($p≤0.001, #p≤0.01 and *p≤0.05 in comparison with control).

2.9. Fluorescence imaging

Uptake of **L1** by cells and its fluorescence properties were visualized using live imaging. **L1** incubated with L929 and Hela cells for 30 min were rapidly internalized in cells and emitted blue fluorescence from intracellular regions (Fig. 20) at excitation 357/44 nm and emission 447/60 nm.

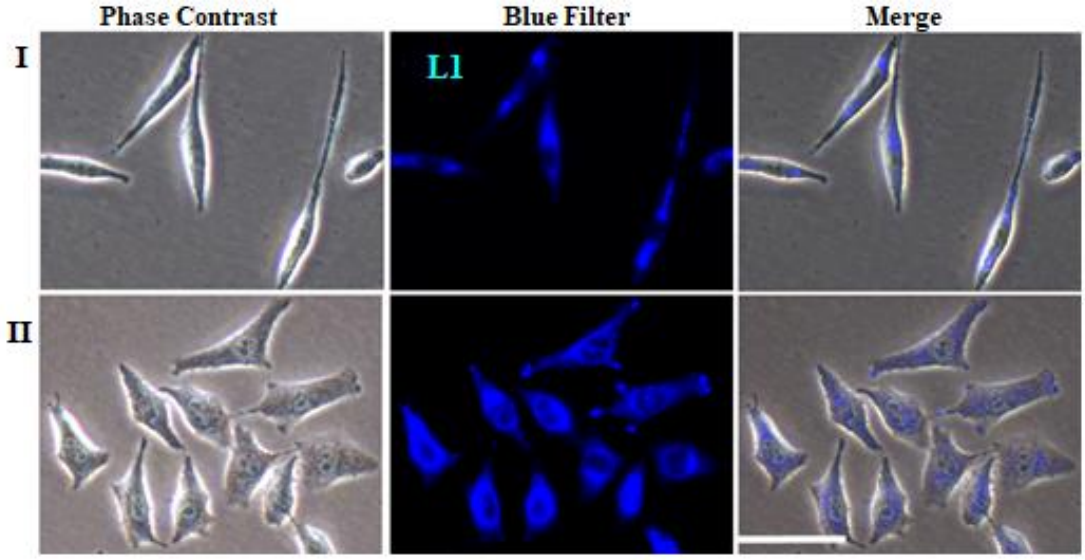

Fig. 20 Internalization of **L1** in (I) L929 and (II) Hela cells examined via visualizing the fluorescence emitted by **L1** using fluorescence microscopy. Scale 100 μm

2.10. Detection of Pd^{2+} in cells

Palladium (Pd^{2+}) in cells was detected in living cells using **L1**. Incubation of Pd^{2+} ions with L929 and Hela cells after **L1** treatment quenched the complete fluorescence emitted by **L1**

(Fig. 21). Pd^{2+} uptake by the cells interacted with **L1** present in the intracellular regions and quenched it, which shows that **L1** helps to detect Pd^{2+} in living cells.

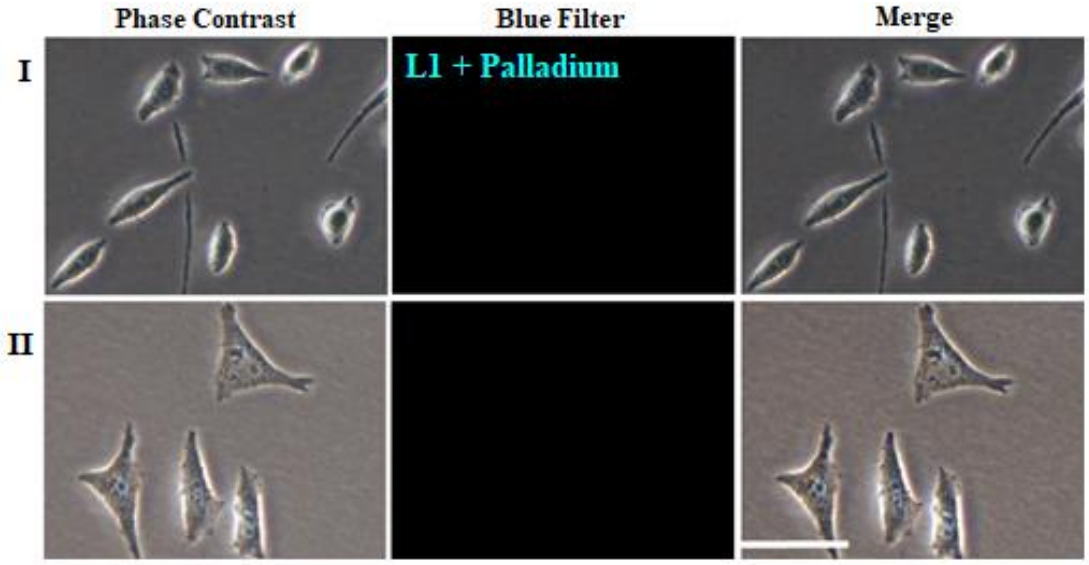

Fig. 21 Presence of palladium(II) ion in (I) L929 and (II) Hela cells detected via visualizing the fluorescence emitted by **L1** using fluorescence microscopy. Scale 100 μm

2.11. Conclusion

In conclusion, it is evident that the probe **L1** is unique in its kind and highly selective in its recognising properties towards Pd^{2+} ions have established itself as a potentially applicable sensor that not only detects Pd^{2+} ion in solution but also in living cells with high accuracy. The limit of detection (0.210 μM) of **L1** is found to be far less than the international standard prescribed by the WHO (47–94 μM). The probe remains intact after several cycles of using as a sensor, which is proved by the reversibility studies performed with Na_2EDTA. The stability of **L1**–Pd(II) complex is very high and it is not affected by the presence any counter anions as examined. The probe was able to perform in water samples taken from various natural sources within the pH range of 2–8. The paper strip test and TLC plate test prove the practical applicability of **L1** for spot tests which makes it easy to use for all practical purposes. The lifetime decay profile of the probe and the complex shows the static nature of quenching which further confirms the complex formation in solution. Theoretical calculations show a decrease in energies of HOMO, LUMO as well as the energy gap between them, consistent with experimentally observed red shift in the complex. A 5 μM solution of **L1** showed low cytotoxicity towards L929 cells and hence it can be used for detection of Pd^{2+} ion in living cells by fluorescence quenching phenomenon. In essence, the probe **L1** can be used as an excellent sensor for Pd^{2+} ion in every practical aspect.

References:

1. M. Wang, X. Liu, H. Lu, H. Wang and Z. Qin, *ACS Appl. Mater. Interfaces*, 2015, **7**, 1284–1289.
2. G. Campiani, S. Butini, C. Fattorusso, F. Trotta, S. Gemma, B. Catalanotti, V. Nacci, I. Fiorini, A. Cagnotto, A. Mereghetti, T. Mennini, P. Minetti, M. A. D. Cesare, M. A. Stasi, S. D. Serio, O. Ghirardi, O. Tinti and P. Carminati, *J. Med. Chem.*, 2005, **48**, 1705–1708.
3. S. Dhoun, I Kaur, P. Kaur and K. Singh, *Dyes Pigments*, 2017, **143**, 361–367.
4. K. C. Nicolaou, P. G. Bulger and D. Sarlah, *Angew. Chem. Int. Ed.*, 2005, **44**, 4442–4489.
5. R. Chinchilla and C. Nájera, *Chem. Soc. Rev.*, 2011, **40**, 5084–5121.
6. C. Torborg and M, Beller, *Adv. Synth. Catal.*, 2009, **351**, 3027–3043.
7. Q. Huang, Y. Zhou, Q. Zhang, E. Wang, Y. Min, H. Qiao, J. Zhang and T. Ma, *Sens. Actuators B: Chem.*, 2015, **208**, 22–29.
8. B. Zhu, C. Gao, Y. Zhu, C. Liu, Y. Li, Q. Wei, Z. Ma, B. Du and X. Zhang, *Chem. Commun.*, 2011, **47**, 8656–8658.
9. M. Z. K. Baig, S. Pawar, R. N. P. Tulichala, A. Nag and M. Chakravarty, *Sens. Actuators B: Chem.*, 2017, **243**, 226–233.
10. U. R. G, F. Ali, N. Taye, S. Chattopadhyay and A. Das, *Chem. Commun.*, 2015, **51**, 3649–3652.
11. Y. Kawata, M. Shiota, H. Tsutsui, Y. Yoshida, H. Sasaki and Y. Kinouchi, *J Dent Res.*, 1981, **60**, 1403–1409.
12. T. Z. Liu, T. F. Lin, D. T. Y. Chiu, K. J. Tsai and A. Stern, *Free Radic. Biol. Med.*, 1997, **23**, 155–161.
13. C. K. S. Pillai and U. S. Nandi, *Biochim. Biophys. Acta*, 1977, **474**, 11–16.
14. J. D. Spikes and C. F. Hodgson, *Biochem. Biophys. Res. Commun.*, 1969, **35**, 420–422.
15. M. D. Shultz, J. P. Lassig, M. G. Gooch, B. R. Evans and J. Woodward, *Biochem. Biophys. Res. Commun.*, 1995, **209**, 1046–1052.
16. C. E. Garrett and K. Prasad, *Adv. Synth. Catal.*, 2004, **346**, 889–900.
17. S. Sun, B. Qiao, N. Jiang, J. Wang, S. Zhang, X. Peng, *Org. Lett.*, 2014, **16**, 1132–1135.
18. W. Shi, X. Sun, S. Zhao and Z. Xie, *New J. Chem.*, 2015, **39**, 8552–8559.

19. Y. C. Wu and S. D. Huang, *Anal. Chem.*, 1999, **71**, 310–318.
20. Z. T. Graber, W. Wangb, G. Singhc, I. Kuzmenkod, D. Vakninb, E. E. Kooijman, *RSC Adv.*, 2015, **5**, 106536–106542.
21. V. Sharma, A. K. Saini and S. M. Mobin, *J. Mater. Chem. B*, 2016, **4**, 2466–2476.
22. N. Behera and V. Manivannan, *J. Photochem. Photobiol. A: Chem.*, 2018, **353**, 77–85.
23. P. Ravichandiran, S. A. Subramaniyan, A. P. Bella, P. M. Johnson, A. R. Kim, K. S. Shim and D. J. Yoo, *Anal. Chem.*, 2019, **91**, 10095−10101.
24. J. Yan, X. Wang Q. Tan, P. Yao, J. Tan and L. Zhang, *Analyst*, 2016, **141**, 2376–2379.
25. Z. Xu, X. Wang, J. Yan, J. Li, S. Guan and L. Zhang, *RSC Adv.*, 2016, **6**, 43539–43542.
26. P. Ravichandiran, A. B. Czubara, M. Masłyk, A. P. Bella, S. A. Subramaniyan, P. M. Johnson, K. S. Shim, H. G. Kim and D. J. Yoo, *ACS Sustainable Chem. Eng.*, 2019, **7**, 17210−17219.
27. S. Farshbaf and P. A. Jr, *Chem. Commun.*, 2019, **55**, 1770–1773.
28. E. Vaishnavi and R. Renganathana *Analyst*, 2014, **139**, 225–234.
29. M. Jin, L. Wei, Y. Yang, M. Runa and C. Yin, *New J. Chem.*, 2019, **43**, 548–551.
30. M. Yang, Y. Bai, W. Meng, Z. Cheng, N. Su and B. Yang, *Inorg. Chem. Commun.*, 2014, **46**, 310–314.
31. Y. Long, Y. Bai, J. Zhou and B. Yang, *J. Photochem. Photobiol. A: Chem.*, 2017, **332**, 422–431.
32. A. K. Adak, R. Purkait, S. K. Manna, B. C. Ghosh, S. Pathak and C. Sinha, *New J. Chem.*, 2019, **43**, 3899–3906.
33. W. Luo, M. Lei, Y. Wang, H. Gao, Y. Wang, Q. Zhou, Z. Xu and F. Yang, Anal. Methods, 2019, **11**, 5886–5892.
34. A. Helal, H. L. Nguyen, A. Al-Ahmed, K. E. Cordova and Z. H. Yamani, *Inorg. Chem.*, 2019, **58**, 1738–1741.
35. V. Sharma, A. K. Saini and S. M. Mobin, *J. Mater. Chem. B*, 2016, **4**, 2466–2476.
36. W. Feng, L. Bai, S. Jia and G Feng, *Sens. Actuators B: Chem.*, 2018, **260**, 554–562.
37. Z. Xu, X. Wang, J. Yan, J. Li, S. Guan and L. Zhang, *RSC Adv.*, 2016, **6**, 43539–43542.
38. P. Kumar, V. Kumar and R. Gupta, *RSC Adv.*, 2017, **7**, 7734–7741.
39. Q. Xia, S. Feng, D. Liu and G. Feng, *Sens. Actuators B: Chem.*, 2018, **258**, 98–104.

40. S. Suresh, N. Bhuvanesh, A. Raman, P. Sugumar, D. Padmanabhan, S. Easwaramoorthi, M. N. Ponnuswamy, S. Kavitha and R. Nandhakumar, *J. Photochem. Photobiol. A: Chem.*, 2019, **385**, 112092.
41. J. P. Kumar and B. B. Mandal, *Food Chem. Toxicol.*, 2019, **123**, 275–287.
42. P. Ravichandiran, A. B. Czubara, M. Masłyk, A. P. Bella, P. M. Johnson, S. A. Subramaniyan, K. S. Shim and D. J. Yoo, *Dyes Pigments*, 2020, **172**, 107828.
43. X. Z. Chen, X. D. Ma, H. M. Wang, M. Wang, Y. Y. Zhang, G. Gao, J. J. Liu and S. C. Hou, *New J. Chem.*, 2017, **41**, 8026–8030.
44. J. Bori, N. Behera, S. Mahata and V. Manivannan, *ChemistrySelect*, 2017, **2**, 11727–11731.
45. International Programme on Chemical Safety, Palladium; Environmental Health Criteria Series 226, World Health Organization, Geneva, 2002.

Appendix:

Table A1 Comparison of recent fluorescent probes for Pd^{2+} ion.

Probe	λ_{em}(nm)	LOD	Application	Solvent	Ref.
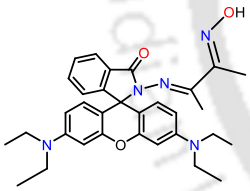	580 "*Turn-on*"	0.200µM	In PC12 cells.	Tris–HCl aqueous buffer solutions with 1% ethanol as co-solvent.	9
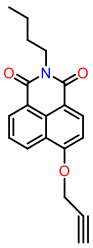	480 Ratiometric	0.07µM	In live RAW 264.7 macrophage cells.	20 mM phosphate buffer saline (PBS), pH 7.4).	11
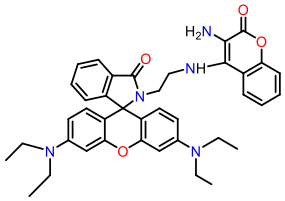	567 "*Turn - on*"	0.1 ppm	In Hct 116 cells.	aq. HEPES buffer–acetonitrile (1 : 1, *v/v*; pH 7.2)	14

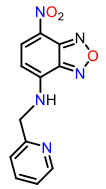	530 "*Turn - off*"	0.34 ppm	In living HeLa cells.	aqueous acetonitrile solution (CH_3CN : H_2O = 4 : 1, *v/v*).	30
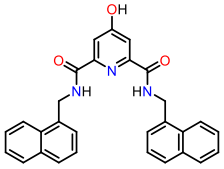	406 "*Turn - off*"	0.93 µM	In HEK-293 and L929 cell.	HEPES buffer containing 1% DMF (10 mM, pH = 7.2)	38
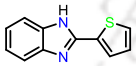	370 "*Turn - off*"	13.3µM	In Artemiasalina.	CH_3CN/ H_2O (1/1 (*v/v*) HEPES=50 mM, pH=7.4	40
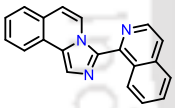	454 "*Turn - off*"	0.210 µM	In Hela and L929 cells.	MeOH / HEPES buffered aqueous solution (5 mM, pH = 7.4, 6:4, *v/v*)	This work

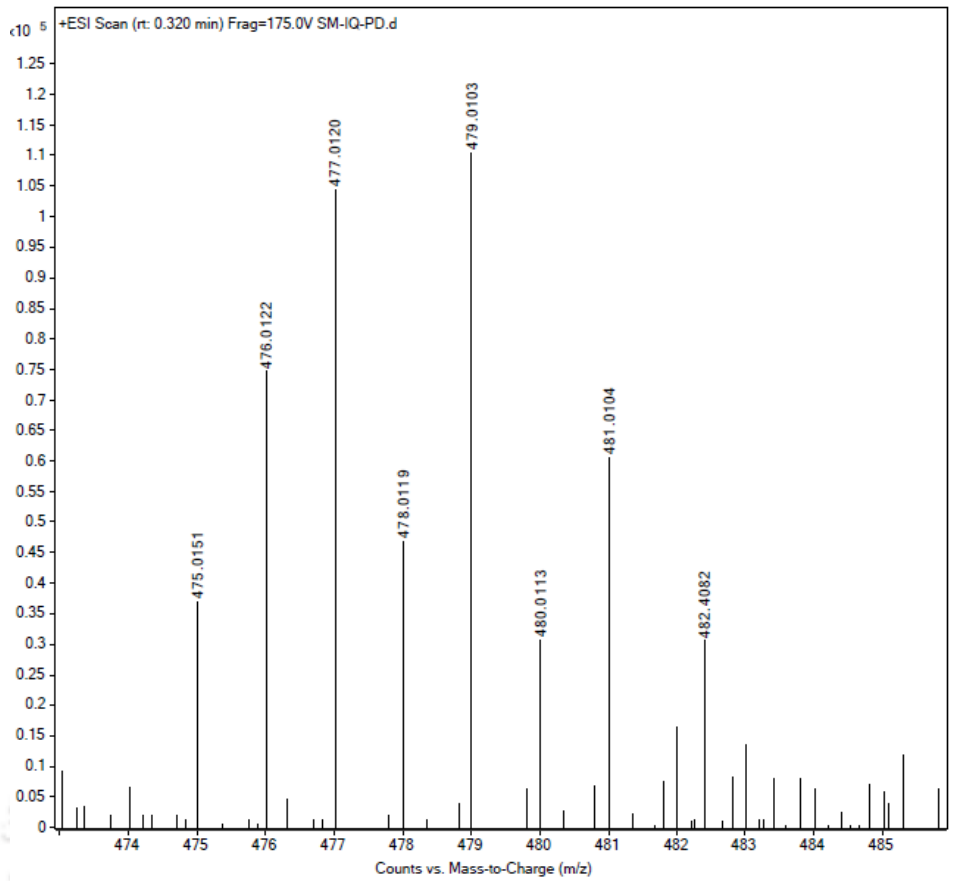

Fig. A1 Experimental mass spectrum of [Pd(**L1**)Cl(CH_3CN)]$^+$ complex ion.

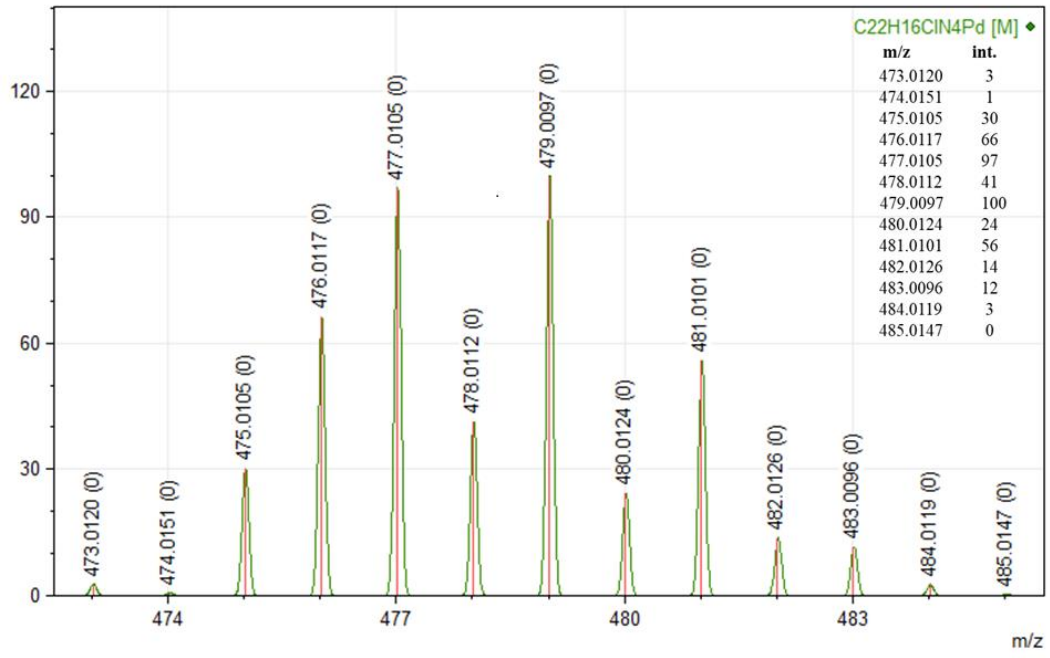

Fig. A2 Theoretical mass spectrum of [Pd(**L1**)Cl(CH_3CN)]$^+$ complex ion using mMass software.

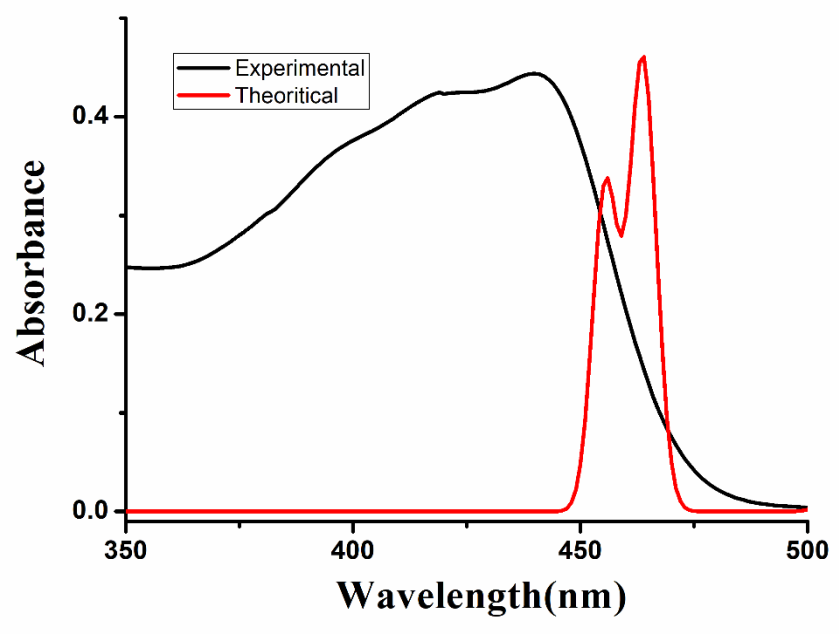

Fig. A3 Experimental and simulated UV-Vis absorption spectra of **L1** and its complex with Pd^{2+} ion.

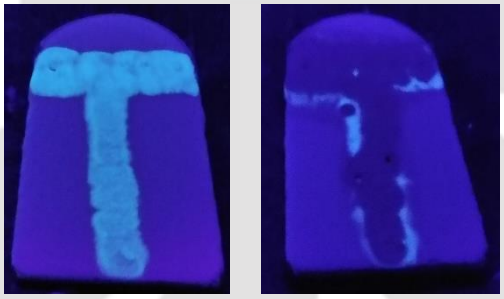

L1 **L1** + $PdCl_2$

Fig. A4 Images TLC plate test under longer UV light.

Chapter 3

3-(2-Hydroxyphenyl)imidazo[5, 1-*a*]isoquinoline as Cu(II) Sensor, its Cu(II) Complex for Selective Detection of CN^- Ion and Biological Compatibility*

Abstract:

The heterocyclic probe 3-(2-hydroxyphenyl)imidazo[5, 1-*a*]isoquinoline (**L2H**) has exhibited specific recognition of Cu^{2+} ion by forming a complex of formula [Cu(**L2**)$_2$], which in turn showed recognition for CN^- ions in CH_3CN/aqueous HEPES-buffer solution (5 mM, pH = 7.4, 6:4, *v/v*). The selective colorimetric and fluorescence response of **L2H** towards Cu^{2+} was achieved over other competing metal ions. Change of color from colorless to yellowish green upon incremental addition of Cu^{2+} into **L2H** solution can be easily observed with naked-eye. Emission intensity of **L2H** was quenched in presence of Cu^{2+} ion due to chelation enhanced quenching (CHEQ) process. From Job's plot and mass spectral analysis the binding stoichiometry was found to 2:1 between **L2H** and Cu^{2+}. Binding of the probe **L2H** with Cu^{2+} ion can be reversed by sequestering Cu^{2+} ion using Na_2EDTA solutions. Red shift in UV-visible spectrum upon addition of Cu^{2+} ion into **L2H** solution was a consequence of decrease in HOMO-LUMO energy gap. From life time decay curve the average fluorescence life time (τ) was found to be 3.8 ns for free **L2H** whereas in presence of Cu^{2+} τ decreased to 2.4 ns. In addition, so formed [Cu(**L2**)$_2$] complex was able to detect cyanide ion over other anions through removal of copper from the complex, as insoluble $[CuCN]_x$. Limit of detection of **L2H** for Cu^{2+} and [Cu(**L2**)$_2$] for CN^- were found to be 0.45 μM and 0.30 μM respectively. Detection of Cu^{2+} and CN^- were also performed in environmental real water samples. Based on the cytotoxic analysis, 5 μM of **L2H** was selected for determining its fluorescence attributes in cellular imaging in MDA-MB-231 and HDF cells. The cell images showed that intracellular Cu^{2+} and CN^- can be detected using **L2H** and [Cu(**L2**)$_2$] complex respectively.

---

*This work has been published in:

S. Mahata, S. Dey, B. B. Mandal and V. Manivannan, *J. Photochem. Photobiol. A: Chem.*, 2022, **427**, 113795.

3.1. Introduction

Synthesis and application of colorimetric and fluorometric probes for selective detection of biologically important metal ions have found enormous utility in applied biochemistry, medicinal biology and biotechnology.[1] Among various metal ions, copper plays its important roles as an essential cofactor in many enzymes as superoxide dismutase, cytochrome c oxidase, ceruloplasmin, dopamine β monooxygenase(DβM) and tyrosinase.[2-5] Homeostatis of copper is required to balance intercellular metabolism and normal functioning of enzymes in living organism.[6-11] However excessive accumulation of Cu^{2+} can create toxicity in some organisms like bacteria and viruses, which may also destroy the biological reprocessing systems in water.[12] Deficiency and excessive accumulation of copper in human may lead to various complications and diseases like neurodegenerative disorders such as, Menkes syndrome, Wilson's disease, Alzheimer's disease etc. and long term exposure causing liver and kidney damage.[13-15] Gradual increase in industrial revolution have led to serious environment problems that involve atmospheric, water and soil pollution leading to risks for human health.[16] Therefore, it is necessary to monitor Cu^{2+} ion concentration in environmental samples for environment protection and human health. The permissible limit of copper in drinking water is 2 ppm (31.5 μM) which is given by World Health Organization.[17] Thus, development of highly sensitive chemosensor capable of detection of Cu^{2+} with lower detection limit and quick response time can be extremely useful.[18]

Detection of cyanide ion is of vital importance because it is extremely toxic and shows lethal biological activity.[19,20] Cyanide ion causes hypoxiation after binding with cytochrome c oxidase results in inhibition of electron transfer in the human body.[21,22] In drinking water the maximum intake capacity of cyanide concentration level is 1.9 μM, as per World Health Organization (WHO) guidelines.[23] Therefore, cyanide ion detection in different consumables like water and food, in environmental systems like soil and air or in biological fluids (Serum, blood and urine) is highly necessary.

There are conventional techniques like (AAS) atomic absorption spectrometry,[24,25] (ICP-MS) inductively coupled plasma-mass spectrometry,[26] electrochemical,[27] potentiometry,[28] polarography,[29] flow injection amperometric[30] and simple titrations[31] for the detection of copper and the cyanide ions but many of these techniques are costly and very time consuming. On the other hand, methods of detection by colorimetric and fluorescence techniques are simple and easily extended to biological applications too.[32-36] However, strong

hydration nature of anions, makes it difficult for the fluorescent sensors to target anions.[37,38] So, indirect way to overcome this barrier is to apply metal displacement approach,[39-41] specifically with metal complex ion "ensemble" being non-fluorescent and free ligand being fluorescent in nature. As a result of metal-ion-induced fluorescence quenching the ensemble becomes non fluorescent. Now, addition of anions into the ensemble solution could trigger dissociation of coordination complex thereby releasing the probe and restoring its original fluorescence.

A di-hydroxycoumarin based copper complex has been reported for selective detection of toxic cyanide in aqueous medium.[32] This complex was applicable for the detection of cyanide in fresh mouse serum and cell images showed that the complex could be used for intracellular CN^- detection. A supramolecular copper metallogel has been used toward cyanide sensing in aqueous medium.[33] An excited state intramolecular proton transfer (ESIPT) process-based chromogenic and fluorogenic probe has been synthesized with the aim of sequential *in situ* detection of Cu^{2+} and CN^- ions.[34] Selective detection of Cu^{2+} and CN^- ions in biological systems was also explained by intracellular bioimaging studies in MCF-7 cell lines. Dipyridylamine and anthracene based Cu^{2+} ensembles have been developed as effective fluorescence turn-on detection of CN^- ion.[42] A triphenylene based copper ensemble prepared *in situ* has been investigated for detection of CN^- ion.[43] Perylene diimide appended with 8-hydroxyquinoline derivatives have been synthesized for the naked eye detection of Cu^{2+} ion and CN^- ion.[48] Coumarin-Cu(II) ensemble-based probe has been designed for detection of cyanide ion in aqueous media with remarkable fluorescence enhancement over other anions.[52] Selective detection of cyanide with this copper ensemble for biological application was also performed in HepG2 cells. A Cu(II)-based ensemble bearing rhodamine-B fluorophore unit has been developed for fluorescence "*turn-on*" detection of CN^-.[53] For distinguishable, controllable and reversible sensing of CN^-, a phenazine based Cu(II) ensemble has been used and it showed a new perspective for the design of reusable multi-functional probes for the successional and distinguishing detection of different analytes in aqueous solution.[54] Cu(II) complex with quinazoline derivative has been reported as fluorescence chemosensor for cyanide detection in aqueous media and bioimaging experiments have been conducted to prove the ability of the complex to detect CN^- in living cells.[56]

Generally, the toxicity of transition metal complexes of cyanide ion is less than free cyanide ion. Copper(II) is known for quenching the fluorescence of organic chromophores, for the

reason of paramagnetic quenching effect. As cyanide has been known to form complexes of the type $[Cu(CN)_x]^{n-}$, upon reaction of CN^- with a preformed non-fluorescent Cu(II)-fluorophore complex, eventually restores the fluorescence intensity of fluorophores.[42,43] Cyanide ion also form polymeric copper(I) cyanide in presence of copper(II) salt.[44,45] Due to polymeric nature, insoluble $[CuCN]_x$ is more stable than monomeric soluble $[Cu(CN)_x]^{n-}$ species. This is one major advantage of the formation of polymeric insoluble copper(I) cyanide over soluble $[Cu(CN)_x]^{n-}$ species. For the detection of cyanide many metal complexes have been reported in the literature *via* colorimetric and fluorescence methods. However, most of the reported copper complex or ensemble requires expensive reactants and rigorous purification processes followed by multiple lengthy characterization techniques.[46-49]

To avoid these expensive reagents and long-time duration characterization techniques we have used a novel heterocyclic probe 3-(2-hydroxyphenyl)imidazo[5, 1-*a*]isoquinoline(**L2H**) which was synthesized in our lab through simple process by using very less expensive reagents and short time duration.[50] This molecule is highly fluorescent in nature and can act as bidentate chelating ligand. To the best of our knowledge, a very few heterocyclic probes are reported for the selective detection of Cu^{2+} and CN^- ion respectively with high precision (Table A1). In this Chapter, the utility of **L2H** as a Cu(II) sensor and thus formed $[Cu(\mathbf{L2})_2]$ as CN^- ion sensor through the formation of insoluble $[CuCN]_x$ along with their biological compatibility, has been described.

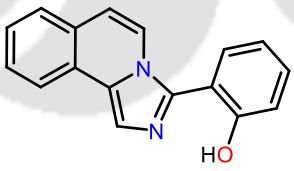

L2H

Scheme 1 Structure of the probe **L2H**.

3.2. Experimental section

Probe **L2H** was synthesised by following reported procedure[50] and all the spectral characteristic of **L2H** matched perfectly with the values reported earlier.

3.2.1. Cell Studies

3.2.1.1. Cell culture

The **L2H** molecule was evaluated for its cytotoxicity and fluorescence properties through *in vitro* cell studies using human triple-negative breast carcinoma cells (MDA-MB-231) and primary human dermal fibroblasts (HDF). MDA-MB-231 cells were procured from National Centre for Cell Science, India and HDF cells were procured from HiMedia Laboratories, India. Both the cell types were cultured and maintained using high glucose Dulbecco's modified Eagle's medium (hDMEM, Thermo Fisher, USA) in a cell culture humidified incubator with 5 % CO_2 at 37 °C. The culture media was supplemented with 10 % (v/v) fetal bovine serum (FBS), and 1X antibiotic-antimycotic solution (Himedia, India).

3.2.1.2. Cytotoxicity studies

The cytotoxic effect of **L2H** molecule on both cell types was determined through MTT assay.[35,55] Briefly, both the cell types were plated in a 96 well plate at a density of 5 x 10^3 cells per well and cultured for 24 h before cytotoxicity evaluation in a cell culture humidified incubator with 5 % CO_2 at 37 °C. Following cellular attachment, both the type of cells was treated for 24 h with the following concentration of **L2H** molecule i.e., 0, 1.25, 2.5, 5, 7.5, and 10 μM in hDMEM. Cell viability was assessed after 24 h of treatment using MTT reagent at 0.5 $mg.ml^{-1}$ for 4 h. After 4 h, 100 μL of DMSO was used for dissolving the formazan crystals and Multiskan Multiplate Reader (Thermo Scientific, USA) was used for recording the absorbance at 570 nm. The percentage (%) of cell viability for both the cell types after treatment with the respective concentration of **L2H** molecule was calculated relative to the control group (consisting of only media).

3.2.1.3. Fluorescence imaging

A non-cytotoxic concentration of 5 μM **L2H** molecule was adopted based on the cell cytotoxicity assay for evaluating the fluorescence properties of only **L2H** molecule, **L2H** molecule after incubation with Cu^{2+} and **L2H** molecule after incubation with Cu^{2+} and CN^- against MDA-MB-231 cells and HDF. Briefly, both the cell types were seeded in a 24 well plate at a density of 2 x 10^4 and maintained for 24 h before fluorescence imaging in a cell culture humidified incubator with 5 % CO_2 at 37 °C. Post 24 h, both the cells were treated with 5 μM **L2H** molecule suspended in high glucose DMEM for 60 min. Correspondingly, cells pre-treated with 5 μM **L2H** molecule was then incubated with 0.25 μM Cu^{2+} for 30 min. Similarly, cells pre-treated with 5 μM **L2H** and 0.25 μM Cu^{2+} was incubated with 12.5 μM CN^- for 45 min. After incubation, both the cell types were washed thrice with PBS

(phosphate buffered saline, pH 7.4) and images were taken using a fluorescence microscopy (EVOS, Life Technologies).

3.2.1.4. Statistical Analysis

All the experiments were carried out in n = 4 samples and the results have been analysed and represented as mean ± SD (standard deviation). One-way ANOVA was carried out between the groups using OriginPro software (Originlab Corporation, USA). ImageJ analysis software (NIH, USA) was used for processing the obtained fluorescence images. The groups were considered to possess significant statistical difference at *$p \leq 0.05$, **$p \leq 0.01$ and $^{\#}p \leq 0.001$.

3.3. Results and discussion

The 3-(2-hydroxyphenyl)imidazo[5, 1-*a*]isoquinoline (**L2H**) has a phenol group at the 3rd position of the fused-ring diazaheterocycle, imidazo[5, 1-*a*]isoquinoline. The related 3-(1-isoquinolinyl)imidazo[5, 1-*a*]isoquinoline bearing imidazo[5, 1-*a*]isoquinoline moiety has been reported to be fluorescent in nature[50] and an efficient sensor for the detection palladium(II) ion.[35] The conjugate base $\mathbf{L2}^-$ is a potential bidentate chelating ligand with the formation of a favorable six-membered chelate ring that can bind metal ions through imidazo-nitrogen present at 2nd position of the fused nucleus and phenolate-oxygen. Thus, **L2H** by virtue of having fluorescent imidazo[5, 1-*a*]isoquinoline moiety and metal ion binding site, could be a potential metal ion sensor. Based on this background, we have evaluated the utility of **L2H** for metal ion sensing by electronic absorption and emission spectroscopic studies in CH_3CN / HEPES buffered (5 mM, pH = 7.4, 6:4, *v/v*) aqueous solution. The metal ions that were used during titration experiments includes chlorides of Na^+, K^+, Li^+, Ca^{2+}, Mg^{2+}, Mn^{2+}, Fe^{2+}, Co^{2+}, Ni^{2+}, Cu^{2+}, Zn^{2+}, Cd^{2+}, Hg^{2+}, Pb^{2+}, Fe^{3+}, Cr^{3+}, Al^{3+}, Pd^{2+}, Pt^{2+} and Au^{3+}. Based on stoichiometry studies a [Cu(**L2**)$_2$] formula has been proposed for the reaction between $CuCl_2$ and **L2H**, *vide infra*.

3.3.1. UV–Vis spectra

Absorption spectral behavior of **L2H** was examined in CH_3CN : HEPES buffer (5 mM, pH = 7.4, 6:4, *v/v*) solution. The characteristic absorption peak for **L2H** was observed at 334 nm which may be due to $n \rightarrow \pi^*$ transition. Upon addition up to two equivalents of various metal chlorides, the absorption maximum remained almost unchanged or slightly decreased (Fig. 1). But, during gradual addition $CuCl_2$ the peak at 334 nm was obscured by the new growing peak at 299 nm along with another appearing at 456 nm (Fig. 2). This also resulted in change

of color of the solution from nearly colorless to greenish-yellow with Cu(II) ion only (Fig. A1). This absorption band at 299 nm may be due to $\pi \rightarrow \pi^*$ transition and its intensity gradually increased upon addition of Cu^{2+} ion indicated that 2-hydroxyphenyl and imidazo[5, 1-*a*]isoquinoline moieties of the ligand are getting nearly planar to each other.

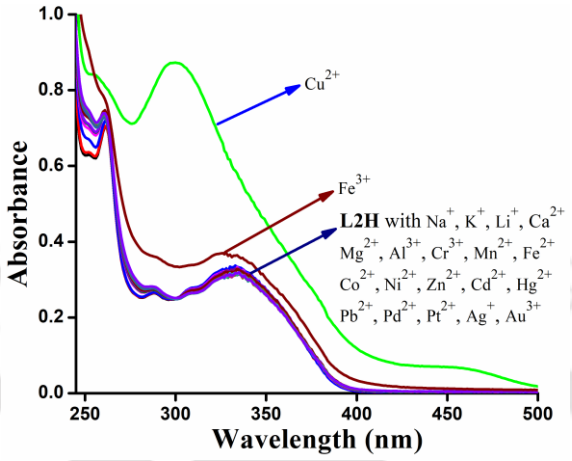

Fig. 1 Absorption spectra of **L2H** (3.3×10^{-5} M) in CH_3CN/aqueous HEPES buffer (5 mM, pH = 7.4, 6:4, *v/v*) with various metal ions (1.7×10^{-5} M).

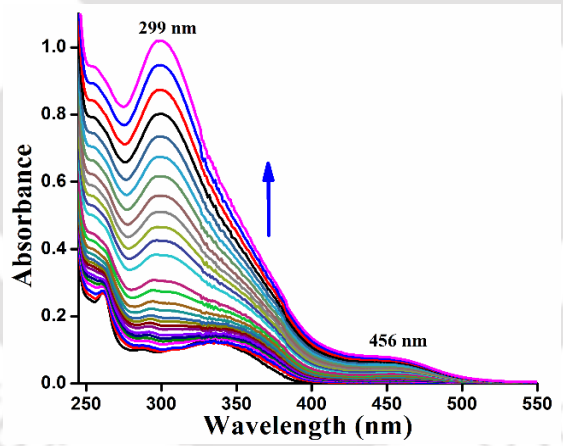

Fig. 2 Changes in UV–Vis spectra of **L2H** (2.1×10^{-5} M) upon gradual addition of $CuCl_2$ (0-1.1) $\times 10^{-5}$ M) in CH_3CN/aqueous HEPES buffer (5 mM, pH = 7.4, 6:4, *v/v*).

3.3.2. Fluorescence spectra

For understanding the sensing mode of **L2H** towards Cu^{2+}, its emission study was carried out. Upon exciting **L2H** with λ_{ex} = 334 nm light, a strong emission at 471 nm was observed and no obvious change in fluorescence intensity was observed after the addition of up to 10 equivalents of chlorides of Na^+, K^+, Li^+, Ca^{2+}, Mg^{2+}, Al^{3+}, Cr^{3+}, Mn^{2+}, Fe^{2+}, Co^{2+}, Ni^{2+}, Zn^{2+}, Cd^{2+}, Hg^{2+}, Pb^{2+}, Ag^+ and Au^{3+} into **L2H** solution (Fig. 3). Fluorescence intensity decreased

only slightly upon addition of Fe^{3+} (Fig. 3) into **L2H** solution. But during gradual addition of $CuCl_2$ there was a remarkable quenching in the fluorescence intensity (Fig. 4 and A1) of **L2H**. This is characterised by greenish yellow coloration when observed under long UV light along with concomitant shift of the emission peak to 455 nm, which can be observed with naked eye (Fig. S1). Reduction in emission intensity of **L2H** in presence of Cu^{2+} ion is due to establishment of chelation enhanced quenching (CHEQ) process upon coordination of **L2H** to Cu^{2+} ion. Metal ion competition study was performed by treating **L2H** (Fig. 5) firstly with excess amount (10 equivalent) of competing metal salts and then adding $CuCl_2$ respectively. It was observed that the fluorescence intensity of **L2H** was quenched properly after the addition of Cu^{2+} ion in presence of different metal salts as well. From this competition study we can conclude that **L2H** can detect selectively Cu^{2+} ion in presence of different metal ions.

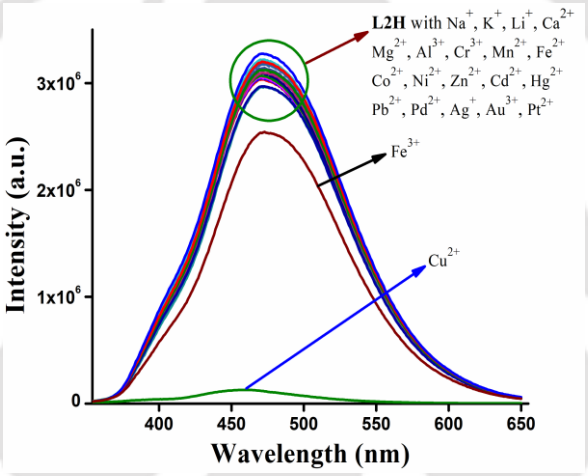

Fig. 3 Fluorescence spectra of **L2H** (3.3×10^{-5} M) in CH_3CN/aqueous HEPES buffer (5 mM, pH = 7.4, 6:4, *v/v*) in presence of various metal ions (1.7×10^{-5} M); λ_{ex} = 334 nm, λ_{em} = 471 nm.

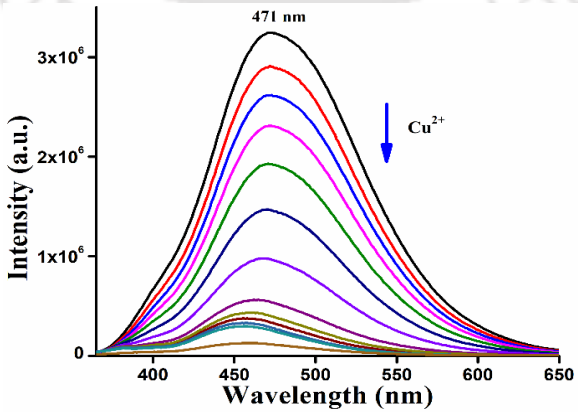

Fig. 4 Fluorescence spectra of **L2H** (3.3×10^{-5} M) upon gradually addition of $CuCl_2$ (0-1 equivalent) in CH_3CN/HEPES-buffer solution (5 mM, pH = 7.4, 6:4, *v/v*), λ_{ex} = 334 nm.

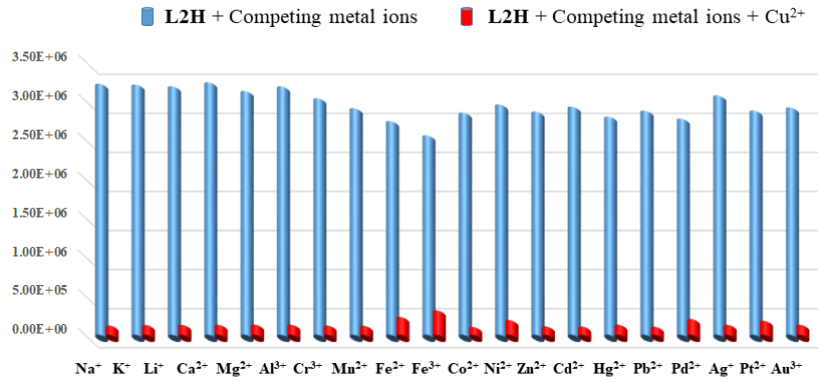

Fig. 5 Bar diagram of **L2H** by adding excess amount (10 equivalent) of various metal chlorides and $CuCl_2$.

The pH dependence of the emission intensities of **L2H** and the [Cu(**L2**)$_2$] complex was investigated in CH_3CN-HEPES buffer solution and HCl or NaOH solution were utilized for adjusting the pH to the desired value. As shown in Fig. 6, the optimum pH range through which emission intensity of **L2H** quenched by Cu^{2+} has been found to be 3 – 12. Below pH 3, **L2H** itself was showing decreased fluorescence intensity which was not altered by addition of $CuCl_2$, which is consistent with the fact that phenolic –OH can get protonated in both **L2H** and its copper(II) complex, thereby inhibiting the process of fluorescence. It was seen that at pH beyond 12 fluorescence intensity was not quenched due to the formation of copper(II) hydroxide. This experiment suggests that **L2H** is a very good chemosensor for selective detection of Cu^{2+} in the wide pH range of 3 – 12 and thus making **L2H** to be suitable for detecting Cu^{2+} ions under the environmental and physiological conditions.

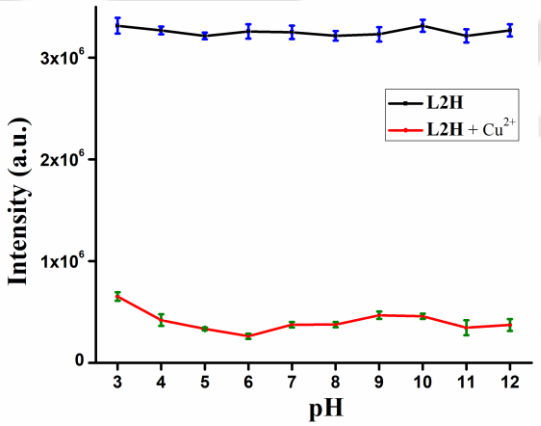

Fig. 6 Plot of pH effect on the fluorescence intensity of **L2H** and [Cu(**L2**)$_2$] complex.

Response time of a sensor is an important factor for quick detection of the analyte and it will be more acceptable if there is quick response by **L2H** towards Cu^{2+} ion. The reaction time for binding of **L2H** with Cu^{2+} was also been determined and it was found that the fluorescence

intensity at 471 nm of **L2H** was instantly quenched to equilibrium point within 32 Sec (Fig. 7). Therefore, this very short reaction time of 32 Sec. is advantageous for the utility of **L2H** for practical purposes.

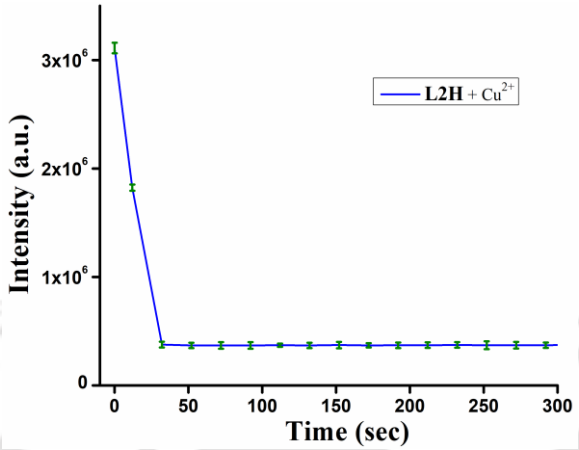

Fig. 7 Determination of fluorescence response time.

Another important aspect related to sensors is reversibility of binding of the probe with analyte and reversible binding of **L2H** with Cu^{2+} ion was evaluated through Na_2EDTA method.[51] After the adding one equivalent of Na_2EDTA solution to the solution of $[Cu(\mathbf{L2})_2]$ complex, emission intensity at 471 nm was restored that was very much comparable to original spectrum of **L2H** (Fig. 8). This indicates that Na_2EDTA effectively sequesters Cu^{2+} ion and releases free **L2H** thereby re-establishing the original fluorescence intensity of free **L2H**. These processes of reversibility can be repeated several times by quenching the emission intensity of **L2H** at 471 nm by adding Cu^{2+} ion and restoring the emission intensity by sequestering Cu^{2+} ion with Na_2EDTA.

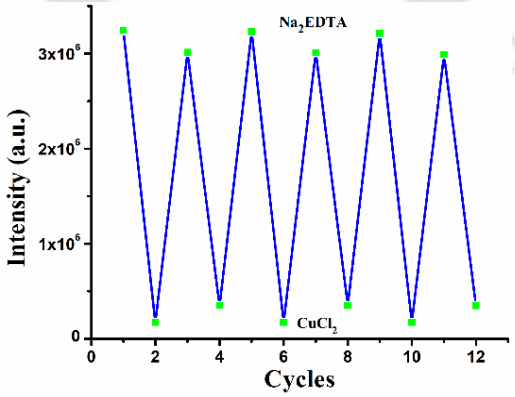

Fig. 8 Reversibility cycle.

3.3.3. Detection of Cu^{2+} in real water samples

Detection of Cu^{2+} ion in real water samples was also performed to assess the practical utility of **L2H** using fluorescence measurement technique. Tap water, drinking water and river water samples were collected from the institute's common facilities and river Brahmaputra (near I.I.T Guwahati campus, Assam, India). Then the water samples were filtered through 0.22 μM membrane filter paper and pH of the solutions was adjusted to 7.4. Firstly, a blank experiment was carried out in order to check the presence of Cu^{2+} ion in samples and found to be negative based on unchanged **L2H** fluorescence intensity. After that fluorescence titration experiment was performed using the solutions of $CuCl_2$ which were prepared from these collected water samples. Emission intensity at 454 nm *vs* Cu^{2+} concentration plot suggests that **L2H** is a perfect probe for the detection of Cu^{2+} ion in these real water samples (shown in Fig. A1).

3.4. Life time measurements

Life time of the excited state of **L2H** has been determined by using time resolved fluorescence spectroscopy. Quenching of emission intensity of **L2H** could be static in nature due to formation of complex with Cu^{2+} ion. Fluorescence decay profile of free **L2H** and in presence of Cu^{2+} is shown in Fig. 9 and Table 1. From the decay curve the calculated average fluorescence life time (τ) was found to be 3.8 ns for free **L2H** whereas in presence of Cu^{2+} the life time decreases to 2.4 ns. This change in life time values could be attributed to the formation of non-fluorescent complex through static quenching.

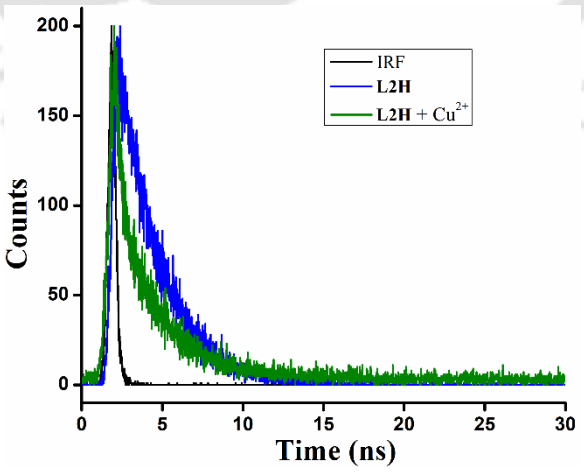

Fig. 9 Life time Decay profile.

Table 1. Fluorescence decay parameters of for life time measurements

Sample	τ (ns)	χ^2
L2H	3.8	1.06
L2H + Cu^{2+}	2.4	1.02

3.5. Binding stoichiometry

In order to ascertain the binding ratio between **L2H** and Cu^{2+}, Job's plot was used and it was found to be 2:1 (Fig. 10). Benesi–Hildebrand plot yielded the binding constant value of 1.16 × 10^5 M^{-1}, which is quite on the higher side.

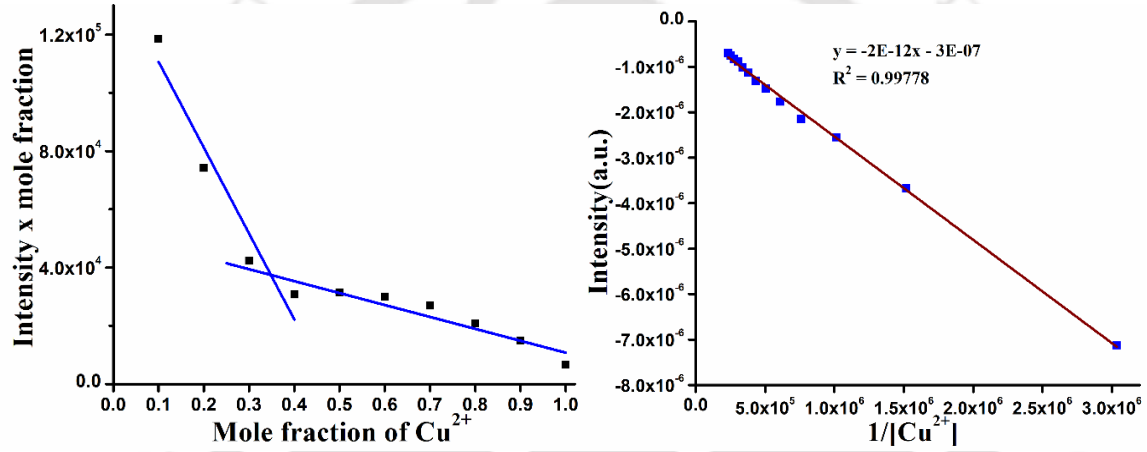

(a) (b)

Fig. 10 (a) Job's plot and (b) Benesi–Hildebrand plot

ESI mass spectrum of **L2H** exhibited a peak at *m*/*z* = 582.108 (calculated for $C_{34}H_{23}CuN_4O_2^+$ = 582.111) that can be assigned to the formula $[Cu(\mathbf{L2})_2(H)]^+$ ion, is also consistent with the formation of 2:1 complex between probe **L2H** and Cu^{2+} ion. Mass spectral fragments calculated using mMass software matched well with that of experimentally observed mass spectrum (Fig. 10).

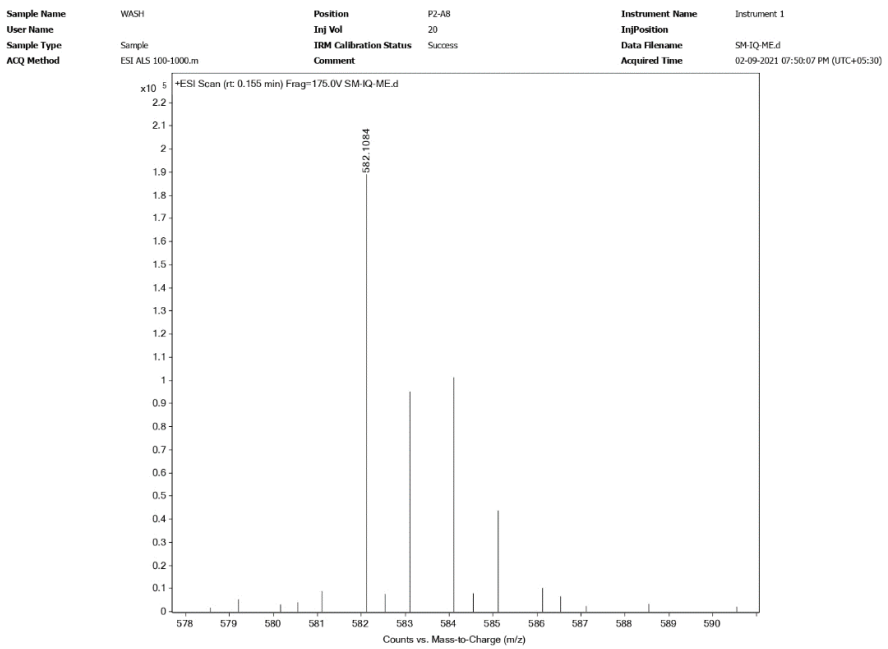

(a)

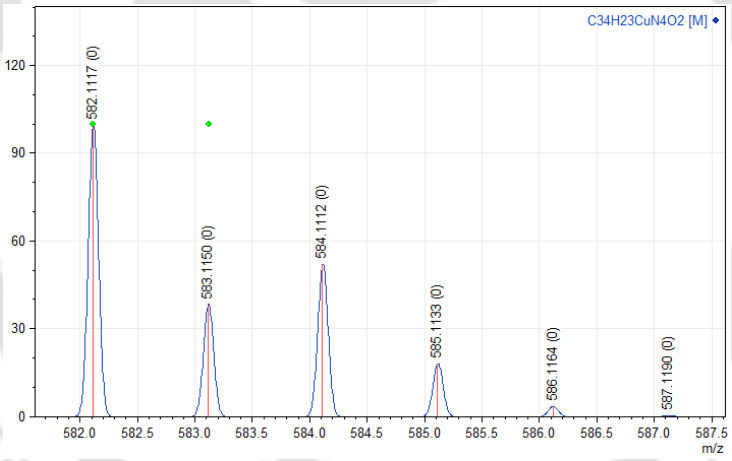

(b)

Fig. 11 (a) Experimental and (b) theoretical mass spectrum $[Cu(\mathbf{L2})_2(H)]^+$ complex ion.

Fluorescence quantum yield of free **L2H** and that of its Cu(II) complex were found to be 0.13 and 0.02 respectively, a decrease of quantum yield upon complexation with Cu^{2+} ion. From Stern–Volmer plot the quenching efficiency by Cu^{2+} ion can be conveniently understood, and constant (K_{SV}) was found to be 1.89×10^5 M^{-1} (Fig. 12a). Using the formula 3σ/k limit of detection was calculated to be 0.45 μM for Cu^{2+} from the fluorescence titration curve (Fig. 12b). It is noticeable that this lowest value of detection limit by **L2H** is very much below the permissible threshold limit for copper (31.5 μM) as directed by WHO. Therefore, we can say

that **L2H** can be used as a fluorescent "*On–Off*" type sensor towards Cu^{2+} with high selectivity and sensitivity.

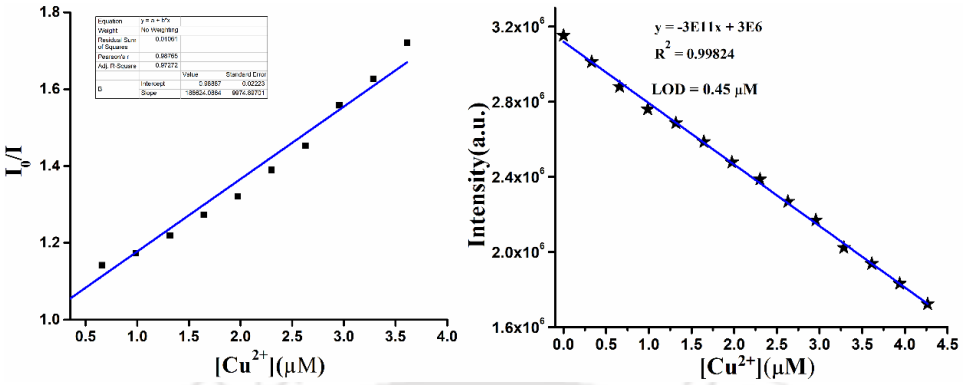

(a) (b)

Fig. 12 (a) Stern volmer plot of **L2H** with Cu^{2+} and (b) calculation detection limit of **L2H** towards Cu^{2+}.

3.6. Computational studies

The DFT/TDDFT calculations were also performed using Gaussian09 program on **L2H** and the complex having the formula [Cu(**L2**)$_2$] that is consistent with binding ratio obtained from Job's plot, ESI-mass spectrometry analysis and ^{1}H NMR titration experiments with binding ratio. Geometry was optimized by setting B3LYP level for calculations and the lanl2dz basis set was assigned for all the elements in complex. The optimized structures of **L2H** and [Cu(**L2**)$_2$] are displayed in Fig. 13 and in [Cu(**L2**)$_2$] central metal ion is bound by two **L2**$^-$ ions in a bidentate fashion and coordinated *via* oxygen from phenolate group and nitrogen atom of imidazo group from imidazo[5, 1-*a*] isoquinoline moiety. Coordination through nitrogen and oxygen atoms from two **L2**$^-$ can offer slightly distorted square planer geometry around the central metal ion.

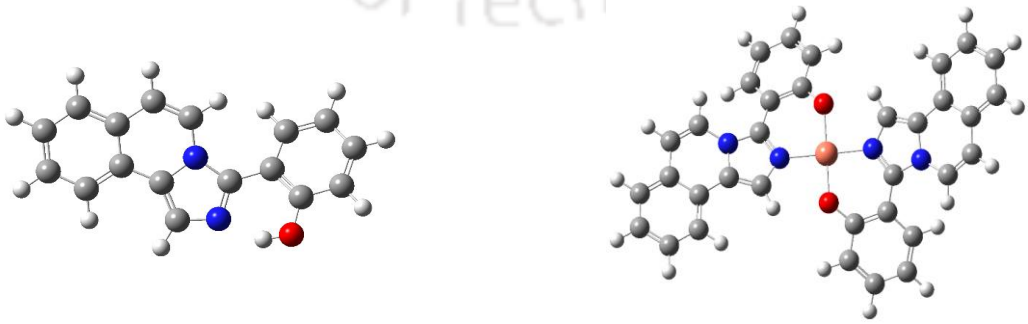

Fig. 13 Optimized structure of **L2H** (left) and [Cu(**L2**)$_2$] complex (right). (atom colors: gray = C, blue = N, white = H, red = O, peach = Cu).

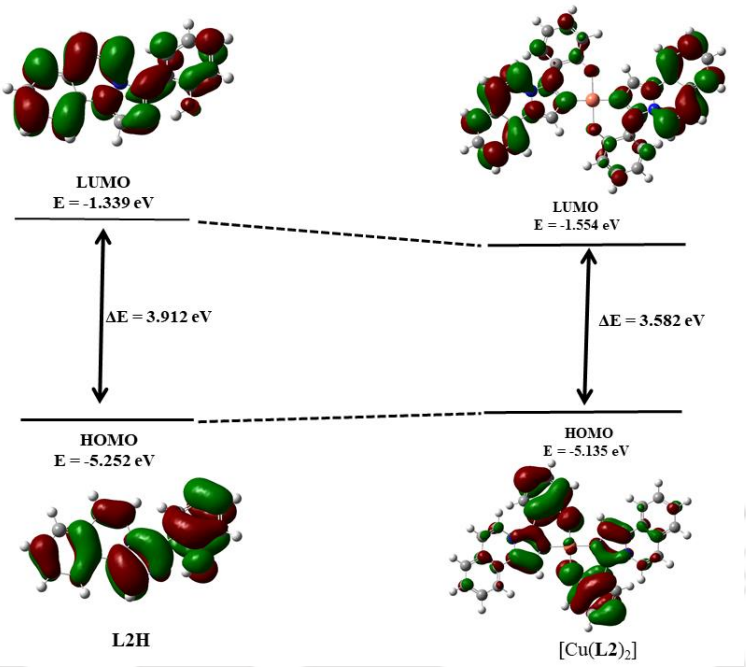

Fig. 14 Energy level diagram indicating HOMO and LUMO in **L2H** and [Cu(**L2**)$_2$].

In the HOMO of **L2H**, π-electron density is distributed over the whole molecule but the LUMO is mostly distributed on the imidazo isoquinoline moiety. In HOMO of [Cu(**L2**)$_2$] complex, the π-electron density is distributed on the imidazole, phenolate group and on copper(II) center. But in LUMO the electron density is localized only on the imidazo-isoquinoline moiety. So after complex formation between **L2**$^-$ and Cu^{2+} ion, the energy of HOMO is increased to the extent of 0.117 eV whereas LUMO is decreased by 0.215 eV as depicted in Fig. 14. So the HOMO-LUMO energy is lowered to 3.582 eV in [Cu(**L2**)$_2$] which was calculated to 3.912 eV in free **L2H**. Upon complexation with Cu^{2+} the net effect is that energy difference between HOMO and LUMO in [Cu(**L2**)$_2$] is lowered. This result also supports the red shift observed in the absorption maximum of free **L2H** upon forming [Cu(**L2**)$_2$] (Fig. A3).

3.7. ^{1}H NMR titration experiment

Binding of **L2H** to Cu^{2+} ion was also investigated using ^{1}H NMR titration experiment (Fig. 15). In spectrum of free **L2H** all signals due to protons were sharp in nature. Upon gradual addition of $CuCl_2$ to **L2H** solution (a) –OH peak at 10.56 ppm started to diminish in intensity which completely disappeared after addition of about 0.5 equivalents; (b) signals of all other protons became broader, which may be due to the paramagnetic effect of Cu^{2+} ion. This

support the fact that upon coordination to the metal ion, the deprotonation of phenolic –OH group occurs and the probe bind in its conjugate base form. Also an aromatic proton signal got shifted slightly from 8.095 to 8.134 ppm during gradual addition of $CuCl_2$ which finally become broad after completion of 0.5 equivalents.

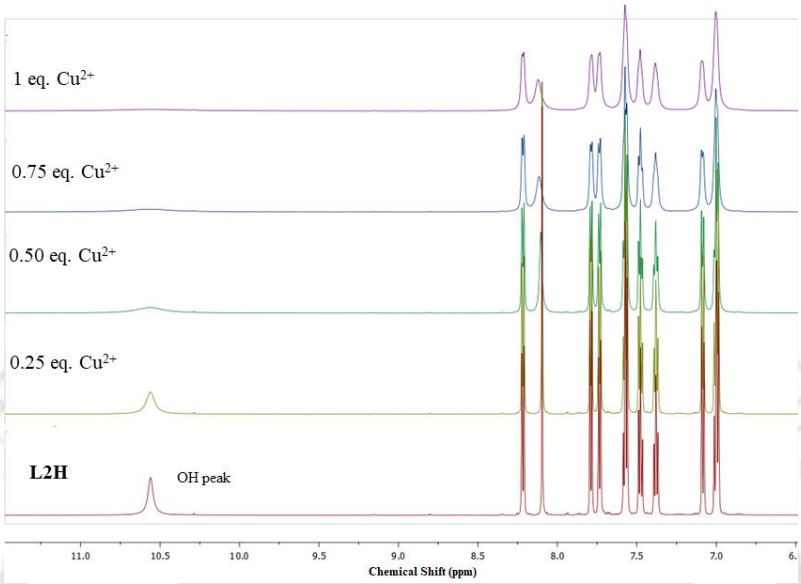

Fig. 15 ^{1}H NMR titration plot of **L2H** with $CuCl_2$ in 1:1 mixture of DMSO-d_6 and MeOD.

3.8. Effect of Cyanide ion on [Cu(L2)$_2$] complex

From the spectral studies described above, it is evident that **L2H** could detect selectively Cu^{2+} in presence of other metal ions which is expressed through a significant change in its absorption and emission spectral characteristics. Now it is important to see that whether thus formed [Cu(**L2**)$_2$] complex could be able to selectively detect any anions. Cyanide ion has long been known to coordinate with Cu(II)/Cu(I) easily by forming very stable complexes.[52,53] Using this known copper-cyanide affinity, we have evaluated the selectivity of [Cu(**L2**)$_2$] complex towards CN^- ion (10 equivalent) in presence of different anions (50 equivalent) like F^-, Cl^-, Br^-, I^-, SO_3^{2-}, SO_4^{2-}, S^{2-}, $S_2O_3^{2-}$, NO_3^-, NO_2^-, CO_3^{2-}, $H_2PO_4^-$, ClO_4^-, AcO^-, PO_4^{3-}, N_3^-, HSO_4^-, HSO_3^- and SCN^- (Fig. 19). In absorption spectroscopic study it was seen that after addition of CN^- into the [Cu(**L2**)$_2$] complex solution the absorption band having the peak at 334 nm (Fig 16 which was seen in case of **L2H** only) re-appeared. But during addition of other anions listed above there was no change in the absorption spectral characteristics of [Cu(**L2**)$_2$] complex.

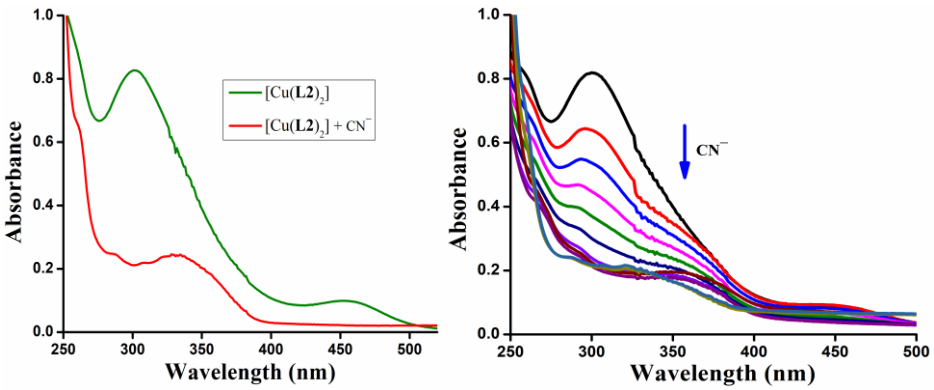

Fig. 16 Absorption spectral behaviour of [Cu(**L2**)$_2$] (1.05 × 10^{-5} M) in CH_3CN/aqueous HEPES buffer (5 mM, pH = 7.4, 6:4, *v/v*) towards CN^- ion (2.65 × 10^{-5} M).

It was also observed that except CN^- all other anions did not restore/alter the fluorescence response due to free **L2H** (Fig. 17), indicating that only CN^- ion was effective in dismantling the [Cu(**L2**)$_2$] complex (Scheme 2). Only in case of S^{2-} there was a small increase in fluorescence intensity, but in presence of CN^- the absorption and emission peaks of **L2H** were regenerated to the full original intensity which understandably is due to displacement of copper from [Cu(**L2**)$_2$] complex (Fig. 18).

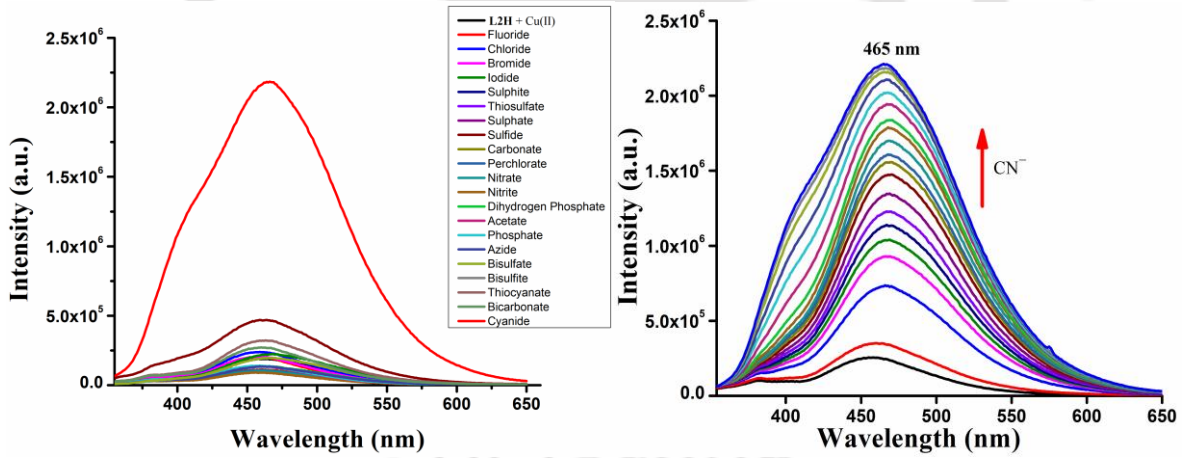

Fig. 17 Changes in fluorescence intensity of [Cu(**L2**)$_2$] (1.05 × 10^{-5} M) in CH_3CN/aqueous HEPES buffer (5 mM, pH = 7.4, 6:4, *v/v*) with 10 equiv. of F^-, Cl^-, Br^-, I^-, SO_3^{2-}, SO_4^{2-}, S^{2-}, $S_2O_3^{2-}$, NO_3^-, NO_2^-, CO_3^{2-}, $H_2PO_4^-$, ClO_4^-, AcO^-, PO_4^{3-}, N_3^-, HCO_3^-, HSO_4^-, HSO_3^- and SCN^- and 2 equiv. of CN^-.

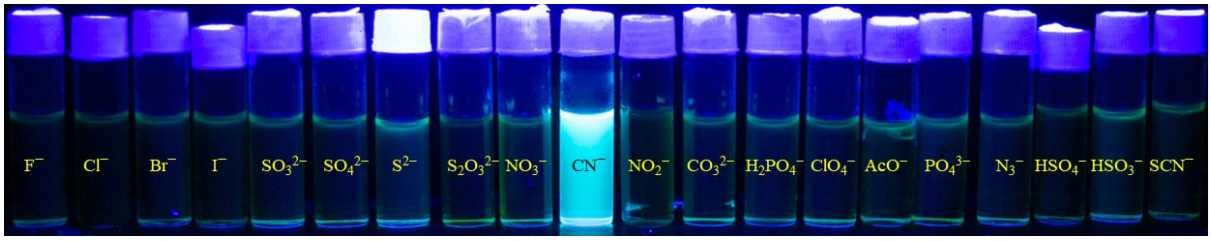

Fig. 18 Emission photographs of [Cu(**L2**)$_2$] in presence of various anions.

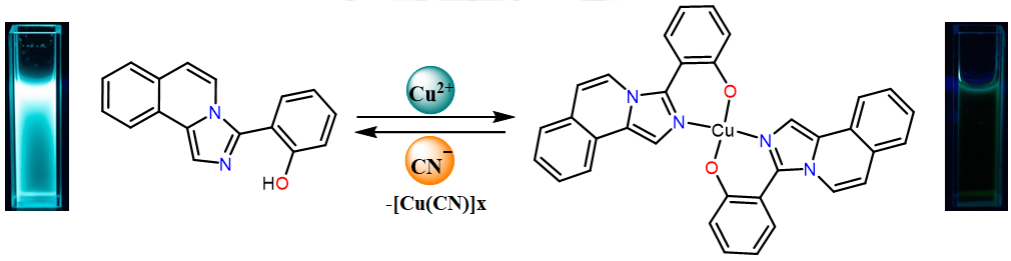

L2H

Fluorescence signal "ON"

[Cu(**L2**)$_2$]

Fluorescence signal "OFF"

CHEQ

Scheme 2 Proposed sensing mechanism.

Regeneration of **L2H** was also accompanied by the solution becoming slightly turbid due to formation of insoluble polymeric copper(I) cyanide, $[Cu(CN)]_x$ and this also reflected by slight broadening of the emission band after addition of CN^- ion to the solution containing [Cu(**L2**)$_2$] (Fig. 17). Formation of insoluble polymeric $[Cu(CN)]_x$ was also evident from appearance of silky white precipitate and following steps has been proposed for direct and selective detection of CN^- ion using **L2H** and Cu(II) salt.

$$\mathbf{L2H} + CN^- \{\text{Fluorescent}\}$$

$$2\mathbf{L2H} + 2CN^- + CuCl_2 \longrightarrow 2\mathbf{L2H} + [Cu(CN)]\downarrow + \tfrac{1}{2}(CN)_2 \{\text{Fluorescent}\}$$

$$2\mathbf{L2H} + 2CN^- + 2CuCl_2 \longrightarrow [Cu(\mathbf{L2})_2] + [Cu(CN)]\downarrow + \tfrac{1}{2}(CN)_2 \{\text{Non-Fluorescent}\}$$

Complex [Cu(**L2**)$_2$] also shown the potential that it was able to detect CN^- ion in presence of other anions as well (Fig. 19). The fluorescence quantum yield for the release of probe from [Cu(**L2**)$_2$] by cyanide ion was found to be 0.16 which is more than the complex itself. The maximum acceptable concentration level of cyanide ion in drinking water is 1.9 μM as prescribed by World Health Organization (WHO). The limit of detection of [Cu(**L2**)$_2$]

complex towards CN^- was found to be 0.30 μM which is far less than maximum acceptable range (Fig. 20a).

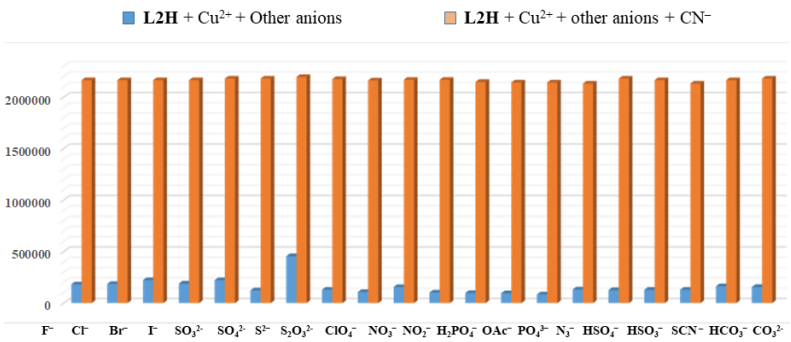

Fig. 19 Bar diagram of [Cu(**L2**)$_2$] complex towards CN^- ion detection. CN^- ion (10 equiv.) and other anions (50 equiv.).

However, detection of cyanide also depends on the stability of [Cu(**L2**)$_2$] complex at different pH values. We have seen that **L2H** was able to detect Cu^{2+} ion in the pH range of 3 – 12 and in case of CN^- detection by [Cu(**L2**)$_2$], the optimum pH range has been found to be 6 – 12 (Fig. 20b). Even though it was not effective with pH < 6, we can conclude that CN^- can be detected under the environmental and physiological conditions. In this regard, detection of CN^- ion in real water samples was achieved with same efficiency (Fig. A4).

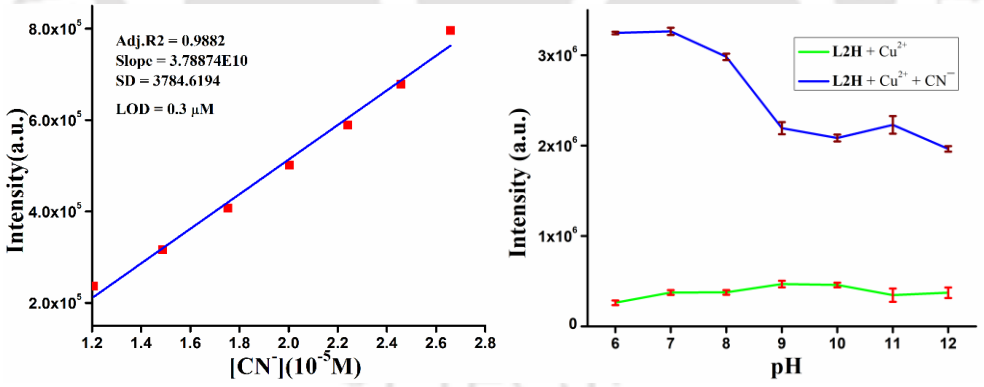

(a) (b)

Fig. 20 (a) Detection limit and (b) Plot of pH *vs* Intensity towards detection of CN^-.

3.9. Cytotoxicity assay

MTT assay was performed to assess the cytotoxicity of the **L2H** molecule. The viability of both the MDA-MB-231 and HDF cells reduced, as the concentration of the **L2H** molecule was increased (Fig. 21). In comparison with the control (untreated cell), the percentage of

MDA-MB-231 cells viability was retained up to 5 μM of **L2H** with no significant difference. The percentage of MDA-MB-231 cell viability reduced significantly to 73.67 ± 9.27 % and 61.10 ± 5.24 % in MDA-MB-231 cells when incubated with 7.5 μM (*p≤0.05) and 10 μM ($^{\#}$p≤0.001) of **L2H** molecule respectively in comparison to control. Similarly, in comparison with the control (untreated cells), the percentage of HDF cells viability was also retained up to 5 μM of **L2H** with no significant difference. In comparison to control, a significant decrease was observed in the percentage of HDF cell viability to 79.43 ± 4.42 % and 73.14 ± 5.10 % when incubated with 7.5 μM (*p≤0.05) and 10 μM (**p≤0.01) of **L2H** molecule respectively. Based on the cytotoxic analysis, 5 μM of **L2H** molecule was selected for further analysis of its fluorescence properties in cellular imaging.

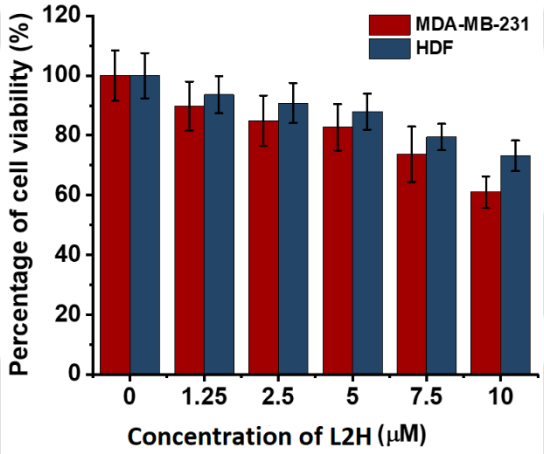

Fig. 21 The assessment of cytotoxic effect of **L2H** molecule against human triple negative breast carcinoma cell line (MDA-MB-231) and primary human dermal fibroblasts (HDF) based on MTT assay. The percentage of cell viability (%) was determined relative to control (only media). Data represented as mean ± SD (n = 4), where *p≤0.05, **p≤0.01 and $^{\#}$p≤0.001 in comparison to control.

3.10. Fluorescence imaging

The fluorescence attributes of only **L2H** molecule, **L2H** molecule after incubation with Cu^{2+} and **L2H** molecule after incubation with Cu^{2+} and CN^{-} was evaluated following treatment for specified time points against MDA-MB-231 (Fig. 22) and HDF cells (Fig. 23). In case of both the cell types, MDA-MB-231 and HDF no fluorescence property on incubation with only media. A strong blue fluorescence emission was observed from the intracellular regions of both the cell types when treated with 5 μM of **L2H** molecule for 60 min. However, both the cell types pre-treated with 5 μM **L2H** molecule displayed weak blue fluorescence

emission from intracellular regions when incubated with 0.25 μM Cu^{2+} for 30 min. Further, both the MDA-MB-231 and HDF cells pre-treated with 5 μM **L2H** and 0.25 μM Cu^{2+} exhibited high blue fluorescence emission from intracellular regions when incubated with 12.5 μM CN^- for 45 min, as observed from fluorescence images. This high blue fluorescence is due to the removal of copper from the [Cu(**L2**)$_2$] complex that is already present in the intracellular region. These experiments revealed that the [Cu(**L2**)$_2$] complex could be used for tracking trace amount of cyanides in living cells.

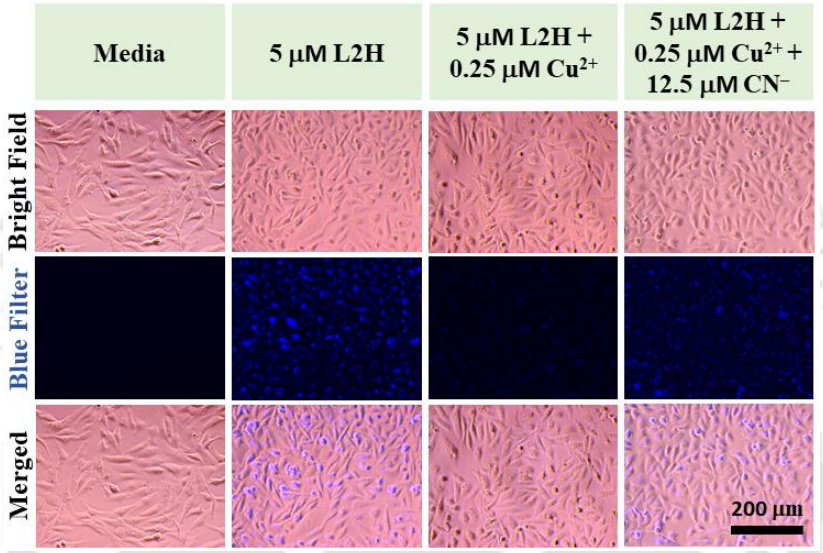

Fig. 22 Bright field and live-cell fluorescence images of human triple negative breast carcinoma cells (MDA-MB-231) after incubation with only **L2H** molecule, **L2H** molecule with Cu^{2+} and **L2H** molecule with Cu^{2+} and CN^- for specified incubation time. Scale bar: 200 μm.

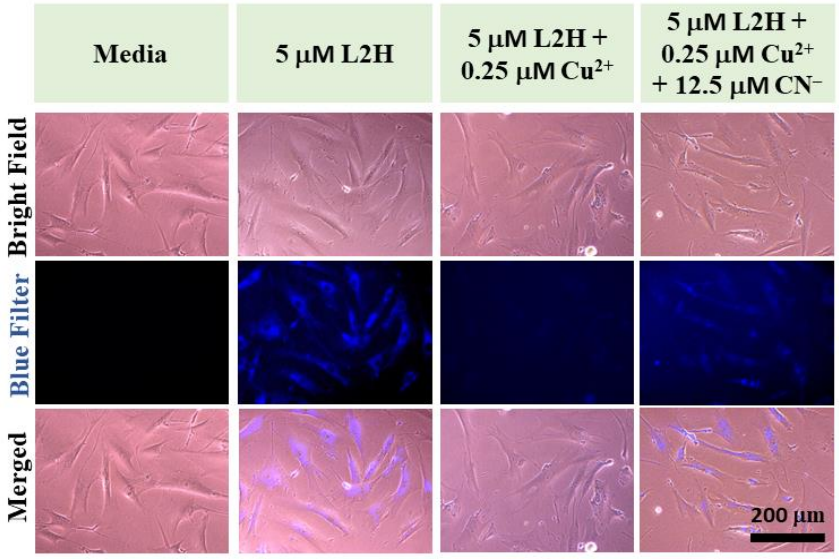

Fig. 23 Bright field and live-cell fluorescence images of human dermal fibroblasts (HDF) after incubation with only **L2H** molecule, **L2H** molecule with Cu^{2+} and **L2H** molecule with Cu^{2+} and CN^- for specified incubation time. Scale bar: 200 μm.

3.11. Conclusion

In the summary, the heterocyclic probe 3-(2-hydroxyphenyl)imidazo[5, 1-*a*]isoquinoline (**L2H**) has the potential for selectively detecting Cu^{2+} ion in presence of various metal ions through *"turn-off"* fluorescence signal. The 2:1 binding ratio of **L2H** towards Cu^{2+} ion was confirmed by Job's plot, Benesi–Hildebrand plot, ESI mass analysis and ^1H NMR titration study. The non-fluorescent [Cu(**L2**)$_2$] complex became fluorescent specifically upon addition of CN^- ion, while other anions failed to restore the fluorescence because **L2H** was not released by them. Limit of detection of both Cu^{2+} and CN^- were found to be very low and both can be detected easily over a wide range of pH. Based on the cytotoxic analysis, 5 μM of **L2H** molecule was selected for determining its fluorescence attributes in cellular imaging. Cell imaging experiments revealed that the [Cu(**L2**)$_2$] complex could be used for tracking trace amount of cyanides in living cells.

Reference

1. R. P. Haugland, The Molecular Probes Handbook: A Guide to Fluorescent Probes and Labeling Technologies, Invitrogen, Carlsbad, CA, 10th edn, 2005.
2. R. McRae, P. Bagchi, S. Sumalekshmy and C. J. Fahrni, *Chem. Rev.*, 2009, **109**, 4780–4827.
3. K. J. Barnham, C. L. Masters and A. L. Bush, *Nat. Rev. Drug Discov.*, 2004, **3**, 205–214.
4. J. Li, Y. Zeng, Q. Hu, X. Yu, J. Guo and Z. Pan, *Dalton Trans.*, 2012, **41**, 3623–3626.
5. H. Kim, Y. J. Na, E. J. Song, K. B. Kim, J. M. Bae and C. Kim, *RSC Adv.*, 2014, **4**, 22463–22469.
6. S. J. Lippard and J. M. Berg, Principles of Bioinorganic Chemistry, University Science Books, Mill Valley, CA, 1994.
7. H. B. Gray, E. I. Stiefel, J. S. Valentine and I. Bertini, Biological Inorganic Chemistry: Structure and Reactivity, University Science Books, Herndon, VA, USA, 2007.
8. E. L. Que, D. W. Domaille and C. J. Chang, *Chem. Rev.*, 2008, **108**, 1517–1549.
9. D. J. Thiele and J. D. Gitlin, *Nat. Chem. Biol.*, 2008, **4**, 145–147.

10. A. V. Davis and T. V. O'Halloran, *Nat. Chem. Biol.*, 2008, **4**, 148–151.
11. D. G. Barceloux and Dr. D. Barceloux, *Clin. Toxicol.*, 1999, **37**, 217–230.
12. C. Barranguet, F. P. van den Ende, M. Rutgers, A. M. Breure, M. Greijdanus, J. J. Sinke and W. Admiraal, *Environ. Toxicol.Chem.*, 2003, **22**, 1340–1349.
13. E. Gaggelli, H. Kozlowski, D. Valensin and G. Valensin, *Chem. Rev.*, 2006, **106**, 1995–2044.
14. I. Bertini and A. Rosato, *Cell. Mol. Life Sci.*, 2008, **65**, 89–91.
15. Y.H. Hung, A.I. Bush and R.A. Cherny, *J. Biol. Inorg. Chem.*, 2010, **15**, 61–76.
16. H. F. Xie, C. J. Yu, Y. L. Huang, H. Xu, Q. L. Zhang, X. H. Sun, X. Feng and C. Redshaw, *Mater. Chem. Front.*, 2020, **4**, 1500–1506.
17. WHO. WHO guidelines values for chemicals that are of health significance in drinking water, Guidelines for Drinking Water Quality, Geneva, 3rd edn, 2008.
18. R. Krämer, *Angew. Chem. Int. Ed.*, 1998, **37**, 772–773.
19. J. D. Johnson, T. L. Meisenheimer and G. E. Isom, *Toxicol. Appl. Pharmacol.*, 1986, **84**, 464−469.
20. D. W. Boening and C. M. Chew, *Water, Air, Soil Pollut.*, 1999, **109**, 67−79.
21. F. Wang, L. Wang, X. Chen and J. Yoon, *Chem. Soc. Rev.*, 2014, **43**, 4312−4324.
22. A. A. Ensafi, N. Kazemifard and B. Rezaei, *RSC Adv.*, 2015, **5**, 40088−40093.
23. H. G. Gorchev and G. Ozolins, WHO Guidelines for Drinking-Water Quality, WHO Chron. 2011, **38**, 104−108.
24. S. L. C. Ferreira, M. A. Bezerra, A. S. Santos, W. N. L. dos Santos, C. G. Novaes, O. M. C. de Oliveira, M. L. Oliveira and R. L. Garcia, *TrAC Trends Anal. Chem.*, 2018, **100**, 1–6.
25. L. Fernández-López, B. Gómez-Nieto, M. J. Gismera, M. T. Sevilla and J. R. Procopio, *Spectrochim. Acta B*, 2018, **147**, 21–27.
26. I. D. la Calle, P. Pérez-Rodríguez, D. Soto-Gómez and J. E. López-Periago, *Microchem. J.*, 2017, **133**, 293–301.
27. L. Tian, J. Qi, K. Qian, O. Oderinde, Q. Liu, C. Yao, W. Song and Y. Wang, *J. Electroanal. Chem.*, 2018, **812**, 1–9.
28. D. Shan, C. Mousty and S. Cosnier, *Anal. Chem.*, 2004, **76**, 178−183.
29. D. Bohrer, C. P do Nascimento, S. Garcia Pomblum, E. Seibert and L. Machado de Carvalho, *Fresenius' J. Anal. Chem.*, 1998, **361**, 780−783.

30. S. Dadfarnia, M. A. Haji Shabani, F. Tamadon and M. Rezaei, *Microchim. Acta*, 2007, **158**, 159−163.
31. D. L. Recalde-Ruiz, E. Andres-Garcia and M. E. Diaz-Garcia, *Analyst*, 2000, **125**, 2100−2105.
32. R. Kaushik, A. Ghosh, A. Singh, P. Gupta, A. Mittal and D. A. Jose, *ACS Sens.*, 2016, **1**, 1265−1271.
33. A. Sebastian and E. Prasad, *Langmuir*, 2020, **36**, 10537−10547.
34. S. Bhardwaj, N. Maurya, A. K. Singh, R. Varshney and P. Roy, *RSC Adv.*, 2016, **6**, 102096–102101.
35. S. Mahata, A. Bhattacharya, J. P. Kumar, B. B. Mandal and V. Manivannan, *J. Photochem. Photobiol. A: Chem.*, 2020, **394**, 112441–112450.
36. S. Mahata, G. Janani, B. B. Mandal and V. Manivannan, *J. Photochem. Photobiol. A: Chem.*, 2021, **417**, 113340.
37. R. Martínez-Máñez and F. Sanceńon, *Chem. Rev.*, 2003, **103**, 4419–4476.
38. E. J. O'Neil and B. D. Smith, *Coord. Chem. Rev.*, 2006, **250**, 3068–3080.
39. C. Siering, H. Kerschbaumer, M. Nieger and S. R. Waldvogel, *Org. Lett.*, 2006, **8**, 1471–1474.
40. M. Royzen, Z. Dai and J. W. Canary, *J. Am. Chem. Soc.*, 2005, **127**, 1612–1613.
41. P. Saluja, N. Kaur, N. Singh and D. O. Jang, *Tetrahedron Lett.*, 2012, **53**, 3292–3295.
42. Y. Xie, Y. Ding, X. Li, C. Wang, J. P. Hill, K. Ariga, W. Zhang and W. Zhu, *Chem. Commun.*, 2012, **48**, 11513–11515.
43. V. Bhalla, H. Singh and M. Kumar, *Dalton Trans.*, 2012, **41**, 11413–11418.
44. R. Parkash and J. Zýka, *Microchem. J.*, 1972, **17**, 309–317.
45. F.R. Duke and W.G. Courtney, *J. Phys. Chem.*, 1952, **56**, 19–21.
46. U. R. G, P. Das, S. Saha, M. Baidya, S. K. Ghosh and A. Das, *Chem. Commun.*, 2013, **49**, 255–257.
47. G. J. Park, G. R. You, Y. W. Choi and Cheal Kim, *Sens. Actuators B: Chem.*, 2016, **229**, 257−271.
48. P. Singh, L. S. Mittal, S. Kumar, G. Bhargava and S. Kumar, *J Fluoresc.*, 2014, **24**, 909–915.
49. L. Long, L. Zhou, L. Wang, S. Meng, A. Gong, F. Dub and C. Zhang, *Anal. Methods*, 2013, **5**, 6605–6610.

50. J. Bori, N. Behera, S. Mahata and V. Manivannan, *ChemistrySelect*, 2017, **2**, 11727–11731.
51. N. Behera and V. Manivannan, *J. Photochem. Photobiol. A: Chem.*, 2018, **353**, 77–85.
52. H. S. Jung, J. H. Han, Z. H. Kim, C. Kang and J. S. Kim, *Org. Lett.*, 2011, **13**, 5056–5059.
53. Y. Liu, X. Lv, Y. Zhao, J. Liu, Y. Q. Sun, P. Wang and W. Guo, *J. Mater. Chem.*, 2012, **22**, 1747−1750.
54. J. Wang, J. He, J. Zhang, Z. Chen, J. Liang and L. Chen, *Spectrochim. Acta, Part A*, 2021, **252**, 119526.
55. G. Janani, M.M. Pillai, R. Selvakumar, A. Bhattacharyya and C. Sabarinath, *Biofabrication*, 2017, **9**, 015016.
56. D. Wang, J.-Q. Zheng, X. Yan, X.-J. Zheng and L.-P. Jin, *RSC Adv.*, 2015, **5**, 64756–64762.

Appendix:

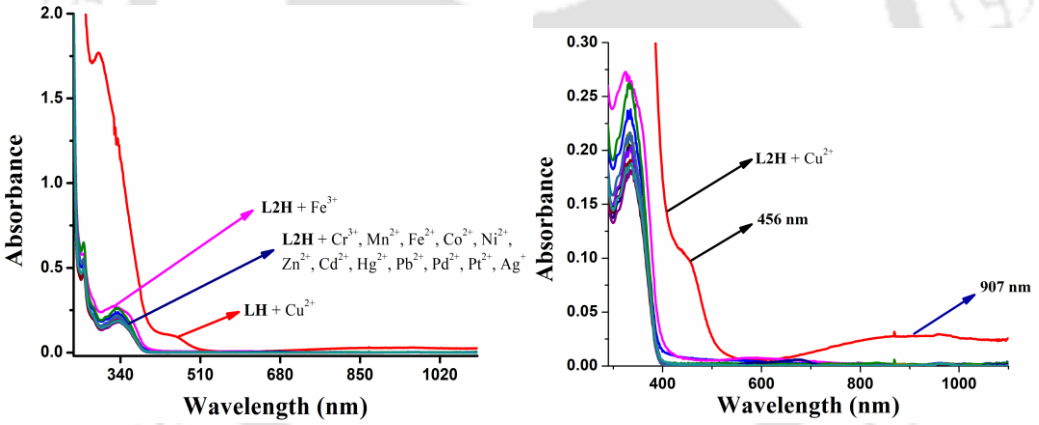

(a) (b)

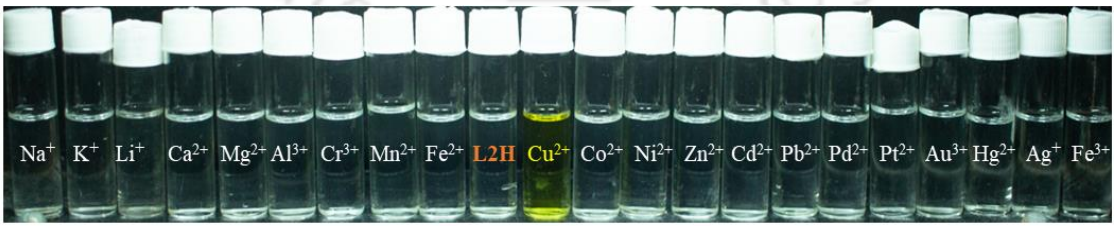

(c)

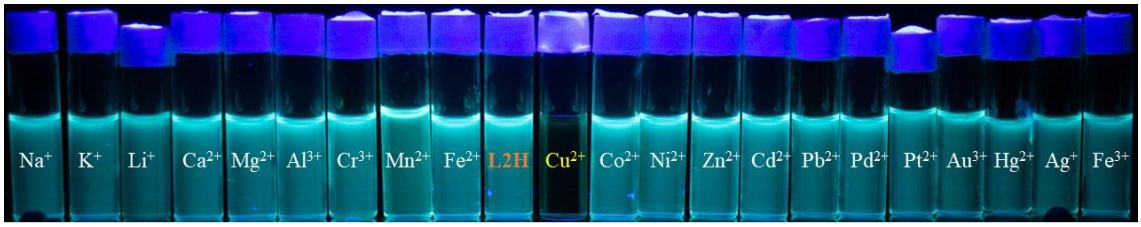

(d)

Fig. A1 (a and b) UV- Vis and NIR spectra of **L2H** in presence of various metal ions and pictures under (c) visible light and (d) long UV light of **L2H** solution in presence of different metal ions.

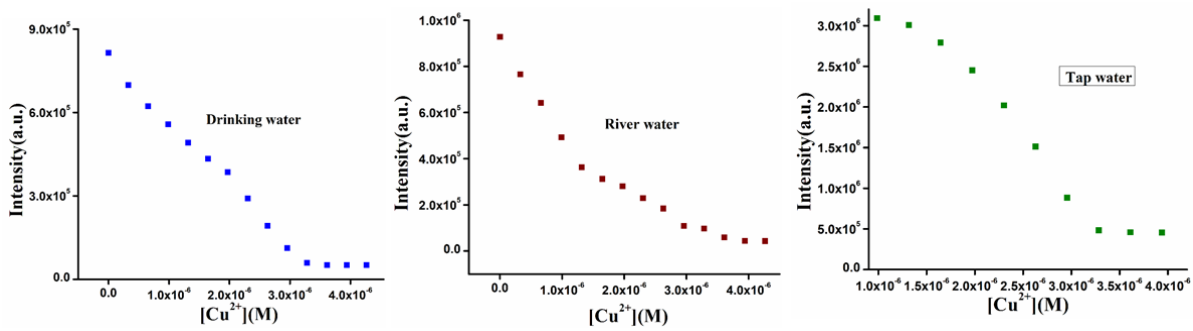

Fig. A2 Plot of fluorescence intensity *vs* [Cu^{2+}] in real water samples.

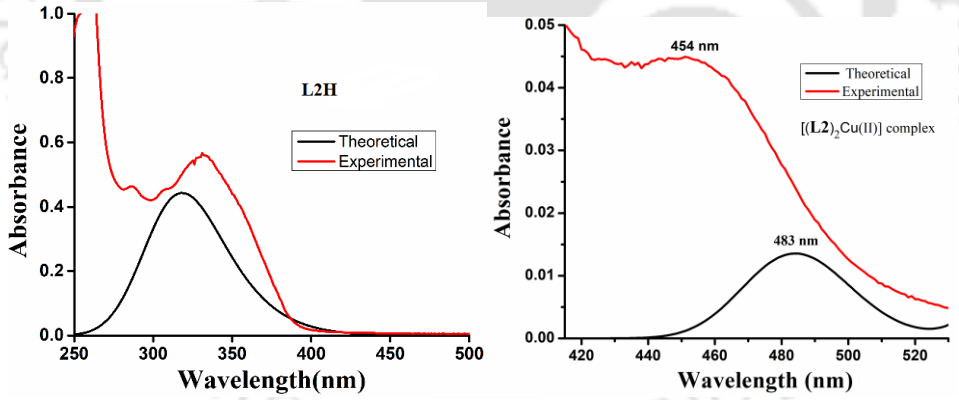

Fig. A3 Experimental and theoretical absorbance plot of **L2H** and its copper complex.

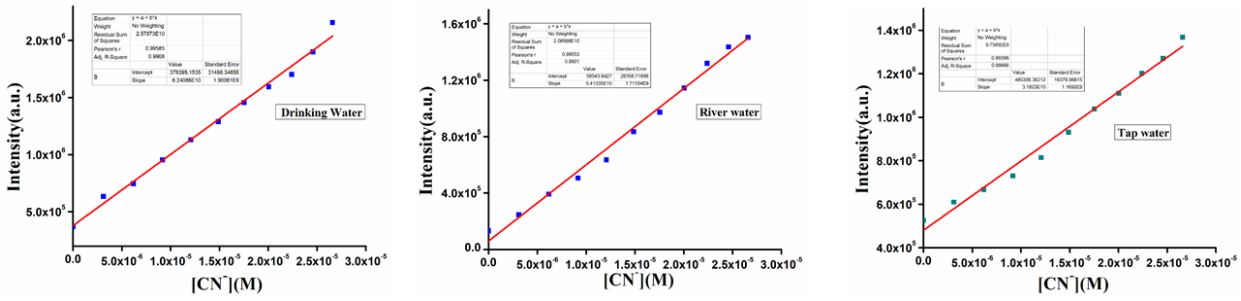

Fig. A4 CN^- detection using [Cu(**L2**)$_2$] complex in drinking water, tap water and tap water.

Table A1 Comparison of **L2H** with some reported probes

Probe	Solvent	LOD	Ref.
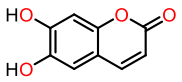	HEPES-DMSO (99:1, 10 mmol, pH = 7.4)	0.12 μM (Cu^{2+}) 5.77 μM (CN^-)	32
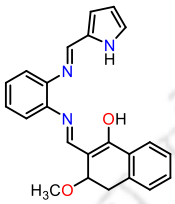	10 mM PBS buffer, pH 7.4, 1.0% DMSO	0.512 μM (Cu^{2+})	34
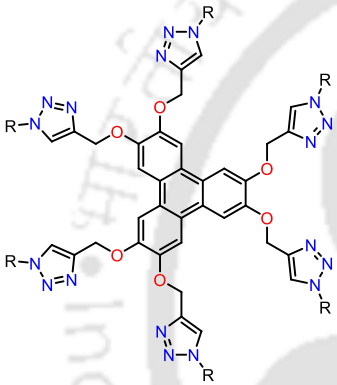 **R = C_6H_{13}**	DMSO.	3.12 μM (Cu^{2+}) 5 μM (CN^-)	43
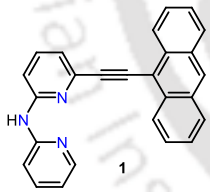 **1**	MeOH–H_2O (4 : 1, *v/v*)	0.3 μM (Cu^{2+}) 0.3 μM (CN^-) in **1** 0.9 μM (Cu^{2+}) 0.2 μM (CN^-) in **2**	42
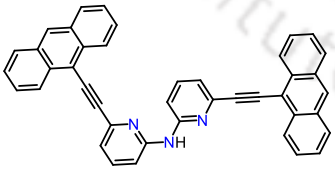 **2**			
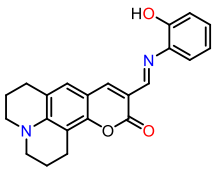	(10 mM PBS buffer, pH 7.4, 1.0% DMSO)	–	52
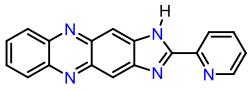	H_2O–DMSO (3:7, *v/v*, pH = 7.0)	0.47 μM (CN^-)	54

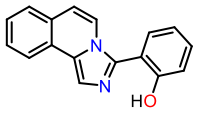	CH_3CN : HEPES buffer (5 mM, pH = 7.4, 6:4, *v/v*)	0.45 µM (Cu^{2+}) 0.30 µM (CN^-)	This work

Chapter 4

A Coumarin Based Visual and Fluorometric Probe for Selective Detection of Al(III), Cr(III) and Fe(III) Ions Through "*Turn-On*" Response and its Biological Application*

Abstract:

A Schiff base (**L3**) containing coumarin and pyrene moieties was synthesized and characterized. It showed excellent selective recognition of M(III) ions (M = Al, Cr and Fe) in presence of monovalent, divalent and other trivalent metal ions. Sensor **L3** itself is non-fluorescent upon excitation with 353 nm light (λ_{ex} = 353) but a very large enhancement in fluorescence intensity was observed during the addition of these three trivalent metal ions into a CH_3OH/aqueous HEPES buffer (5 mM, pH = 7.4, 6:4, *v/v*) solution of **L3**. This prominent "OFF-ON" fluorescence switching can be observed with naked eye, in which "OFF" is due to operation of PET process in free **L3** but PET is inhibited upon complexation thereby allowing CHEF (Chelation enhanced fluorescence) process to operate. Detection limits of Al^{3+}, Cr^{3+} and Fe^{3+} using **L3** have been found to be 0.79 nM, 1.15 µM, and 1.28 µM respectively in the pH range of 6−10. Additionally, "OFF-ON" fluorescence can be reversed by sequestering M(III) ions using $[EDTA]^{4-}$ solutions. Analysis of mass spectra and Job's plot revealed a binding ratio of 1:1 for all three metal ions with **L3**. The imine nitrogen and carbonyl oxygen atoms of **L3** are involved in binding with Al^{3+}, Cr^{3+} and Fe^{3+} ions, as revealed by ^1H NMR titration and IR spectroscopic analysis. Results of quantum yield (Φ), time resolved photoluminescence (TRPL) and computational studies (DFT/TDDFT) studies were also reported. Fluorescence intensity of these M(III) bound **L3** complexes is quenched by fluoride ions. From cytotoxicity analysis, 7.5 µM of probe **L3** was selected to analyze its fluorescence attributes in cellular imaging. Using human breast cancer cell line (MDA-MB-231) and primary human dermal fibroblasts (HDF), the potentiality of the probe **L3** was confirmed through fluorescence cell imaging experiments.

---

*This work has been published in:

S. Mahata, G. Janani, B. B. Mandal and V. Manivannan, *J. Photochem. Photobiol. A: Chem.*, 2021, **417**, 113340.

4.1. Introduction:

Presence of traces of several kinds of heavy metal ions increases the toxicity quotient of the environment and is detrimental to human health. Contributing factors to increasing levels of them include metal corrosion, atmospheric deposition, soil erosion and leaching, leather tanning, emissions of exhaust gases from vehicles, mining and smelting operations, industrial production and usage etc. These are consequences of an increase in urbanization with social economic activities and also by petroleum hydrocarbons as well as domestic and municipal garbage.

As a result, there is a very high possibility of contamination of many toxic metal ions in drinking water and in our daily food. Therefore, many researchers are trying to detect toxic elements like aluminium,[1] chromium,[2] cadmium,[3] copper,[4] arsenic,[5] iron,[6] palladium,[7] mercury,[8] zinc,[9] lead[10] in water and food samples. A large number of chemosensors are being reported for single analyte and some chemosensors for multiple metal ions (Al^{3+}, Fe^{3+} and Cr^{3+}) as well. Among various metal ions, need of chemosensors for detection of trivalent metal ions like Al^{3+}, Fe^{3+} and Cr^{3+} in living system as well as in environment is important.

Even though aluminium is third most abundant element in the earth's crust, there is no importance of it in biology but its presence may create various health issues. Accumulation of Al^{3+} ion in human organs like brain, liver, kidney and bone is detrimental to health,[11–13] may cause renal failure[14] and many other problems associated with aging.[15] Excessive accumulations in human beings lead to damages in central nervous system and cause several diseases such as Parkinson's disease, neurodementia, Alzheimer's disease, osteomalacia, dialysis encephalopathy and rickets.[16–18]. WHO has given a limitation on safe aluminium concentration of up to 200 μg L^{-1}, in drinking water.[19] The intake capacity of aluminium in the human body per week is approximately 7 mg kg^{-1}.[20] Therefore, the detection of aluminium has become very important nowadays.

Trivalent chromium ion is important in the metabolism of protein, fat, carbohydrate and nucleic acids.[21] Deficiency of nutritional ingestion of Cr^{3+} ions may cause cardiovascular diseases and diabetes.[21] But excess amounts of Cr(III) ion in human body may lead to binding to DNA, which affects cellular structures negatively causing damage to the cellular components of living systems.[22,23]. Chromium is considered to be a serious environmental pollutant and its discharge from industrial and agricultural sources.[24] Iron is one of the most essential trace elements which is present in many proteins and enzymes as well as acts as

cofactor for many cellular reactions of living organisms.[25] Iron plays a very important role in electron transfer reaction and in biochemical processes at the cellular level.[26] In the oxygen transport systems of many organisms, iron plays a great role in the form of haemoglobin.[27]. The deficiencies or excesses of Fe^{3+} ion can create several diseases, like Alzheimer's, Huntington's, Parkinson's, etc.[28]

There are expensive and time-consuming analytical techniques available for quantitative and qualitative detection of metal ions e.g., AAS (Atomic absorption Spectroscopy), NAA (Neutron activation analysis), ICP-MS (Inductively coupled plasma mass spectrometry), XRF (X ray fluorescence), ICP-AES (Inductively coupled plasma – atomic emission spectrometry) etc.[29–35]. However, the colorimetric and fluorescence- based methods are very simple, highly sensitive, low cost with real-time monitoring and can be used for biological applications.[36–39] Detection of multiple metal ions that are abundant in the earth crust by a single probe enables analyst with the ability to practically utilise it in environmental and biological samples.[40,41] There are several mechanism of sensing based on change in fluorescence intensity which are photoinduced electron transfer (PET), exited state proton transfer (ESIPT), intra ligand charge transfer (ICT), chelation enhanced fluorescence (CHEF), C = N isomerisation etc.[42,43] It is more efficient to develop "turn-on" fluorescent sensors than that of "turn-off" sensors.[44–46] In general it is seen that due to the paramagnetic nature, Fe^{3+} and Cr^{3+} ions are the perfect fluorescence quenchers,[47] which makes it very challenging to synthesize a "turn-on" fluorescence sensor. A very few "turn-on" molecules have been reported for Fe^{3+} and Cr^{3+} ions till now with cell imaging applications.[48–50] Whereas, Al^{3+} is diamagnetic in nature and binding to the probes generally results in enhancing the fluorescence intensity.[51]

There are some reports on utility of chemosensors for selective detection of trivalent metal ions, which are based on rhodamine,[52–57] rhodamine-naphthalic anhydride,[58] schiff base,[59–62] benzoxazole,[63] morpholine-naphthalimide,[64] spiropyran,[65] naphthalimide,[66] nitrobenzoxadiazole-appended calix [4] arene,[67] rhodamine–naphthalimide dyad,[32] naphthalimide–quinolone,[68] aminocyanine,[69] quinoline,[70] pyridine[71] units. Many of the sensors having coumarin moiety are highly fluorescent, and it has been incorporated in this Schiff base which also contain pyrene unit.[72] Pyrene derivatives show excellent photophysical property for its stability, high quantum yield and long fluorescence lifetime.[73–75] This Chapter describes synthesis of the probe (**L3**) through condensation of 3-aminocoumarin and pyrene aldehyde. Sensor **L3** showed remarkable color change from

yellow to colorless which is observable through naked-eye upon binding exclusively with Al^{3+}, Fe^{3+} and Cr^{3+} ions. Furthermore, **L3** had been applied in living cells for cytotoxicity and live cell imaging studies.

4.2. Experimental section:

4.2.1. Cell Studies

4.2.1.1. Cell culture

Human triple-negative breast carcinoma (MDA-MB-231, National Centre for Cell Science, India) cells at passage number 48 and primary human dermal fibroblasts (HDF, HiMedia Laboratories, India) at passage number 12 were used for evaluating the cytotoxicity and fluorescence attributes against the probe **L3**. The MDA-MB-231 and HDF cells were cultured and maintained using a high glucose DMEM (Dulbecco's modified Eagle's medium, Gibco, Thermo Fisher Scientific, USA) supplemented with 10% v/v Fetal Bovine Serum, 50 mg/mL Penicillin, and 50 µg/mL Streptomycin.

4.2.1.2. Cytotoxicity studies

The cytotoxicity analysis against the developed probe (**L3**) on both (i) human cancerous MDA-MB-231 cell line and (ii) human primary HDF cells was investigated *in vitro* using standard MTT assay.[7,76] MDA-MB-231 and HDF cells were plated at a density of 5×10^3 cells suspended in 100 µL of high glucose DMEM in a 96-well plate and cultured for 24 h at 37°C, 5% CO_2 in a humidified incubator. After cellular attachment, both MDA-MB-231 and HDF cells were exposed to the increasing concentration of **L3** at 0, 1.25, 2.5, 5, 7.5, and 10 µM in high glucose DMEM for 24 h. After 24 h of treatment, the cell viability was assessed using the MTT reagent (Sigma Aldrich, USA), where the media was aspirated from wells, and cells were treated with a 1:10 ratio of 5 mg/mL MTT for 4 h. Further, the formed formazan crystals were dissolved in 100 µL of DMSO, followed by absorbance recorded at 570 nm using Multiskan Multiplate Reader (Thermo Scientific, USA). The percentage (%) of cell viability after exposure to an individual concentration of **L3** was calculated relative to control (only media).

4.2.1.3. Fluorescence imaging

From the cell cytotoxicity assay, a non-cytotoxic concentration of 7.5 µM **L3** was adopted to assess the fluorescence properties of the only probe (**L3**) and probe (**L3**) after incubation with

trivalent metal ions (Al^{3+}, Fe^{3+}, and Cr^{3+}) against breast carcinoma cell-like MDA-MB-231 and primary dermal fibroblasts (HDF). Both cells were seeded at a density of 2×10^4 in a 24-well plate at 37°C, 5% CO_2 in a humidified incubator, and cultured for 24 h. Post cell attachment, both the cell types were incubated with only 7.5 µM **L3** suspended in high glucose DMEM for 60 min. Correspondingly, cells pre-treated with 7.5 µM **L3** was then incubated with three trivalent metal ions (i) 7.5 µM Al^{3+} for 60 min, 7.5 µM Fe^{3+} for 60 min, and 5 µM Cr^{3+} for 30 min. After the specified incubation time, MDA-MB-231 and HDF cells were washed twice with 0.1 M PBS followed by a bright field, and fluorescence images in a blue excitation filter were captured at 20 × magnification using EVOS fluorescence microscopy (Life Technologies).

4.2.1.4. Statistical analysis

All the experiments were performed from n=4 samples and analyzed data were represented as mean ± SD (standard deviation). Statistical analysis between the groups was evaluated following One-way ANOVA using OriginPro software (Originlab Corporation, USA), and captured fluorescence images were processed using ImageJ analysis software (NIH, USA). A * $p \leq 0.05$, ** $p \leq 0.01$ and # $p \leq 0.001$ between groups were considered statistically significant.

4.2.2. Synthesis of (E)-3-((pyren-1-ylmethylene)amino)-2H-chromen-2-one (**L3)**:

To a hot methanolic (40 mL) stirred solution of 3-aminocoumarin (22 mg, 0.137 mmol), 1-pyrenecarboxaldehyde (31.42 mg, 0.137 mmol) was added. Then the reaction mixture was refluxed for 8 h. After that, the reaction mixture was kept slowly for cooling into room temperature. The orange yellow coloured precipitate of **L3** was observed and separated by filtration by washing with ice-cold methanol. Yield: 46 mg (90%). We have also obtained the crystal structure of **L3** using slow evaporation method from DMF and acetonitrile mixture (1:1, *v/v*). Needle sized orange crystal was found after two days. The ^{1}H-NMR, ^{13}C-NMR, HRMS and IR spectra are provided in Fig. **A1-A4**. Anal. Calcd. for $C_{26}H_{15}NO_2$: C, 83.63; H, 4.05; N, 3.75. Found: C, 83.50; H, 3.98; N, 3.69. ESI-MS (+): m/z Calcd. for $[C_{26}H_{15}NO_2]^+$ 373.1103 found (M^+ + H) 374.0872. 600 MHz ^{1}H NMR: (δ (J, Hz), $CDCl_3$): 10.23 (1H, s), 8.96 (1H, d, 9.6), 8.79 (1H, d, 8.4), 8.26-8.22 (4H, m), 8.16 (1H, d, 9.0), 8.09 (1H, d, 8.4), 8.05 (1H, t, 7.5), 7.73 (1H, s), 7.56 (1H, d, 7.2), 7.51 (1H, t, 7.8), 7.39 (1H, d, 7.8), 7.31 (1H, t, 7.8). 150 MH_Z ^{13}C NMR (δ, $CDCl_3$): 162.24, 158.68, 152.12, 136.00, 134.00, 132.46, 131.23, 131.17, 130.74, 130.53, 129.36, 129.30, 128.22, 127.83, 127.47, 126.37, 126.34,

126.28, 126.17, 125.05, 124.82, 124.69, 124.49, 122.36, 120.13, 116.37. FTIR (KBr, cm^{-1}): 3411(m), 3025(w), 1718(s), 1618(s), 1568(m), 1530(w), 1483(w), 1448(m), 1390(w), 1320(w), 1285(w), 1239(m), 1157(w), 1122(w), 1029(s), 854(m), 831(m), 749(s), 714(s), 584(w), 469(w).

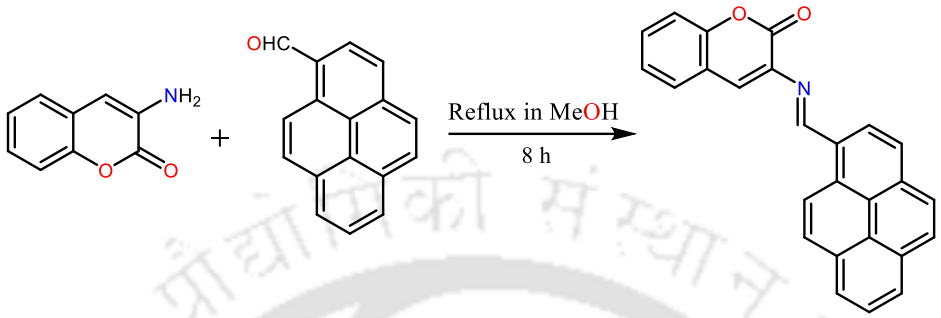

L3

Scheme 1 Synthesis of **L3**.

4.3. Results and discussions:

4.3.1. Crystal structure of **L3**

The crystal structure of **L3** was obtained through slow evaporation of 1:1 DMF and CH_3CN solution which crystallized in $P2_1/c$ space group and its ORTEP diagram is shown in Fig. 1.

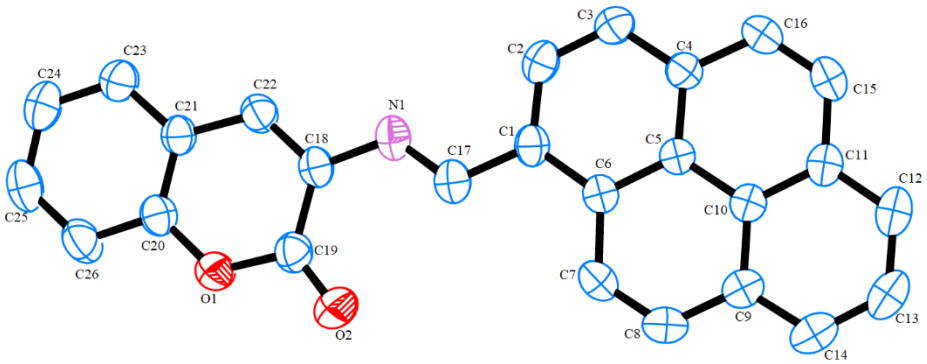

Fig. 1 ORTEP (50% probability ellipsoids) diagram of **L3**. Hydrogen atoms in **L3** are omitted for clarity. Selected bond distances: C18–N1 = 1.400, C17–N1 = 1.272, C20–O1 = 1.371, C19–O1 = 1.387 and C19–O2 = 1.201 Å).

4.3.2. UV–Vis absorption properties of L3 in presence of various metal ions

Sensing ability of **L3** towards various metal chloride salts was initially examined through naked-eye as well as UV-Vis spectroscopy. The absorbance spectral behaviour of **L3** with three categories of metal ions like (a) same period metal ions such as Cr^{3+}, Mn^{2+}, Fe^{3+}, Fe^{2+}, Co^{2+}, Ni^{2+}, Cu^{2+}, and Zn^{2+}; (b) some toxic heavy metal ions such as Cd^{2+}, Hg^{2+}, Pb^{2+}, Pd^{2+}, Pt^{2+}, Ag^{+}, Au^{3+} and (c) groups IA, IIA and IIIA metal ions such as Na^{+}, K^{+}, Li^{+}, Ca^{2+}, Mg^{2+} and Al^{3+} ions, were investigated in CH_3OH–HEPES buffer solution (6:4, *v/v*). The probe **L3** showed absorption bands at 290 nm due to the conjugated $\pi \rightarrow \pi^*$ transition, and two bands at 383 nm and 405 nm may be due to $n \rightarrow \pi^*$ transition (Fig. 2). Upon the gradual addition of $AlCl_3$, $FeCl_3$ and $CrCl_3$ solution into **L3**, peaks at 383 nm and 405 nm gradually diminished in intensity and four bands having their maximum at 274, 312, 328 and 343 nm were observed which showed a blue shift of these two absorption band. These were accompanied by two isosbestic points at 353 and 307 nm (Fig. 3-5), indicating that only two species *viz*., free **L3** and **L3**-bound M^{3+} ions (M = Al, Cr, Fe) are involved during the titration. Significantly yellow colour of **L3** became colourless upon gradual addition of Cr^{3+}, Fe^{3+} and Al^{3+} ions, which is observable through naked eye indicating that **L3** is a suitable candidate for visual detection of these trivalent ions. Noticeably, with rest of the metal ions such disappearance of yellow colour of **L3** due to blue shift of absorption bands was not observed. From this point of view, we can say that **L3** is selective towards Al^{3+}, Fe^{3+} and Cr^{3+} ions.

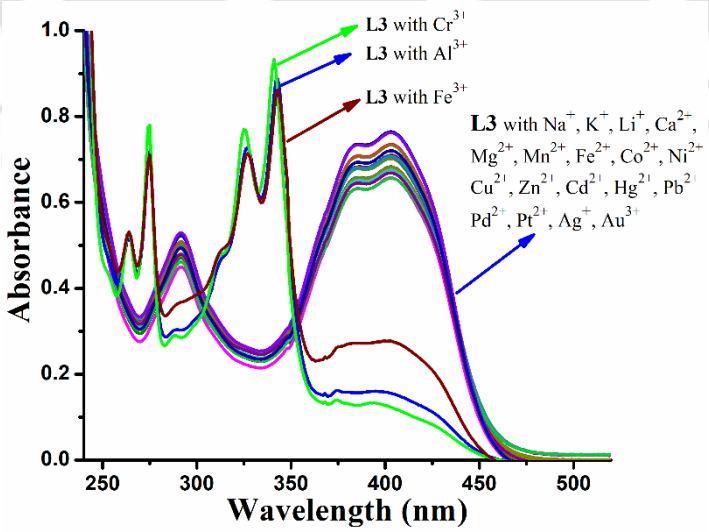

Fig. 2 The absorption spectra of **L3** with various metal chloride salts along with Al^{3+}, Fe^{3+} and Cr^{3+} ion in MeOH : aqueous HEPES buffer (6:4, *v/v*).

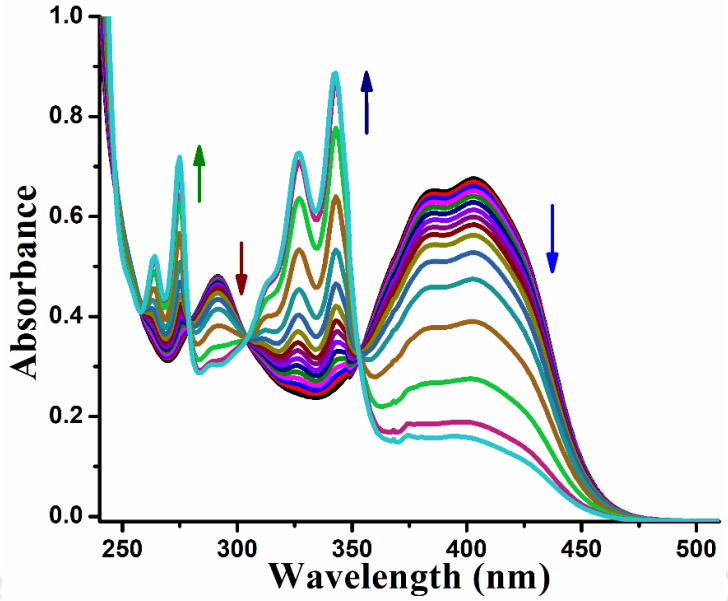

Fig. 3 Changes in the UV-Vis absorption spectra of **L3** after addition of $CrCl_3$.

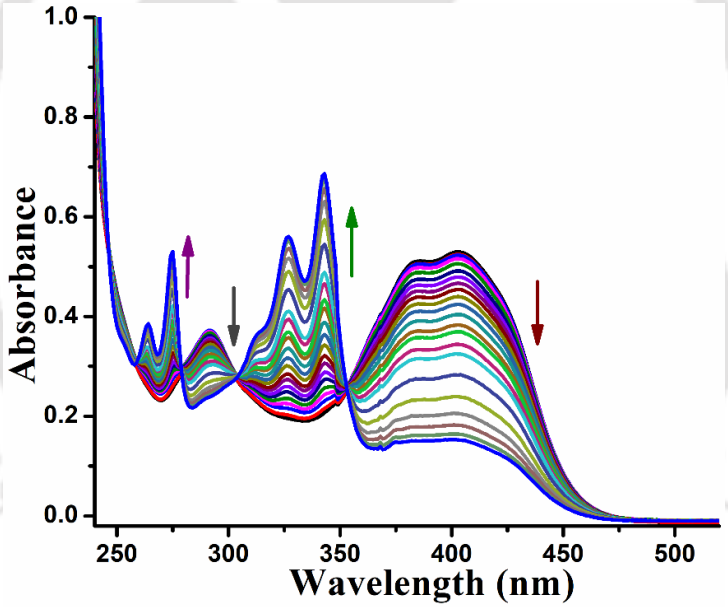

Fig. 4 Changes in the UV-Vis absorption spectra of **L3** after addition of $AlCl_3$.

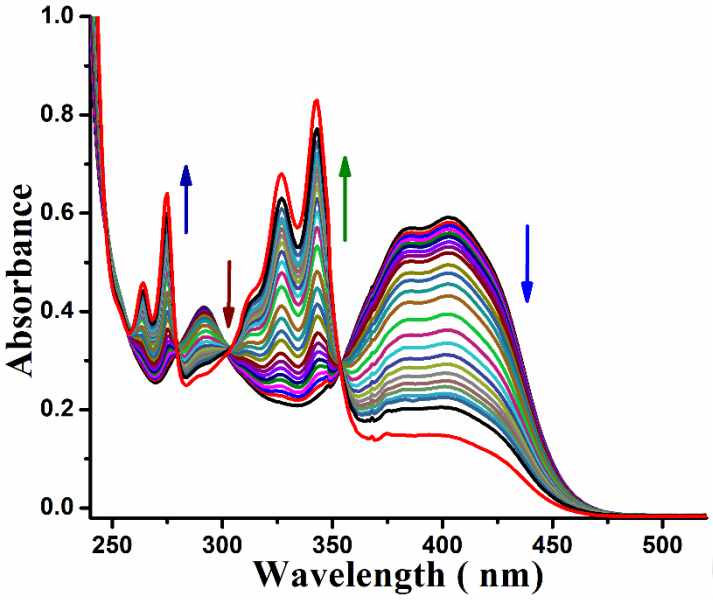

Fig. 5 Changes in the UV-Vis absorption spectra of **L3** after addition of $FeCl_3$.

4.3.3. Fluorescence spectral behaviour of L3 with various metal salts:

Upon irradiation of **L3** with λex = 353 nm using an emission slit of 3 nm the emission band having the peak at λem = 458 nm was observed in MeOH – HEPES buffer solution. To check the emission properties of **L3** with the trivalent ions (Al^{3+}, Fe^{3+}, Cr^{3+}), fluorescence experiment was performed with different metal chlorides. After the addition of the chloride salts of Na^{+}, K^{+}, Li^{+}, Ca^{2+}, Mg^{2+}, Mn^{2+}, Fe^{2+}, Co^{2+}, Ni^{2+}, Cu^{2+}, Zn^{2+}, Cd^{2+}, Hg^{2+}, Pb^{2+}, Pd^{2+}, Pt^{2+}, Ag^{+}, Au^{3+}, the position and emission intensity of **L3** at 458 nm remained almost unchanged (Fig. 6) and the same result has been observed with Ga^{3+}, In^{3+} and Ce^{3+} ions (Fig. 7) as well. But in presence of Al^{3+}, Cr^{3+} and Fe^{3+} ions, there is a significant increase in the emission intensity of **L3** (Fig. 8-10) and the solution colour changed from yellow to sky blue.

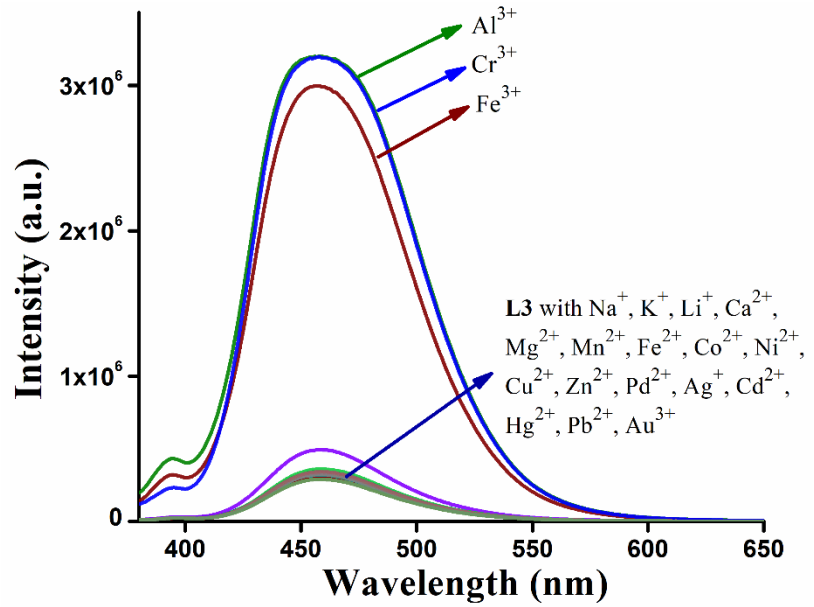

Fig. 6 Emission spectra of **L3** (λ_{em} = 458 nm) with various metal salts.

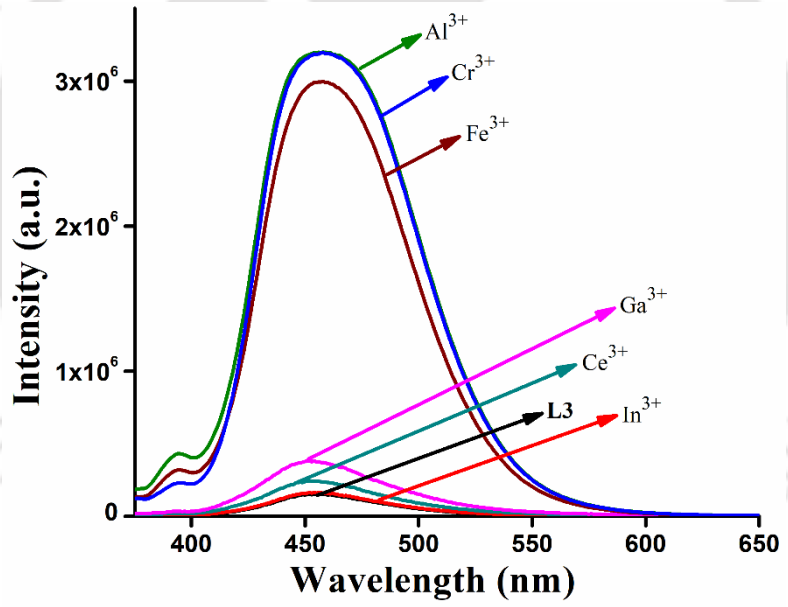

Fig. 7 Changes in emission intensity upon gradual addition of Ga^{3+}, In^{3+}, Ce^{3+} into **L3** solution.

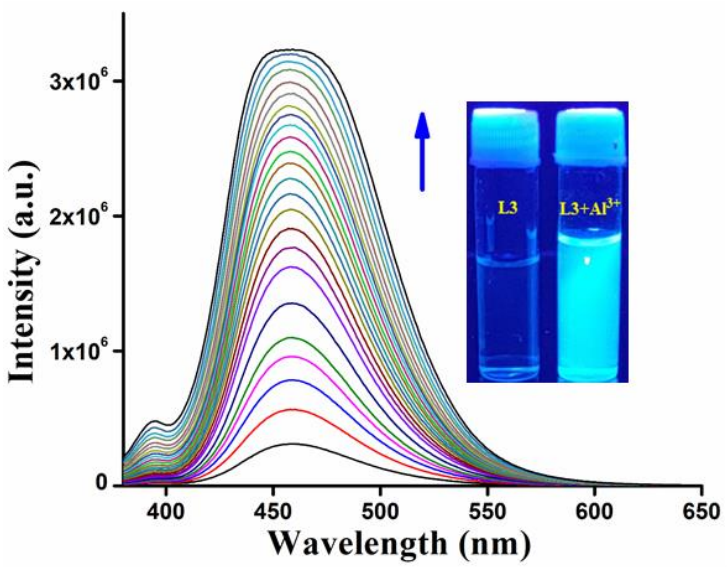

Fig. 8 Changes in the emission behaviour of **L3** upon gradual addition of Al^{3+}.

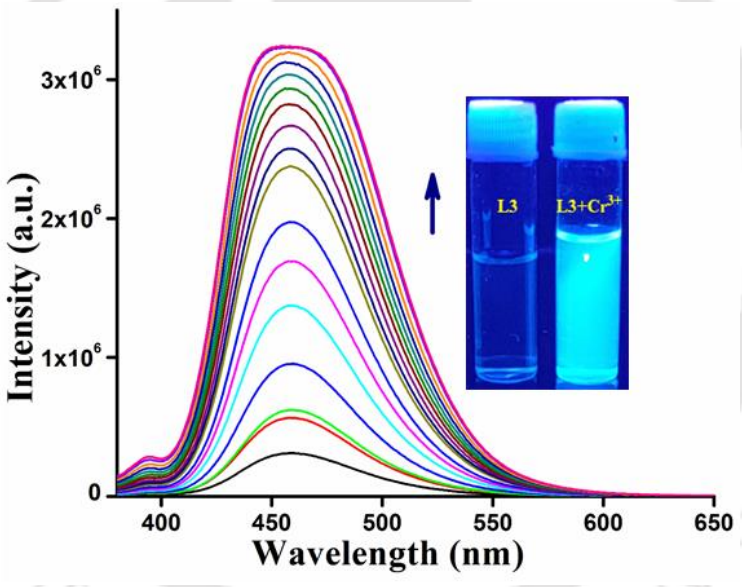

Fig. 9 Changes in the emission behaviour of **L3** upon gradual addition of Cr^{3+}.

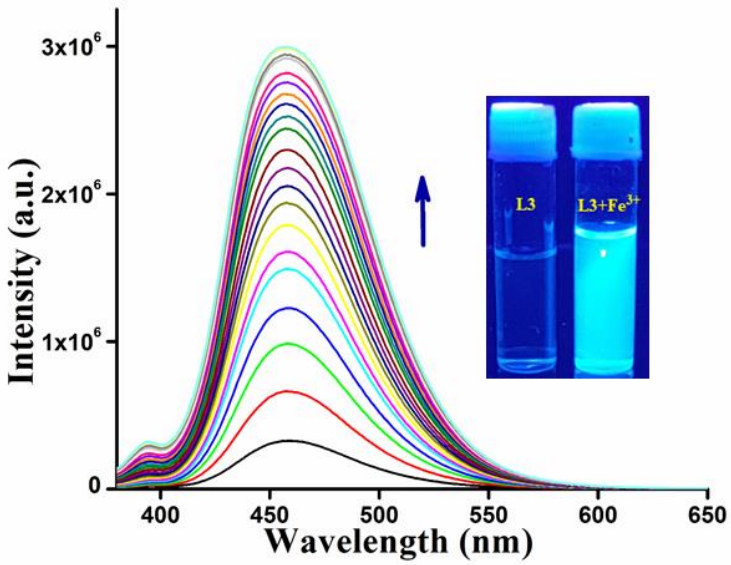

Fig. 10 Changes in the emission behaviour of **L3** upon gradual addition of Fe^{3+}.

These colour changes are easily observable through naked eye (Fig. 11). So, it is evident that **L3** can selectively recognise the trivalent metal ions Al^{3+}, Fe^{3+} and Cr^{3+} in presence of other metal ions. The enhancement of emission intensity of **L3** solution in the presence of these trivalent metal ions is due to the chelation of the trivalent ions by **L3**. In other words, the "*turn-on*" signal of **L3** towards these trivalent ions was through the chelation enhanced fluorescence (CHEF) pathway. The photo induced electron transfer (PET) process might be in play, the reason for weak fluorescence emission of **L3**.[77] The electron transfer from the N atom of imine (CH = N-) group to the conjugated pyrene unit (PET process) is hindered upon coordination with the trivalent metal ions as the lone pair on N atom is coordinated. As a result, the chelation enhanced fluorescence (CHEF) occurred causing large enhancement in the fluorescence intensity.[78]

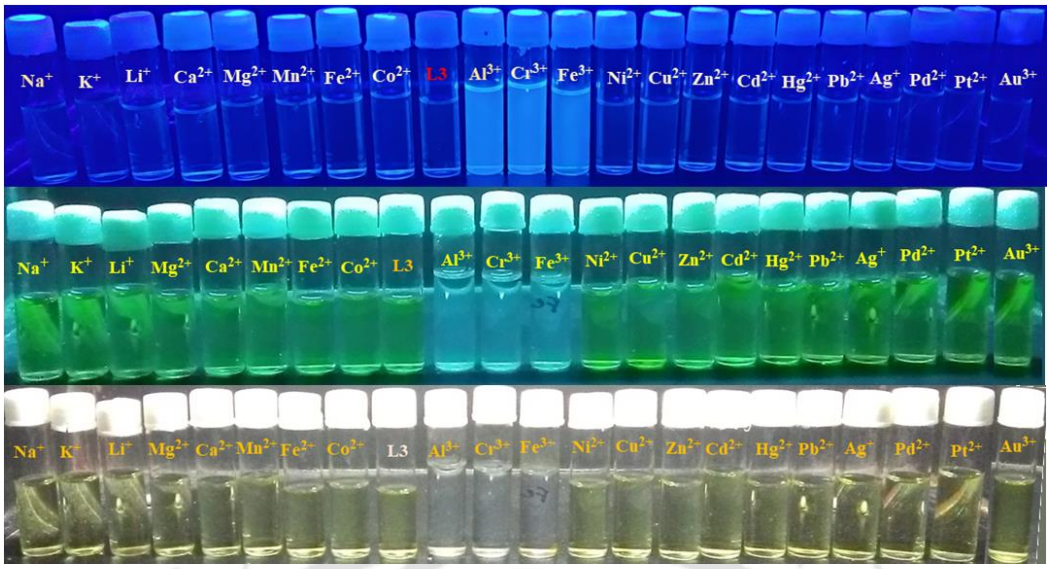

Fig. 11 Photographs depicting distinct behaviour of **L3** in presence of Cr^{3+}, Fe^{3+} and Al^{3+} chlorides compared to other metal ions under long UV light (top), short UV light (middle) and visible light (bottom).

To understand if there is any interference due to the presence of other metal ions, competition experiments were performed by adding the equimolar amount of competing metal salts followed by the addition of the trivalent metal salts (Fig. 12). From this experiment it was observed that the fluorescence intensity of **L3** increases to a large extent by the trivalent ions in the presence of other metal ions. So, we can say that in presence of different metal ions **L3** selectively binds with these trivalent metal ions.

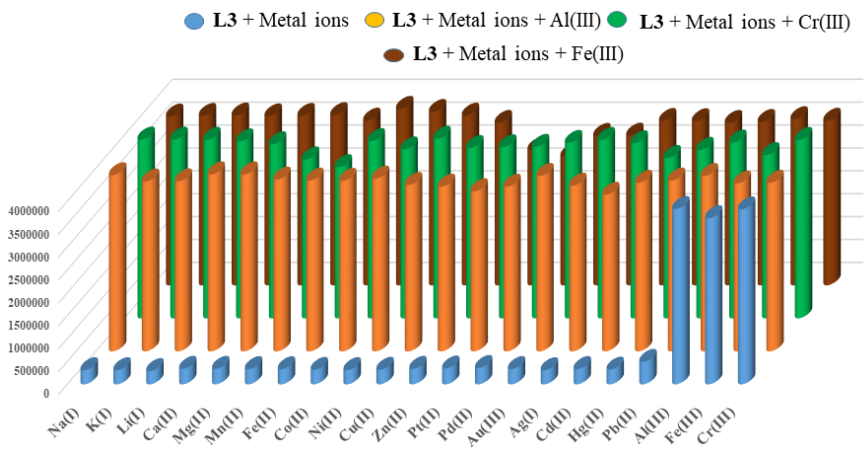

Fig. 12 Bar diagram showing the effect on emission intensity of **L3** and other metal chlorides upon adding of equimolar amounts of $AlCl_3$, $CrCl_3$ and $FeCl_3$.

As short response time of fluorescent probes is highly desirable, it is very important to determine the fluorescence response time of the probe **L3** upon the binding process of M^{3+} (M = Al, Cr, Fe) ions. After addition of Al^{3+} ion into the probe solution, the fluorescence intensity of the probe increased rapidly well within one minute (29 sec) beyond which remained almost invariant (Fig. 13). Similarly, it was observed that **L3** reacted below 1 minute with both Cr^{3+} (60 sec) and Fe^{3+} (59 sec) ions and the response time remained almost invariant beyond 1 min (Fig. 14-15).

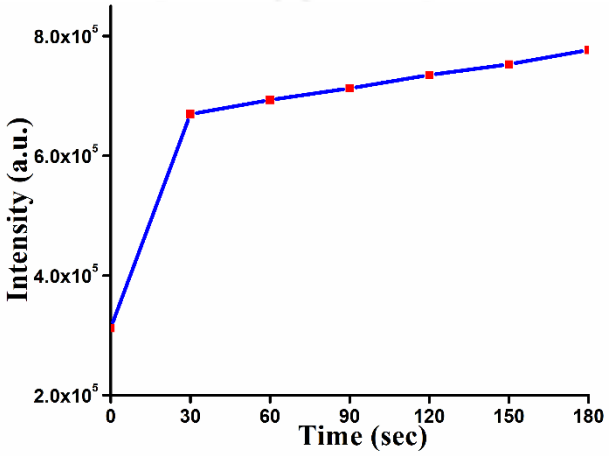

Fig. 13 Fluorescence enhancement profile for addition of $AlCl_3$ into **L3** solution.

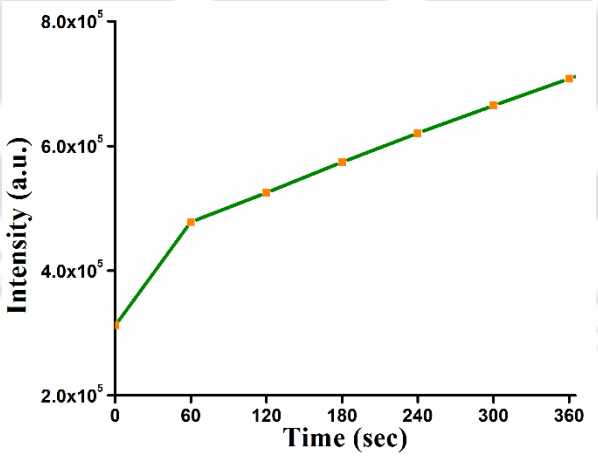

Fig. 14 Fluorescence intensity increasing plot after addition of $CrCl_3$ to the **L3** solution from 1 min to 40 min.

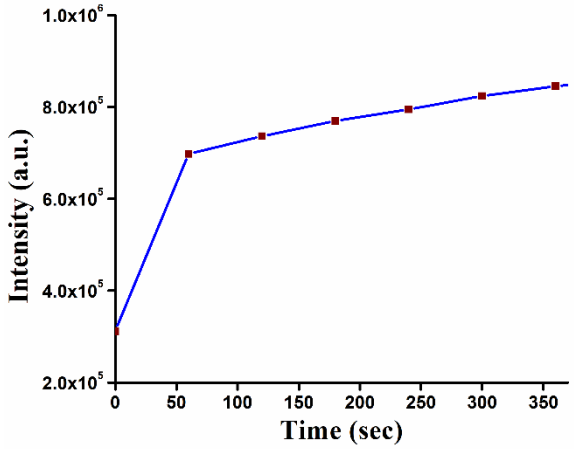

Fig. 15 Fluorescence intensity increasing plot after addition of $FeCl_3$ to the **L3** solution.

It is also very important to examine the utility of **L3** as a chemosensor for measuring specific metal ions in the biological pH range. To understand the pH effect, the emission intensity of **L3** was recorded between the pH range from pH = 2 to 14 in absence and presence of Al^{3+}, Cr^{3+} and Fe^{3+} by adjusting pH using HCl or NaOH solutions. It was seen that for free **L3**, the emission intensity enhanced a small amount in the acidic pH range from 2 to 5 due to the protonation of the nitrogen atom of imine group thus leading to a decrease in chelation ability. In the pH range 6–10, there is a significant increase in emission intensity of **L3** upon addition of Al^{3+}, Cr^{3+} and Fe^{3+} ions. But in basic region, emission intensity decreases as there is formation of metal hydroxides precipitation (Fig. 16-17). Therefore, from this experiment we can say that, the emission intensity is stable in the pH range from pH = 6 to 10 and our probe **L3** can work appropriately under physiological pH conditions for practical application.

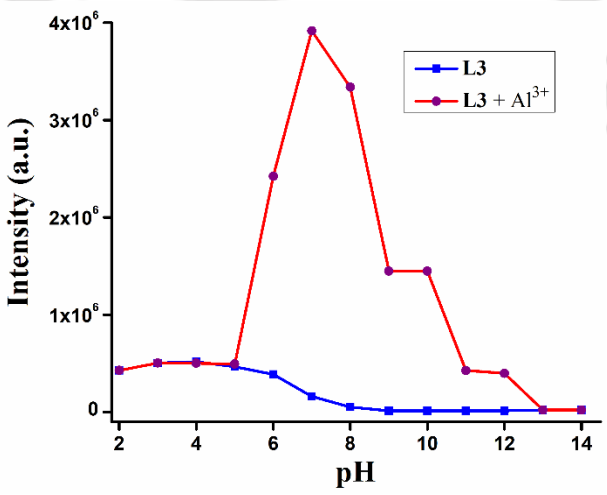

Fig. 16 pH dependence on fluorescence intensity of **L3** and its complex with $AlCl_3$.

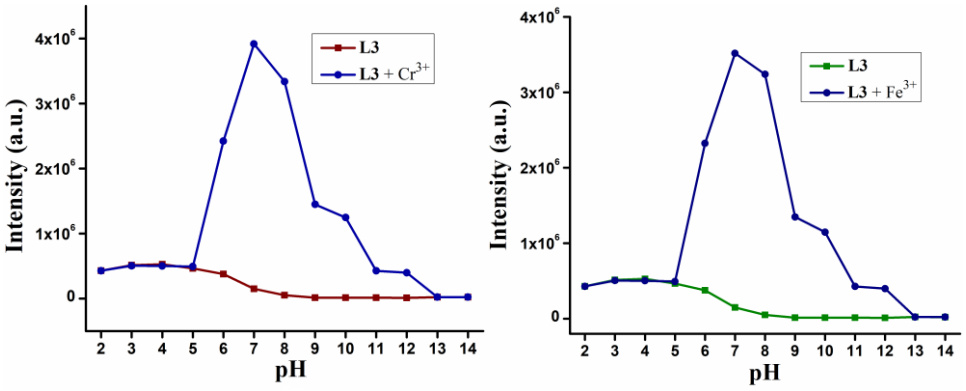

Fig. 17 pH dependence on fluorescence intensity of **L3** and its complex with (a) $CrCl_3$ and (b) $FeCl_3$.

4.3.4. Fluorescence studies of $[Al(L3)Cl_2(H_2O)(CH_3CN)]^+$, $[Cr(L3)Cl_2(H_2O)_2]^+$ and $[Fe(L3)Cl_2(H_2O)_2]^+$ towards various anions:

An "ON–OFF" reversible fluorescence property of **L3** was observed after the addition of M^{3+} (M = Al, Cr, Fe) and F^- ions in fluorescence study. Fluorescence responses obtained after titrating **L3** with Al^{3+}, Cr^{3+} and Fe^{3+} chlorides, were further titrated again with anions such as F^-, Cl^-, Br^-, I^-, CN^-, SCN^-, PO_4^{3-}, S^{2-}, $S_2O_3^{2-}$, CO_3^{2-}, HCO_3^-, AcO^-, ClO_4^- and $C_2O_4^{2-}$ $H_2PO_4^-$, HPO_4^{2-}, NO_3^-, SO_4^{2-}, $P_2O_7^{4-}$, HSO_4^- solutions. All these anions did not create any interference towards the complexes except only F^- ions. After gradual addition of F^- ion, the emission intensity of the three complexes has been properly quenched and the resultant spectrum resembles the free **L3** as shown in Fig. 18-19. From this experimental results it can be concluded that F^- ion releases free **L3** into the solution by forming complex with respective metal ions in accordance with HSAB principle. The reusability of our probe **L3** can be well established from this reversibility test.

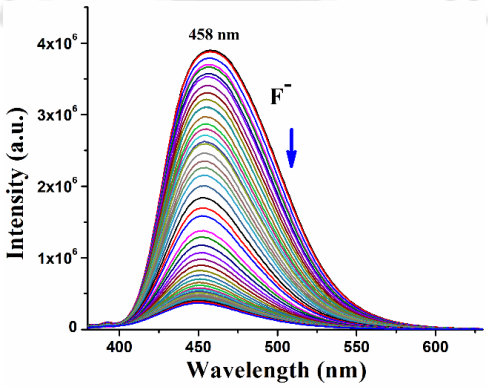

Fig. 18 Changes in fluorescence intensity upon gradual addition of F^- ion into **L3** + Cr^{3+} complex ion solution.

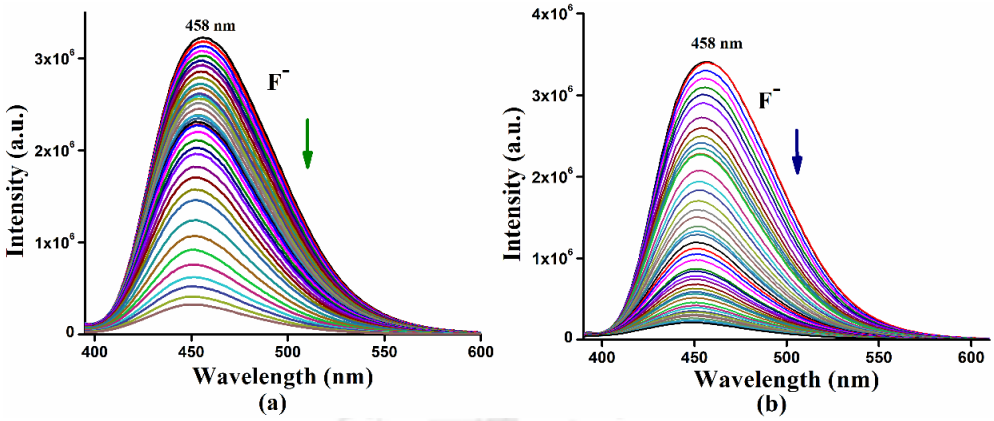

Fig. 19 Changes in fluorescence intensity upon gradual addition of F^- ion into (a) **L3** + Al^{3+} and (b) **L3** + Fe^{3+} complex ion solution.

The limit of detections towards F^- are found 0.90, 0.65 and 2.24 μM respectively for **L3** + Al^{3+}, **L3** + Cr^{3+} and **L3** + Fe^{3+} complex ions (Fig. 20).

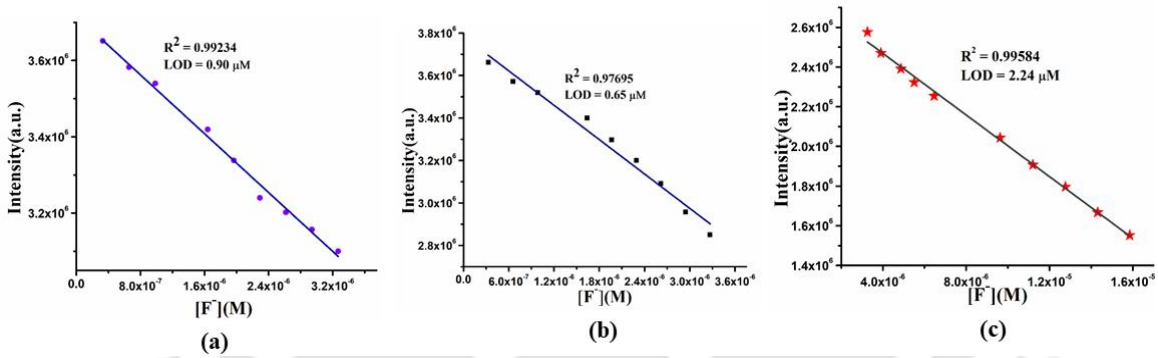

Fig. 20 Plot for determination of limit of detection for fluoride ion towards (a) **L3** + Al^{3+}, (b) **L3** + Cr^{3+} and (c) **L3** + Fe^{3+} complex respectively.

Using Na_2EDTA the reversibility of interaction of **L3** with these trivalent ions was also established. Emission intensity at 458 nm of **L3** bound with M^{3+} (M = Al, Cr, Fe) ion, was re-established after addition of one equivalent of $EDTA^{4-}$ solution (Fig. 21-22) (prepared by adding two equivalents of triethylamine into Na_2EDTA solution). This indicates that $EDTA^{4-}$ effectively sequesters these trivalent ions and thereby releasing free **L3** into the solution. By adding another equivalent of $AlCl_3$, $CrCl_3$ and $FeCl_3$ into the solution fluorescence intensity at 458 nm was enhanced again. Therefore, it can be supposed that binding of **L3** is reversed and it can be utilised for multiple times.

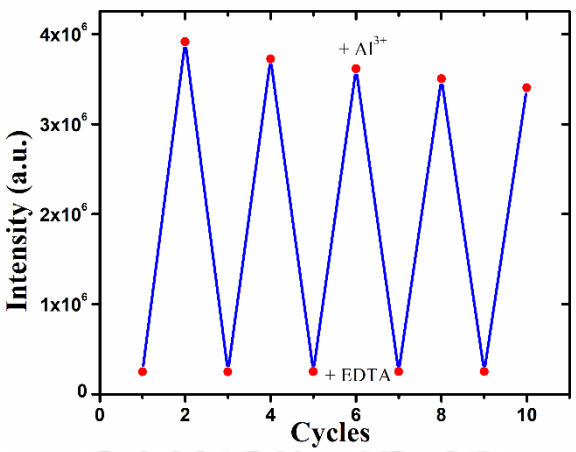

Fig. 21 Reversible switching cycles of emission intensity of **L3** by alternate addition of Al^{3+} (1 equiv.) and $EDTA^{4-}$ (1 equiv.).

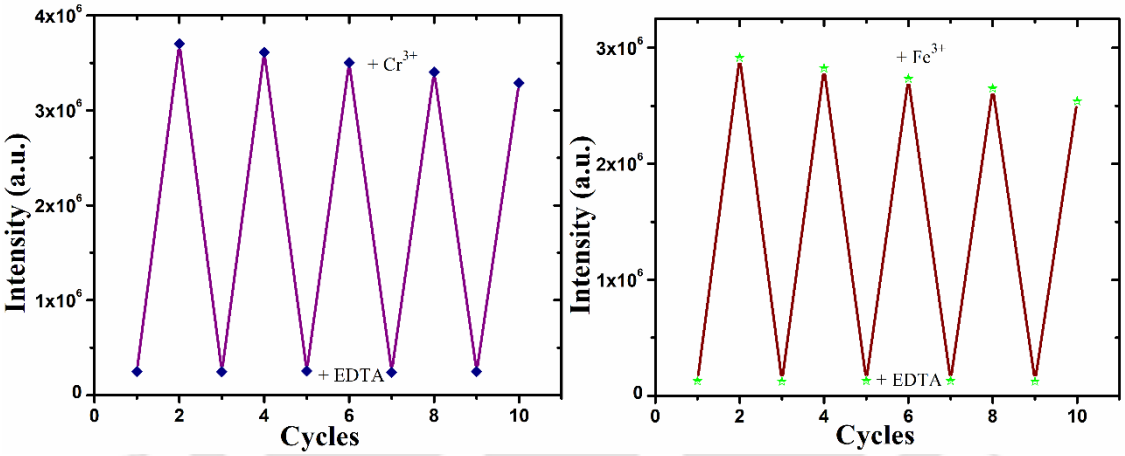

Fig. 22 Reversible switching cycles of **L3** after adding Cr^{3+} (left) and Fe^{3+} (right) along with EDTA respectively.

4.3.5. Detection of Al^{3+}, Cr^{3+} and Fe^{3+} in real water samples:

Using real water samples, the practical utility of **L3** for detecting Al^{3+}, Cr^{3+} and Fe^{3+} ions was evaluated through fluorescence titration experiment. Tap water and drinking water were taken from the institute, river water from the river Brahmaputra (near IIT Guwahati campus, Assam, India). Then water samples were filtered through 0.22 μM membrane and adjusted the pH to 7.4. Firstly, to check the presence of these trivalent ions in these real water samples a blank experiment was performed and was found to be negative. For fluorescence titration experiments solutions of $AlCl_3$, $CrCl_3$, $FeCl_3$ were prepared using these real water samples. Emission intensity *vs* Al^{3+}, Cr^{3+} and Fe^{3+} concentration plot (Fig. 23) revealed that the

intensity increased rapidly well below one-minute confirming that **L3** is a perfect probe for the detection of these trivalent ions in these water samples.

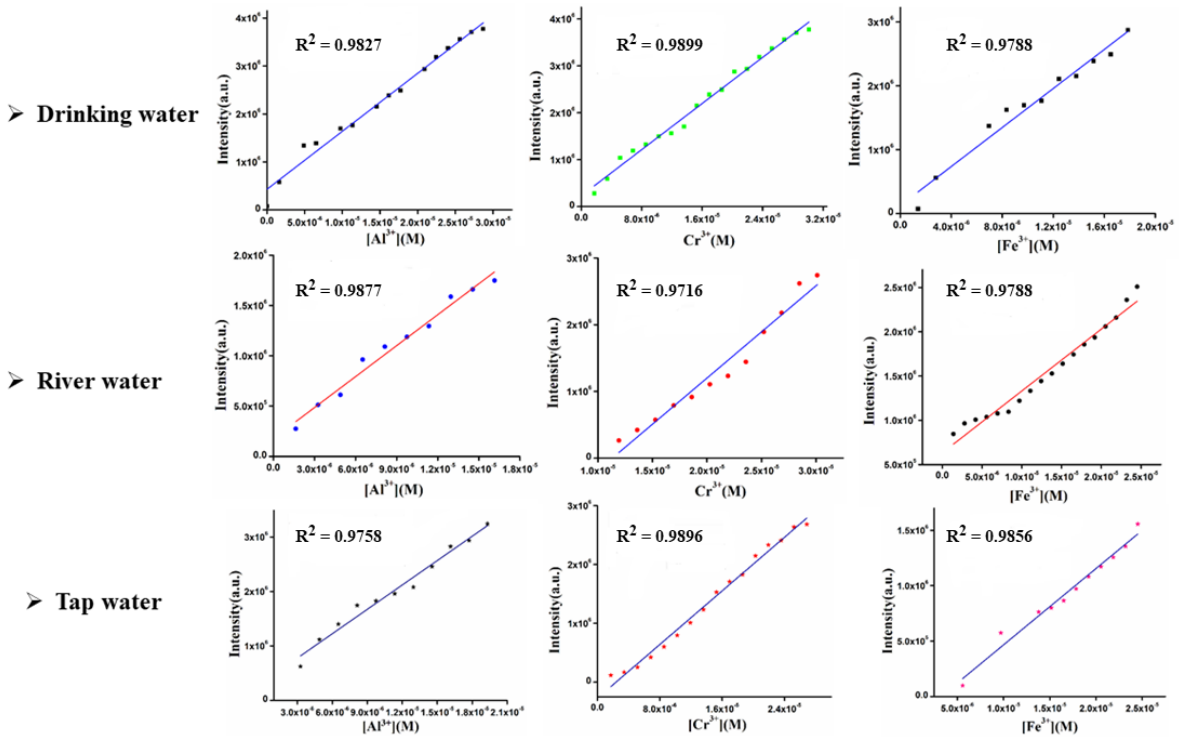

Fig. 23 Fluorescence intensity changes of **L3** with gradual addition of $AlCl_3$, $CrCl_3$ and $FeCl_3$ solution in real water samples.

4.3.6. IR and ^{1}H-NMR titration experiment of L3 in the presence of Al^{3+}, Cr^{3+} and Fe^{3+} ions:

The proposed mode of the formation of complex between **L3** and M^{3+} ion is by coordination of the imine nitrogen atom and oxygen atom of carbonyl group. From IR studies it was seen that the characteristic stretching vibrational frequencies of the imine $\nu_{C=N}$ getting shifted from 1618 cm^{-1} to 1674 cm^{-1} (in Al^{3+}), 1637 cm^{-1} (in Cr^{3+}), 1677 cm^{-1} (in Fe^{3+}) and such shift to the higher wave-number is consistent with the involvement of the lone-pair of electron in coordination to the trivalent ions. However, coumarin $\nu_{C=O}$ has been shifted slightly to the lower wave-number from 1718 cm^{-1} to 1706 cm^{-1} (in Al^{3+}), 1710 cm^{-1} (in Cr^{3+}) and 1708 cm^{-1} (in Fe^{3+}) indicate the delocalisation of lone-pair of electron on ester oxygen with the carbonyl group (Fig 24-25). These shifts in stretching frequencies indicate the binding of **L3** with Al^{3+}, Cr^{3+} and Fe^{3+} ions through nitrogen and oxygen atom of imine and carbonyl group respectively.

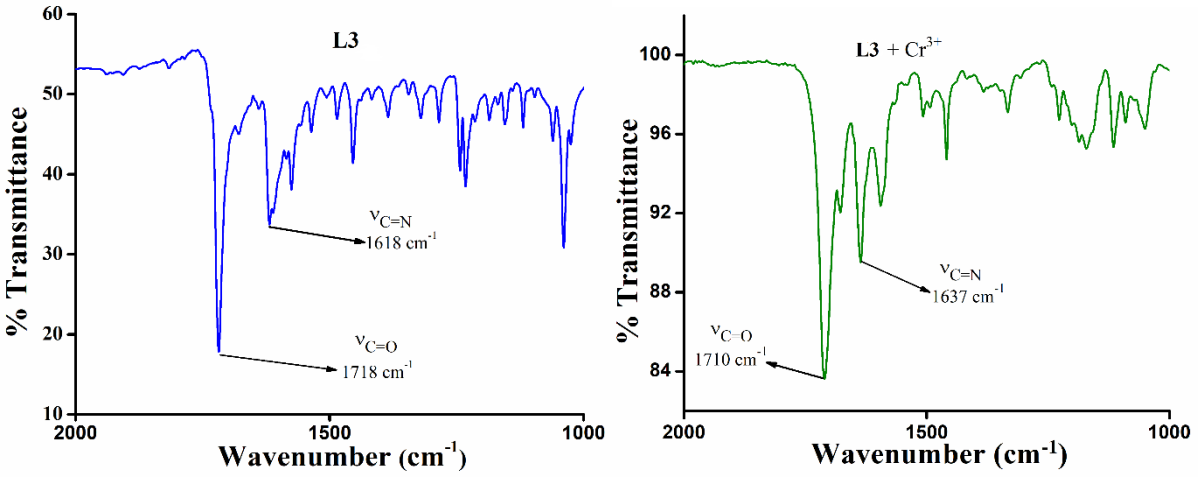

Fig. 24 IR spectra of **L3** and **L3** + Cr^{3+}.

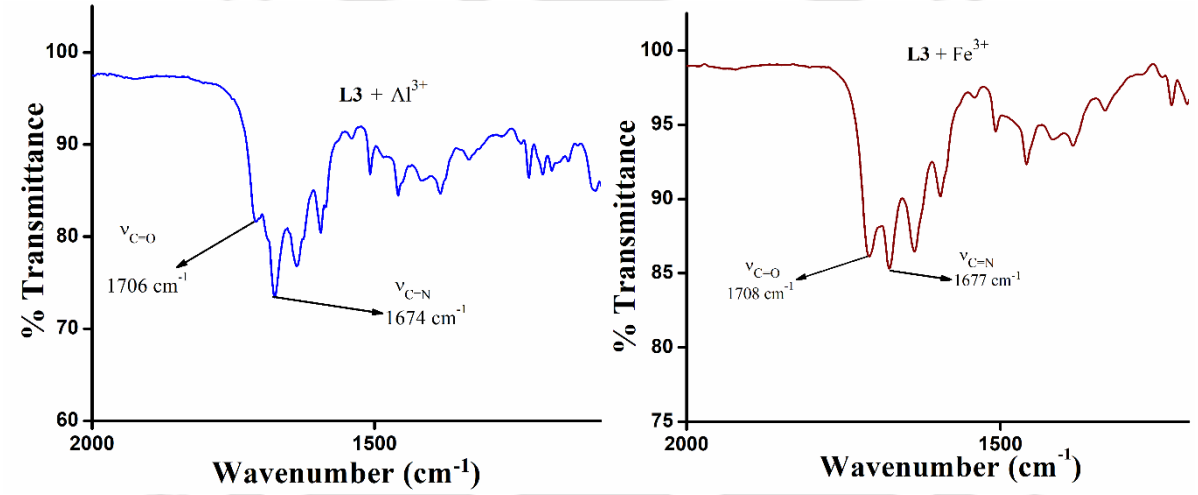

Fig. 25 IR spectral changes of **L3** after complex formation with Al^{3+} and Fe^{3+}.

The ^{1}H NMR titration experiment has been carried out, which confirmed the interaction between the trivalent metal ions and the probe **L3** (Fig. 26).

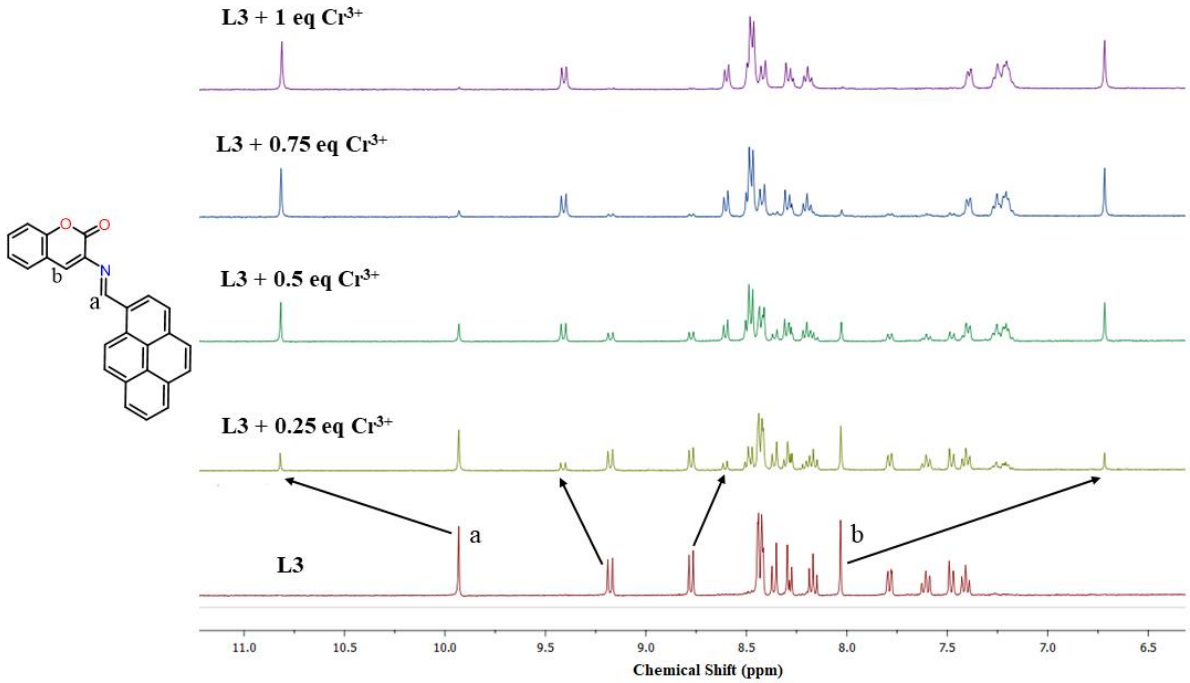

Fig. 26 ^{1}H NMR titration of **L3** with Cr^{3+} in DMSO-d_6.

Upon addition of 0.25 equivalent of $CrCl_3$ in DMSO-d_6 to the **L3** solution singlet peak due to the imine proton (marked as ***a***) exhibited a down field shift from 9.93 ppm to 10.82 ppm. As the titration progressed, the peak at 9.93 ppm started to disappear gradually with a concomitant growth at 10.82 ppm, ostensibly due to the coordination of imine nitrogen of **L3** with Cr^{3+} ion. In addition, the doublet at 9.18 ppm shifted to 9.41 ppm and another doublet exhibited an upfield shift from 8.76 ppm to 8.60 ppm. The singlet signal at 8.03 ppm due to a proton in coumarin ring (marked as ***b***) also shown an upfield shift to 6.72 ppm as a consequence of binding to Cr^{3+} ion. Other signals in the region 7.25–7.80 ppm also exhibited an upfield shift due to increment in electron density on **L3** probe. This ^{1}H NMR titration clearly indicates the involvement of imine group in Cr^{3+} binding. Similar shifts were found after titrating with Fe^{3+} as shown in Fig. A5. Whereas in presence of Al^{3+}, singlet signal due to proton marked as ***a*** in imine bond shifted downfield from 9.99 ppm to 10.81 ppm. The singlet also (marked as ***b***) got shifted upfield from 8.09 ppm to 6.72 ppm after addition of Al^{3+} ion (Fig. A6). The doublet (as noted in Cr^{3+}) shifted downfield from 9.23 ppm to 9.41 ppm and another doublet shifted upfield from 8.83 ppm to 8.58 ppm.

4.4. Binding stoichiometry for Al^{3+}, Cr^{3+} and Fe^{3+} ions with L3:

We plotted according to Job's method of continuous variation to determine the binding ratio between the metal ions (Al^{3+}, Cr^{3+} & Fe^{3+}) and **L3**. For all three of the metal ions the value is

found to be near about 0.5 (Fig. 27). This clearly shows 1:1 binding ratio between **L3** and the metal ions. A higher value of binding constants, 7.3 ×10^4 M^{-1}, 2.8 × 10^4 M^{-1} and 1.1 ×10^5 M^{-1} were observed for Al^{3+}, Cr^{3+} and Fe^{3+} respectively from the Benesi–Hildebrand plot (Fig. 28).

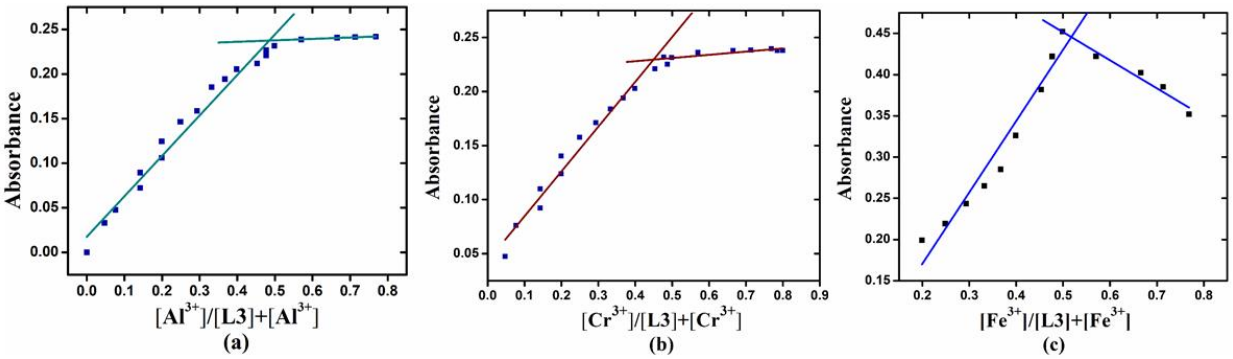

Fig. 27 The Job's plot **L3** with (a) Al^{3+}, (b) Cr^{3+} and (c) Fe^{3+} ion.

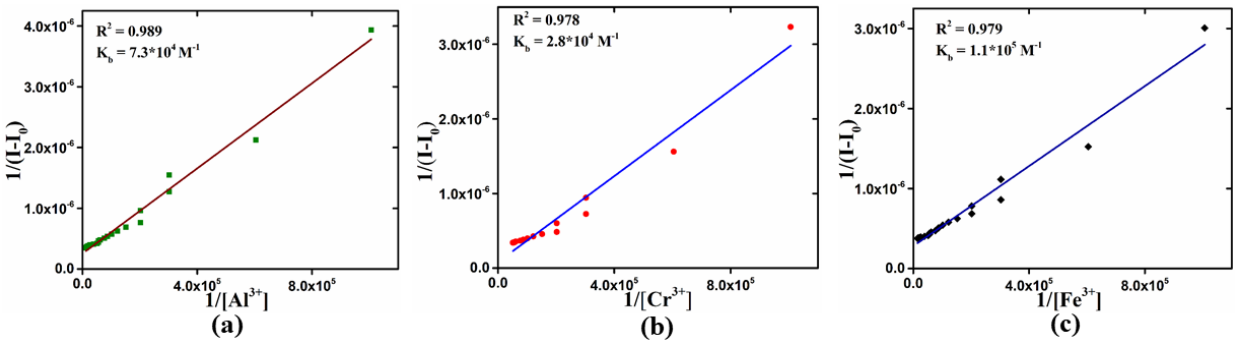

Fig. 28 The Benesi–Hildebrand plot of **L3** + Al^{3+}, **L3** + Cr^{3+} and **L3** + Fe^{3+} complex to determine the binding constants.

Mass spectral analysis supports the experimental findings of Job's plot. In ESI-mass spectrum, the significant peak at *m*/*z* = 529.1799 (calculated for $AlC_{28}H_{20}{}^{35}Cl_2N_2O_3$ = 529.0666) assignable to $[Al(\mathbf{L3})Cl_2(H_2O)(CH_3CN)]^+$ ion, *m*/*z* = 531.3878 (calculated for $CrC_{26}H_{19}{}^{35}Cl_2NO_4$ = 531.0096) assignable to $[Cr(\mathbf{L3})Cl_2(H_2O)_2]^+$ ion and *m*/*z* = 536.1655 (calculated for $FeC_{26}H_{19}{}^{35}Cl_2NO_4$ = 536.0119) assignable to $[Fe(\mathbf{L3})Cl_2(H_2O)_2]^+$ ion further confirms the formation of the 1:1 complex between **L3** and Al^{3+}, Cr^{3+} and Fe^{3+} ions respectively (Fig. A7-A9). The detection limit is found to be remarkably low for the probe **L3** which are 0.79 nM, 1.15 µM, and 1.28 µM for Al^{3+}, Cr^{3+} and Fe^{3+} ions respectively (Fig. 29) and it is lower than many other probes reported by others (Table A1). The quantum yield of free **L3** was found to be 0.09, whereas after adding $AlCl_3$, $CrCl_3$ and $FeCl_3$ the value increases to 0.41, 0.39, 0.24 respectively.

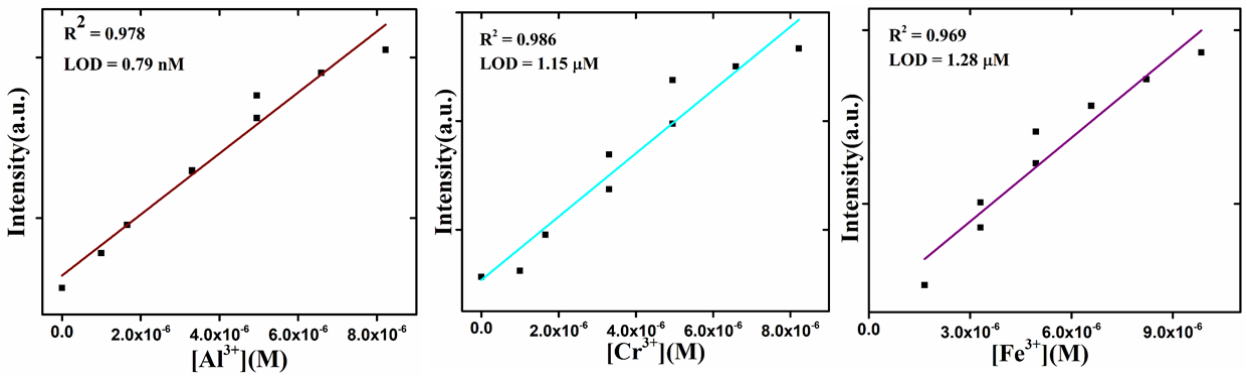

Fig. 29 Fluorescence intensity *vs.* concentration of M^{3+} ions plot for determination of detection limit.

4.5. TRPL measurement:

The time resolved fluorescence lifetime experiment was performed to determine the lifetime of **L3** upon binding with Al^{3+}, Fe^{3+} and Cr^{3+} ions and the decay profiles are shown in Fig. 30. The life time (τ) of free **L3** was found to be 1.56 ns. Upon addition of $AlCl_3$, $CrCl_3$ and $FeCl_3$ the average fluorescence lifetimes (Table 1) increased to 3.26, 3.16 and 3.15 ns, respectively. This result suggests that binding of these trivalent metal ions with **L3** allows CHEF to become operational and thereby increases the life time of the emissive species compared to free **L3**. Due to active PET process in free **L3** there was no fluorescence. But, after complexation with Al^{3+}, Fe^{3+} and Cr^{3+} ions PET process have been locked and fluorescence was observed. Therefore, complexation stops non radiative decay process and an increase in life times has been observed (Scheme 2).

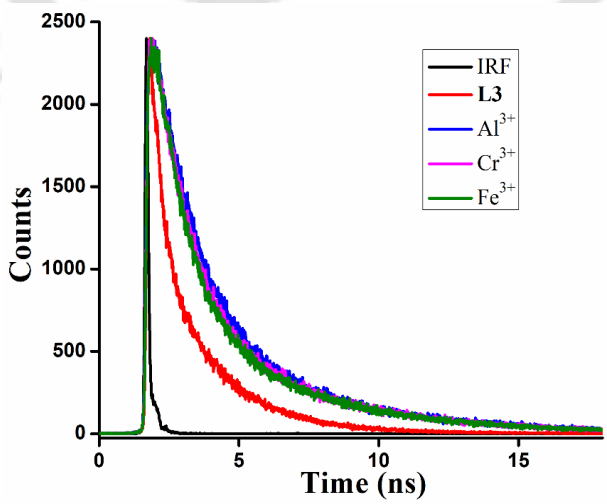

Fig. 30 Time-resolved fluorescence decay profile of **L3** in absence and presence of $AlCl_3$, $CrCl_3$ and $FeCl_3$.

Table 1 Fluorescence decay parameters of **L3** and its complexes with Al^{3+}, Cr^{3+} and Fe^{3+}.

Sample	τ(ns)	χ^2
L3	1.56	1.072
L3 + Al^{3+}	3.26	1.008
L3 + Cr^{3+}	3.16	1.018
L3 + Fe^{3+}	3.15	1.019

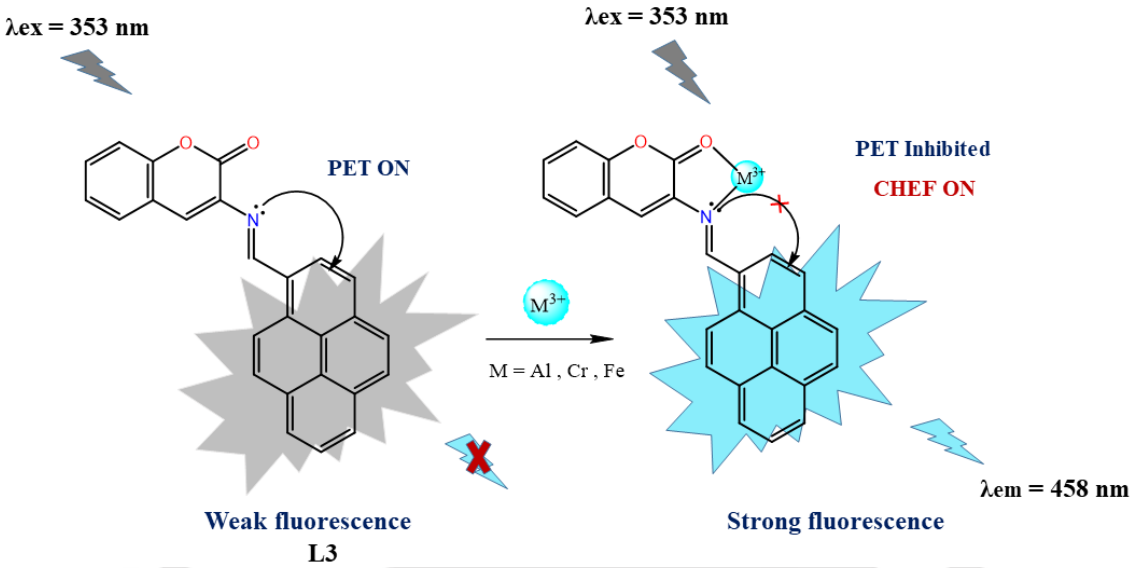

Scheme 2 Probable sensing mode of **L3** towards Al^{3+}, Cr^{3+}, Fe^{3+}

4.6. Computational studies:

DFT/TDDFT calculation was performed on the complexes of **L3** with Al^{3+}, Cr^{3+} and Fe^{3+} in terms of molecular and electronic level using Gasssian09 program. The optimised structures of **L3** and $[Al(\mathbf{L3})Cl_2(H_2O)(CH_3CN)]^+$, $[Cr(\mathbf{L3})Cl_2(H_2O)_2]^+$ and $[Fe(\mathbf{L3})Cl_2(H_2O)_2]^+$ ions (compositions are based on the mass spectra) are shown in Fig 31-32, which illustrates that M^{3+} (M = Al, Cr, Fe) ions are bound by **L3** in a bidentate fashion *via* the nitrogen atom of imine bond and carbonyl oxygen atom of coumarin group. The nitrogen atom of acetonitrile molecule, two chlorine atom and one oxygen atom of water molecule makes pseudo-octahedral geometry around the aluminium ion, whereas in case of chromium and iron complex two chlorine atom and two oxygen atoms of water molecules make pseudo-octahedral geometry around these ions.

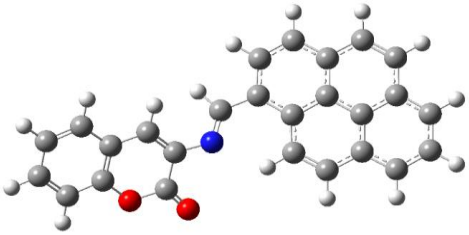

Fig. 31 Energy Optimised structure of **L3**.

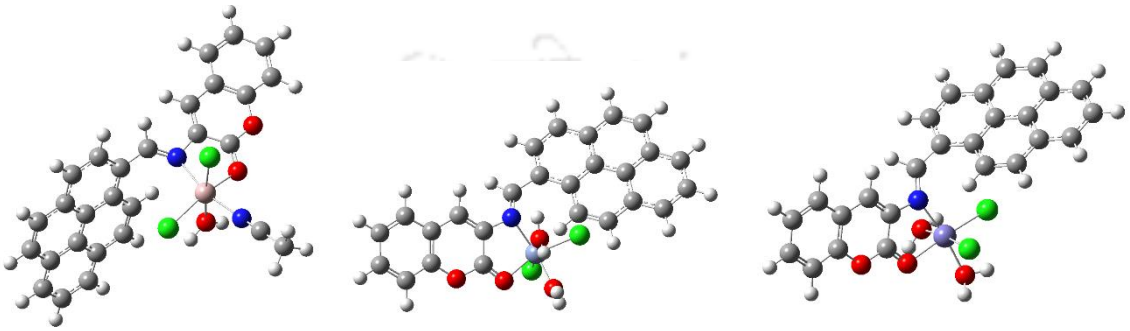

Fig. 32 Energy optimised structure of $[Al(\mathbf{L3})Cl_2(H_2O)(CH_3CN)]^+$ (left), $[Cr(\mathbf{L3})Cl_2(H_2O)_2]^+$ (middle) and $[Fe(\mathbf{L3})Cl_2(H_2O)_2]^+$ (right) complex ions.

The π electron density in HOMO of **L3** is localized mainly on pyrene moiety, whereas the LUMO mostly concentrated on the imine bond and pyrene moiety. Upon coordination of **L3** to Fe^{3+} ion, HOMO is spread over the whole molecule of **L3** and also on two chlorine atoms. On the other hand, LUMO is mainly laid over the central Fe^{3+} ion along with coumarin group. The net effect of complexation on the frontier orbitals is that the energy of HOMO is stabilized to the extent of 4.097 eV while that of LUMO by 3.2836 eV in $[Fe(\mathbf{L3})Cl_2(H_2O)_2]^+$ ion as depicted in Fig. 33. Complex formation of **L3** with Fe^{3+} increases the HOMO-LUMO energy gap from 3.1023 eV to 3.9157 eV, which is reliable with the blue shift observed in the absorption maximum of **L3** upon binding to Fe^{3+} ion.

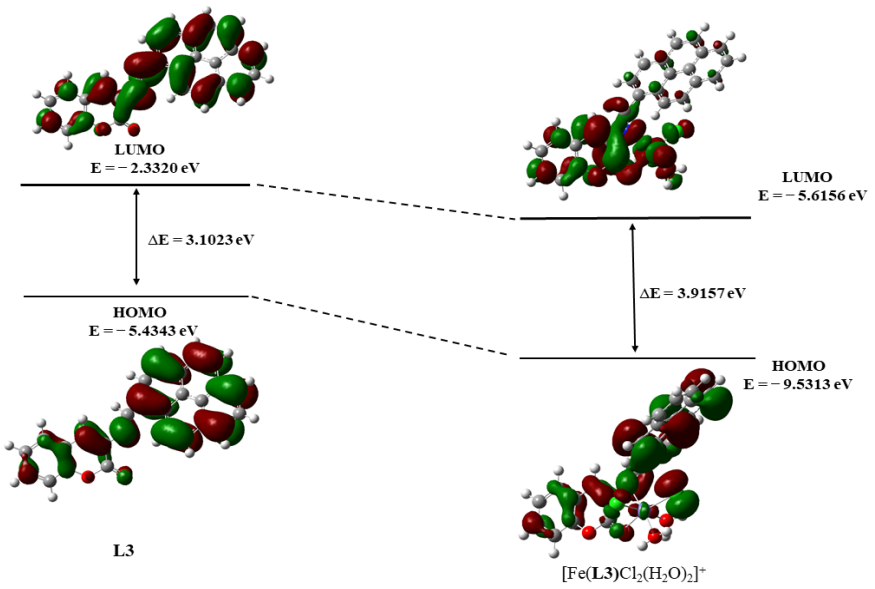

Fig. 33 Energy levels diagram depicting HOMO and LUMO in **L3** and $[Fe(\mathbf{L3})Cl_2(H_2O)_2]^+$ ion.

For chromium complex HOMO is localized on the pyrene ring, central Cr^{3+} ion and two chlorine atoms. Whereas LUMO is distributed mostly within coumarin moiety and imine bond (Fig. 34). Here HOMO and LUMO both are stabilized to the extent of 3.405 eV and 2.6365 eV respectively. This resulted in an increase in HOMO-LUMO energy gap to 3.8708 eV from the value of 3.1023 eV for free **L3**, which is also consistent with blue shift observed in the absorption maximum of **L3** upon binding to Cr^{3+} ion.

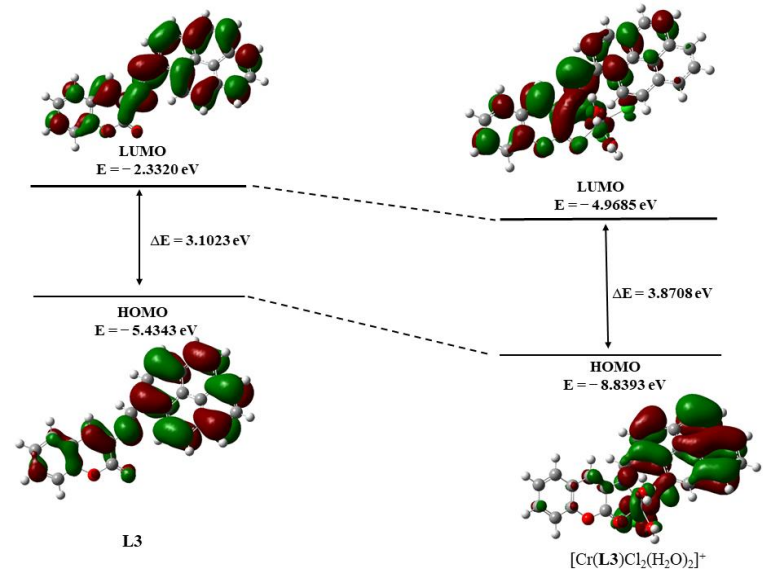

Fig. 34 Energy levels diagram depicting HOMO and LUMO in **L3** and (a) $[Cr(\mathbf{L3})Cl_2(H_2O)_2]^+$

In case of aluminium complex HOMO is distributed on atoms of pyrene ring and on imine bond. The LUMO is localized on both pyrene and coumarin moieties. Both HOMO and LUMO are stabilized to the extent of 3.802 eV and 3.5698 eV respectively, with energy gap between them being increased to 3.3345 eV (in complex ion) from the value of 3.1023 eV for free **L3**. This is also matching with blue shift observed in the absorption maximum of **L3** upon binding to Al^{3+} ion (Fig. 35).

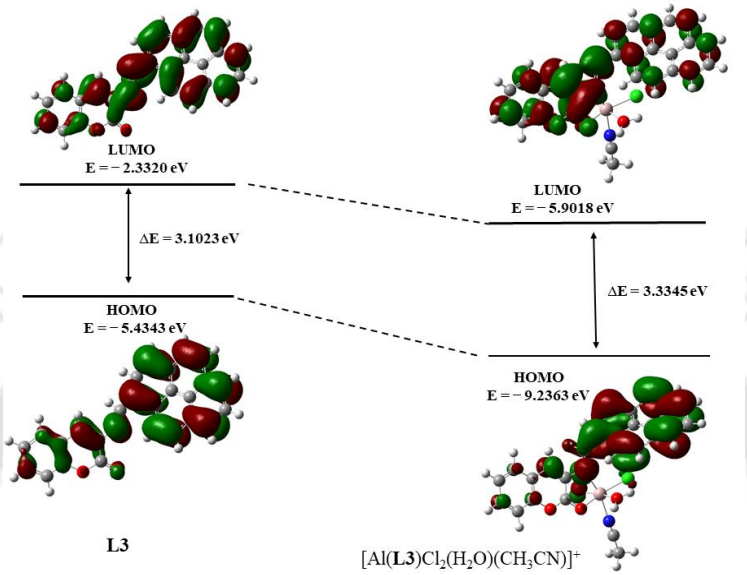

Fig. 35 Energy levels diagram depicting HOMO and LUMO in **L3** and $[Al(\mathbf{L3})Cl_2(H_2O)(CH_3CN)]^+$ complex ion.

4.7. Cytotoxicity assay:

The MTT study revealed that the viability of MDA-MB-231and HDF cells was reduced with an increase in the concentration of probe **L3** (Fig. 36). Upon treatment with MDA-MB-231, the percentage of cell viability was retained up to 7.5 µM of **L3** and showed no significant difference with control (untreated cells). However, the percentage of cell viability significantly reduced to 86.2 ± 2.7% in MDA-MB-231 cells incubated with 10 µM of probe **L3** compared to control ($p \leq 0.001$). Notably, a dose-dependent cytotoxic behaviour of probe **L3** was observed on primary human dermal fibroblasts HDF. A significant decline in the percentage of cell viability was observed in HDF cells with 84.3 ± 2.7 %, 84.5 ± 2.0 %, and 63.0 ± 3.9 % upon treating with 5 µM, 7.5 µM, and 10 µM of probe **L3** ($p \leq 0.001$) compared to control. Interestingly, MDA-MB-231 and HDF cells demonstrated a distinct cytotoxic behaviour, where the viability of HDF cells reduced remarkably upon treating with 7.5 µM ($p \leq 0.05$) and 10 µM ($p \leq 0.01$) of probe **L3** in comparison with MDA-MB-231 cells. From

cytotoxicity analysis, a concentration of 7.5 µM of probe **L3** was selected to analyze its fluorescence attributes in cellular imaging.

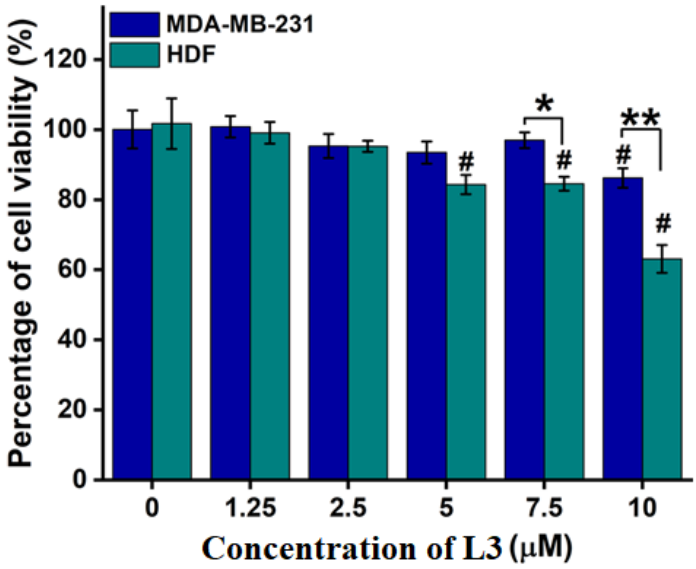

Fig. 36 The cytotoxicity of increasing concentration of probe **L3** against human breast carcinoma cell line (MDA-MB-231) and primary human dermal fibroblasts (HDF) as assessed using MTT assay. The percentage of cell viability (%) was calculated relative to control (only media). * $p \leq 0.05$ and ** $p \leq 0.01$ between the groups. # $p \leq 0.001$ in comparison to control.

4.8. Fluorescence imaging:

The fluorescence property of only probe **L3** and **L3** along with trivalent metal ions (Al^{3+}, Fe^{3+}, and Cr^{3+}) was assessed after incubation for specified time points in MDA-MB-231 and HDF cells (Fig. 37 and 38). Both MDA-MB-231 and HDF cells didn't exhibit any fluorescence when incubated with only media and 7.5 µM of probe **L3**. To comprehend the fluorescence property of probe along with trivalent metal ions, cells pre-incubated with probe 7.5 µM **L3** and exposed to 7.5 µM Al^{3+}, 7.5 µM Fe^{3+}, and 5 µM Cr^{3+}, individually indicated blue fluorescence emission from intracellular regions. In comparison with Cr^{3+}, Al^{3+} and Fe^{3+} incubation on MDA-MB-231 and HDF cells displayed a large number of cells with bright blue fluorescence, as observed from fluorescence images.

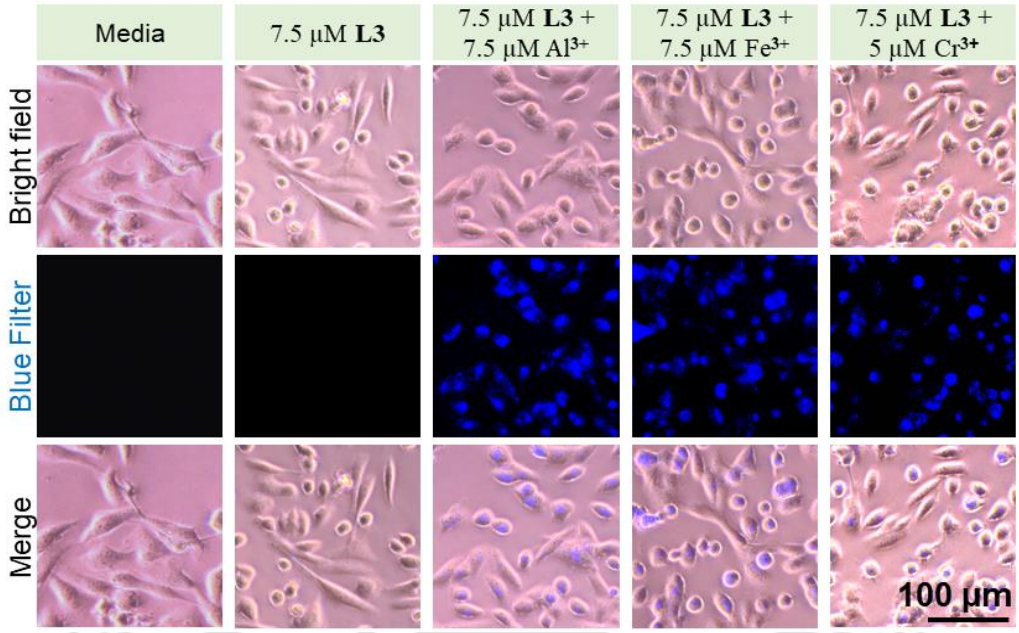

Fig. 37 Bright field and live-cell fluorescence images of human breast carcinoma (MDA-MB-231) cells after incubation with only probe **L3** and incubation with probe **L3** along with trivalent metal ions, Al^{3+}, Fe^{3+}, and Cr^{3+} at 37°C for specified incubation time. Scale bar: 100 µm.

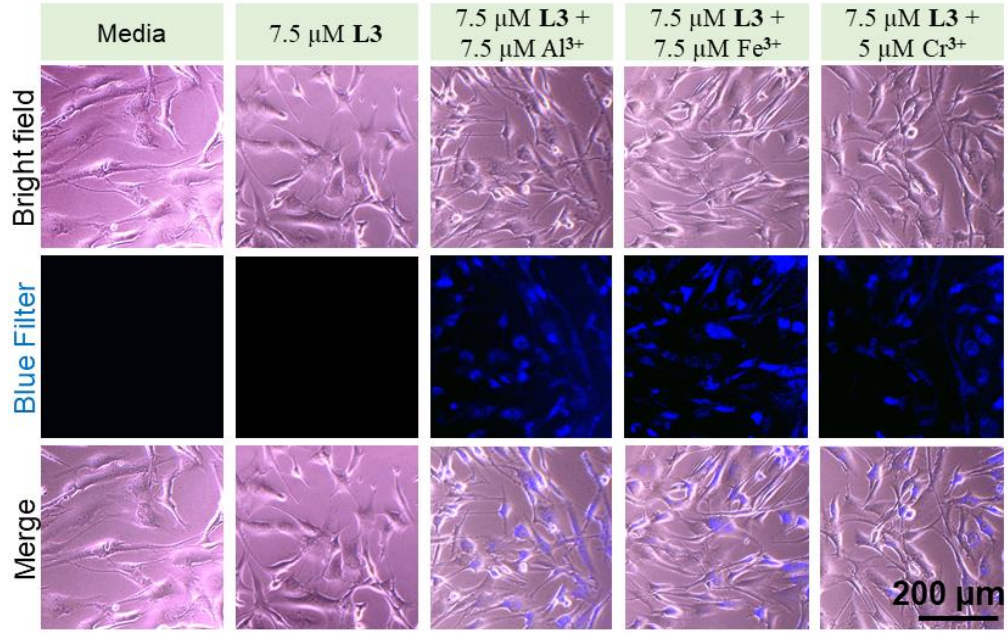

Fig. 38 Bright field and live-cell fluorescence images of primary human dermal fibroblasts (HDF) after incubation with only probe **L3** and incubation with probe **L3** along with trivalent metal ions, Al^{3+}, Fe^{3+}, and Cr^{3+} at 37°C for specified incubation time. Scale bar: 200 µm.

4.9. Conclusion:

In conclusion we have demonstrated that the probe **L3** having both coumarin and pyrene moieties is unique and highly selective in its property of recognising trivalent (Al^{3+}, Cr^{3+} and Fe^{3+}) ions. The fluorescence in active **L3** remained silent in the presence of monovalent and bivalent cations such as Na^{+}, K^{+}, Li^{+}, Ca^{2+}, Mg^{2+}, Mn^{2+}, Fe^{2+}, Co^{2+}, Ni^{2+}, Cu^{2+}, Zn^{2+}, Cd^{2+}, Hg^{2+}, Pb^{2+}, Pd^{2+}, Ag^{+} as well as Au^{3+} ions. But the silent probe **L3**, in presence of Al^{3+}, Fe^{3+}, and Cr^{3+} ions became fluorescence active and exhibited a "turn-on" response. The limit of detection was found for 0.79 nM, 1.15 µM, and 1.28 µM for Al^{3+}, Cr^{3+} and Fe^{3+} ions respectively, which are far less than prescribed by the WHO far a safe drinking water. The probe **L3** has higher values of binding constants with these three trivalent ions, their interaction ratios were found as 1:1 and can be an ideal probe for practical applications at physiological pH. Time-resolved fluorescence decay profile suggested that addition of these trivalent metal ions into **L3** solution allows CHEF to become operational and increases the life time of the emissive species compared to free **L3**. From theoretical calculations, it was observed that both HOMO and LUMO are stabilized upon binding of **L3** to these three ions. But extent of stabilization is more on HOMO which resulted in increase in the energy gap between them, consistent with experimentally observed blue shift in complex species. A 7.5 µM concentration of probe **L3** showed higher percentage of cell viability in the cytotoxicity study and hence it can be used for intracellular detection of M(III) ions [M = Al, Cr, Fe] in living cells through "*turn-on*" fluorescence phenomenon

References:

1. Z. Liu, K. Ren, Y. Chen, Y. Li, J. Xie, Y. Ding, L. Li, K. Li, W. Zhu, W. Yang and Z. Xu, *RSC Adv.*, 2017, **7**, 38160–38165.
2. K.S. Mani, R. Rajamanikandan, G. Ravikumar, B.V. Pandiyan, P. Kolandaivel, M. Ilanchelian and S.P. Rajendran, *ACS Omega*, 2018, **3**, 17212−17219.
3. Q. Zhao, R.F. Li, S.K. Xiang, X.M. Liu, T.L. Hu and X.H. Bu, *Inorg. Chem.*, 2011, **50**, 10041−10046.
4. A. Majumdar, C.S. Lim, H.M. Kim and K. Ghosh, *ACS Omega*, 2017, **2**, 8167−8176.
5. V.C. Ezeh and T.C. Harrop, *Inorg. Chem.*, 2012, **51**, 1213−1215.
6. K. Ghosh and S. Rathi, *RSC Adv.*, 2014, **4**, 48516−48521.

7. S. Mahata, A. Bhattacharya, J. P. Kumar, B. B. Mandal and V. Manivannan, *J. Photochem. Photobiol. A: Chem.*, 2020, **394**, 112441−112450.

8. M. Tian and H. Ihmels, *Chem.Commun.*, 2009, **22**, 3175−3177.

9. M. Shyamal, P. Mazumdar, S. Maity, S. Samanta, G.P. Sahoo and A. Misra, *ACS Sens.*, 2016, **1**, 739−747.

10. P. Li, J. Li, M. Bian, D. Huo, C. Hou, P. Yang, S. Zhang, C. Shen and M. Yang, *Anal. Methods*, 2018, **10**, 3256−3262.

11. B. Valeur and I. Leray, *Coord. Chem. Rev.*, 2000, **205**, 3−40.

12. Z. Krejpcio and R.W.P Wojciak, *Int. J. Environ. Stud.*, 2002, **11**, 251−254.

13. M.R. Wills, C.D. Hewitt, B.C. Sturgill, J. Savory and M.M. Herman, *Ann. Clin. Lab. Sci.*, 1993, **23**, 1−7.

14. G. Sahin, I. Varol, A. Temizer, K. Benli, R. Demirdamar and S. Duru, *Biol. Trace Elem Res.*, 1994, **41**, 129−135.

15. A.C. Alfrey, *Advance in Clinical Chemistry*, 1983, **23**, 69−91.

16. J. Barcelo and C. Poschenrieder, *Environ. Exp. Bot.*, 2002, **48**, 75–92.

17. T.P. Flaten and M. Odegard, *Food Chem, Toxic.*, 1988, **26**, 959–960.

18. E. Delhaize and P.R. Ryan, *Plant Physiol.*, 1995, **107**, 315–321.

19. T. Han, X. Feng, B. Tong, J. Shi, L. Chen, J. Zhi and Y. Dong, *Chem. Commun.*, 2012, **48**, 416–418.

20. D. Maity and T. Govindaraju, *Chem. Commun.*, 2010, **46**, 4499–4501.

21. R.A. Anderson, *Regul. Toxicol. Pharm.*, 1997, **26**, S35–S41.

22. H. Arakawa, R. Ahmad, M. Naoui and H.A. Tajmir-Riahi, *J. Biol. Chem.*, 2000, **275**, 10150–10153.

23. D.A. Eastmond, J.T. MacGregor and R.S. Slesinski, *Crit. Rev Toxicol.*, 2008, **38**, 173–190.

24. A.M. Zayed and N. Terry, *Plant Soil*, 2003, **249**, 139–156.

25. J. Wang and K. Pantopoulos, *Biochem. J.*, 2011, **434**, 365–381.

26. P. Aisen, M. Wessling-Resnick and E. Leibold, *Curr. Opin. Chem. Biol.*, 1999, **3**, 200–206.

27. S. Sen, S. Sarkar, B. Chattopadhyay, A. Moirangthem, A. Basu, K. Dharad and P. Chattopadhyay, *Analyst*, 2012, **137**, 3335–3342.

28. D.J. Bonda, H. Lee, J.A. Blair, X. Zhu, G. Perry and M.A. Smith, *Metallomics*, 2011, **3**, 267–270.

29. W. Shi, X. Sun, S. Zhao and Z. Xie, *New J. Chem.*, 2015, **39**, 8552–8559.

30. Z.T. Graber, W. Wang, G. Singh, I. Kuzmenko, D. Vaknin and E.E. Kooijman, *RSC Adv.*, 2015, **5**, 106536–106542.

31. X. Chen, X.Y. Shen, E. Guan, Y. Liu, A. Qin, J.Z. Sun and B.Z. Tang, *Chem Commun.*, 2013, **49**, 1503–1505.

32. N.R. Chereddy, P. Nagaraju, M.V.N. Raju, V.R. Krishnaswamy, P.S. Korrapati, P.R. Bangal and V.J. Rao, *Biosens. Bioelectron*, 2015, **68**, 749–756.

33. T. Simon, M. Shellaiah, V. Srinivasadesikan, C.C. Lin, F.H. Ko, K.W. Sun and M.C. Lin, *Sens. Actuators B: Chem.*, 2016, **231**, 18–29.

34. A. Singh, R. Singh, M. Shellaiah, E.C. Prakash, H.C. Chang, P. Raghunath, M.C. Lin and H.C. Lin, *Sens. Actuators B: Chem.*, 2015, **207**, 338–345.

35. M. Shellaiah, T. Simon, V. Srinivasadesikan, C.M. Lin, K.W. Sun, F.H. Ko, M.C. Lin, and H.C. Lin, *J. Mater. Chem. C*, 2016, **4**, 2056–2071.

36. N. Behera and V. Manivannan, *J. Photochem. Photobiol. A: Chem.*, 2018, **353**, 77–85.

37. P. Ravichandiran, S.A. Subramaniyan, A.P. Bella, P.M. Johnson, A.R. Kim, K.S. Shim and D.J. Yoo, *Anal. Chem.*, 2019, **91**, 10095–10101.

38. N. Behera and V. Manivannan, *ChemistrySelect*, 2017, **2**, 11048–11054.

39. S. Goswami, K. Aich, S. Das, A.K. Das, D. Sarkar, S. Panja, T.K. Mondal and S. Mukhopadhyay, *Chem. Commun.*, 2013, **49**, 10739–10741.

40. A. Liu, L. Yang, Z. Zhang and D. Xu, *Dyes Pigments*, 2013, **99**, 472–479.

41. A. Ghorai, J. Mondal, S. Chowdhury and G.K. Patra, *Dalton Trans.*, 2016, **45**, 11540–11553.

42. L. He, B. Dong, Y. Liu and W. Lin, *Chem. Soc. Rev.*, 2016, **45**, 6449–6461.

43. J. Wu, W. Liu, J. Ge, H. Zhang and P. Wang, *Chem. Soc. Rev.*, 2011, **40**, 3483–3495.

44. H. Zhu, J. Fan, B. Wang and X. Peng, *Chem. Soc. Rev.*, 2015, **44**, 4337–4366.

45. B. Shirinfar, N. Ahmed, Y.S. Park, G.S. Cho, I.S. Youn, J.K. Han, H.G. Nam and K.S. Kim, *J. Am. Chem. Soc.*, 2013, **135**, 90−93.

46. A.J. Weerasinghe, C. Schmiesing, S. Varaganti, G. Ramakrishna and E. Sinn, *J. Phys. Chem. B.*, 2010, **114**, 9413–9419.

47. J. Miao, L. Wang, W. Dou, X.L. Tang, Y. Yan and W.S. Liu, *Org. Lett.*, 2007, **9**, 4567−4570.

48. R. Alam, R. Bhowmick, A.S.M. Islam, A. Katarkar, K. Chaudhuri and M.A. Ali, *New J. Chem.*, 2017, **41**, 8359−8369.

49. D. Das, R. Alam, A. Katarkar and M. Ali, *Photochem. Photobiol. Sci.*, 2019, **18**, 242–252.

50. O. Sunnapu, N.G. Kotla, B. Maddiboyina, G.S. Asthana, J. Shanmugapriya, K. Sekar, S. Singaravadivel and G. Sivaraman, *Sens. Actuators, B Chem.*, 2017, **246**, 761–768.

51. A. Sahana, A. Banerjee, S. Lohar, B. Sarkar, S.K. Mukhopadhyay and D. Das, *Inorg. Chem.*, 2013, **52**, 3627–3633.

52. S. Hou, Z. Qu, K. Zhong, Y. Bian and L. Tang, *Tetrahedron Lett.*, 2016, **57**, 2616–2619.

53. S. Dey, S. Sarkar, D. Maity and P. Roy, *Sens. Actuators B: Chem.*, 2017, **246**, 518–534.

54. D. Singha, T. Das, L. Satyanarayana, P. Roy and M. Nandi, *New J. Chem.*, 2019, **43**, 15563–15574.

55. H. Kilic and E. Bozkurt, *J. Photochem. Photobiol. A: Chem.*, 2018, **363**, 23–30.

56. X. Yue, C. Li and Z. Yang, *J. Photochem. Photobiol. A: Chem.*, 2018, **351**, 1–7.

57. X. Wan, T. Liu, H. Liu, L. Gub and Y. Yao, *RSC Adv.*, 2014, **4**, 29479–29484.

58. S. Paul, A. Manna and S. Goswami, *Dalton Trans.*, 2015, **44**, 11805–11810.

59. P.N. Borase, P.B. Thale, S.K. Sahoo and G.S. Shankarling, *Sens. Actuators B: Chem.*, 2015, **215**, 451–458.

60. R. Chandra, A.K. Manna, K. Rout, J. Mondal and G.K. Patra, *RSC Adv.*, 2018, **8**, (35946–35958.

61. M. Venkateswarulu, T. Mukherjee, S. Mukherjee and R. R. Koner, *Dalton Trans.*, 2014, **43**, 5269–5273.

62. S. Samanta, S. Goswami, A. Ramesh and G. Das, *Sens. Actuators B: Chem.*, 2014, **194**, 120–126.

63. J. Wang, Y. Li, N.G. Patel, G. Zhang, D. Zhou and Y. Pang, *Chem. Commun.*, 2014, **50**, 12258–12261.

64. F. Ye, N. Wu, P. Li, Y.L. Liu, S.J. Li and Y. Fu, *Spectrochim. Acta A*, 2019, **222**, 117242–117253.

65. M. Huang, J. Zhou, X. Zheng, Y. Zhang, S. Xu and Z. Li, *Inorg. Chem. Commun.*, 2020, **117**, 107968–107975.

66. S. Janakipriya, N. R. Chereddy, P. Korrapati, S. Thennarasu and A. B. Mandal, *Spectrochim. Acta A*, 2016, **153**, 465–470.

67. S. K. Dinda, A. Upadhyay, S. Polepalli, M. A. Hussain and C. P. Rao, *ACS Omega*, 2019, **4**, 7723−7733.

68. S. Goswami, K. Aich, A. K. Das, A. Manna and S. Das, *RSC Adv.*, 2013, **3**, 2412–2416.

69. X. Zhao, G. Yin, D. Jin, X. Yan, Y. Li and L. Chen, *J Fluoresc.*, 2015, **25**, 327–333.

70. S. Tao, Y. Wei, C. Wang, Z. Wang, P. Fan, D. Shi, B. Ding and Jieshan Qiu, *RSC Adv.*, 2014, **4**, 46955–46961.

71. A. J. Beneto and A. Siva, *ChemistrySelect*, 2016, **1**, 3548 – 3554.

72. D. Cao, Z. Liu, P. Verwilst, S. Koo, P. Jangjili, J.S. Kim and W. Lin, *Chem. Rev.*, 2019, **119**, 10403–10519.

73. H.F. Wang and S.P. Wu, *Sens. Actuators B: Chem.*, 2013, **181**, 743–748.

74. J.Y. Choi, D. Kim and J. Yoon, *Dyes Pigments*, 2013, **96**, 176–179.

75. M. Kaur, P. Kaur, V. Dhuna, S. Singh and K. Singh, *Dalton Trans.*, 2014, **43**, 5707–5712.

76. G. Janani, M. M. Pillai, R. Selvakumar, A. Bhattacharyya and C. Sabarinath, *Biofabrication*, 2017, **9**, 015016.

77. A.P.D. Silva, T.S. Moody and G.D. Wright, *Analyst*, 2009, **134**, 2385–2393.

78. S. Das, S. Goswami, K. Aich, K. Ghoshal, C.K. Quah, M. Bhattacharyya and H.K. Fun, *New J. Chem.*, 2015, **39**, 8582–8587.

Appendix:

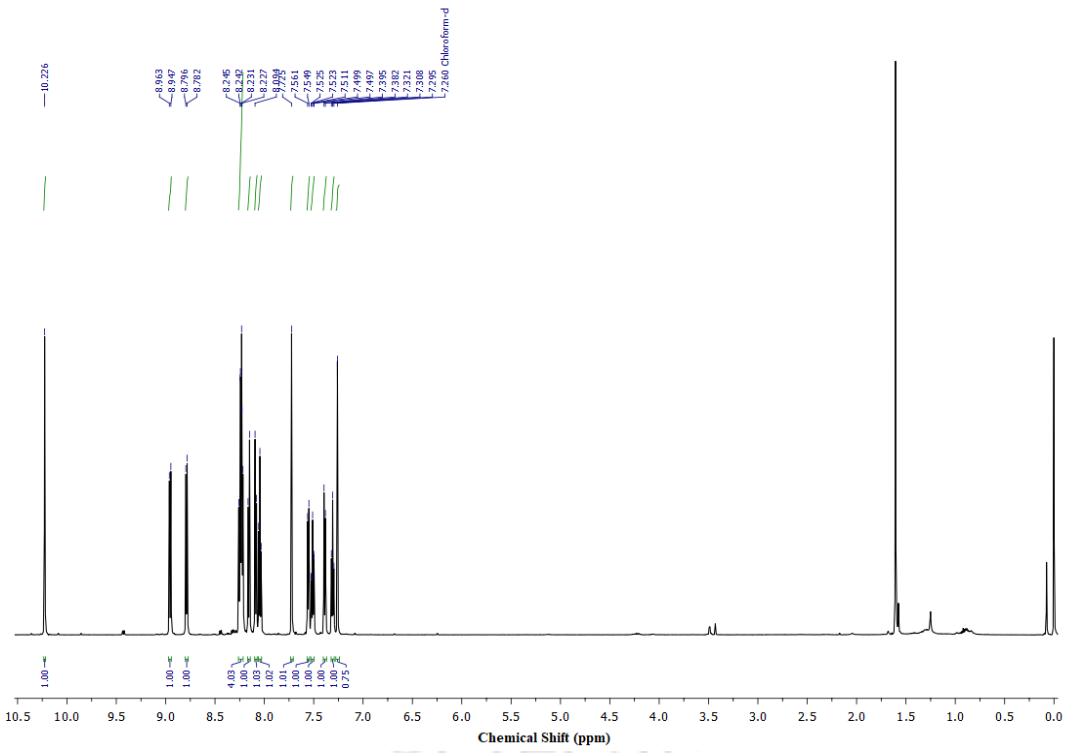

Fig. A1 ^{1}H NMR spectra of **L3**.

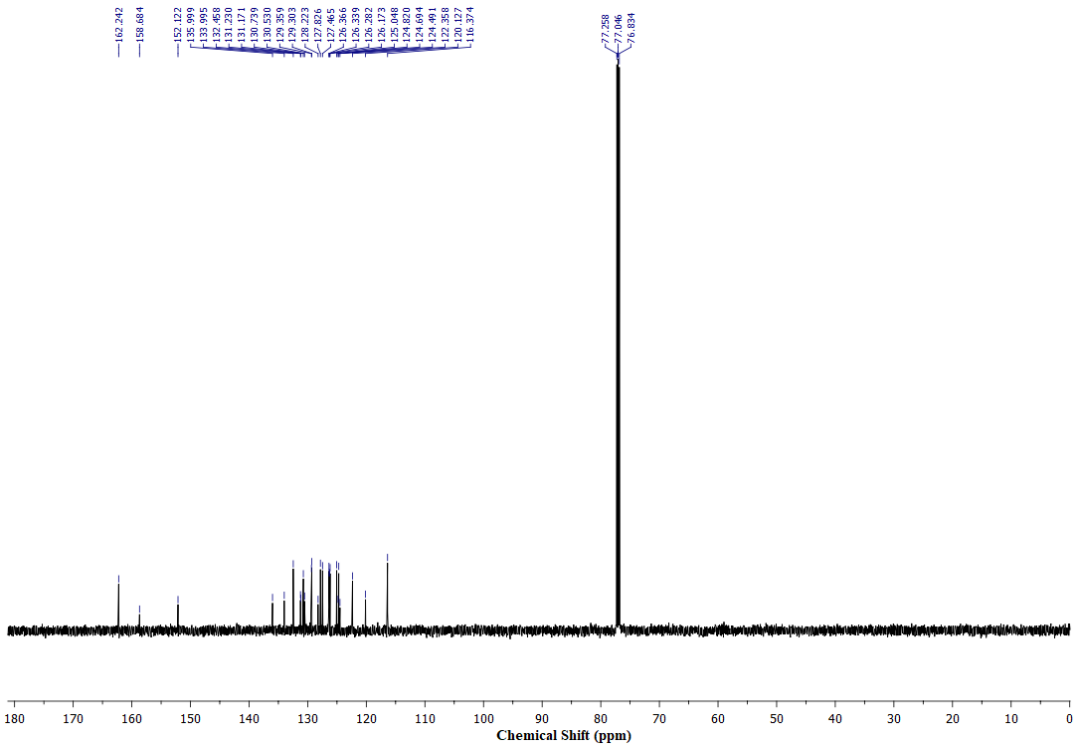

Fig. A2 ^{13}C NMR spectra of **L3**.

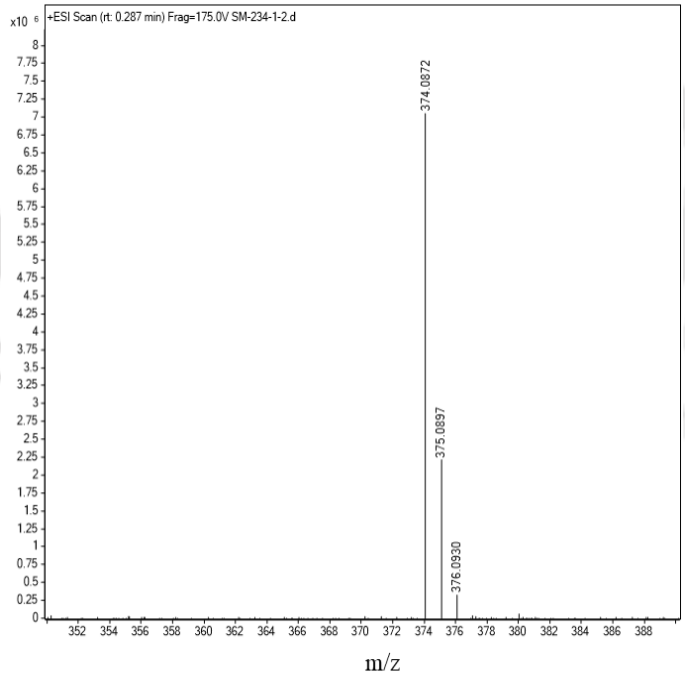

Fig. A3 Mass spectrum of **L3**.

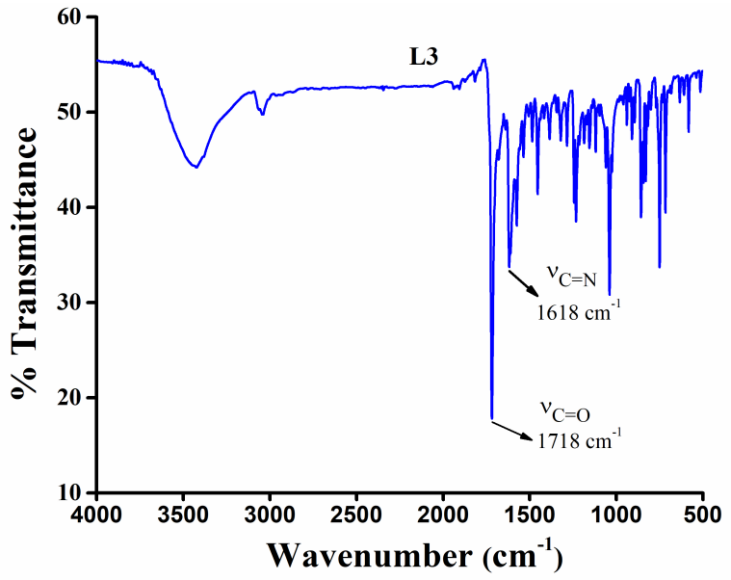

Fig. A4 IR spectra of **L3**.

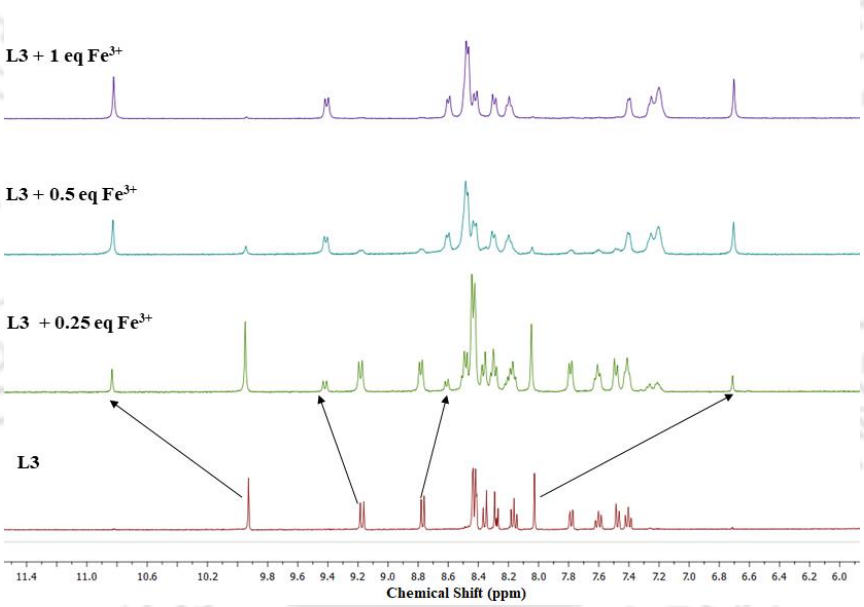

Fig. A5 ^{1}H NMR titration of **L3** with Fe^{3+}

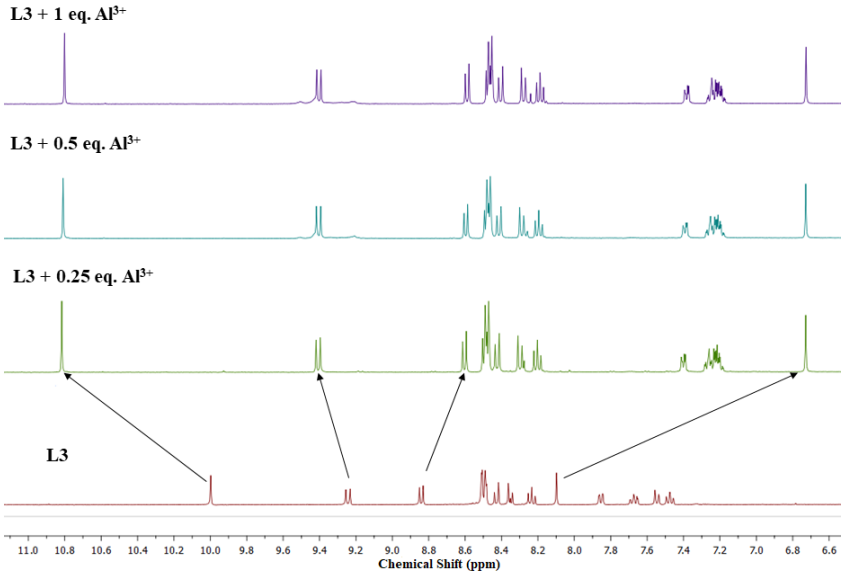

Fig. A6 ^{1}H NMR titration of **L3** with Al^{3+}

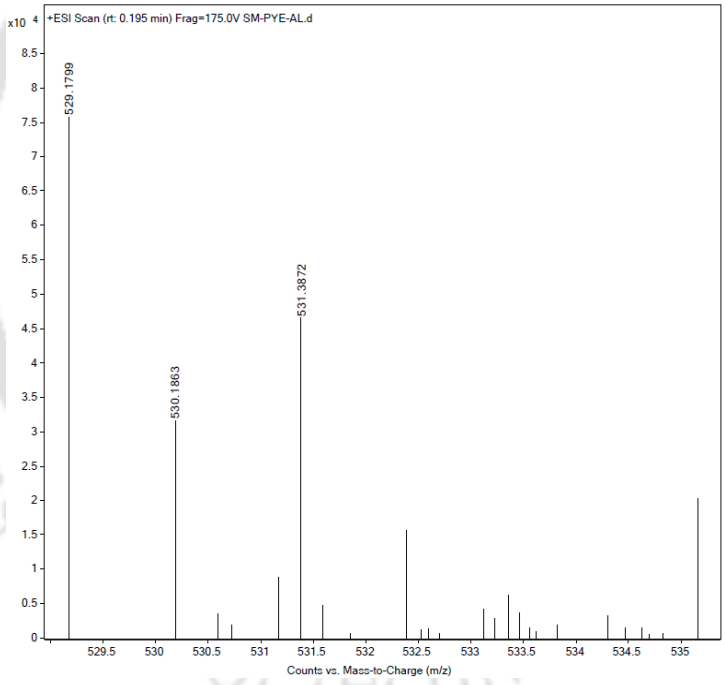

Fig. A7 Mass spectrum of $[Al(\mathbf{L3})Cl_2(H_2O)(CH_3CN)]^+$ complex ion.

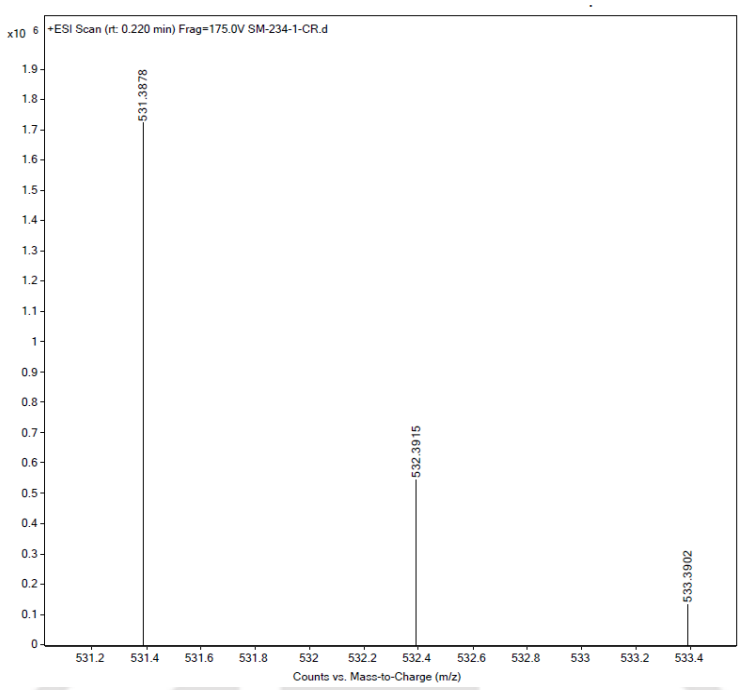

Fig. A8 Mass spectrum of $[Cr(\mathbf{L3})Cl_2(H_2O)_2]^+$ complex ion.

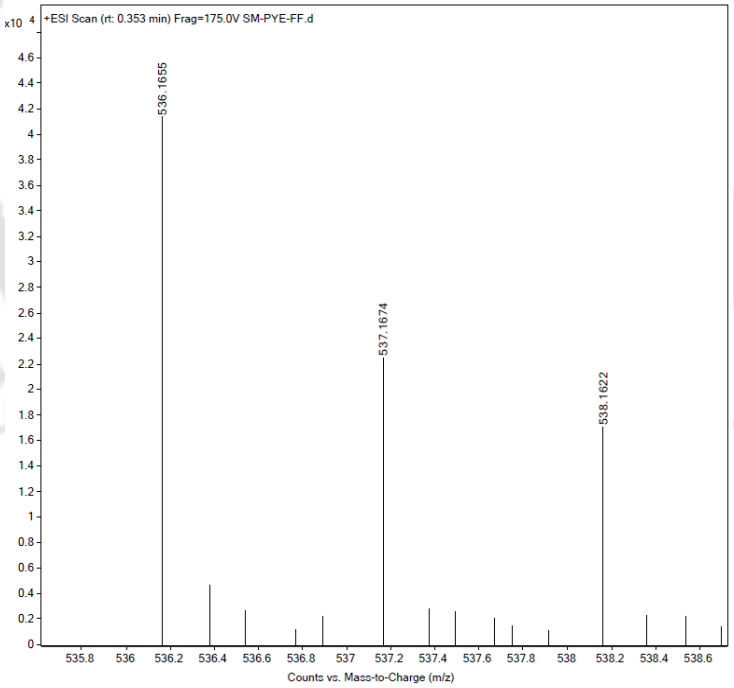

Fig. A9 Mass spectrum of $[Fe(\mathbf{L3})Cl_2(H_2O)_2]$ complex.

Table A1 Comparison of **L3** with some reported probes.

Probe	Solvent	LOD	K_a	Ref.
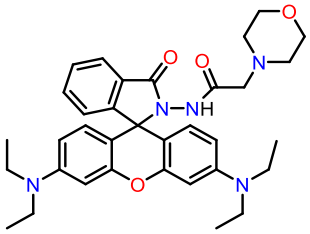	CH_3OH/H_2O (8:2, *v/v*, Tris 10 mM, pH 7.4)	2.7×10^{-3} M (Al^{3+}) 3.5×10^{-3} M (Cr^{3+}) 1.9×10^{-3} M (Fe^{3+})	3.3×10^4 M^{-1} (Al^{3+}) 3.7×10^4 M^{-1} (Cr^{3+}) 4.3×10^4 M^{-1} (Fe^{3+})	52
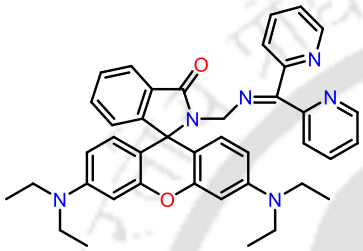	$EtOH/H_2O$ (1:1, *v/v*)	1.17 μM (Al^{3+}), 2.50 μM (Fe^{3+}) 3.16 μM (Cr^{3+})	1.42×10^3 M^{-1} (Fe^{3+}), 3.88×10^3 M^{-1} (Al^{3+}) 9.16×10^3 M^{-1} (Cr^{3+}).	55
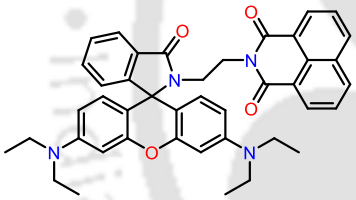	$CH_3OH–H_2O$ (6:4, *v/v*) pH = 7.1, 20 mM HEPES buffer	1.74 nM (Al^{3+}), 2.36 μM (Cr^{3+}) 2.90 μM (Fe^{3+})	1×10^4 M^{-1} (Al^{3+}) 2.6×10^2 M^{-1} (Cr^{3+}) 1.2×10^2 M^{-1} (Fe^{3+})	58
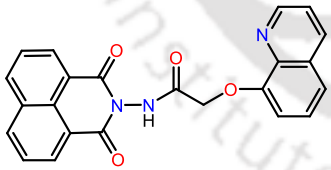	CH_3CN–HEPES buffer(4/6,*v/v*)	23 μM (Al^{3+}) 20 μM (Fe^{3+}) 25 μM (Cr^{3+})	8.77×10^4 M^{-1} (Al^{3+}) 1.08×10^4 M^{-1} (Fe^{3+}) 5.67×10^4 M^{-1} (Cr^{3+})	68
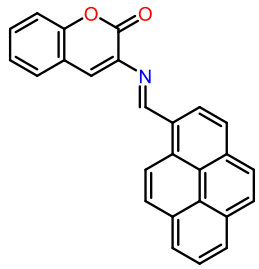	$MeOH/H_2O$ (6:4, *v/v*, pH=7.4, 10 mM HEPES buffer)	0.79 nM (Al^{3+}) 1.15 μM (Cr^{3+}) 1.28 μM (Fe^{3+})	7.3×10^4 M^{-1} (Al^{3+}) 2.8×10^4 M^{-1} (Cr^{3+}) 1.1×10^5 M^{-1} (Fe^{3+})	This Work

Chapter 5

A probe with Hydrazinecarbothioamide and 1,8-Naphthalimide Groups for "*Turn-On*" Fluorescence Detection of Hg^{2+} and Ag^{+} Ions and Live-Cell Imaging Studies*

Abstract:

The probe (**L4**) having hydrazinecarbothioamide and 1,8-naphthalimide moieties was synthesized and evaluated for its metal ion sensing ability. It exhibits a selective and sensitive colorimetric as well as fluorescent recognition of Hg^{2+} and Ag^{+} ions in CH_3OH - HEPES buffer solution (5 mM, 7:3, *v/v*, pH = 7.4) in presence of other metal ions. Probe **L4** is weakly fluorescent upon excitation with 410 nm light, but after gradual addition of $HgCl_2$ and $AgNO_3$ enhancement in fluorescent intensity was observed. Detection limits of Hg^{2+} and Ag^{+} using **L4** have been found to be 20 nM (Hg^{2+}) and 40 nM (Ag^{+}) over the pH range of 6 – 10 that is suitable for practical application under physiological pH conditions. The reversibility of interaction of **L4** with Hg^{2+} ion was monitored using Na_2EDTA by emission titration. The *"OFF-ON''* fluorescence switching can be observed with naked eye, in which fluorescent "*OFF*'' is due to operation of PET process in free **L4**. Whereas upon complexation with these two metal ions, PET is restricted and CHEF process becomes operational. Mass spectral analysis and Job's plot yielded a binding ratio of 1:1 for both metal ions. ^1H NMR titration studies are consistent with binding of Hg^{2+} or Ag^{+} to NH group (attached with naphthalimide moiety) and sulfur atom of hydrazinecarbothioamide group. From cytotoxicity assay, 5 μM solution of **L4** was considered in cellular imaging study and the potentiality of the probe **L4** was established by using human breast cancer cell line (MDA-MB-231) and primary human dermal fibroblasts (HDF), through fluorescence cell imaging experiments for tracking both Hg^{2+} and Ag^{+} in living cells.

---

*This work has been published in:

S. Mahata, S. Kumar, S. Dey, B. B. Mandal and V. Manivannan, *Inorg. Chim. Acta*, 2022, **535**, 120876.

5.1. Introduction

Selective detection of heavy transition metal ions using colorimetric and fluorescence chemosensors continue to gain more significance.[1-3] Accumulation of heavy metal ions, in living organisms is undesirable as they can be toxic and carcinogenic.[4] Among them Hg^{2+} and Ag^{+} ions are common hazards as they create long-term adverse effects on liver, kidney and central nervous system.[5,6] Mercury is notorious, which is believed to be the cause of Minamata disease.[7,8] High exposure of mercury creates adverse effect on the health causing kidney dysfunction, prenatal brain damage as well as cognitive and motion disorders.[9-11]. The permissible concentration of Hg^{2+} ion in drinking water is 2 $\mu g.L^{-1}$ set by the US Environmental Protection Agency.[12]

Excessive utilization of silver in industry, photographic production, manufacturing of fungicides, electronic and electrical accessories enhances the silver content in environmental systems.[13] Excess silver ion also has an adverse effect on health due to its ability to inactivate the sulfhydryl group and also combine with imidazole, amine and carboxyl groups of various high molecular weight protein and metallothioneins.[14-16] For drinking water, the maximum acceptable concentration of Ag^{+} ion is 0.5 μM given by World Health Organisation (WHO).[17]

Conventional methods like inductively coupled plasma mass spectrometry (ICP-MS), atomic emission spectrometry, atomic absorption spectrometry (AAS), fluorescence anisotropy assays, polarography method, quantum dot based assays, inductively coupled plasma atomic emission spectrometry (ICP-AES) and electrochemical method, can be utilized for the detection of Hg^{2+} and Ag^{+} ions.[18-21] But drawbacks like high cost, time-consuming detection process and need of proper experts to handle the instruments, make them difficult to avail within limited resource setting. In comparison fluorescence based analytical techniques are popular due to high sensitivity, simplicity, facile sample preparation, low cost and rapid detection.[22-30] Most of the reported fluorescence based sensors towards detection of Hg^{2+} and Ag^{+} ions are based on fluorescence quenching mechanism as both Hg^{2+} and Ag^{+} are known fluorescence quenchers.[31-34] Most of the previously reported probes are selective towards either Hg^{2+} or Ag^{+} (Table A1) through fluorescence "*turn on*" or *"turn off"* response along with some drawbacks like higher value of detection limit and interference from other transition metal ions. A probe containing coumarin moiety combined with an N′-acetyl thioureido group was developed as a fluorescence switch for the detection of Hg^{2+} and Ag^{+}

which function through the desulfurization process.[43] For selective dual detection of Ag^{+} and Hg^{2+} ions, a bifunctional supramolecular pseudorotaxane chemosensor,[44] a cholesterol appended 4-hydroxybenzaldehyde derived Schiff base involving sol–gel technique,[45] bis-BODIPY linked-triazole based on catechol core[46] were reported in the literature. Thus need for "*turn-on*" chemosensor for the selective detection of Hg^{2+} and Ag^{+} ions, still persists.

Fluorescent probes bearing the naphthalimide group as fluorophore have been widely used due to its high fluorescence quantum yield, photostability, large stokes shift and high absorption coefficient.[47,48] Since both Hg^{2+} and Ag^{+} ions are soft Lewis acids in nature and hence presence of soft sulfur-containing group at the metal binding site will function well for their recognition. Combining these aspects, this Chapter describes a hydrazinecarbothioamide appended napthalimide probe for the detection of Hg^{2+} and Ag^{+} ions.

5.2. Experimental section:

5.2.1. Cell Studies

5.2.1.1. Cell culture

The probe **L4** was evaluated as a fluorescent probe for the detection of Hg^{2+} and Ag^{+} through *in vitro* cell studies using human triple-negative breast carcinoma cells (MDA-MB-231) and primary human dermal fibroblasts (HDF). MDA-MB-231 cells were procured from National Centre for Cell Science, India and HDF cells were procured from HiMedia Laboratories, India. Both MDA-MB-231 and HDF cells were cultured and maintained in high glucose Dulbecco's modified Eagle's medium (hDMEM, Thermo Fisher, USA) supplemented with 10% (v/v) fetal bovine serum (FBS), 100 $\mu g.mL^{-1}$ streptomycin and 100 $IU.mL^{-1}$ penicillin at 37 °C in a humidified incubator with 5% CO_2.

5.2.1.2. Cytotoxicity studies

To evaluate the cytotoxicity of probe **L4** on MDA-MB-231 and HDF cells, MTT (3-(4,5-dimethylthiazol-2-yl)-2,5-diphenyl tetrazolium bromide) assay was performed.[28,51] Both MDA-MB-231 and HDF cells were seeded in a 96-well plate at a density of 5×10^3 cells per well and cultured for 24 h before cytotoxicity evaluation at 37 °C in a humidified incubator with 5% CO_2. Both cell types were then treated with an increasing concentration of **L4** at 0, 1.25, 2.5, 5, 7.5 and 10 μM for 24 h followed by addition of MTT reagent at 0.5 $mg.mL^{-1}$ for 4 h to check the cytotoxicity. Thereafter, the formazan crystals formed were dissolved in 100 μL of dimethyl sulfoxide (Sigma-Aldrich, USA) and the absorbance was taken at 570 nm

using the Multiskan Multiplate Reader (Thermo Scientific, USA). From the data obtained, the percentage of cell viability was determined relative to the control group (consisting of only media).

5.2.1.3. Fluorescence imaging

Based on the MTT assay, 5 μM **L4** was considered to evaluate the fluorescence property of probe **L4** alone and probe **L4** with Hg^{2+} or Ag^{+} against MDA-MB-231 and HDF cells. Both cell types were seeded in a 24-well plate at a density of 2 x 10^4 cells per well and maintained for 24 h at 37 °C in a humidified incubator with 5% CO_2. Post 24 h, cells were treated with 5 μM **L4** alone for 40 min and 5 μM **L4** with 0.5 μM Hg^{2+} or 0.5 μM Ag^{+} for 30 min. After incubation, the cells were washed thrice with PBS (phosphate buffered saline, pH 7.4) and images were taken using a fluorescence microscopy (EVOS, Life Technologies).

5.2.1.4. Statistical anal*ysis*

All the experimental studies were performed in n = 4 samples and the results are represented as mean ± standard deviation. Statistical analysis of data was performed following one-way analysis of variance (ANOVA) using OriginPro software (Originlab Corporation, USA). ImageJ analysis software (NIH, USA) was used for processing the fluorescence images. Differences of * $p \leq 0.05$, ** $p \leq 0.01$ and $^{\#}$ $p \leq 0.001$ between groups were considered to be statistically significant.

Compounds **1** and **2** were prepared by following reported procedures.[49]

5.2.2. Synthesis of 2-(2-(2-hydroxyethyl)-1,3-dioxo-2,3-dihydro-1*H*-benzo[*d,e*]isoquinolin-6-yl)-*N*-(naphthalen-1-yl)hydrazine-1-carbothioamide (**L4**)

Acetonitrile solution (25 ml) of naphthylisothiocyanate (0.151g, 0.811 mmol) was added drop wise to **2** (0.200g, 0.738 mmol) dissolved in acetonitrile (25 ml). The resulting mixture was stirred under reflux (82 °C) for 72 h, and then the solution was allowed to cool to room temperature. Precipitate of **L4** that was deposited as a yellowish green solid was collected by filtration, washed thoroughly with ice-cold CH_3CN and dried in vacuum. Yield 0.287g (85%). (HRMS) ESI-MS (+): *m/z* calcd. for {$[C_{25}H_{20}N_4O_3S]^+$ + H} 457.1329 found (M^+ + H) 457.1335. 600 MHz, ^{1}H NMR: (δ (J, Hz), DMSO-d_6) : 10.38 (1H, s, NH), 10.27 (1H, s, NH), 10.07 (1H, s, NH), 8.73 (1H, d, 9, ArH), 8.54 – 8.49 (2H, m, ArH), 7.94 – 7.92 (1H, m, ArH), 7.86 – 7.77 (3H, m, ArH), 7.53-7.49 (3H, m, ArH), 7.37 (1H, d, 7.2, ArH), 7.18 (1H, d, 8.4, ArH), 4.85 (1H, s, broad, OH), 4.15 (2H, t, 6.6, CH_2), 3.63 – 3.60 (2H, m, CH_2). 150 MHz

^{13}C NMR (δ, DMSO-d_6) : 183.4 (1C, *C*=S), 164.3, 163.6 (2C, *C*=O), 150.4, 136.0 (2C, Ar*C*-NH), 134.2, 134.1, 131.3, 131.0, 129.9, 129.5, 128.4, 127.4, 127.0, 126.4, 126.4, 125.9, 125.2, 123.9, 122.3, 119.9, 112.0, 105.7 (18C, Ar*C*), 58.4 (1C, *C*H_2), 42.0 (1C, *C*H_2).

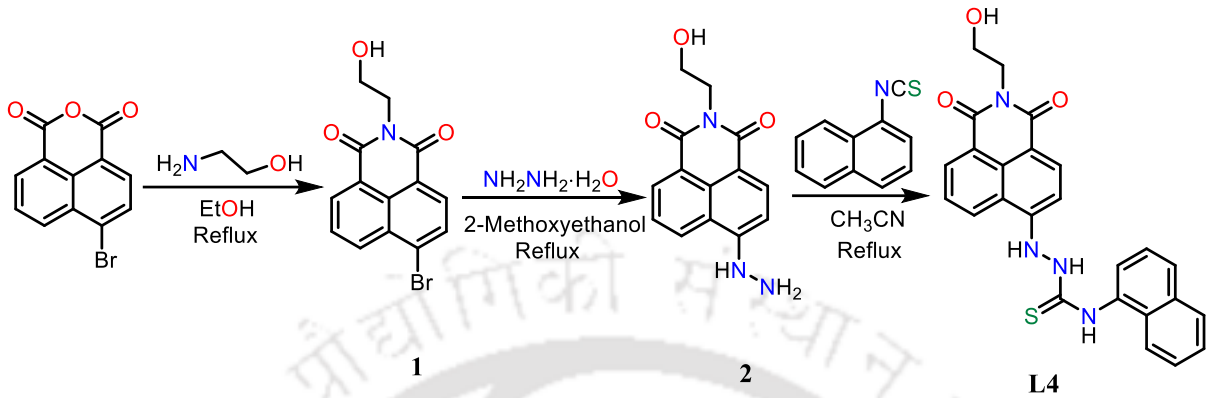

Scheme 1 Synthesis of probe **L4**.

5.3. Results and discussion

5.3.1. Synthesis and characterization

Probe **L4** has been synthesised by nucleophilic addition of **2** to 1-naphthylisothiocyanate (Scheme 1) and has been characterized unequivocally (Fig. A1–A3). This probe contains the fluorophore in the form for naphthalimide moiety and metal ion binding site as hydrazinecarbothioamide group. ESI mass spectrum showed the M^+ + H *m/z* peak at 457.134, consistent with the expected value of 456.126 for **L4**. The ^{1}H-NMR spectrum of **L4** contains signals at 10.38, 10.27, and 10.07 ppm, assignable to protons of three different N–H groups present in hydrazinecarbothioamide group, labelled as *a*, *b* and *c* respectively. A doublet at 8.73 ppm (*g*) and a pair of doublets closer together at 8.54 – 8.49 ppm are due to protons *h* and *q* of naphthalimide and naphthyl rings, respectively. A multiplet at 7.94 – 7.92 ppm is due to one proton of naphthalimide ring (*i*) and multiplet signal at 7.86 – 7.77 ppm is due to a proton from naphthalimide unit (*k*) and two from naphthyl ring (*l* and *o*). Another multiplet at 7.53-7.49 ppm is due to three protons present in naphthyl ring (*m*, *n* and *p*). Two doublets appearing at 7.37 and 7.18 ppm are due one proton of naphthalimide ring (*j*) and another of naphthyl ring (*r*) respectively. Signal of proton in –OH group appear as a broad singlet at 4.85 ppm. The triplet at 4.15 ppm corresponds to CH_2 protons (*f*) and a multiplet at 3.63 – 3.60 ppm to CH_2 proton (*e*). Notable signals in the ^{13}C NMR spectrum of **L4** are: thiourea (C=S) carbon at 183.41 ppm; carbon of C=O groups at 164.28 and 163.62 ppm; carbon of naphthalimide at 150.40 (bonded to –NH) and carbon of napthyl ring (bonded to –NH) at

136.04 ppm. Signals in the range 134.22 – 105.69 ppm are due to 18 aromatic carbons. Two signals due to aliphatic carbon at 58.38 and 42.03 ppm are also present.

5.3.2. UV –vis absorption study of L4 with various metal ions

We have examined the electronic absorption spectral characteristics of **L4** in presence of various metal ions in CH_3OH - HEPES buffer solution (5 mM, 7:3, *v/v*, pH = 7.4). The probe **L4** has an absorption band with a maximum at 410 nm. During addition of up to two equivalents of chloride salts of Li^+, Na^+, K^+, Ca^{2+}, Mg^{2+}, Al^{3+}, Cr^{3+}, Mn^{2+}, Fe^{2+}, Co^{2+}, Ni^{2+}, Cu^{2+}, Zn^{2+}, Cd^{2+}, Pb^{2+}, Pd^{2+}, Pt^{2+}, Au^{3+} and Fe^{3+} ions to **L4**, the intensity of band at 410 nm remained unchanged or with slight variations (Fig. 1).

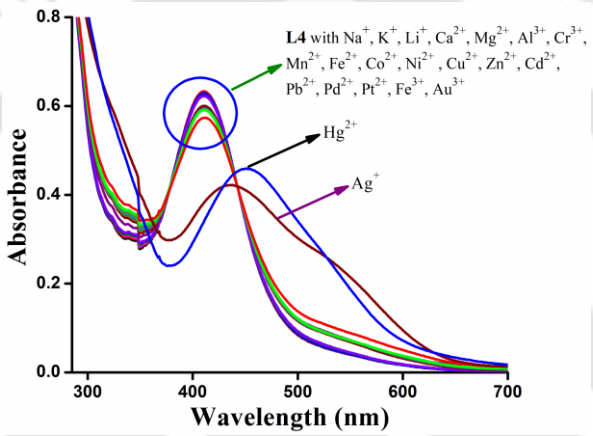

Fig. 1 Absorption spectra of **L4** (2.0×10^{-5} M) in presence of metal ions.

However, upon gradual addition of $HgCl_2$ into **L4** solution, the intensity of peak at 410 nm slowly diminished and a new peak at 452 nm appeared along with an isosbestic points at 446 nm. The same decrease in intensity of 410 nm was also observed with $AgNO_3$ but two new peaks at 432 and 528 nm appeared along with the isosbestic point at 442 nm (Fig. 2). Presence of an isosbestic point in both indicates that only two species *viz.*, **L4** and **L4** bound to Hg^{2+} / Ag^+ are taking part during the titration experiment. A remarkable colour change from the initial yellowish-green to reddish-brown (for $HgCl_2$) and brown (for $AgNO_3$) can be observed through naked eye (Fig. A4). These colour change also confirm the red shift in the absorption band. So we can say that **L4** enables visual detection of Hg^{2+} and Ag^+ salts in solutions. It is also pertinent that such red shift was not observed with other metal ions.

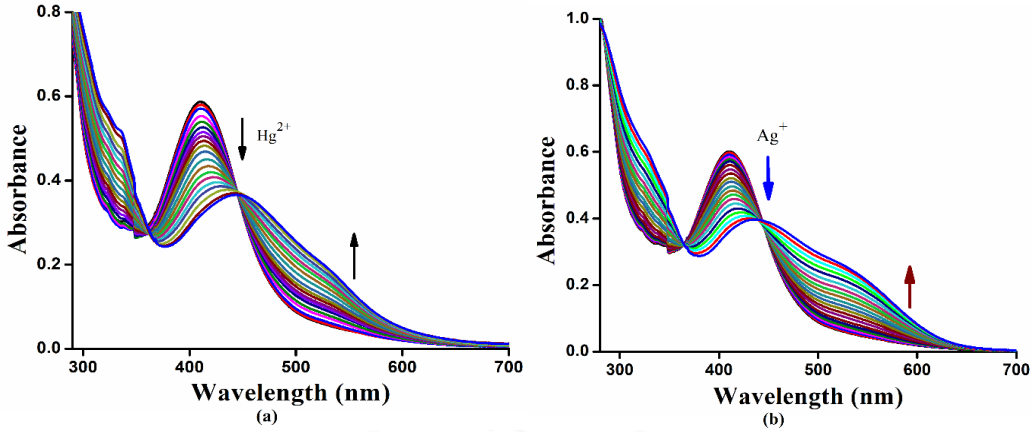

Fig. 2 Absorption spectra upon gradual addition of $HgCl_2$ (2.3×10^{-5} M) and $AgNO_3$ (2.1×10^{-5} M) into **L4** (2.0×10^{-5} M) in CH_3OH - HEPES buffer solution (5 mM, 7:3, *v/v*, pH = 7.4).

5.3.3. Emission spectroscopic studies of L4 with various metal ions

Upon exciting with 410 nm light, **L4** exhibited a weak fluorescence with an emission peak at 529 nm and its fluorescent behaviour has been examined by titration with various metal ions. It was observed that there was no (or a subtle) change in emission properties of **L4** when titrated with Li^+, Na^+, K^+, Ca^{2+}, Mg^{2+}, Al^{3+}, Cr^{3+}, Mn^{2+}, Fe^{2+}, Co^{2+}, Ni^{2+}, Cu^{2+}, Zn^{2+}, Cd^{2+}, Pb^{2+}, Pd^{2+}, Pt^{2+}, Au^{3+} and Fe^{3+}. However, both Hg^{2+} and Ag^+ ions displayed a dramatic increase in fluorescence intensity (Fig. 3).

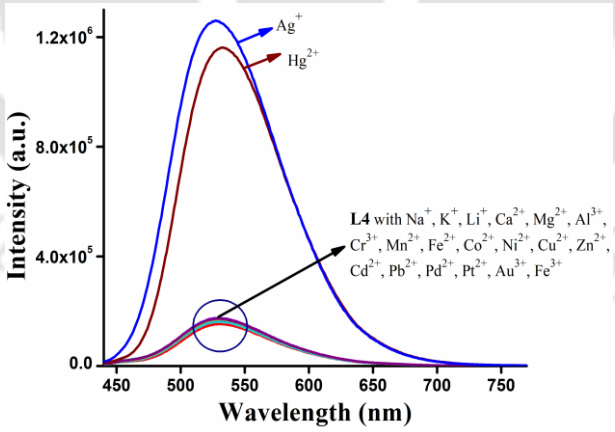

Fig. 3 Emission spectra of **L4** (2.0×10^{-5} M) in presence of various metal ions.

With incremental addition of Hg^{2+} to **L4**, fluorescence intensity increased gradually and emission peak got shifted to 533 nm thereby imparting a yellowish-green fluorescent color. Similarly, after addition of Ag^+ into **L4** solution fluorescence intensity increased and emission peak shifted slightly to 527 nm along with an orange fluorescence (Fig. 4).

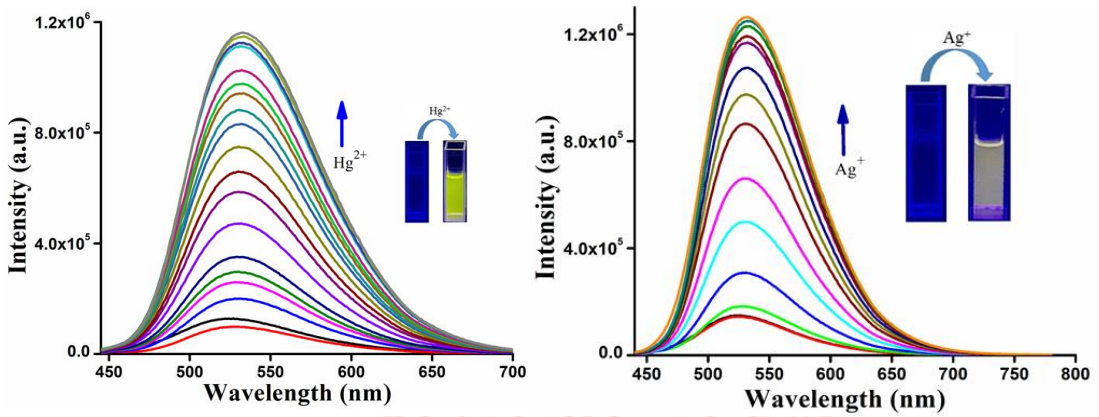

Fig. 4 Changes in emission characteristics of **L4** (2.0×10^{-5} M) during gradual addition of (left) $HgCl_2$ (2.3×10^{-5} M) and (right) $AgNO_3$ (2.1×10^{-5} M) solution.

In the typical metal ion competition study, **L4** was first treated (Fig. 5) with same equivalent of a competing metal ion and then with Hg^{2+}or Ag^{+} ion, respectively. It was observed that emission intensity of **L4** got enhanced after the addition of Hg^{2+} and Ag^{+} even in the presence of different metal ions. Therefore, **L4** is an efficient fluorescence sensor for the detection of Hg^{2+} and Ag^{+} ions even in the existence of other metal ions with excess amount (10 equivalent) in the same sample solution.

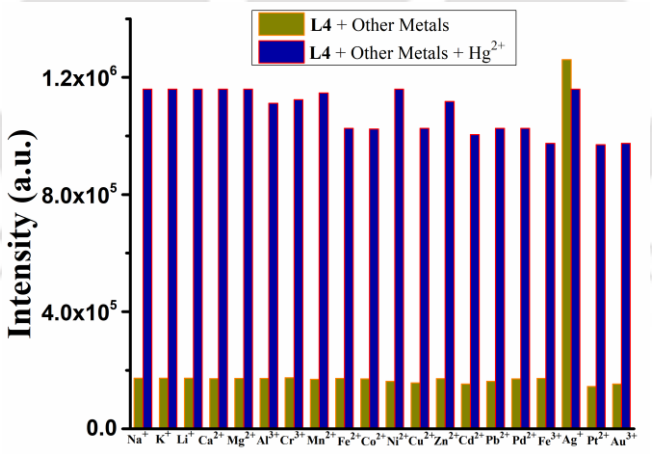

(a)

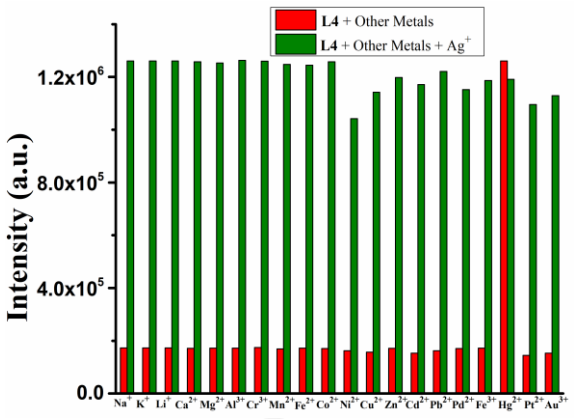

(b)

Fig. 5 Bar diagram for metal ion competition experiment showing the effect on fluorescence intensity of **L4**.

The pH dependence study was performed to check the utility of **L4** as a chemosensor for the selective detection of $Hg^{2+}$and Ag^{+} ions in the physiological pH. Typically, emission intensity of **L4** was recorded in absence and presence of Hg^{2+} and Ag^{+} ions separately, in the range 2 – 12, by adjusting pH using dilute HCl or NaOH solutions. Upon addition of $HgCl_2$ the emission intensity of **L4** began to increase with a plateau from 6 – 9 (Fig. 6), indicating the viable pH range as 6 – 9, for detecting Hg^{2+} ion efficiently. Similarly, for the addition of $AgNO_3$, emission intensity increased gradually from 6 with a maximum at 9 and hence the optimum pH range was observed to be that is 6 – 9 (Fig. 6). So, from this pH dependence study it was observed that the emission intensity remained stable over the pH range of 6 – 9 that is suitable for practical application under physiological pH conditions.

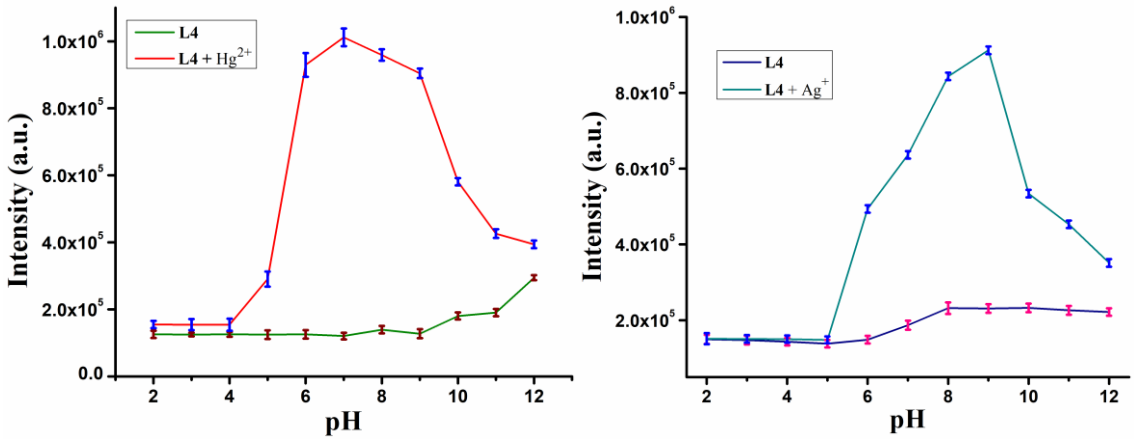

(a) (b)

Fig. 6 Luminescence spectroscopy results pH dependence profile for detection of Hg^{2+} and Ag^{+} ion.

Fluorescent solutions of Hg^{2+} and Ag^{+} bound **L4** were also examined for interference of anions such as F^{-}, Cl^{-}, Br^{-}, I^{-}, CN^{-}, SCN^{-}, HSO_4^{-}, $H_2PO_4^{-}$, HPO_4^{2-}, CO_3^{2-}, HCO_3^{-}, PO_4^{3-}, S^{2-}, $S_2O_3^{2-}$, NO_3^{-}, SO_4^{2-}, AcO^{-}, $P_2O_7^{4-}$, ClO_4^{-} and $C_2O_4^{2-}$ by titrating with respective salt solutions (Fig. 7). It has been seen that above-mentioned anions show no interference effect towards detection of Hg^{2+} and Ag^{+} ion using **L4**.

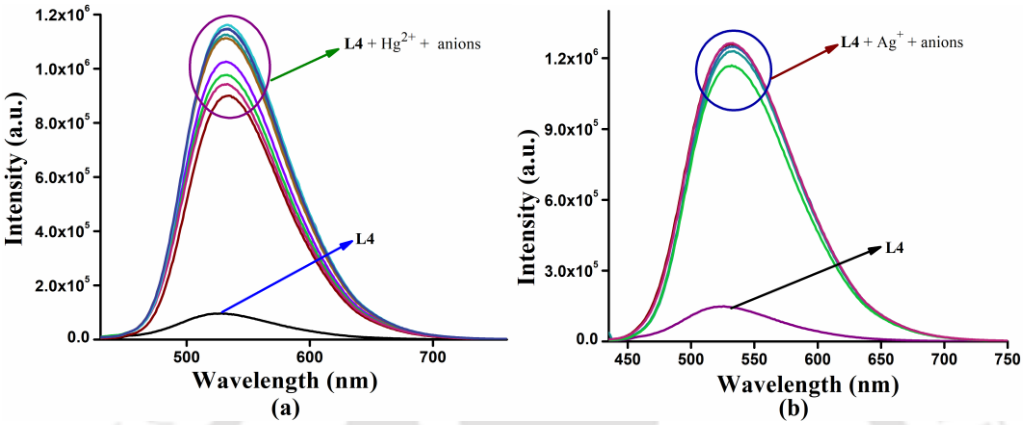

Fig. 7 Anion interference study towards (a) **L4**-Hg^{2+} (1.0×10^{-5} M) and (b) **L4**-Ag^{+} (1.5×10^{-5} M) upon addition of 50 equivalent of the anions.

Reversibility of interaction of **L4** with Hg^{2+} ion was monitored using Na_2EDTA by emission titration (Fig. 8). Emission intensity at 529 nm was lost after addition of equimolar amount Na_2EDTA solution into Hg^{2+} bound **L4**. This has been observed several times by sequential alternate addition of Hg^{2+} and Na_2EDTA solutions to **L4**. Thus the reusability of **L4** was established towards Hg^{2+} detection. In contrast, Ag^{+} emission intensity was not affected after addition of equimolar amount of Na_2EDTA solution into **L4**-Ag^{+}, indicating that Ag^{+} was not sequestered by $EDTA^{4-}$ ion and binding of Ag^{+} ion with **L4** was intact. Thus probe **L4** by virtue of having a soft sulfur donor atom at the metal-binding site, firmly binds the soft metal ion Ag^{+} ion.

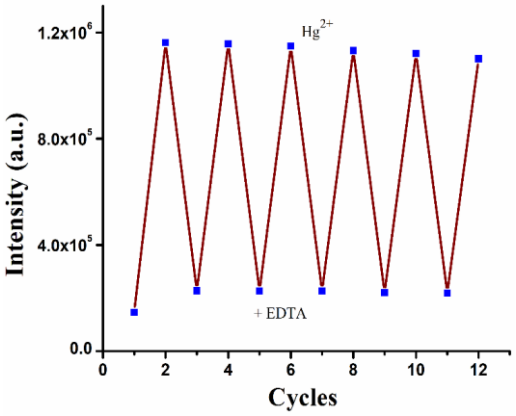

Fig. 8 Reversibility study for detection of Hg^{2+} ion with **L4**.

In order to evaluate the practical utility of **L4** for detection of Hg^{2+} and Ag^{+} ions, emission titration experiments were performed using real water samples. Samples of drinking water and tap water were collected from the institute and that of river water was collected from Brahmaputra (near IIT Guwahati campus, Assam, India). By using 0.22 μM membrane filter paper all the water samples were filtered and their pH was adjusted to 7.4. A blank experiment was performed to check the presence of these two ions in these water samples and found to be was negative. Hg^{2+} and Ag^{+} ion solutions were prepared using these real water samples for titration studies. From emission intensity *vs* Hg^{2+} and Ag^{+} ion concentration plot (Fig. A5), it was observed that emission intensity increased within one-minute thus confirming the usability of **L4** for detecting Hg^{2+} and Ag^{+} in real water samples.

5.3.4. Spectra

Comparing IR spectra of **L4** with solid obtained after treating **L4** with $HgCl_2$ and $AgNO_3$ indicated shifts in characteristic stretching frequencies of the secondary amine (ν_{N-H}) from 3468, 3360, 3233 (in **L4**) to 3425, 3329, 3201 (in **L4** + $HgCl_2$) and 3432, 3335, 3220 cm^{-1} (in **L4** + $AgNO_3$) (Fig. 9). Also in case of NH linked thiocarbonyl group, a strong vibrational coupling becomes operative and three bands consistently appeared in the regions 1395-1570, 1260-1420 and 940-1140 cm^{-1}.[50] These three bands are designated as "HN–C=S I, II and III bands" respectively. These I, II and III bands appeared at 1571, 1382, 1072 cm^{-1} in **L4** got shifted to 1590, 1388, 1050 cm^{-1} (in **L4** + $HgCl_2$) and 1593, 1375, 1051 cm^{-1} (in **L4** + $AgNO_3$). These shifts in stretching frequencies indicate binding of Hg^{2+} and Ag^{+} ions with –NH and C=S group present in **L4**.

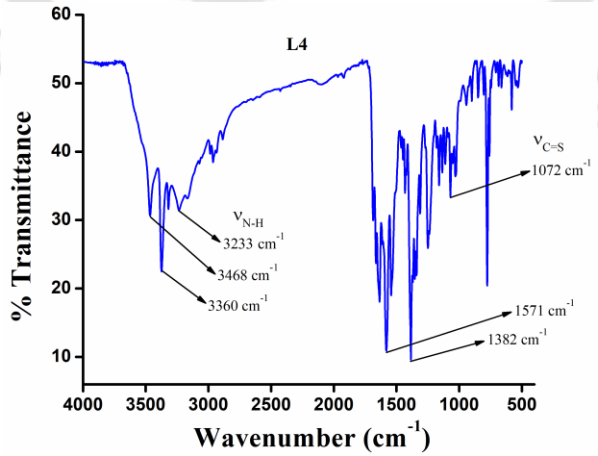

(a)

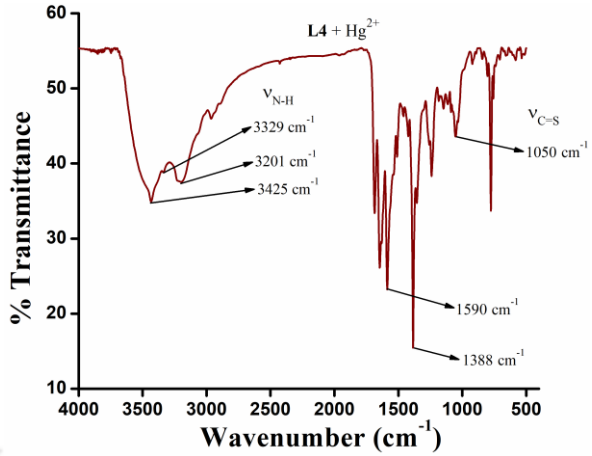

(b)

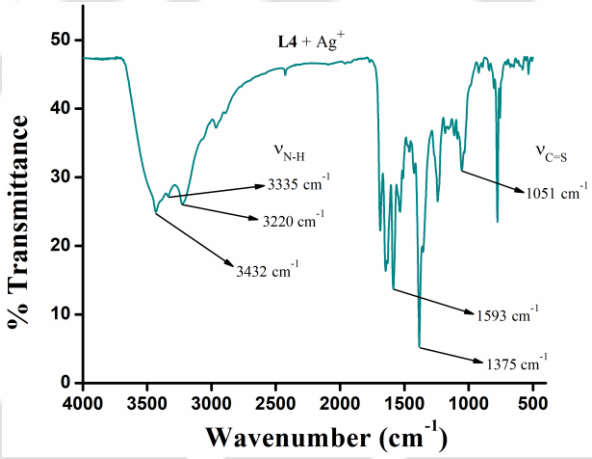

(c)

Fig. 9 IR spectra of (a) **L4**, (b) **L4** + $HgCl_2$ and (c) **L4** + $AgNO_3$.

Interaction between **L4** with Hg^{2+} and Ag^{+} ions have been followed by ^{1}H NMR titration experiments. Upon addition of 1 equivalent of $HgCl_2$ into DMSO-d_6 solution of **L4**, three singlet signals due to NH proton at 10.38 (*a*), 10.26 (*b*) and 10.06 (*c*) ppm exhibited a downfield shift to 11.30, 11.12 and 10.29 ppm, respectively along with broadening of the peaks. Other signals in the aromatic region 8.72 – 7.17 ppm broadened during the course of incremental addition of mercuric chloride salt (Fig. 10a).

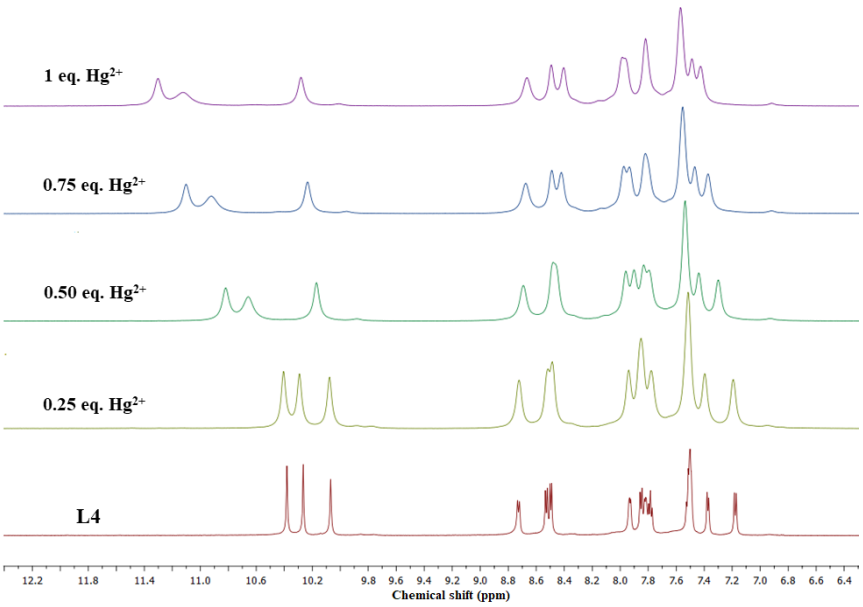

(a)

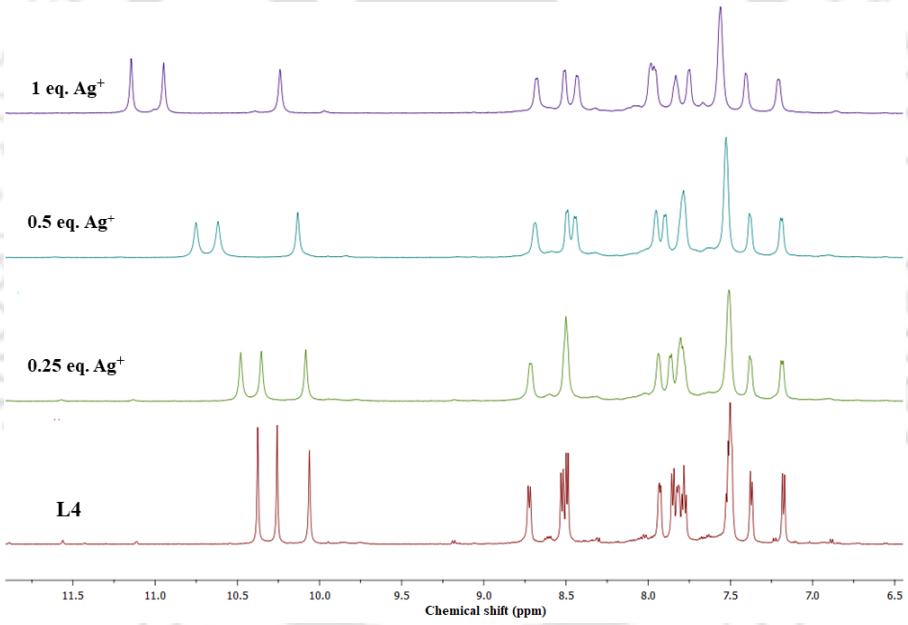

(b)

Fig. 10 ^{1}H NMR titration study upon addition of (a) $HgCl_2$ and (b) $AgNO_3$ into **L4** solution in DMSO-d_6.

Similar changes were observed during gradual addition of one equivalent $AgNO_3$ into **L4** in DMSO-d_6. Singlet peaks at 10.38 (*a*), 10.26 (*b*) and 10.06 (*c*) shifted downfield to 11.23, 10.94 and 10.30 ppm, respectively. Notably, NH proton of **L4** gets deprotonated in presence Hg(II) ion, due to Lewis acidic nature of Hg(II) ion. But in case of Ag(I)-based titration (Fig. 10b) such broadening of NH peaks were not observed may be due to poor Lewis acidic nature of Ag(I) compared to Hg(II). Other signals broadened gradually with gradual addition of

$AgNO_3$ (Fig. 10). There are consistent with binding of Hg^{2+} or Ag^{+} to NH group (attached with naphthalimide moiety) and sulphur atom of hydrazinecarbothioamide group (Scheme 2).

5.4. Binding ratio

The binding ratio between **L4** and these two metal ions was calculated to be 1:1 ratio using Job's plot (Fig. 11). The calculated binding constants are 1.9 $\times 10^5$ M^{-1} and 0.9 $\times$ $10^5 M^{-1}$ for Hg^{2+} and Ag^{+} respectively (Fig. A6). This 1:1 complex formation was also confirmed (Fig. A7) by ESI-mass spectral analysis. The molecular ion peak for the formula [Hg(**L4**)Cl]$^{+}$.is expected at *m*/*z* = 693.065 (for $^{202}Hg^{35}ClC_{25}H_{20}N_4O_3S$) but it was observed at *m*/*z* = 691.067. This indicates a loss of two hydrogen atoms ($^{202}Hg^{35}ClC_{25}H_{18}N_4O_3S$ = 691.045) and probably the hydrazinecarbothioamide moiety in **L4** might have converted to diazenecarbothioamide group under the conditions of ESI(+) mode of analysis only. The *m*/*z* peak at 563.038 (calculated for $AgC_{25}H_{20}N_4O_3S$ = 563.031) was fitting well with the formula [Ag(**L4**)]$^{+}$.

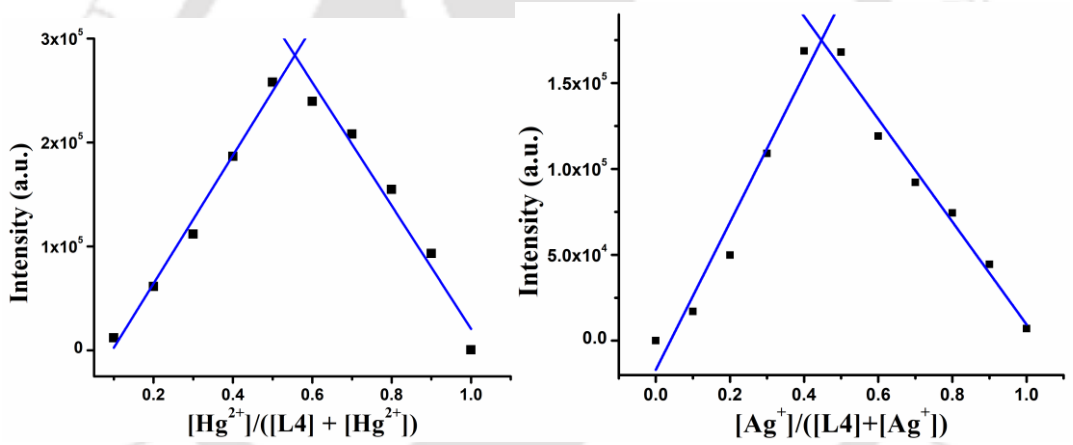

Fig. 11 Job's plots indicating 1:1 binding of **L4** with Hg^{2+} and Ag^{+}.

Limit of detection was obtained from the formula (3σ/k) by using the data from the fluorescence titration plot (Fig. A8). Detection limit was calculated to be 20 (Hg^{2+}) and 40 nM (Ag^{+}) using **L4**, which are less than many other reported probes (Table A1). Probe **L4** has a quantum yield value of 0.04 and which in presence of Hg^{2+} and Ag^{+} ion changed to 5.79 and 2.79 respectively.

5.5. Lifetime measurement

Using Time-Resolved Photoluminescence experiment, lifetimes of free **L4** and **L4** bound with Hg^{2+} and Ag^{+} ions were determined and lifetime decay curves are shown in Fig. 12. The

average life time (τ) of free **L4** was found to be 5.90 ns, which after addition of $HgCl_2$ and $AgNO_3$ (Table 1) changed to 6.29 and 5.98 ns, respectively. This result suggests that CHEF process became operational in probe after binding with Hg^{2+} or Ag^{+} which resulted in the small changing of life time of the emissive species compared to free **L4**. In the case free **L4**, fluorescence was not observed due to presence of active PET process and after binding with Hg^{2+} and Ag^{+} ion PET process was restricted and "*turn-on*" fluorescence signal was generated (Scheme 2).

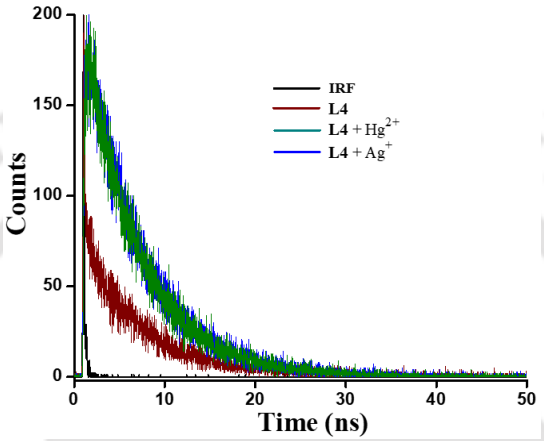

Fig. 12 Life time decay profile.

Table 1. Fluorescence decay parameters of **L4** and its complexes with Hg^{2+} and Ag^{+}.

Sample	τ(ns)	χ^2
L4	5.90	1.093
[Hg(**L4**)Cl_2] (**3**)	6.29	1.007
[Ag(**L4**)(NO_3)(H_2O)] (**4**)	5.98	1.002

5.6. Proposed sensing mechanism

After addition of Hg^{2+} and Ag^{+} salts into a solution of **L4**, fluorescence intensity increased due to restriction of PET (Photo induced electron transfer) (Scheme 2) and on set of CHEF processes. The PET process could occur involving the lone-pair of electron present in NH groups of hydrazinecarbothioamide unit and π* orbitals of carbonyl groups located in naphthalimide part of **L4**, which is responsible for the "*turn-off*" fluorescence signal in **L4**. Whereas after coordination with Hg^{2+} and Ag^{+} centers, lone-pair of electron in NH groups becomes unavailable thereby restricting PET process and CHEF (Chelation enhanced fluorescence) process getting activated and generating "*turn-on*" fluorescence signals.

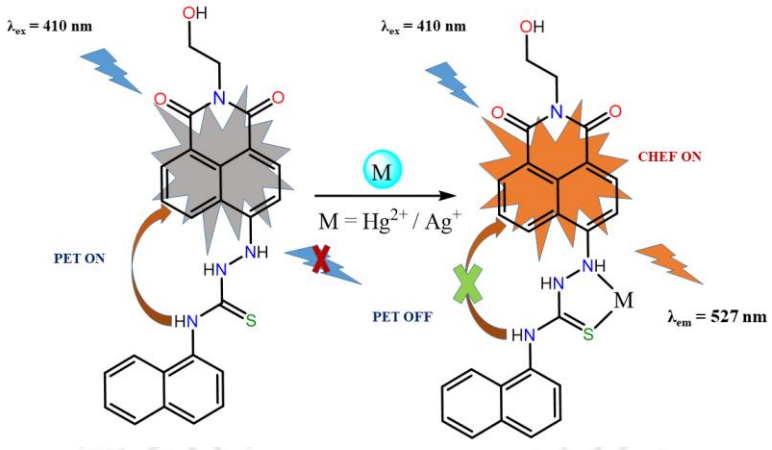

Scheme 2 Proposed binding mode of Hg^{2+} and Ag^{+} ions with **L4**.

5.7. Computational studies

The DFT/TDDFT calculations on **L4**, **L4**-Hg^{2+} and **L4**-Ag^{+} were carried out using Gaussian09 program to ascertain the binding mechanism. Both Job's plot and mass spectral analysis indicated the stoichiometric ratio as 1:1 between **L4** and Hg^{2+}/Ag^{+}, calculations were performed using this ratio. Both Hg^{2+} and Ag^{+} are d^{10} ions and are generally expected to have coordination number of 4 having a tetrahedral geometry. Thus, formulae [Hg(**L4**)Cl_2] (**3**) and [Ag(**L4**)(NO_3)(H_2O)] (**4**) were chosen for calculation purpose, with **L4** being coordinated through S and N atoms of hydrazinecarbothioamide moiety, forming a favourable 5-membered chelate ring. Structures were optimised using B3LYP/6-31G (d, p) for **L4** and CAM-B3LYP/LanL2DZ basis set for **3** and **4** (Fig. 13). The calculations were done based on the Gas-phase. The central metal ion in **3** and **4** has a distorted tetrahedral geometry. In HOMO of **L4**, electron density is located on hydrazinecarbothioamide and naphthalimide moieties, whereas in LUMO electron density is mainly located over naphthalimide ring. In HOMO of **3**, the electron density is localised on hydrazinecarbothioamide unit and naphthalimide ring, whereas in LUMO it is mainly located on mercury and naphthalimide ring (Fig. 14). In **4**, electron density in HOMO is spread mainly over naphthalimide moiety and silver. But in LUMO electron density is located on the naphthalimide ring (Fig. 15).

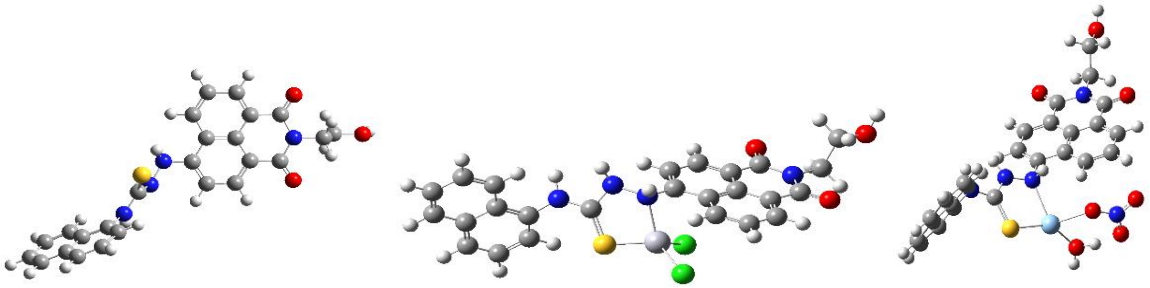

Fig. 13 DFT Optimised structures of **L4** (left), **3** (middle) and **4** (right).

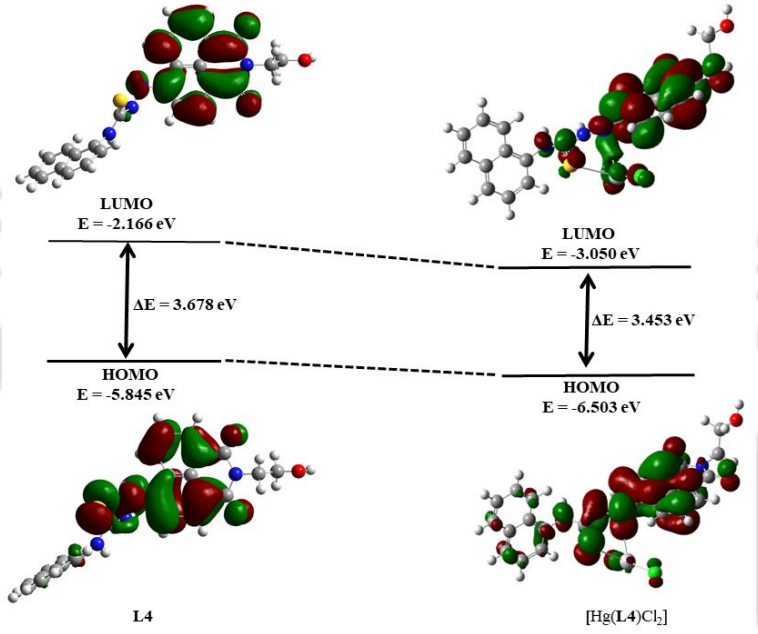

Fig. 14 Energy level diagram in **L4** and **3**.

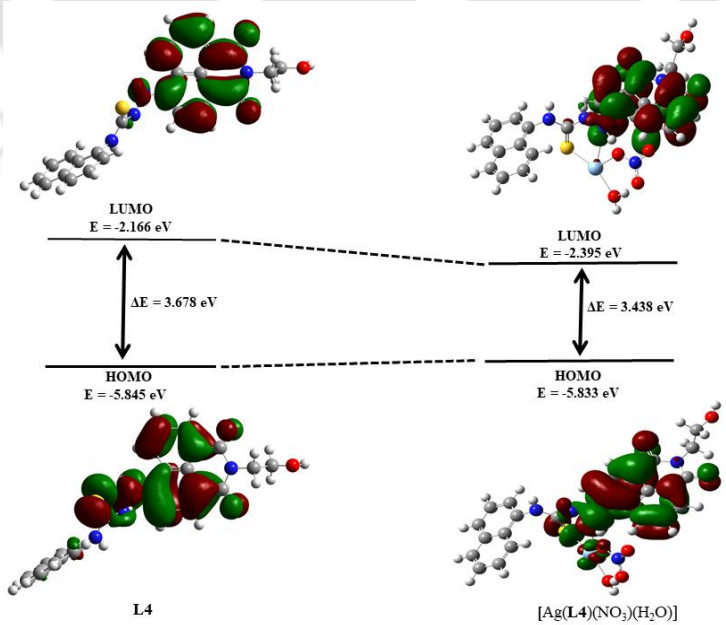

Fig. 15 Energy level diagram depicting HOMO-LUMO in **L4** and **4**.

The effect of complex formation has been found on the energy of HOMO being stabilized by 0.658 eV in **3** and destabilised by 0.012 eV in **4**, while that of LUMO is stabilised (by 0.884 eV in **3** and by 0.229 eV in **4**) in both. The net effect is that HOMO-LUMO energy gap decreased from 3.678 to 3.453 eV in **3** and from 3.678 to 3.438 eV in **4**, which is consistent with the red shift observed in the absorption spectra of **L4** after addition of Hg^{2+} and Ag^{+} ions.

5.8. Cytotoxicity assay

The percentage of cell viability of both cell types was assessed using MTT Assay (Fig. 16). Upon treatment with probe **L4**, the percentage of cell viability in case of both cell types (MDA-MB-231 and HDF cells) were retained up to 5 μM of **L4** with no significant difference with the untreated cells (control). The percentage of cell viability reduced significantly to 91 ± 5 and 87 ± 3 in case of MDA-MB-231 cells when treated with 7.5 μM (*$p \leq 0.05$) and 10 μM (**$p \leq 0.01$) of probe **L4,** respectively when compared to control. Similarly, a significant reduction in cell viability to 92 ± 2 and 86 ± 4 was also observed in case of HDF cells when treated with 7.5 μM (*$p \leq 0.05$) and 10 μM ($^{\#}p \leq 0.001$) of probe **L,** respectively with respect to the control. Based on the results obtained from the cytotoxic assay, 5 μM concentration of probe **L4** was considered for evaluating its fluorescence attributes in cellular imaging.

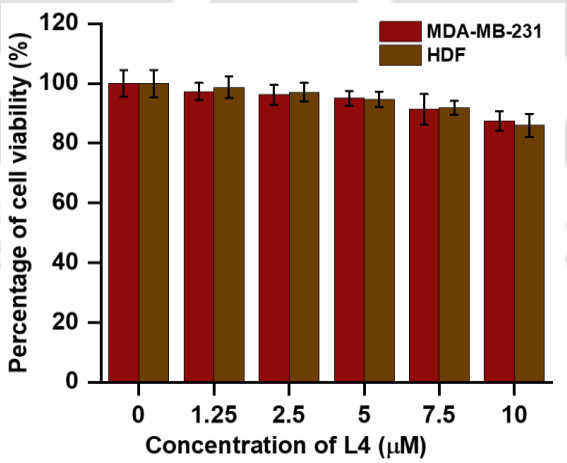

Fig. 16 The evaluation of cytotoxic effect of probe **L4** against MDA-MB-231 and HDF cells based on MTT assay. Data represented as mean ± SD (n = 4), where *$p \leq 0.05$, **$p \leq 0.01$ and $^{\#}p \leq 0.001$ in comparison to control.

5.9. Fluorescence imaging

The fluorescence attributes of probe **L4** alone and probe **L4** along with Hg^{2+} or Ag^{+} was evaluated against both MDA-MB-231 and HDF cells after treating the cells for specified time points (Fig. 17 and Fig. 18). No fluorescence was observed when cells were incubated with only media and 5 μM of probe **L4.** To evaluate the fluorescence property of probe **L4** along with Hg^{2+} or Ag^{+}, cells pre-treated with 5 μM **L4** were incubated with 0.5 μM Hg^{2+} or 0.5 μM Ag^{+} respectively. Following specified incubation time, the cells indicated green fluorescence emission from the intracellular regions. In comparison to Ag^{+}, Hg^{2+} exhibited greater number of cells with intense green fluorescence in both MDA-MB-231 and HDF cells, as observed from the fluorescence images. These experiments revealed that probe **L4** can be used for tracking both Hg^{2+} and Ag^{+} in living cells.

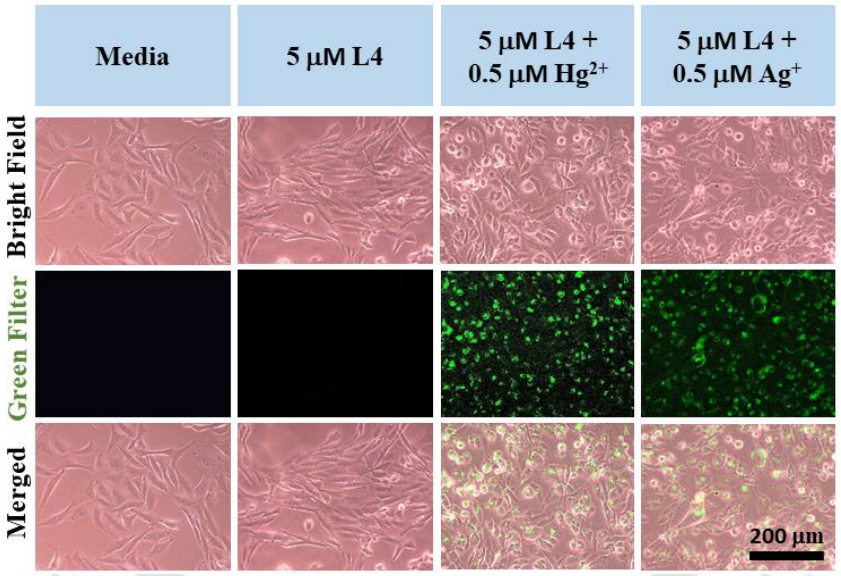

Fig. 17 Bright field and live-cell fluorescence images of MDA-MB-231 cells after incubation with only probe **L4**, probe **L4** with Hg^{2+} and probe **L4** with Ag^{+} for specified incubation time. Scale bar: 200 μm.

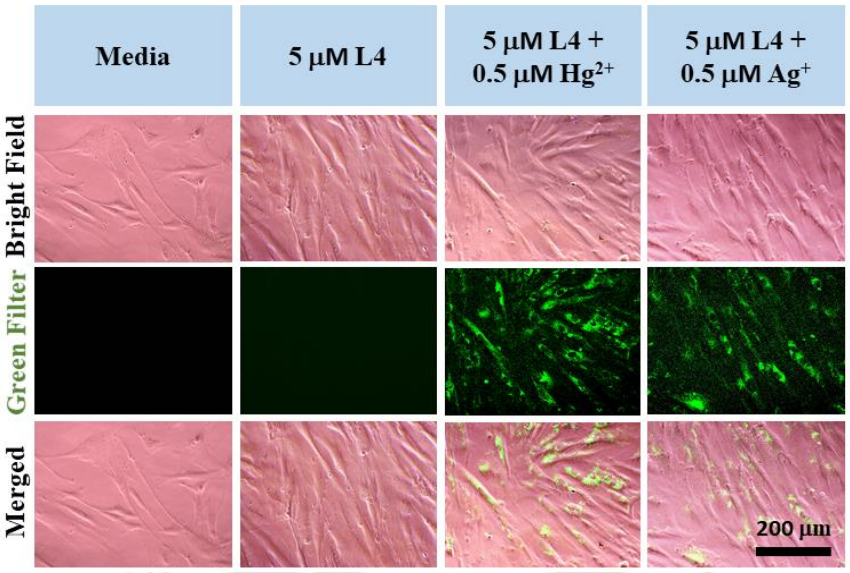

Fig. 18 Bright field and live-cell fluorescence images of HDF cells after incubation with only probe **L4**, probe **L4** with Hg^{2+} and probe **L4** with Ag^{+} for specified incubation time. Scale bar: 200 μm.

5.10. Conclusion

In summary, the potential bidentate ligand **L4** having hydrazinecarbothioamide group appended with 1,8-naphthalimide moiety has been synthesised and characterized. By the virtue of having a soft sulfur donor in the metal-binding site and a fluorophore, **L4** exhibited a colorimetric and fluorometric "*off-on*'' specificity towards the detection of Hg^{2+} and Ag^{+} in presence of other metal ions. The probe **L4** is weakly emissive in nature due to photo induced electron transfer process involving the electron releasing amino group of hydrazinecarbothioamide unit. Upon excitation with 410 nm light an emission peak appeared at 529 nm in presence of Hg^{2+} and peaks at 533 and 527 nm with Ag^{+} ion. The increase in emission intensity indicated that PET process is restricted, after binding of Hg^{2+} and Ag^{+} to **L4**. Detection limit for analyte concentrations were 20 (Hg^{2+}) and 40 nM (Ag^{+}) and these values are less than many other reported probes to the best of our knowledge. Binding of **L4** to Hg^{2+} can be reversed using Na_2EDTA but cannot be reversed with Ag^{+} ion. The sensibility of **L4** towards Hg^{2+} and Ag^{+} ions was not affected by counter anions and also useful for real water samples as well as under physiological pH. A 1:1 binding ratio between Hg^{2+} and Ag^{+} with **L4** was established from Job's plot and mass spectra. Life time decay profile suggested that addition of Hg^{2+} and Ag^{+} ions allows CHEF process to become effective and increased life time of the emissive species formed compared to free **L4**. The DFT/TDDFT calculation indicated a decrease in energy of the HOMO-LUMO gap in **3** and **4** thereby supporting the

experimentally observed red shift in absorption bands. Based on the cytotoxic assay, 5 μM concentration of probe **L4** was considered for intracellular detection of Hg^{2+} and Ag^{+} ions in MDA-MB-231 and HDF cells through "*turn-on*" fluorescence response.

References:

1. M. Formica, V. Fusi, L. Giorgi and M. Micheloni, *Coord. Chem. Rev.*, 2012, **256**, 170–192.
2. E.M. Nolan and S.J. Lippard, *Chem. Rev.*, 2008, **108**, 3443–3480.
3. M.E. Jun, B. Roy and K.H. Ahn, *Chem. Commun.*, 2011, **47**, 7583–7601.
4. Y. Zhang, H. Jiang and X. Wang, *Anal. Chim. Acta*, 2015, **870**, 1–7.
5. M.M. Valko, H. Morris and M.T. Cronin, *Curr. Med. Chem.*, 2005, **12**, 1161−1208.
6. Z.X. Wang and S.N. Ding, *Anal. Chem.*, 2014, **86**, 7436−7445.
7. H.H. Harris, I.J. Pickering and G.N. George, *Science*, 2003, **301**, 1203.
8. B. Weiss, *Toxicol. Sci.*, 2007, **97**, 223–225.
9. P.B. Tchounwou, W.K. Ayensu, N. Ninashvili and D. Sutton, *Environ. Toxicol.*, 2003, **18**, 149–175.
10. J. Mutter, J. Naumann, R. Schneider, H. Walach and B. Haley, *Neuroendocrinol Lett.*, 2005, **26**, 439–446.
11. W.D. Atchison and M.F. Hare, *FASEB J.*, 1994, **8**, 622–629.
12. Mercury Update: Impact on Fish Advisories; *EPA Fact Sheet EPA-823-F-01-001*, Environmental Protection Agency, Office of Water, Washington, DC, 2001.
13. H.-X. Shi, W.-T. Li, Q. Li, H.-L. Zhang, Y.-M. Zhang, T.-B. Wei, Q. Lin and H. Yao, *RSC Adv.*, 2017, **7**, 53439–53444.
14. K. Matsuda, N. Hiratsuka, T. Koyama, Y. Kurihara, O. Hotta, Y. Itoh and K. Shiba, *Clin. Chem.*, 2001, **47**, 763–766.
15. A. Coskun and E.U. Akkaya, *J. Am. Chem. Soc.*, 2005, **127**, 10464–10465.
16. J.L. Sessler, E. Tomat and V.M. Lynch, *J. Am. Chem. Soc.*, 2006, **128**, 4184–4185.
17. M. Hu, J. Fan, J. Cao, K. Song, H. Zhang, S. Sun and X. Peng, *Analyst*, 2012, **137**, 2107–2111.
18. D. Kagan, C.P. Marzal, S. Balasubramanian, S. Sattayasamitsathit, K.M. Manesh, G.U. Flechsig and J. Wang, *J. Am. Chem. Soc.*, 2009, **131**, 12082–12083.
19. D. Karunasagar, J. Arunachalam and S. Gangadharan, *J. Anal. At. Spectrom.*, 1998, **13**, 679–682.

20. Y. Li, C. Chen, B. Li, J. Sun, J. Wang, Y. Gao, Y. Zhao and Z. Chai, *J. Anal. At. Spectrom.*, 2006, **21**, 94–96.
21. L.G. Martin, L.T. Jongwana and A.M. Crouch, *Electrochim. Acta*, 2010, **55**, 4303–4308.
22. S. Goswami, S. Das and K. Aich, *Tetrahedron Lett.*, 2013, **54**, 4620–4623.
23. N. Behera and V. Manivannan, *J. Photochem. Photobiol. A: Chem.*, 2018, **353**, 77–85.
24. N. Behera and V. Manivannan, *ChemistrySelect*, 2017, **2**, 11048–11054.
25. J.P. Nandre, S.R. Patil, S.K. Sahoo, C.P. Pradeep, A. Churakov, F. Yu, L. Chen, C. Redshaw, A.A. Patil and U.D. Patil, *Dalton Trans.*, 2017, **46**, 14201–14209.
26. A. Manna, D. Sarkar, S. Goswami, C.K. Quah and H.K. Fun, *RSC Adv.*, 2016, **6** 57417–57423.
27. S. Goswami, A.K. Das and S. Maity, *Dalton Trans.*, 2013, **42**, 16259–16263.
28. S. Mahata, A. Bhattacharya, J.P. Kumar, B.B. Mandal and V. Manivannan, *J. Photochem. Photobiol. A: Chem.*, 2020, **394**, 112441.
29. S. Khatua and M. Schmittel, *Org. Lett.*, 2013, **15**, 4422–4425.
30. S. Mahata, G. Janani, B.B. Mandal and V. Manivannan, *J. Photochem. Photobiol. A: Chem.*, 2021, **417**, 113340.
31. H.C. Hung, C.W. Cheng, Y.Y. Wang, Y.J. Chen and W.S. Chung, *Eur. J. Org. Chem.*, 2009, **36**, 6360–6366.
32. J. Fan, C. Chen, Q. Lin and N. Fu, *Sensors Actuators B: Chem.*, 2012, **173**, 874–881.
33. Z.E. Chen, H. Zhang and Z. Iqbal, *Spectrochim. Acta – Part A Mol Biomol. Spectrosc.*, 2019, **215**, 34–40.
34. F. Ye, X.-M. Liang, K.-X. Xu, X.-X. Pang, Q. Chai and Y. Fu, *Talanta*, 2019, **200**, 494–502.
35. R. Roy, S. Rakshit, S. Bhar and S.C. Bhattacharya, *RSC Adv.*, 2015, **5**, 67833–67840.
36. D. Singhal, N. Gupta and A.K. Singh, *RSC Adv.*, 2015, **5**, 65731–65738.
37. Y. Lv, L. Zhu, H. Liu, Y. Wu, Z. Chen, H. Fu and Z. Tian, *Anal. Chim. Acta*, 2014, **839**, 74–82.
38. X. Zhang, Y. Xu, P. Guo and X. Qian, *New J. Chem.*, 2012, **36**, 1621–1625.
39. W. Shi, Y. Chen, X. Chen, Z. Xie and Y. Hui, *J. Lumin.*, 2016, **174**, 56–62.
40. S. Chen, W. Wang, M. Yan, Q. Tu, S.W Chen, T. Li, M.S. Yuan and J. Wang, *Sensors Actuators B: Chem.*, 2018, **255**, 2086–2094.
41. W. Shen, L. Wang, M. Wu and X. Bao, *Inorg. Chem. Commun.*, 2016, **70**, 107–110.

42. S.Y. Lee, K.H. Bok and C. Kim, *RSC Adv.*, 2017, **7**, 290–299.
43. K. Tsukamoto, Y. Shinohara, S. Iwasaki and H. Maeda, *Chem. Commun.*, 2011, **47**, 5073–5075.
44. Y.-M. Zhang, X.-P. Chen, G.-Y. Liang, K.-P. Zhong, Q. Lin, H. Yao and T.–B. Wei, *New J. Chem.*, 2018, **42**, 10148–10152.
45. A. Panja and K. Ghosh, *New J. Chem.*, 2019, **43**, 5139–5149.
46. W. Saiyasombat and S. Kiatisevi, *RSC Adv.*, 2021, **11**, 3703–3712.
47. M.H. Lee, J.H. Han, J.H. Lee, H.G. Choi, C. Kang and J.S. Kim, *J. Am. Chem. Soc.*, 2012, **134**, 17314–17319.
48. P.A. Panchenko, O.A. Fedorova and Y.V. Fedorov, *Russ. Chem. Rev.*, 2014, **83**, 155–182.
49. Z. Bao, C. Qin, J.-J. Wang, J. Sun, L. Dai, G. Chen and F. Mei, *Sensors Actuators B: Chem.*, 2018, **265**, 234–241.
50. C.N.R. Rao and R. Venkataraghavan, *Spectrochim. Acta*, 1962, **18**, 541–547.
51. G. Janani, M.M. Pillai, R. Selvakumar, A. Bhattacharyya and C. Sabarinath, *Biofabrication*, 2017, **9**, 015016.

Appendix:

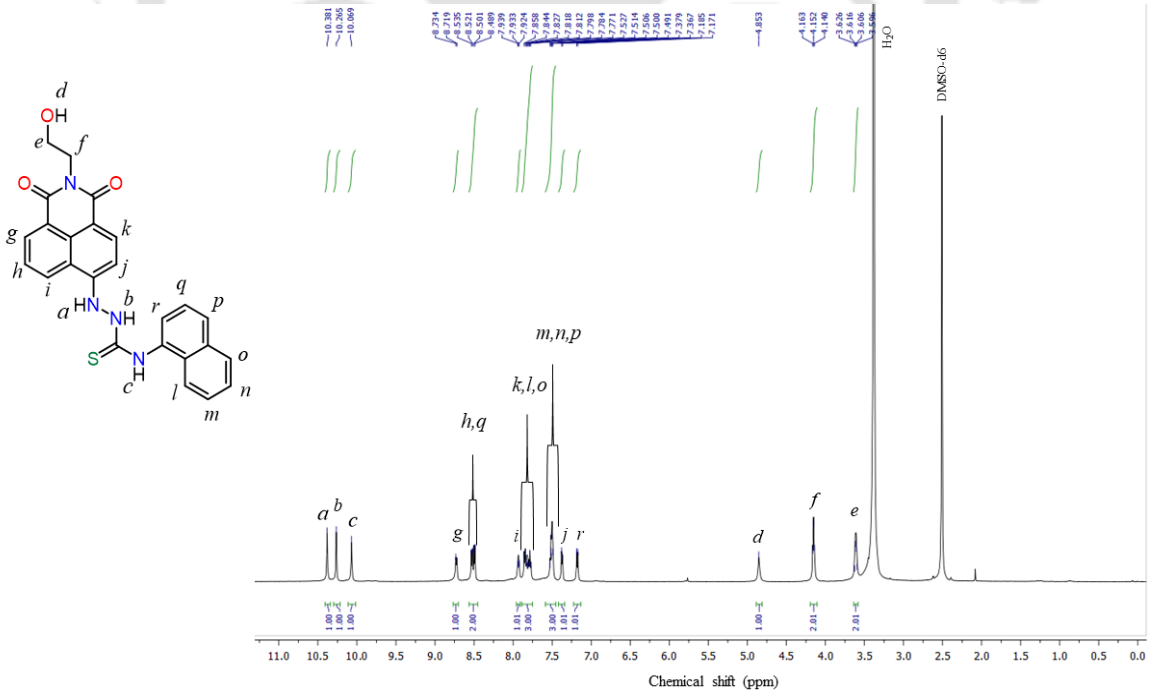

Fig. A1 ^{1}H NMR of **L4**

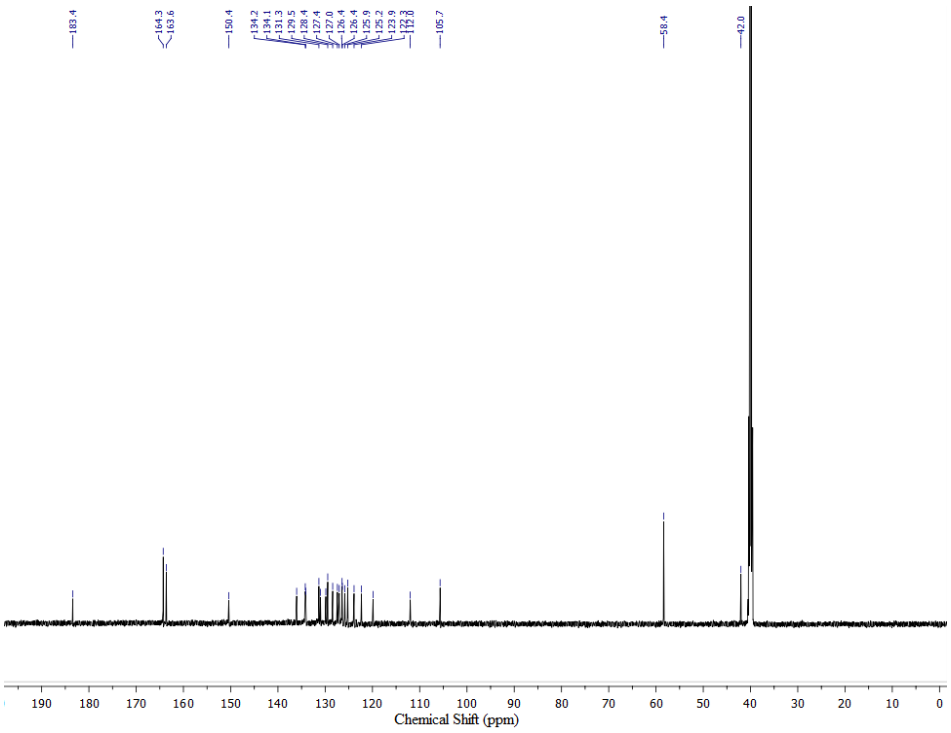

Fig. A2 ^{13}C NMR of **L4**

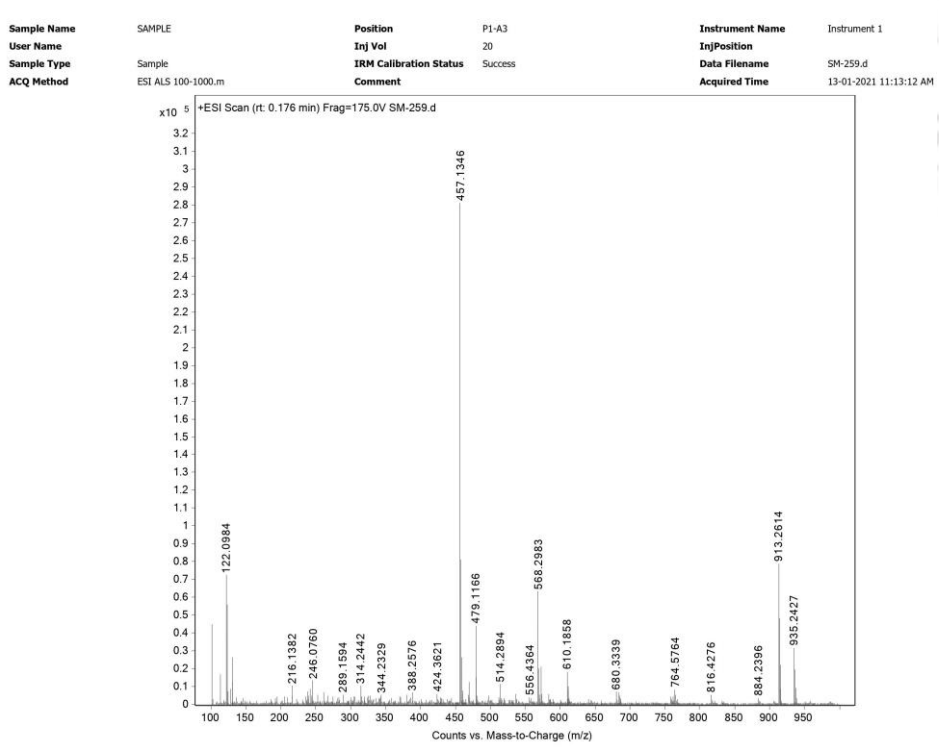

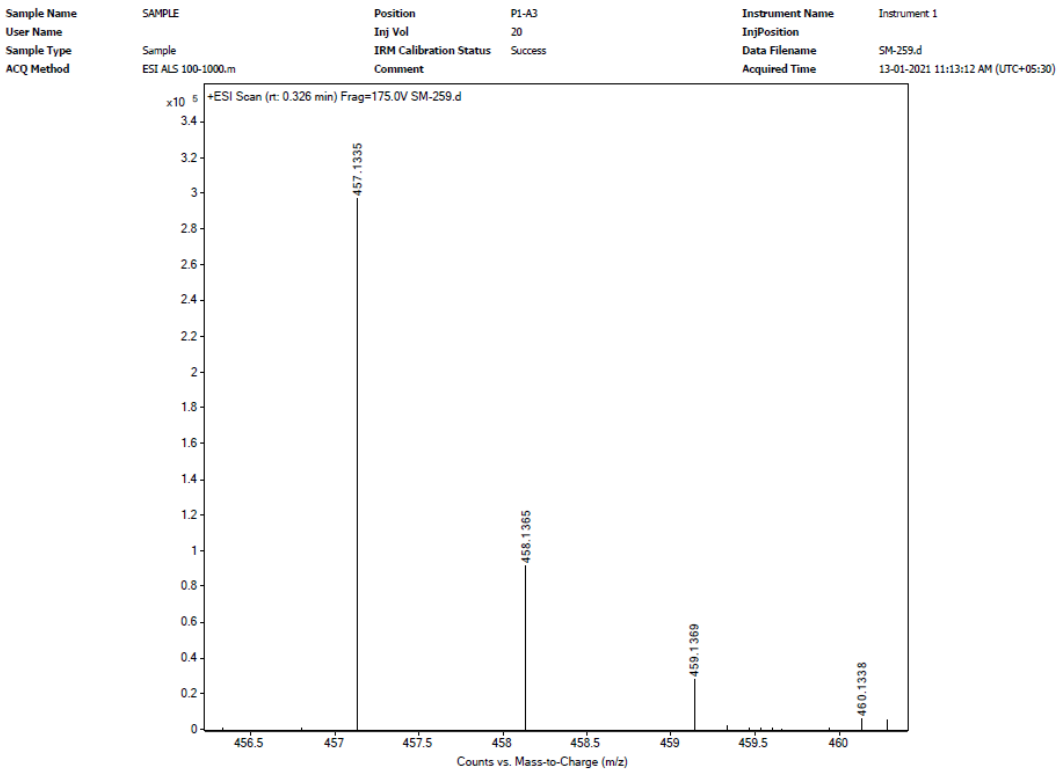

Fig. A3 HRMS-ESI (+) Full Mass spectrum of **L4** (top) and expanded (bottom).

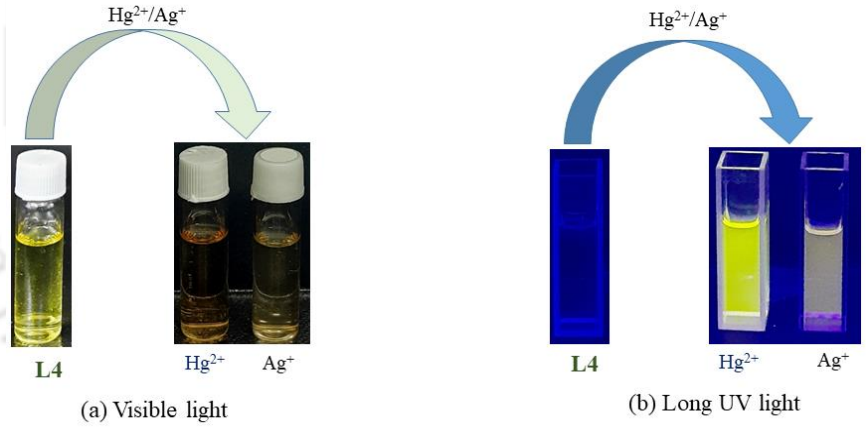

Fig. A4 Images under (a) visible light and (b) long UV light of **L4** solution upon addition of Hg^{2+} and Ag^{+} ions.

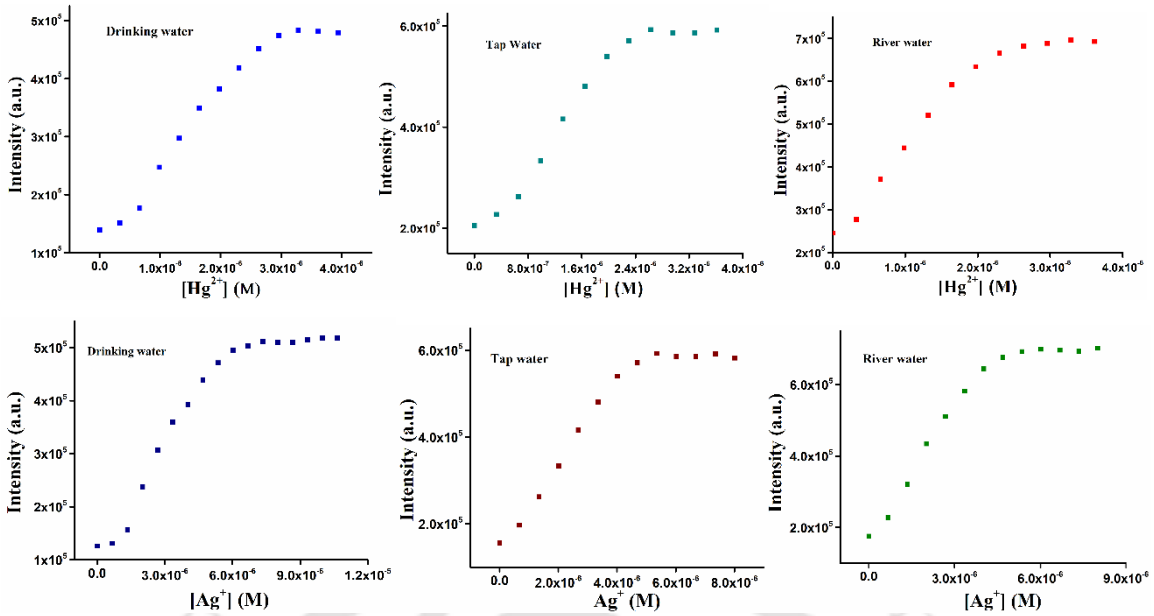

Fig. A5 Detection of Hg^{2+} and Ag^{+} in real water samples.

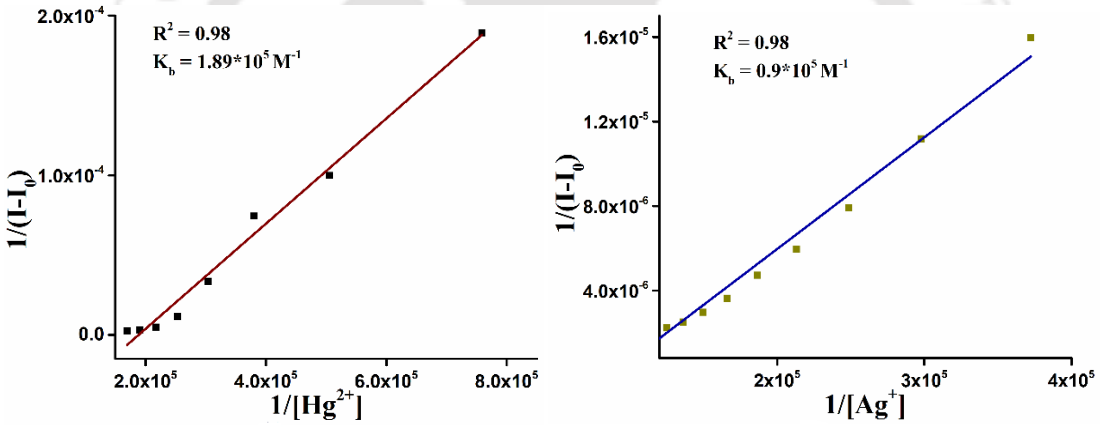

Fig. A6 Benesi-Hildebrand plots for the determination of binding constant.

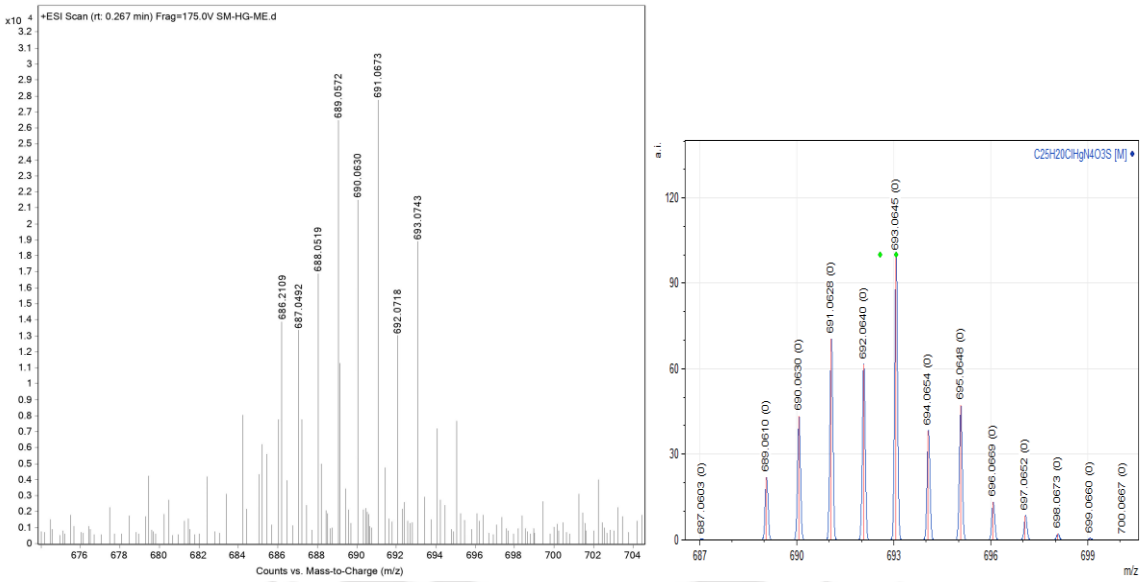

(a)

Sample Name	WASH	**Position**	P1-A10	**Instrument Name**	Instrument 1
User Name		**Inj Vol**	20	**InjPosition**	
Sample Type	Sample	**IRM Calibration Status**	Success	**Data Filename**	SM-HG-ME.d
ACQ Method	ESI ALS 100-1000.m	**Comment**		**Acquired Time**	06-09-2021 02:50:59 PM (UTC+05:30)

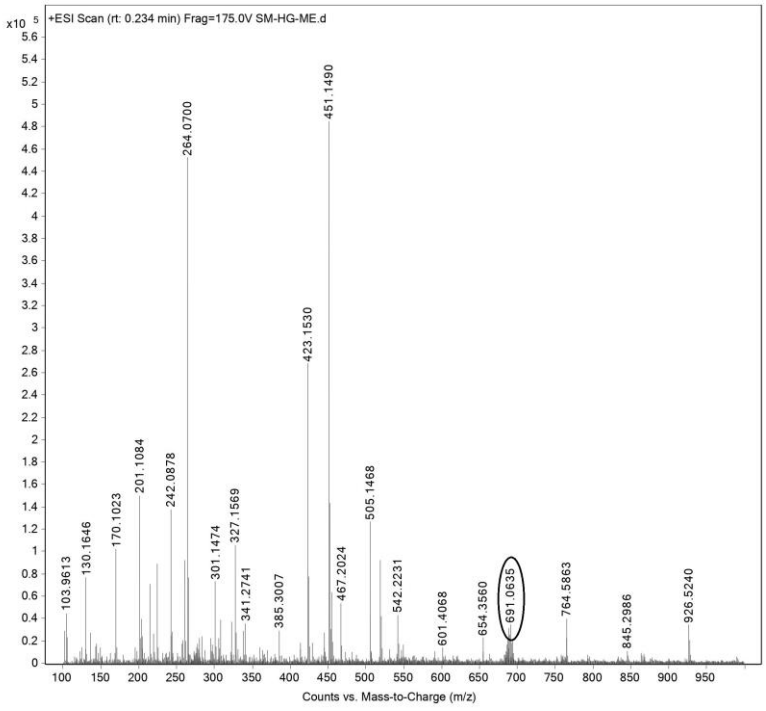

(b)

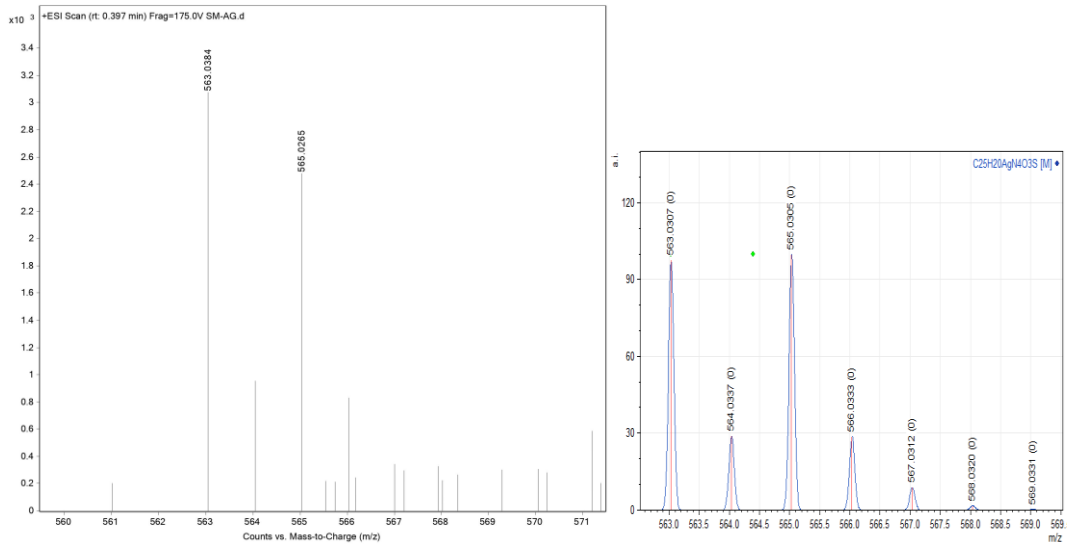

(c)

Fig. A7 Experimental (left) and calculated (right) mass spectrum using mMass software of (a) [Hg(**L4**)Cl]$^+$ and (b) full mass spectrum of [Hg(**L4**)Cl]$^+$ and (c) [Ag(**L4**)]$^+$.

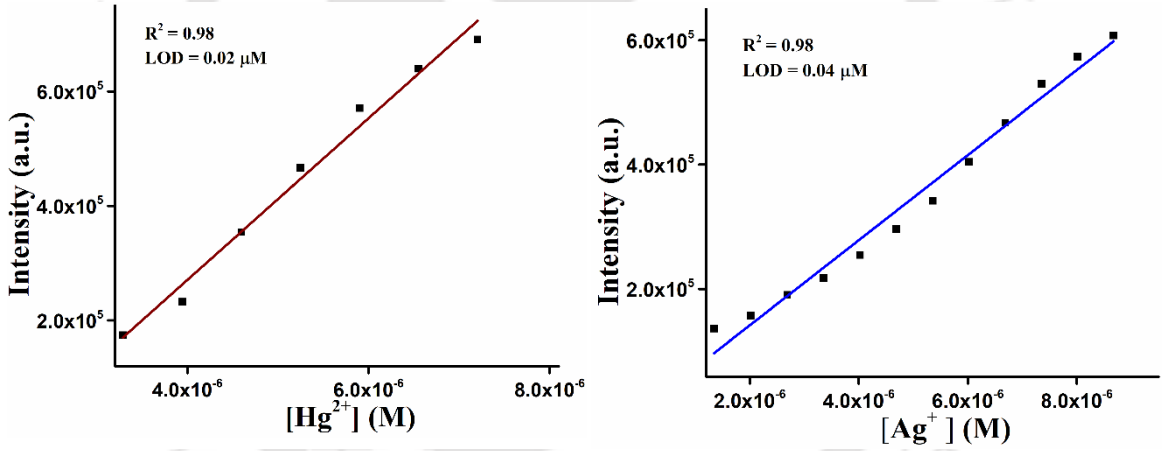

Fig. A8 Detection limit plot for (left) Hg^{2+} and (right) Ag^+.

Table A1. Comparison table using some reported probes towards detection of Hg^{2+} and Ag^+ with **L4**.

Probes	Metal ion	Solvent	LOD	Ref.
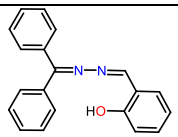 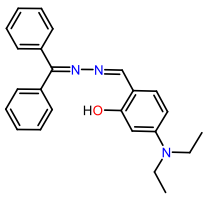	Hg^{2+}	$CH_3CN:H_2O$ (4 : 1 *v/v*)	3.82 µM 0.56 µM	35

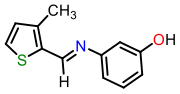	Hg^{2+}	CH_3OH/H_2O (8/2; *v/v*)	20 μM	36
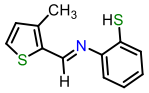				
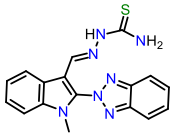	Hg^{2+} (“*turn off*”) Ag^{+} (“*turn on*”)	CH_3CN/MOPS (*v/v*) of 15/85,	142 nm (Hg^{2+}) 97 nm (Ag^{+})	37
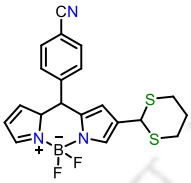	Hg^{2+} and Ag^{+}	THF–water (85 : 15 *v/v*)	0.14 mM (Hg^{2+}) 0.65 mM (Ag^{+})	38
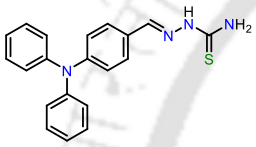	Hg^{2+} (“*turn off*”) Ag^{+} (bathochromic shift)	(DMSO/ H_2O) 9:1(*v:v*),	0.19 μM (Hg^{2+}) 0.59 μM (Ag^{+})	39
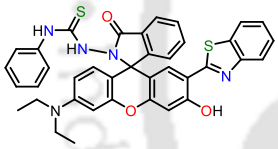	Hg^{2+} and Ag^{+}	HEPES (10 mM, pH 7.4) 40% THF (*v/v*).	0.27 μM (Hg^{2+}) 0.45 μM (Ag^{+})	40
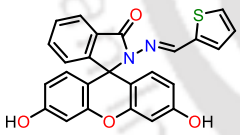	Hg^{2+} and Ag^{+}	Ethanol–H_2O (3:2, *v/v*),	0.21 μM. Hg^{2+} 0.009 μM. Ag^{+}	41
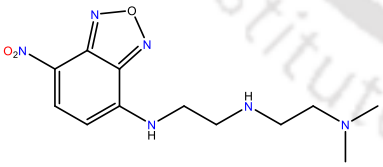	Hg^{2+} and Ag^{+}	Buffer–CH_3CN (7 : 3, *v/v*)	0.05 μM (Hg^{2+}) 0.12 μM (Ag^{+})	42
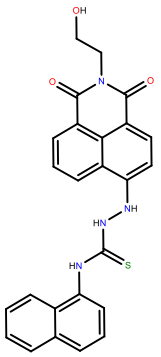	Hg^{2+} and Ag^{+} (“*turn on*”)	CH_3OH : HEPES buffer solution (5 mM, 7:3, *v/v*, pH = 7.4)	0.02 μM (Hg^{2+}) 0.04 μM (Ag^{+})	This work

Thesis Summary:

This dissertation includes five chapters out of which Chapter 1 contains introduction about fluorescence and various other sensing processes. Some recent developments in metal ion sensing probes have been discussed. Along with this, materials, methods and instrumental details have been described. In Chapter 2, heterocyclic probe 3-(1-isoquinolinyl)imidazo[5, 1-*a*]isoquinoline (**L1**) was evaluated as a unique probe for selective detection of Pd^{2+} ion. It has been found that **L1** not only detects Pd^{2+} ion in solution but also in living cells with high accuracy. Similarly, in Chapter 3, 3-(2-hydroxyphenyl)imidazo[5, 1-*a*]isoquinoline (**L2H**) an analogues of **L1** is found to be Cu(II) sensor and its Cu(II) complex for selective detection of CN^- ion. **L2H** has exhibited specific recognition of Cu^{2+} ion by forming a complex of formula [Cu(**L2**)$_2$], which in turn showed recognition for CN^- ions in CH_3CN/aqueous HEPES-buffer solution (5 mM, pH = 7.4, 6:4, *v/v*). The cell images showed that intracellular Cu^{2+} and CN^- can be detected using **L2H** and [Cu(**L2**)$_2$] complex respectively. In Chapter 4, a Schiff base (**L3**) containing coumarin and pyrene moieties is synthesized and characterized. Probe **L3** is unique and highly selective in its property of recognising trivalent (Al^{3+}, Cr^{3+} and Fe^{3+}) ions. A 7.5 μM concentration of probe **L3** showed higher percentage of cell viability in the cytotoxicity study and hence it can be used for intracellular detection of M(III) ions [M = Al, Cr, Fe] in living cells through "*turn-on*" fluorescence phenomenon. The probe (**L4**) having hydrazinecarbothioamide and 1,8-naphthalimide moieties was synthesized and evaluated for its metal ion sensing ability in Chapter 5. It exhibits a selective and sensitive colorimetric as well as fluorescent recognition of Hg^{2+} and Ag^+ ions in CH_3OH - HEPES buffer solution (5 mM, 7:3, *v/v*, pH = 7.4). Based on the cytotoxic assay, 5 μM concentration of probe **L4** is considered for intracellular detection of Hg^{2+} and Ag^+ ions in MDA-MB-231 and HDF cells through "*turn-on*" fluorescence response.

Future Perspective:

In Chapter 2 and 3 we have seen that 3-(1-isoquinolinyl)imidazo[5, 1-*a*]isoquinoline and its analogous 3-(2-hydroxyphenyl)imidazo[5, 1-*a*]isoquinoline are acting as fluorescent probes for the selective detection of Pd^{2+} and Cu^{2+} ion along with CN^- ion respectively. So various probe molecules bearing imidazo[5, 1-*a*]isoquinoline unit can act as a novel fluorophore unit for the detection of various analyte along with cell imaging studies. Among several types of chemosensors, that are able to detect the analytes have very favourable future prospect. The probe molecules having the ability to detect the various analytes/ions in aerobic and aqueous

medium will be highly required in future. For the selective detection of rare earth metal ions, the design of chemosensors is a hard challenge mainly due to their poor coordination properties in aqueous environment. In the field of environmental analysis, sensors such as chemical or biological sensors have become more accurate and small, by making their usage very practical in distant and inaccessible areas where manual sampling is difficult or unsafe.

List of Publications

From Thesis:

1. S. Mahata, A. Bhattacharya, J. P. Kumar, B. B. Mandal and V. Manivannan, *J. Photochem. Photobiol. A: Chem.*, 2020, **394**, 112441.
2. S. Mahata, G. Janani, B. B. Mandal and V. Manivannan, *J. Photochem. Photobiol. A: Chem.*, 2021, **417**, 113340.
3. S. Mahata, S. Dey, B. B. Mandal and V. Manivannan, *J. Photochem. Photobiol. A: Chem.*, 2022, **427**, 113795.
4. S. Mahata, S. Kumar, S. Dey, B. B. Mandal and V. Manivannan, *Inorg. Chim. Acta*, 2022, **535**, 120876.

Others:

1. J. Bori, N. Behera, S. Mahata and V. Manivannan, *ChemistrySelect*, 2017, **2**, 11727–11731.
2. J. Bori, S. Mahata and V. Manivannan, *Inorg. Chim. Acta*, 2020, **506**, 119506.
3. A. Bhattacharya, S. Mahata, A. Bandyopadhyay, B. B. Mandal and V. Manivannan, *Luminescence*, 2022, 1. https://doi.org/10.1002/bio.4232.